The University Of Sheffield.

Developing Smoothed Particle Methods for Modelling Continuum Mechanical and Thermal Behaviour in Nuclear Fuel and Cladding

Thesis
for the award of
DOCTOR OF PHILOSOPHY

by
Matthew Horton

March 2022

1st Supervisor: Dr Karl Travis 2nd Supervisor: Dr Amy Gandy

Industrial Sponsor: Dr Mark Bankhead (NNL)

University of Sheffield

Department of Materials Science and Engineering

0.1 Abstract

The purpose of this work is to explore the validity of using smoothed particle methods for future applications within nuclear fuel modelling. The particle nature of the method makes it attractive for modelling the complex multi-physics environment of nuclear fuel. This work however focuses on the fundamental accuracy of the method within the bounds of current simple fuel performance models.

The thesis is separated into four main sections: examination of simple heat flow models, the effect of particle arrangement, complex heat flow within thermal models of nuclear fuel and finally simple mechanical models.

The examination of heat flow by smoothed particle methods begins with simple 1D models. Three approaches to modelling heat flow identified in the literature are tested and the results compared using errors calculated from the complimentary analytical models. One method is selected for further use within this work due to achieving the lowest error in results. Particular attention is given to the effect of boundary conditions on the models. Two main methods for handling boundaries are explored: the use of fixed boundary particle values against the use of dynamically assigned values. Dynamic boundaries are shown to offer reduced error compared to the fixed case. The effect of these boundaries are further explored for 2D models under both transient and steady state conditions. Dynamic boundaries are shown to suffer for discontinuous boundaries and more complex boundary shapes. A method is proposed for handling these issues and is shown to offer reduced error in the analytical model compared with the fixed boundary case.

The effect of particle arrangement is explored for the more complex circular geometry which is applicable to models of nuclear fuel used within licensing codes. Three main particle arrangements are tested: square lattice, triangular lattice and concentric particle rings. The effect of relaxing these particle structures under density-dependent forces is also explored. Each of these particle arrangements are tested using the smoothed particle equation for heat flow identified in the earlier section. The model used is steady state heat flow in a 2D annulus and is considered due to the existence of a well-defined analytical model. This model is considered as a good simplified model for internally heated cladding around nuclear fuel. The triangular lattice is identified as the superior choice for particle arrangement for further use within this work due to the low errors demonstrated coupled with the fast construction and applicability to other geometries.

These findings are then applied to a simple 2D model of nuclear fuel, equivalent to those found within current codes used for fuel licensing. This model is built up using simple 1D models for the purposes of validation. Each model presented has a well-defined analytical solution and introduces a new aspect of complexity in isolation of the others for the purposes of validation. A method for including heat generation is proposed by modification of methods given in the literature. This method is shown to be successful with boundary conditions being the largest contributing factor to the error. A modification to the heat equation to handle thermal interfaces is tested. The results although successful show room for further improvement by consideration of the boundary position between particle pairs. Multiple equations to handle a convective boundary condition within smoothed particle methods are proposed. One of these methods is shown to give acceptable results however future improvements are discussed. These complexities are then combined into the 2D fuel model and the results are shown to converge. This chapter findings support the notion that smoothed particle methods are capable of reproducing models currently in use within fuel licensing codes and is therefore worthy of further exploration by the National Nuclear Laboratory (NNL).

Finally the work is extended to examine mechanical behaviours within simple nuclear fuel models. The equations for handling thermally induced strains within smoothed particle methods are introduced. The validity of these equations are first tested within 1D simple simulations using various corrective factors: velocity smoothing, density evolution and artificial viscosity. Velocity smoothing is found to make little impact on the simulation results, however the other two methods are shown to be required, particularly under the use of dynamic boundaries. These findings are then applied to a simplified cladding model with thermally induced strains in 2D. The model results are shown to converge with the analytical results. The future scope of the implementation of mechanical behaviour is outlined and a path toward future implementation of smoothed particle methods within nuclear fuel licensing codes is discussed.

0.2 Acknowledgements

Thanks to the EPRSC and NNL for providing the funding for this research. Special thanks is given to my supervisor Dr Karl Travis for all of his support and guidance throughout this work, without which, it would not have been possible. I am also thankful to Mark Bankhead for all the insight he provided me. Finally of course I must thank my partner Ellie, without her love, support and patient support this thesis would have never been written.

Nomenclature

α	Thermal expansively
Δ_P	Particle spacing
$\dot{q}$	Heat generation per unit length
ϵ	Strain
κ	Thermal conductivity
λ	Signal wavelength
ν	Poisson's ratio
Π	Artificial dissipation term
ρ	Density
σ	Stress tensor
A	Signal amplitude
c_0	Speed of sound in the medium at density ρ_0
C_p	Specific heat
D_T	Thermal diffusivity
dt	Time step
E	Young's modulus
E_K	Kinetic energy
E_P	Potential energy
H	Weight function cut off length
h	Coefficient of convection
i, j	Particle indexes
L	Length
M	Total mass
m_i	Mass of particle i
N	Number of particles

P	Pressure
Q	Heat flux
r_i	Position of particle i
T	Temperature
t	time
U	Residual Error
V	Volume
v	velocity
W	Weight function
x	x co-ordinate
y	y co-ordinate

Contents

List of Figures

List of Tables

Chapter 1

Motivation & Review of Fuel Performance Modelling

1.1 Motivation

Significant change has taken place since the first commercial-scale nuclear reactors were proposed in the UK in 1955 [1, 2]. Now with the fourth generation phase of nuclear reactors on the horizon both in the UK and worldwide there is widespread interest in new fuel compositions and reactor designs. The novel nature of these proposals means that robust testing must take place before any new fuel composition or reactor design can be accepted for commercial use. Proposals have already been made within the UK for advanced modular reactors [3]. For these designs to be put into use after development, safety cases must be created. Of particular note is the Rolls Royce Small Modular Reactor (SMR) development program which is 'forecast to create 40,000 regional UK jobs by 2050 and generate £52bn in economic benefit' [4]. This SMR program will require creation of new licensing codes to satisfy the regulator, an issue on which the National Nuclear Laboratory (NNL) will undoubtedly need to consult.

The nuclear safety technical assessment guide [5] states that 'computer code analysis of plant design and operation forms an important part of a modern safety case'. Computer based modelling will therefore play an integral part in the licensing of GEN IV reactors. It is therefore an opportunity for current fuel performance codes (FPCs) to be reviewed and new methodologies proposed and explored.

The codes currently used within British nuclear fuel licensing are primarily 1D codes such as ENIGMA [6]. These codes primarily track the material temperature, stress and strain. The models assume axial symmetry which allows the circular fuel rod geometry to be represented as 1D. This assumption disregards a large amount of the complex multi-physics phenomenon which occurs within nuclear fuel. This means that there is a great amount of improvement which can be made to the predictions of the next generation of fuel licensing codes if some or all of these more complex behaviours are added.

Nuclear fuel operating within a reactor represents an extremely complex environment [7]. The fuel assembly usually consists of many fuel pins within an outer sleeve as shown in Fig.1.1 and Fig.1.2. Each fuel pin contains many fuel pellets stacked on top of each other with an outer cladding tube. The process of nuclear fission which occurs within the fuel elements causes fission products to be produced. These can be heavy elements such as plutonium and caesium or light elements such as hydrogen gas. The process of fission generates heat. This heat causes the thermal and mechanical properties of the fuel material to change, however this is accompanied by the change in properties due to the conversion of the fissile elements to fission products. This conversion also affects the micro structure as grain densification can take place as well as micro bubbles and micro cracks forming due to the fission gas. These can then form into cracks due to pore migration and a build up of gas. The conversion of the fissile elements is measured as 'burn up'. Refuelling occurs on a time scale of years which mean burn up varies very slowly compared to the time scales of the mechanical issues of the fuel element. This complexity is taken further as the fuel distorts outward into an 'hourglass' shape and therefore applies an uneven distribution of pressure on the cladding. The metal of the cladding is also effected by the cycles of ramping up and down the power output of the reactor which causes the heat to vary. This can cause strain softening and creep. The final result is that if not monitored and correctly predicted, then this behaviour can cause cracking of the fuel cladding and the release of active material.

This complexity of nuclear fuel means that there are benefits and opportunities for the production of more complex modelling methods within the licensing codes. Many modern nuclear fuel performance codes (FPCs) have already been developed to examine one or multiple of the behaviours discussed. Unfortunately however many modern nuclear fuel performance codes are poorly adapted to fast modelling of multi-physics phenomena. This is due mainly to the Finite Element Method (FEM) mathematical framework onto which they are constructed. FEM, although a well established and reliable modelling method, requires re-meshing of the system to be completed when modelling phenomena such as crack propagation and bubble formation, both of which are important for initial fuel evaluation by FPCs. FEM also requires large amounts of computation when dealing with material interfaces, also essential to full fuel pin modelling.

One potential alternative method to be explored in this work is Smoothed Particle Applied Mechanics (SPAM) also referred to as Smoothed Particle Hydrodynamics (SPH). SPAM offers the potential for a significant reduction in computational time due to the reduction of the governing Partial Differential Equations (PDEs) to Ordinary Differential Equations (ODEs) in its formulation. The scope of this reduction was recently demonstrated with the SWIFT code, a massively parallel code, with task based parallelism, created primarily for Astrophysical modelling [9] as well as the fast Graphics Processing Unit (GPU) based codes of the DualSPHysics [8] program capable of running on a basic office workstation. This work aims to explore the agreement of a variety of SPAM models with increasing complexity with both analytical solutions and models created using FEM, such as those currently used within FPCs or for the validation of current FPCs.

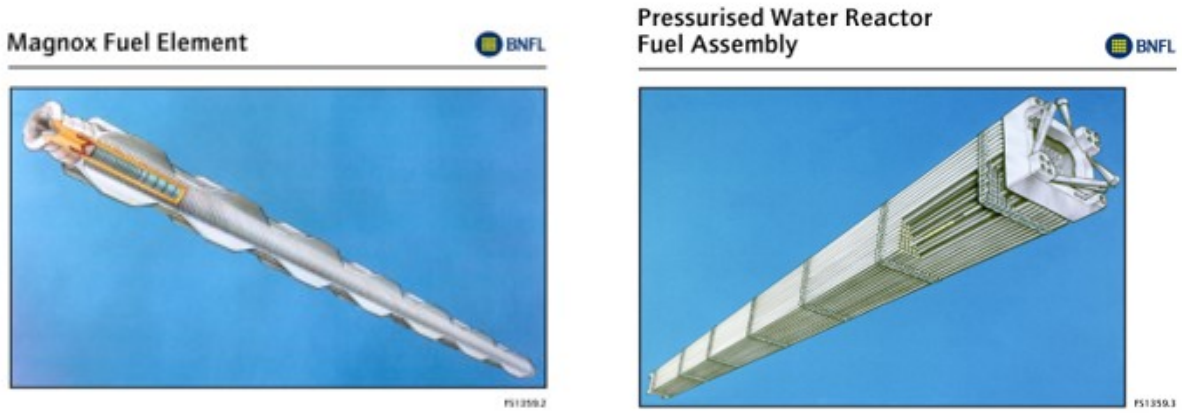

Figure 1.1: Two different fuel assemblies designed for different nuclear reactors. Magnox (left) and PWR (right). Copyright National Nuclear Laboratory.

SPAM has the potential to bring more efficient modelling methods in the cases of crack propagation and interactions across material interfaces. In the case of nuclear fuel these phenomena can be seen at every length scale of interest. Under the FRA-ANP specification for European RG MOX the mean grain size is limited to $50\mu m$ [10]. Molecular dynamics studies of micro-crack initiation from Helium bubbles in UO_2 fuel have already been carried out by CEA researchers at sub-grain scales for bubbles up to a diameter of $10\mu m$ [11]. At the far end of the spectrum, a typical AGR fuel rod assembly (Fig.1.2) is approximately 1m in length with each pellet 14.5mm in diameter and approximately the same length [12]. At this scale an example of work that has already been carried out is the examination of crack formation under cyclic loading in individual pellets using peridynamics [13]. Similarly some work has been done examining crack formation due to Pellet Cladding Mechanical Interactions (PCMI) [14]. Within all of these studies the main challenges presented are the material interfaces: grain boundaries, gas bubble grain interfaces, cladding pellet interface with gas, new surface interface generation in crack formation. The particulate nature of SPAM offers the potential for more robust simulation of these interfaces, however such simulations will require multi-physics phenomena which will present certain challenges as yet unexplored within SPAM.

Unfortunately before SPAM can be applied at the level of modern FPCs, more simple validation cases must be considered. As already discussed the current standard of licensing codes does not exceed 1D. ENIGMA has seen some further developments to include whole core simulations [15] however this is still achieved with a single dimension and simplified physics used to represent each individual element within the core. It is therefore important that if SPAM is to be seriously considered for further development within FPCs its accuracy at reproducing simple models such as those demonstrated by the licensing standards of ENIGMA must be examined and these simple models validated.

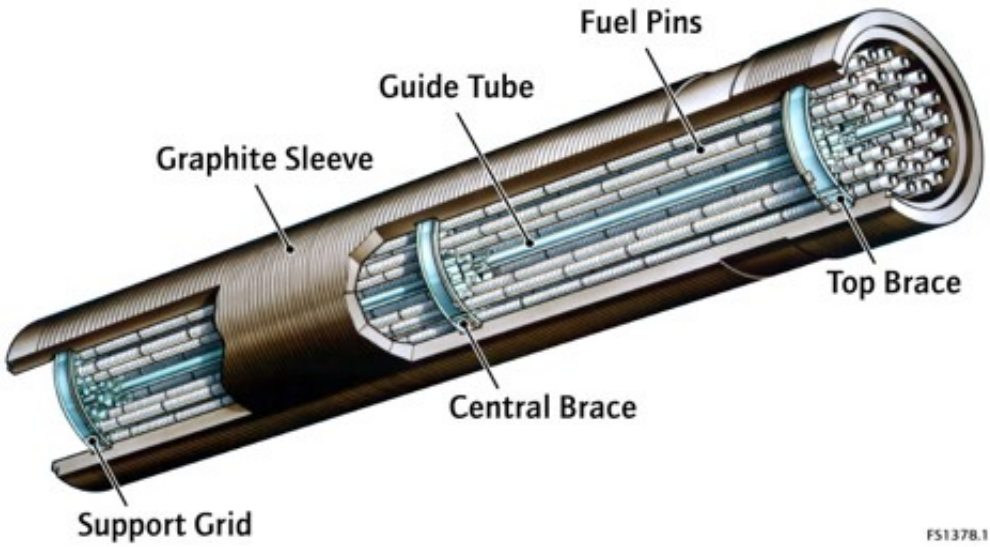

Figure 1.2: A look inside a typical fuel assembly. Copyright National Nuclear Laboratory.

1.2 Fuel Performance Codes

Nuclear Fuel rod Performance Codes (FPCs) are produced and used by academic institutions, government nuclear bodies and nuclear fuel vendors amongst others. The primary function of FPCs is to predict the behaviour of fuel rods under either normal operating conditions or accident conditions. Examples of codes used for simulating accident conditions are FRAPTRAN (USA), TRANSURANUS (Germany) and SCANAIR (France). On the other hand codes used for simulating normal operation conditions are BISON (USA), COMETHE (Belgium) and ENIGMA (UK) [16]. Due to the nature of the research being carried out, the methods of continuum mechanics being developed may have future applicability to both these fields of FPCs however only those designed for normal operating conditions will be examined and referred to from here onward. The reason for this is that data surrounding the normal operation of reactors is more prevalent and useful data within the same regimes can be produced with the tools available within the academic environment.

To understand the problems faced by these FPCs, and thus the scope for improvement that is the purpose of this research, it is first helpful to examine the general basis of current fuel performance codes and the various features and capabilities that have already been successfully implemented.

1.2.1 Basis of Current FPCs: Continuum Mechanics

The vast majority of FPCs are continuum mechanics based such as BISON, FALCON and ENIGMA [17–19]. Continuum mechanics models a material as continuous matter, ignoring the true particle-like nature of the atoms which make up the material. The material being modelled must therefore be above an appropriate length scale, usually defined as the scale at which there is no density variation between microscopic volumes being considered. For solids this is roughly on the order of $1\mu m$ [20]. From here the continuum description models variables such as density, velocity and energy density as fields, requiring them to be continuous everywhere within the medium. These fields are then converted into the fields of interest such as the stress, or heat flux, by means of

the constitutive relations [21]. The simplest example of these constitutive relations is the ideal gas law, but many exist. From here the fields generated by the constitutive relations coupled with the equations of motion allows the evolution of the original field variables to be determined. This means the system evolution in continuum mechanics is dependant on partial differential equations (PDEs) unlike the ordinary differential equations (ODEs) found in Molecular Dynamics (MD). The methods employed to solve these PDEs take two forms: Finite Element Modelling (FEM) and Finite Difference Modelling (FDM). The principle difference is that FEM uses weighted residuals and shape functions, where as FDM approximates derivatives as finite difference quotients. [20].

One of the most advanced continuum based FPCs currently in use is the BISON fuel performance code developed by Idaho National Laboratory (INL). The code is FEM based, object oriented (using the MOOSE framework), massively parallel and has been under development since 2009. The capabilities of this code represent some of the most advanced and robust currently available to the industry, however it is not accepted as a licensing code for safety cases of nuclear fuel. This is important to note as the multi-physics phenomena demonstrated by this code make validation difficult. The focus of this work will therefore be mainly towards rigorous validation of smoothed particle methods and demonstration of the inherent errors within the method. The full technical details of the BISON code are laid out in [17], however a more accessible description of the capabilities with example cases is given in [22] and will be referred to extensively throughout this section.

1.2.2 Thermodynamic Modelling

Accurate prediction of the thermodynamic behaviour of fuel pellets has always been one of the primary concerns for FPCs. Standard UO_2 fuel (as well as other oxide fuels) has a poor ability to conduct heat causing very high temperature gradients when considering the entire reactor system. The FPCs are used as a tool to help ensure that no fuel melting occurs and that the internal fuel rod pressure is kept below safe limits [16].
The thermal conductivity of UO_2 below $\sim$ 1200K has long been known and is dominated by contributions from lattice conduction (phonons) with the general form [23]:

$$\kappa_{ph}(T) = \frac{1}{a + bT} \tag{1.1}$$

Here a corresponds to phonon scattering by lattice imperfections and b corresponds to phonon-phonon scattering. Experimental data for higher temperatures has long been studied [24], and is attributed to electronic contributions of the form:

$$\kappa_{el}(T) = \frac{C}{T^2} e^{-\frac{W}{k_B T}} \tag{1.2}$$

where C and W are related to the formation energy and migration enthalpy of semiconducting carriers. These ideas are included within this report simply to demonstrate the complicated temperature dependence of thermal conductivity within nuclear fuel. It is heavily dependant on the amounts, types and distributions of lattice impurities. Impurities and imperfections in the UO_2 matrix caused by irradiation include but are not limited to production of fission products such as caesium, generation of fission gasses such as helium, bubble formation by pore migration (Fig.1.3), crack formation and propagation and not forgetting any initial imperfections due to manufacturing. This means the thermal conductivity changes over time and depends on a large number of variables which is problematic for FPCs.

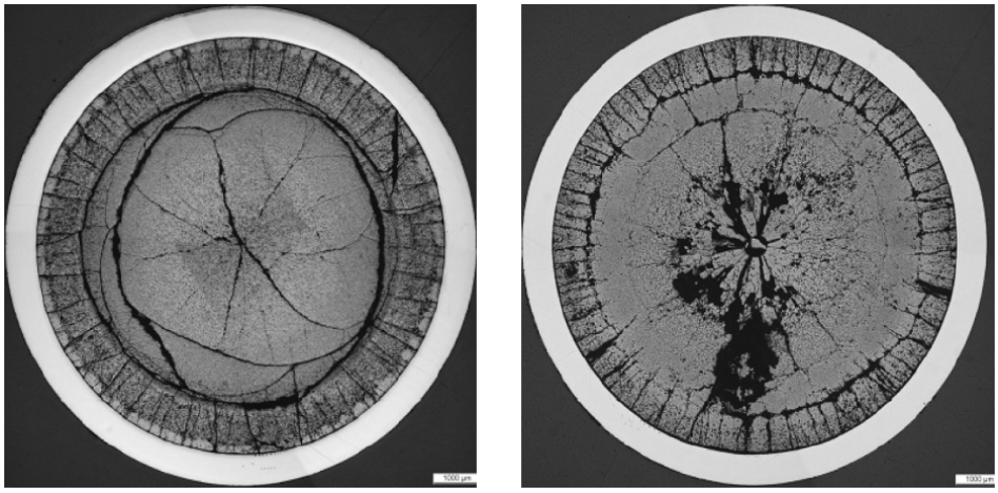

Figure 1.3: A photo of material defects forming in a fuel pellet after irradiation. Copyright National Nuclear Laboratory.

Some extensive theoretical work has been done accounting for fuel burn up and very high temperature schemes as well as for the addition of plutonium into the lattice to create so called MOX (Mixed OXide) fuel [25–28]. Alternatively thermal conductivity can be calculated through simulations by considering models on the scales of the pore structures seen within irradiated UO_2. Different simulation techniques applied to this include molecular dynamics [29], Monte Carlo Potts model [30, 31] and phase field models [32]. The Potts and phase field models do not directly calculate thermal conductivity but rather the grain structure of the fuel for given initial structure and irradiation. This structure can then be used with further simulation techniques to give a value of thermal conductivity across the test structure.

The BISON code uses one of these more recently developed methods to simulate thermal conductivity in-situ, namely the phase field model. The phase field model was originally developed to simulate the evolution of microstructures, with a wide range of applications including solidification, grain growth and coarsening, crack propagation, surface pattern formation and electromigration [33]. This was later adapted specifically to model grain growth and pore migration in irradiated materials [32]. The Potts model shows equal success in this task [34] however it is reasonable to assume that the phase field model was chosen due to it being continuum based allowing adaptation of the MOOSE framework for its implementation in BISON.

The structure produced by the phase field model can be used as an effective test sample for the thermal conductivity of the fuel pellet. The general idea is that each phase in the model (for a simple model the phases of the pellet would simply be UO_2 and fission gas) is assigned a thermal conductivity based on the complex functions derived in the theory. A new continuum simulation is then run with each side of the sample held at two different constant temperatures. This allows an effective thermal conductivity for the whole sample to be calculated based on the steady state conductivity relation [35]:

$$\nabla \cdot \left(\kappa'(r)\nabla T\right) = 0 \tag{1.3}$$

The thermal conductivity that arises from this is then fit using a dynamic curve fitting method to account for the randomness of the structure predicted by the phase field model. This process can be completed for each time step within the FPC, accounting for the changing burnup, with the result informing the next step in the model. A full methodology for multiscale modelling of this kind has been developed [36], and has been implemented in the BISON code using the MARMOT framework [37]. This allows BISON to capture physics taking place from the scale of micro seconds to years through the coupling of the two models.

All of this demonstrates the same fundamental idea. Accurate thermodynamic modelling of nuclear fuel requires the use of multi-physics modelling. This is well beyond the scope of the current licensing codes used for FPCs. As outlined work has been done to implement these concepts in various fuel models in isolated cases. The case for smoothed particle modelling within FPCs is therefore strengthened as the decoupling of PDEs to ODEs achieved by the method allows for easier implementation of multi-physics phenomena. The thermodynamic modelling used within this work will widely assume constant thermal conductivities in order to validate the models against existing analytical ones however the full thermodynamic modelling described here has the potential to be implemented in future models, making the method sufficiently robust to future improvements.

1.2.3 Mechanics Modelling

Correctly modelling the mechanical behaviour within nuclear fuel rods is of equal importance to the thermodynamics. The pellet is prone to cracking both mid-height and radially (Fig.1.4) which places additional strain on the cladding as does any manufacturing defect within the pellet. The Pellet Cladding Mechanical Interaction (PCMI) can place large amounts of stress on small areas of the cladding that can result in fracture (Fig.1.5). If the cladding fractures, the fuel rod is said to have failed and the result is the dispersion of radioactive material into the reactor core. For the best case this still makes the process of changing the fuel rods more expensive, time consuming and risky. For this reason there has been much interest recently in developing the ability of FPCs to model explicit crack formation.

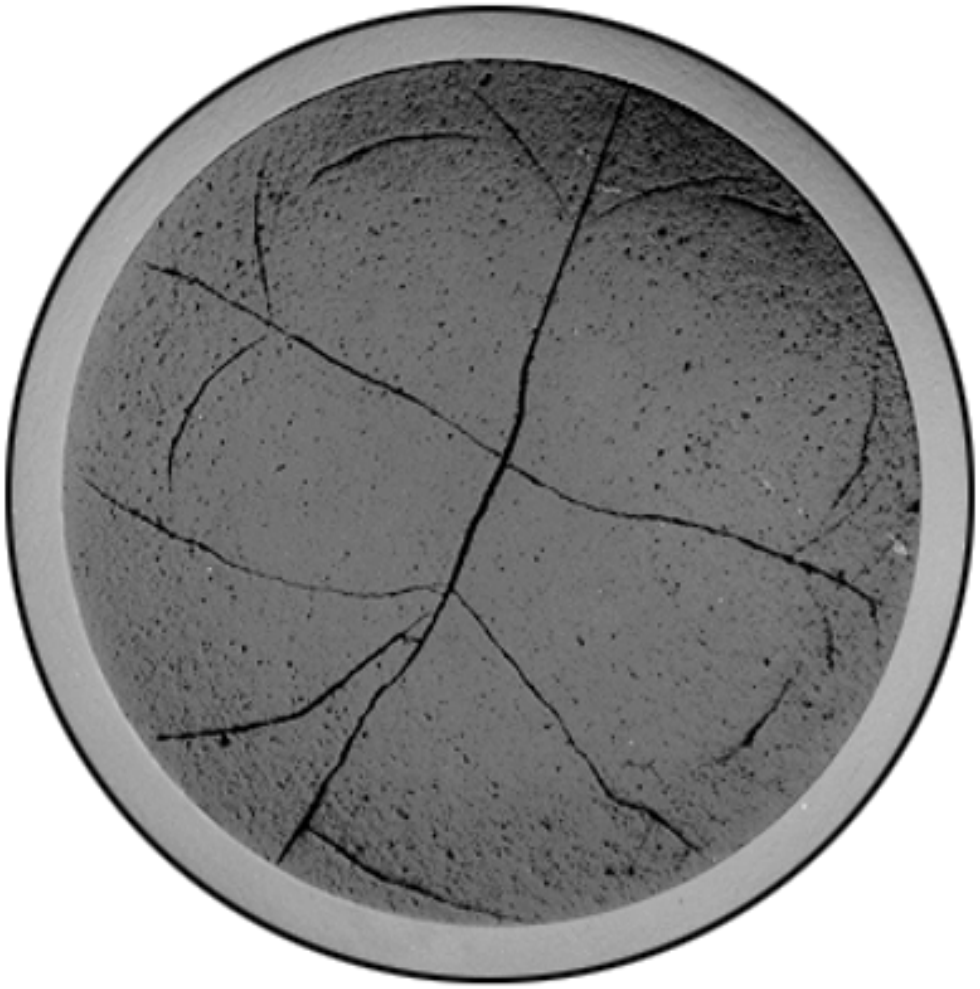

Figure 1.4: A photo of cracks formed in a UO_2 fuel pellet after irradiation. Copyright National Nuclear Laboratory.

The BISON code can be used in spherically symmetric (1D), axisymmetric (2D) or full 3D geometry modes. BISON fuel pellet models for UO_2 already include swelling due to solid and gaseous fission products, densification, thermal and irradiation creep and fission gas generation and release. BISON also contains models for fracture via relocation or smeared cracking [38].

Smeared cracking analysis (SCA) was originally developed for analysis of concrete pressure vessels [39]. SCA is FEM based and uses the calculated stress and strain values at each time step for each element to define crack formation and propagation within the model. A criterion on the stress and strain values is derived to define the values for which the material fails. The original model considers both yielding and cracking criteria. For each cracked and yielding element new stiffness and loads are calculated using equilibrium equations derived for each state. This then allows the FEM model to deform each element relative to whether or not it has failed. The method is known as smeared cracking as it does not directly show elements breaking apart but instead allows elements to deform to a far greater extent to mirror that of a cracking element.

Despite its success, the original formulation of SCA has many flaws. Over time more advanced

models have been produced with smeared cracking to address these. In its basic state SCA does not account for the orientation of crack formation which leads the model to deform equally in all directions from the cracked element. Several methods have been implemented to overcome this. One such model created in the software ALCYONE (developed by CEA in France) calculates the yield stresses for elements in 3 principal directions, the unit vectors of the chosen co-ordinate system, so that the element stiffness may only be modified in the directions for which the yield strength is reached, thus giving orientation to the crack formation within the element [14].

The same study implemented a crack closure criterion. Due to cyclic thermal loading of fuel pellets in reactors, crack closure can occur. The implementation allows for cracks to close as the strain on them reduces. However, a memory of the crack remains within the lower tensile strength of the element. The model only allows crack closure in the absence of stress normal to the plane of the crack - a limitation that is not present in reality but allows for easier implementation.

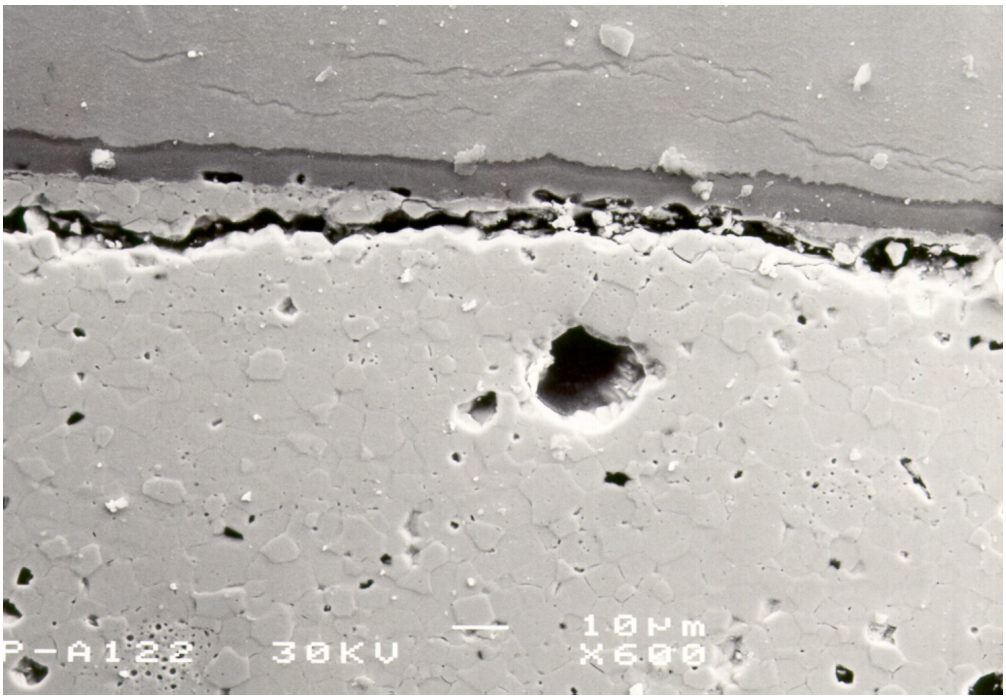

Figure 1.5: A photo of damage within the micro structure due to PCMI as well as irradiation. The top image portion shows the cladding, the lower portion the fuel. Copyright National Nuclear Laboratory.

The method of smeared cracking has seen many developments and wide ranging success, including within FPCs such as BISON. The core problem of smeared cracking is one which effects all cracking models within FEM - the mesh. In FEM, a mesh is the separation of the overall material geometry into tessellating elements on which the PDEs are evaluated. To properly evaluate areas of high stress and strain within FEM it is necessary to refine the mesh within the effected area. However, as is discussed in the study within ALCYONE [14], the material laws for softening required for SCA are mesh size dependent which restricts the model mesh size and variation. This also means that knowledge of crack locations ideally should be known ahead of time within the models - to allow for

proper evaluation of the elements in question. The amount the mesh deforms is also limited. This is due to the fact that the evaluation of the PDEs requires that the mesh not be discontinuous, thus limiting how far it can deform before the calculations begin to diverge.

The complex mechanical modelling described here is beyond the scope of the smoothed particle models produced for this work, however the deep discussion is included to again highlight the true complexity of the problem of nuclear fuel modelling. It is believed these complexities can be successfully implemented into advanced smoothed particle models within future research which makes the smoothed particle method an appealing avenue to explore ahead of GEN IV reactors.

1.2.4 Scope of Thermodynamic and Mechanical Modelling

The above review highlights not only the complexity but also the importance of both thermodynamic and mechanical modelling of nuclear fuel. The focus of the models created within this work will be the validation of thermodynamic and mechanical modelling. For any new methodology to be accepted as a licensing code within the safety case for new reactor technology it must first be validated for simple and well-defined models. The method must be shown to accurately predict the temperature and stress profiles occurring within materials with any sources of error explored and taken into account. Material and thermal properties are assumed to be independent of the state variables T, P as well as any stress and strain rates in all validation work reported here.

1.3 Alternative Modelling Methods

A large amount of the problems found in current FPCs are due to the choice of modelling method used. The problems discussed in the previous section are fundamentally absent, either in part or entirely, from alternative modelling methods. Some success has already been achieved in showing fuel pellet crack patterns with continuum based peridynamics. Monte Carlo methods have already been discussed as an alternative to phase field models for the evaluation of pore structure and grain growth. Molecular Dynamics (MD) has been successfully applied to model neutron flux and thermal conductivity and Smoothed Particle Applied Mechanics (SPAM) has been demonstrated to have inherent failure. Here these methods are discussed in order to justify the chosen exploration and application of smoothed particle methods for the simulations presented within this thesis.

1.3.1 Peridynamics

The original reformulation of elastic theory known as peridynamics by Silling was created with the aim of dealing with discontinuities arising from solid mechanics such as crack formation [40]. The issue with discontinuities in continuum methods such as FEM arises from the PDEs which need to be evaluated to evolve the system. To circumvent this issue peridynamics uses integral formulations to calculate the forces which evolve the system rather than the standard differentiation. This method allows many types of discontinuities to be modelled without the use of special techniques such as those detailed in SCA.

Peridynamics has already been applied to the case of fuel pellet fracture with good initial results. It has been shown with a model created in LAMMPS [41] that peridynamics can give reasonable estimates of crack distributions when only parameterised by the fracture strain of UO_2 [13]. The same study showed however that the correlation of crack count with that of Post Irradiation Data (PID) were less reliable as the damaged volume of the pellet overtook that of the undamaged volume.

A more recent study developed the more advanced Thermo-Mechanical Bond-Based PeriDynamics model (TM-BB-PD) [42]. This model involves multi-rate time integration to account for the different time scales on which thermal and mechanical behaviours can effect deformation and fracturing within the fuel pellets. The study produced data with good agreement to PID. It was shown that radial cracking occurs during power ramps as opposed to circumferential cracking which occurs during power drops. The model, although more advanced, operated only in 2D. The complexity of the equations used make the run time of a fully 3D realised version potentially problematic.

1.3.2 Molecular Dynamics

MD follows the basic principles of Newtonian mechanics. A potential function is defined, along with initial and boundary conditions for the system, and from this the motions of all particles within the system can be calculated. The particulate nature of MD gives rise to inbuilt failure mechanics; as the particles of the system are pulled apart by thermal and mechanical physics within the system, the forces acting on the particles decrease allowing crack formation. MD simulations offer faster computations of each time step due to the system being defined by ODEs rather than the PDEs of continuum FEM. MD simulations however are limited by scale. The particulate nature of MD is used for atomistic simulations and although systems of 1 billion particles are achievable with current computing technology, if we assume 2D simulations of solids with atomic spacing on the order of $1\mathring{A}$, this means we are limited to material squares on the order of $1\mu m$ at the limit of feasible simulation times. Similarly the time steps represent those on the order of atomistic events. This is problematic for simulating nuclear reactors which can be operated for multiple years before refuelling.

One appealing element of MD simulations is however that the transport properties are emergent and can thus be calculated from the simulation. To this effect MD has been used to calculate the thermal conductivity of UO_2 from a more theoretical standpoint [43] as well as with consideration of the impurities due to manufacturing and irradiation [44]. Similar studies have been completed to calculate other transport coefficients from MD through the use of the Green-Kubo theory and nonequilibrium simulations. For instance the SLLOD equations of motion are used to create non-equilibrium shear flow from which shear viscosity and bulk viscosity can be calculated [45]. Such properties can be used to construct stress tensors, for example in smoothed particle simulations, which are important to the study of fracture among other things. A similar examination of transport coefficients has been studied within smoothed particle methods due to its particulate nature, however the difference in scale means that these transport coefficients are artificial, thus the true transport coefficients are still required to inform the evolution of smoothed particle simulations [46].

MD has already seen successful applications to nuclear fuel [47]. It has been proposed as an essential part of multi-scale modelling for nuclear fuel with material and thermodynamic properties obtained from MD modelling and used in higher level continuum modelling similar to the idea of phase field models presented earlier. These MD models have already been applied to the problem of GEN IV reactors [48]. It is believed that the development in this area with respect to nuclear fuel modelling is already demonstrating the potential of MD models for nuclear fuel applications. Therefore it may be considered a valid extension of this work to attempt to couple MD and SPAM simulations of nuclear fuel with SPAM providing the continuum scale modelling. SPAM has seen little to no development specific to the area of FPCs however and thus the demonstration of the application

of this method to nuclear fuel is deemed to be more beneficial.

1.3.3 Smoothed Particle Methods

Smoothed Particle Hydrodynamics (SPH) was first developed in 1977 by three researchers for applications to astrophysics problems [49, 50]. Throughout this work we refer instead to the name SPAM. Hoover coined the term SPAM (Smoothed Particle Applied Mechanics) to refer to the applicability to solids as well as fluids. The method uses a set of particles as interpolation points for the usual continuum field variables found in FEM methods. The properties defined at each particle can then be evaluated anywhere within the system through the use of a weight function (kernel) estimation technique. This is based on the idea of estimating probability densities from sample values, but more physically can be seen as a method of smoothing the effect of each particle across space, thus maintaining a material continuum. Despite the use of probability functions within the evolution, one advantage of SPAM is its exact treatment of the flow of heat and matter (advection) that makes it effective at modelling fluids [51].

There are several other features of SPAM that make it potentially very well suited to the application of nuclear fuel modelling. The particle nature of SPAM allows for fracture mechanics to be demonstrated within the continuum in a more natural way. Simulations of impact and fracture within SPAM were first proposed in the 1990s by the inclusion of a strength model and von Mises yielding relation [52]. The same group then demonstrated full realisation of solids within SPAM by showing the 3D fracture of a solid rod under tension [53]. The fracture demonstrated is independent of the particle resolution size used, and has the natural inclusion of the effects of friction and bulking between the fragments produced without the inclusion of specific descriptions of these physical effects. The results produced only considered tensile failure and not failure due to shear, however it is reasonable to assume a modified version of the model could demonstrate both.

More recent work by Hoover has looked at the isomorphisms between SPAM and MD [54]. Hoover explored the meaning of the inherent transport coefficients within SPAM simulations with respect to isomorphic MD simulations [55]. From his work models of solid fracture have been produced, parameterised though MD simulations [56]. It has been found however, that for high strength models the data produced is not in line with that predicted by MD simulations. It is speculated that this is due to the absence of certain energy inclusions in the model, such as thermal and rotational energy [56].

Beyond failure mechanics, SPAM has seen over the years the derivation, inclusion and testing of suitable models for a wide variety of physical phenomena. Heat conduction has long been implemented and studied in SPAM and found to give good agreement with analytical examples where possible [57]. Solidification and melting within systems has been implemented in a variety of ways. One of the first proposed methods was through the transfer of liquid particle mass to a static grid for particles undergoing solidification, however the use of extra particles causes unnecessary computation [58]. More recently an alternative method has been outlined which more directly includes latent heat within the heat capacity and then introduces a new method within the SPAM in which the superposition of two kernels is used. The work suggests the new method is both fast and easy to implement [59].

In addition, multiple studies of various potential instabilities within SPAM codes have been conducted [54, 60]. These studies suggest that although instabilities within the method can occur they

are usually restricted to specific regimes such as perfectly regular structures (odd-even instability) or specific sound speeds (problems in the interaction between kernel and constitutive relations). These instabilities can therefore be removed with rigorous formulation and testing. Finally the recent production of the SWIFT code at Durham University by the joint efforts of the School of Engineering and Computer Science and the Institute for Computational Cosmology is an exciting prospect for the potential run-times of SPAM codes [9]. Task based, massively parallel codes could allow FPCs to run in a fraction of the time they currently do, allowing simulations to take precedence over experimental work as the first step in evaluation of new fuel types and designs. For these reasons, the development of the SPAM method of continuum modelling with respect to modelling nuclear fuel will be attempted with the specific goal of examining its validity for the case of fuel rod failure.

1.4 Aims of This Work

The above review highlights the importance of both thermodynamic and mechanical behaviour of nuclear fuel. All safety cases are built primarily around demonstrating safe operating conditions specifically defined by the maximum temperature and stress values which occur within the nuclear fuel model. Within this work the relatively new method of smoothed particle modelling will be applied to nuclear fuel. For smoothed particle methods to be attempted for the licensing codes of any nuclear fuel it is essential that first the accuracy of both thermodynamic and mechanical modelling within SPAM is quantified and validated to a high degree of confidence.

This work aims to begin this process by creating basic models of nuclear fuel containing both stress and temperature behaviour within SPAM. These model will be constructed as a series of smaller models each with well-defined analytical solutions in order to exactly show the deviation of the SPAM results from the expected. The main focus of this report is highlight the sources of error within basic SPAM models of nuclear fuel and to explore many of the proposed mitigation methods and their effect on the validity of the results.

This work is supported by the National Nuclear Laboratory and thus is designed to provide a detailed analysis of SPAM modelling so that the merits of the method can be properly assessed and further advanced projects may be put forward.

1.5 Conceptual Fuel Model

To allow for in-depth validation at each stage, the conceptual fuel model presented within this work is deliberately simplified. The simplifications are as follows:

- All material properties are assumed to remain constant. This removes the thermal effects on properties as well as the effects of burn up of the fuel. It also removes the complex nature of the thermal conductivity of the UO_2.
- Material boundaries are assumed to be static, this is selected to allow for validation against analytical solutions, all of which have boundary conditions which do not move in space. This means that the effect of fuel swelling as well as the deeper complexity of PCMI is removed from the model.
- The materials are assumed to be homogeneous. This removes the effect of micro crack initi-

ation as well as bubble formation from the fuel.

- The mechanical behaviour is assumed to be elastic-plastic for all materials. This removes complex stress-strain behaviour such as strain hardening and creep.
- The model is assumed to be at steady state. This removes the time dependent failure of nuclear fuel due to ramping up and down the fuel temperature in cycles.
- The height of a fuel pellet is assumed to be much larger than its width. This allows for mechanical behaviour to be modelled as plane strain and the model reduced to 2D. This removes the hourglass effect of deforming fuel pellets.

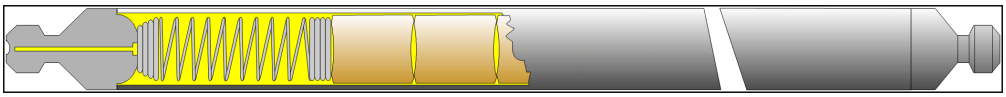

Figure 1.6: An outline of the internal structure of a fuel rod. This structure will be simplified for the conceptual model. Copyright National Nuclear Laboratory.

With these assumptions the conceptual model is described. The structure is simplified to 2D thus ignoring the more complex fuel rod geometry such as the stacking of pellets and springs shown in Fig.1.6. The model is divided into 3 sections: fuel, cladding and coolant. These are modelled as concentric annular rings as shown in Fig.1.7. The fuel is assumed to have constant radius R_F and the cladding R_C. The fuel and cladding are assumed to have constant thermal conductivities κ_F, κ_C respectively. The thermodynamic behaviour is assumed to follow the heat diffusion equation:

$$\frac{\partial T}{\partial t} = D_T \nabla^2 T - \dot{q} \tag{1.4}$$

Here D_T is the thermal diffusivity of the material. The coolant is assumed to remove heat from the cladding via convection with a coefficient of convection h. The fuel element is assumed to produce heat at a rate $\dot{q}$ per unit time, per unit volume due to the nuclear reaction.

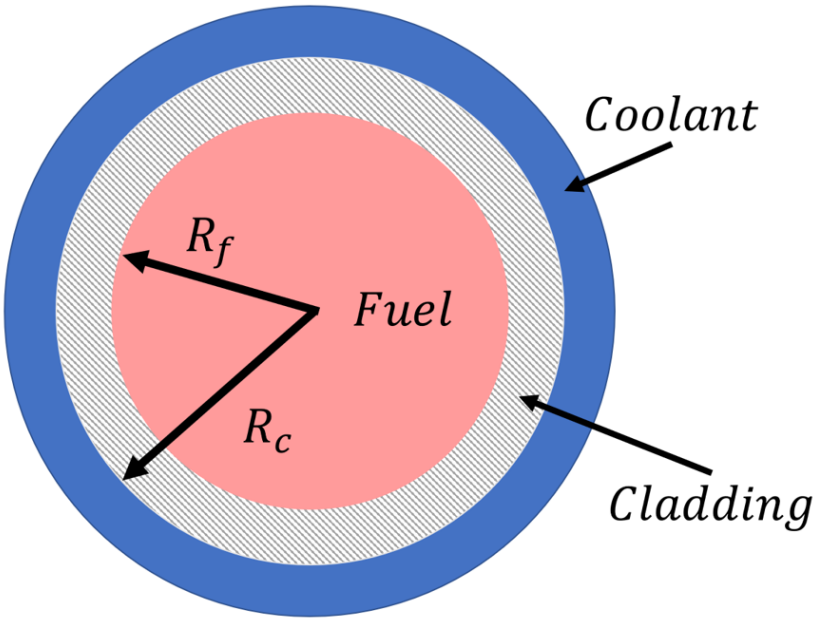

Figure 1.7: A diagram of the simplified fuel and cladding model

The materials are assumed to be homogeneous with a constant initial density ρ_0. The mechanical behaviour is assumed to follow Hooke's law with Young's modulus E and Poisson's ratio ν. The materials are assumed to undergo thermal expansion with linear expansion coefficient α. This gives the stress strain relationship for the materials as:

$$\epsilon_x + \epsilon_y + \epsilon_z = \frac{1-2\nu}{E}[\sigma_x + \sigma_y + \sigma_z] \tag{1.5}$$

where ϵ represents the strains and σ the stresses. The material is assumed to have plasticity defined by the von Mises stress and yield criteria with tensile strength σ_T and yield strength σ_Y.

To achieve this model within SPAM the thesis is broken down into 5 chapters. The first is a review of smoothed particle methods with simple interpolation tests completed. The second deals with heat flow in both the transient and steady state conditions with particular emphasis on the effect of boundary conditions. The third chapter explores the effects of particle arrangement on SPAM accuracy. The fourth is dedicated to more complex heat flow problems, dealing with heat generation and convection within SPAM. The final chapter introduces mechanical behaviour. The final model is restricted in the mechanical behaviour shown.

Chapter 2

Smoothed Particle Methods

2.1 Smoothed Particle Modelling

Smoothed particle methods are widely referred to through the literature as Smoothed Particle Hydrodynamics (SPH) [51], however the alternative name: Smoothed Particle Applied Mechanics or SPAM for short, was popularised by Hoover [54]. The rationale for this based on the fact that there is nothing intrinsic in the method which restricts it to the study of fluid flow.

Smoothed particle refers to the method of breaking a continuous problem domain into a set of discrete points, referred to as particles, and using a modified set of continuum equations to calculate how the properties of the domain evolve over time at these points. These values can then be interpreted anywhere within the domain to return the continuous nature of the original properties. This can be considered analogous to the finite element method in which the domain is broken into a set of spatial pieces, called elements, and then properties are evolved and evaluated on the vertices of these elements. The key difference between the two methods is that the volume occupied by each point in smoothed particle methods is not defined unlike the highly structured finite element meshes, The weight function support areas for each of the particles overlap. An illustration of this idea is given in Fig.2.1. For finite element methods two elements need not be the same size and shape, as demonstrated by the elements marked i, j. It does however simplify the computation in most cases. The same is true of smoothed particles. Regular distributions of points are not required but often simplify the problem.

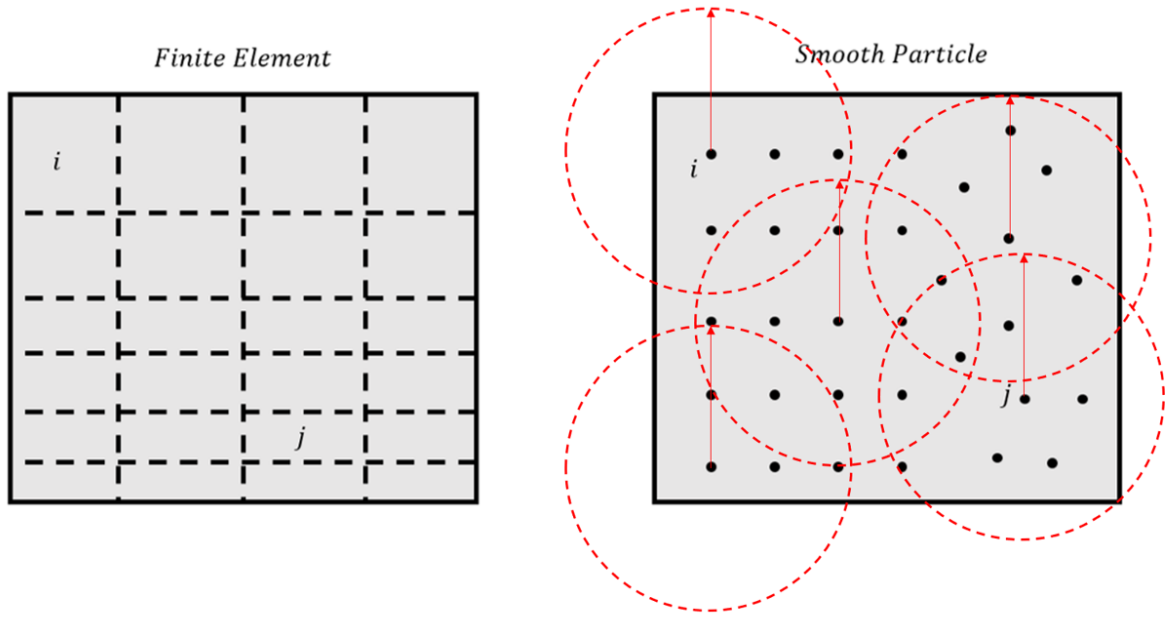

Figure 2.1: An outline the difference in domain division for finite elements vs smoothed particles. Two examples of elements and particle points are marked i, j. As shown the domain divisions may be non symmetric and disordered. A few examples of the overlapping weight function support are shown in red.

Once a domain is divided into particle points each particle i is then assigned individual properties such as mass, velocity and temperature denoted m_i, v_i, T_i respectively. The 'smoothed' nature of smoothed particle methods arises from the use of weight functions (kernels). For example the value of density can be evaluated anywhere within the material at some arbitrary position r at which there is no particle point. This is done by a sum over all particles points which lie in the support of the kernel. Each particle mass m_i then contributes toward the density ρ_r, however the strength of each particle mass contribution is given a weight w within the sum based on the distance away $|r - r_i|$. For the example of density this gives a sum of the form:

$$\rho(r) = \rho_r = \sum_i m_i w(r - r_i) \tag{2.1}$$

A more rigorous derivation of the smoothed particle equations, including Eq.2.1 is given in sec.2.3, however it is useful to first examine the conditions on the function w, and understand its effect on the properties calculated by smoothed particle methods as it is fundamental to successful implementation.

2.2 Weight Functions

The weight function is also often referred to as the smoothing function or the kernel function throughout the literature. The weight function must be Gaussian-like in order to spread the particles influence within space with the correct distribution This idea is highlighted further within the discretisation in Sec.2.3. Every weight function domain is however chosen to be finite to reduce computation. A 'cut off' or 'smoothing' length H is chosen such that the function is zero for all

values of particle distance greater $w(r) = 0 : r > H$. This definition is inline with that used by Hoover [54]. Five properties are defined [54] which restrict the possible choices for function w:

1. Normalisation: $\int_0^H w(r)d\mathbf{r} = 1$
2. $w'(0) = 0$
3. $w(H) = 0$
4. $w'(H) = 0$
5. $w''(H) = 0$

(2.2)

The deviation also assumes that $W \to \delta$ as $H \to 0$. Some authors also require that W is n times differentiable, where n is based on the required uses of the weight function and its derivatives. Many functions have been proposed as possible candidates for weight functions, a comprehensive analysis of the error for each is given in Quinlan et al. [61]. A representation of the weight function shapes explored are shown in Fig.2.2. Here only two examples of bell shaped functions are explored for illustration purposes.

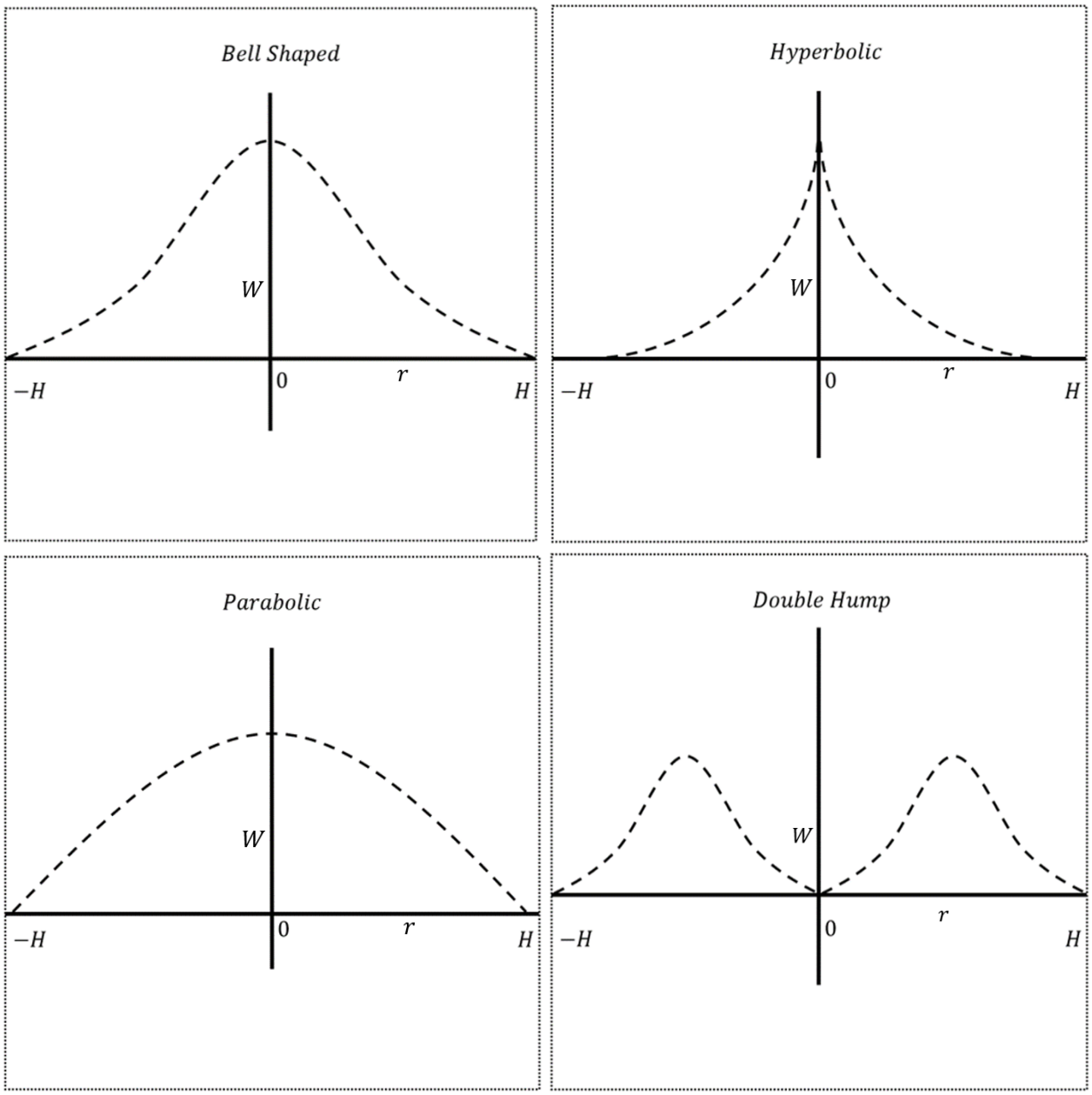

Figure 2.2: Outlines of function shapes which satisfy the weight function criteria layed out in Eq.2.2

2.2.1 Example Weight Functions

One example of a bell-shaped weight function which satisfies the criterion was proposed by Lucy [49]:

$$w^n_{Lucy}\left(r < H\right) = c\left[1 + 3\frac{r}{H}\right]\left[1 - \frac{r}{H}\right]^3 \tag{2.3}$$

The constant c is determined by the condition of normalisation, it can be normalised for any number of dimensions n. A more widely used alternative function, based on cubic splines, was proposed by

Monaghan [51]:

$$w^n_{Monaghan} = \begin{cases} c\left(\frac{1}{2} - 3\frac{r^2}{H^2} + 3\frac{r^3}{H^3}\right) & if \quad \left(0 < \frac{r}{H} < \frac{1}{2}\right) \\ c\left(1 - \frac{r}{H}\right)^3 & if \quad \left(\frac{1}{2} < \frac{r}{H} < 1\right) \end{cases} \tag{2.4}$$

The constant c can be calculated for $n = 1$ as follows:

$$\int_0^H 2w^{1D}(r)dr = 1 \tag{2.5}$$

For the Lucy weight function this gives:

$$\int_0^H 2c\left[1 + 3\frac{r}{H}\right]\left[1 - \frac{r}{H}\right]^3 dr = 1 \tag{2.6}$$

Integrating to:

$$2c\left[-\frac{3r^5}{5H^4} + \frac{2r^4}{H^3} - \frac{2r^3}{H^2} + r\right]_0^H dr = 1 \tag{2.7}$$

This gives the constant of normalisation for this weight function in one dimension:

$$c_{1D} = \frac{5}{4H} \tag{2.8}$$

The normalisation functions for $2D$ and $3D$ are respectively:

$$\int_0^H 2\pi r w^{2D}(r)dr = 1 \tag{2.9}$$

$$\int_0^H 4\pi r^2 w^{3D}(r)dr = 1 \tag{2.10}$$

For Lucy's weight function this gives respective normalisation factors of:

$$c_{2D} = \frac{5}{\pi H^2} \qquad\qquad c_{3D} = \frac{105}{16\pi H^3} \tag{2.11}$$

Similarly for Monaghan's weight function the normalisation constants are:

$$c_{1D} = \frac{8}{3H} \qquad\qquad c_{2D} = \frac{80}{7\pi H^2} \qquad\qquad c_{3D} = \frac{16}{\pi H^3} \tag{2.12}$$

Each of these example weight functions along with their first and second derivatives are shown for $1D$ normalisation and a smoothing length $H = 3$mm in Fig.2.3. It is seen immediately that the second derivative of Monaghan's weight function is not smoothed. This is due to the piece wise nature of the function. Smoothness within the second derivative is not required by the weight function criteria and the use of the second derivative is far more uncommon than the first.

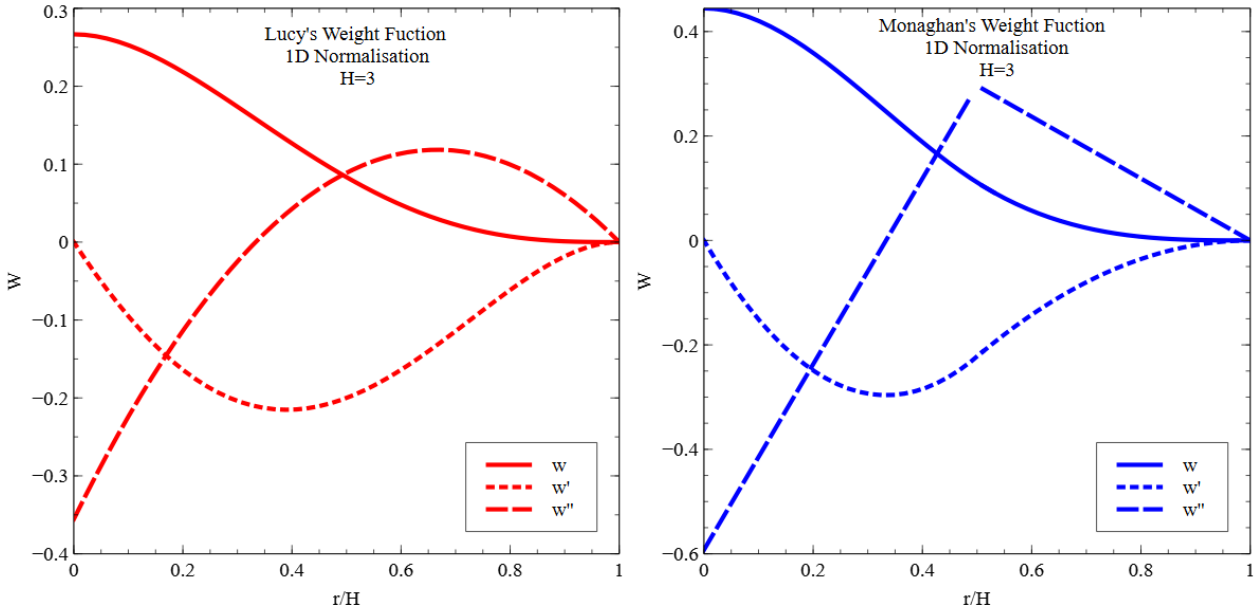

Figure 2.3: Left: Lucy's weight function given by Eq.2.3. Right: the more common choice of Monaghan's weight function given by Eq.2.4. Both weight functions are given with their first and second derivatives.

The smoothing length H has a significant effect on the interpolation of values within the SPAM through the weighted sum such as Eq.2.1. Herein, the smoothing length is defined as the radius of the compact support, but in the majority of SPH literature, the radius of the kernel compact support is a coefficient times the initial particle spacing. To find the most appropriate length H we test the lattice density for both weight functions in $1D$ and $2D$. The particle arrangements used consist of unit mass particles $m_i = 1g$ with a regular structure and unit spacing. Such a structure has an expected density of $\rho_0 = 1\text{g/mm}^3$, these arrangements are shown in Fig.2.4.

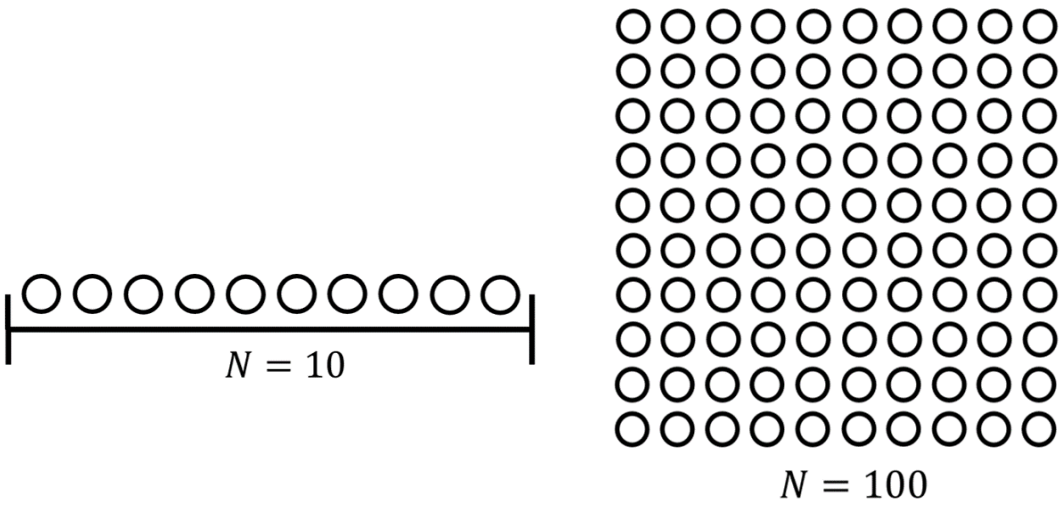

Figure 2.4: Left: 1D regular chain of 10 particles. Right: 2D regular lattice of 100 particles. Both have unit mass particles in unit grid spacing.

The smoothed particle density is computed with Eq.2.1. To ensure the interpolated density is the same everywhere we use periodic boundary conditions. The reasons for this are discussed in Sec.2.4 and a more in-depth description of periodic boundary conditions is given later in this chapter. The results for a range of smoothing length H are given in Fig.2.5

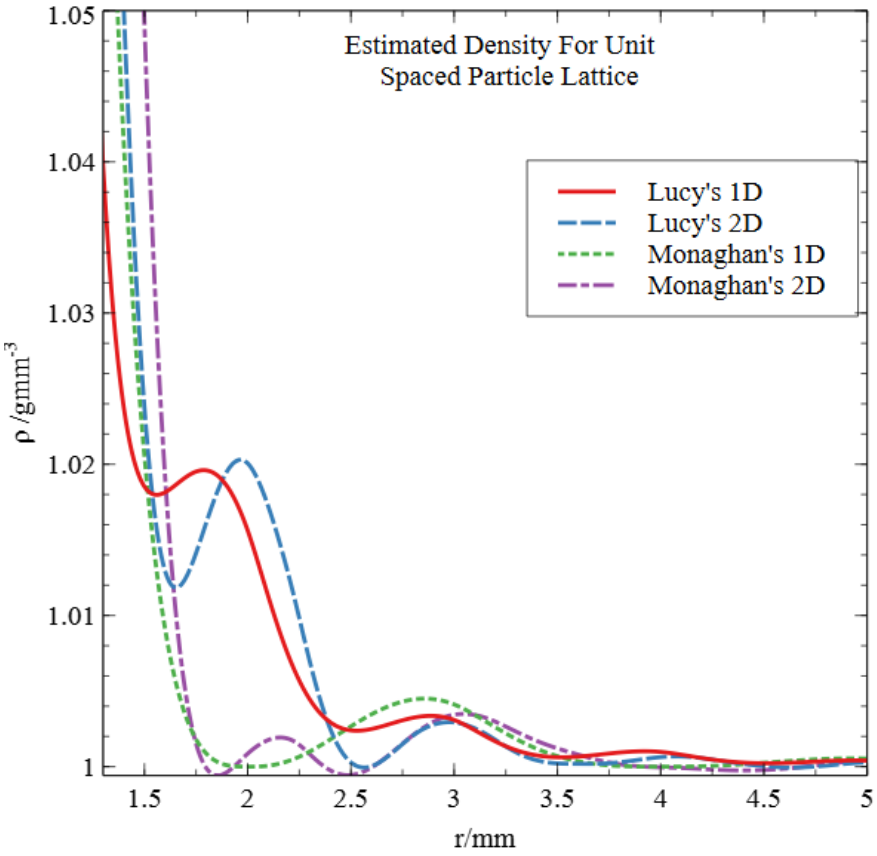

Figure 2.5: The estimated density given by the smoothed particle weighted sum. The expected lattice density is $\rho_0 = 1\text{g/mm}^3$. The lattices are 1D and 2D uniform spaced lattices with unit mass shown in Fig.2.4. The estimation is shown for Lucy's and Monaghan's weight function, Eq.2.3 and Eq.2.4 respectively.

The error is seen to quickly decrease for both weight functions as the size of H increases. For higher values of $H \approx 3$mm Lucy's function has the least error, however Monaghans's does better at lower values of $H \approx 2$mm. It is important to consider the number of particles within range of H. We require that sufficient neighbouring particles are included such that gradients within the SPAM can be accurately calculated. It is therefore more ideal to use values of at least $H > 2\Delta_P$ where the average particle separation for this test is $\Delta_P = 1$mm. This allows two neighbouring particles in each direction to be included.

For the simulations completed in this work Lucy's weight function will be used due to its smoothed second derivative with relatively small difference in density error when compared with Monaghan's.

2.2.2 Interpolation Error

Interpolation errors in SPAM have been studied and it has been found to depend directly on the smoothing length and particle spacing [62]. The error is demonstrated to be driven by two separate mechanisms and these are referred to as the smoothing error and the discretisation error. A simple study is given here to highlight these important ideas for the simulations completed within this work.

The interpolated density for each weight function shown in Fig.2.5 gives a general idea of 'interpolation errors' within SPAM algorithms. However this is a simple case of constant density material. This work will examine non-equilibrium heat flow within SPAM extensively. It is therefore beneficial to examine how smoothing lengths and particle number densities affect the SPAM interpolation of more complex underlying functions. Fourier transforms of heat conduction solutions suggest that all heat flow problems can be broken into a sum of sinusoidal functions. For the interpolation tests in this section we therefore examine the SPAM algorithms ability to interpolate a temperature distribution of the form $T = Asin(\frac{2\pi x}{\lambda})$.

The simplest case of this test is demonstrated in Fig.2.6. Here $\lambda = 100$mm, $A = 1$K. As before unit mass $m_i = 1$g particles with unit spacing $\Delta_P = 1$ are used. The number of particle is $N = 100$. Each particle is assigned a temperature $T_i = Asin(\frac{2\pi x_i}{\lambda})$. The interpolated temperature anywhere within the material at position x_r is then given (in kelvin) by:

$$T(x_r) = \sum_i T_i \frac{m_i}{\rho_i} w(x_r - x_i) \tag{2.13}$$

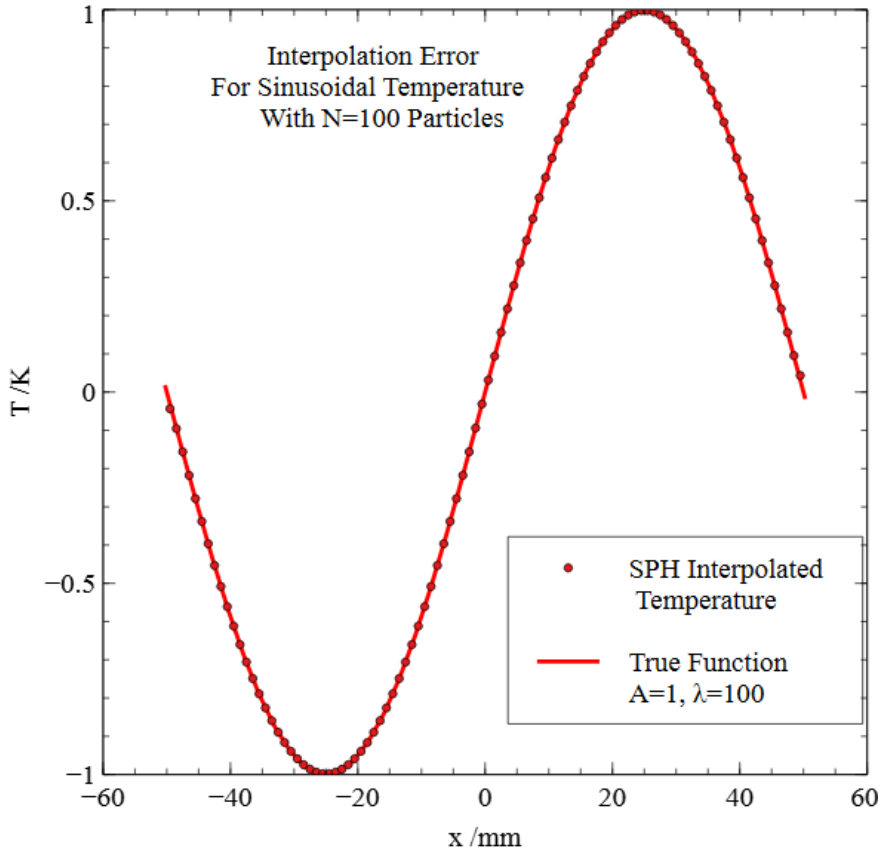

Figure 2.6: The SPAM interpolated temperature vs the expected temperature for $\lambda = 100$mm, $A = 1$K, with $N = 100$ particles and a smoothing length $H = 3$mm

Fig.2.6 shows the ability of the interpolation to reproduce the underlying temperature distribution given to the particles. The error for this interpolation in negligible. However if we instead look at

the same unit spaced particles but with a small wavelength temperature distribution $\lambda = 10$, this time acting across only $N = 10$ particles it becomes quickly apparent that the interpolation error is not guaranteed to be zero.

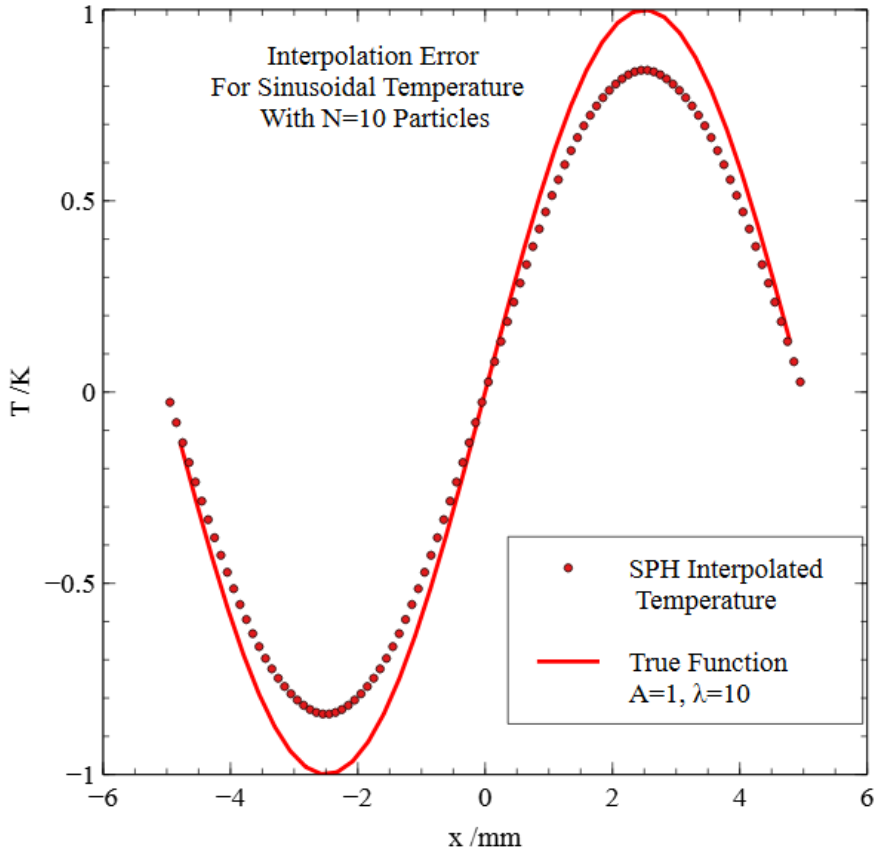

Figure 2.7: The SPAM interpolated temperature vs the expected temperature for $\lambda = 10$mm, $A = 1$K, with $N = 10$ particles and a smoothing length $H = 3$mm

Fig.2.7 shows a significant interpolation error in the peak values of the temperature distribution. Again here $H = 3$mm. Fig.2.8 shows that adapting the particle density to a greater $N = 100$ or adapting the smoothing length to a smaller value $H = 0.5$mm are insufficient to solve the interpolation error in isolation. The reduced smoothing length improves interpolation at the peak value but the loss of nearest neighbour particles creates clear oscillations in the interpolated value.

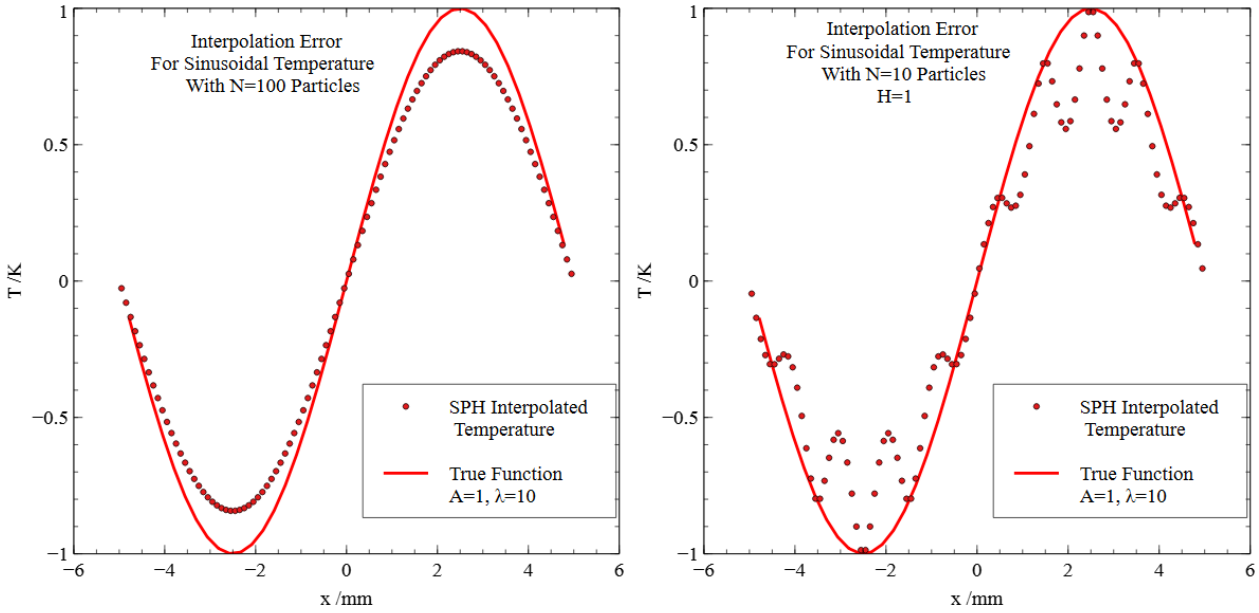

Figure 2.8: The SPAM interpolated temperature vs the expected temperature for $\lambda = 10$, $A = 1$. Left with $N = 100$ particles and a smoothing length $H = 3$. Right with $N = 10$ particles and a smoothing length $H = 1$.

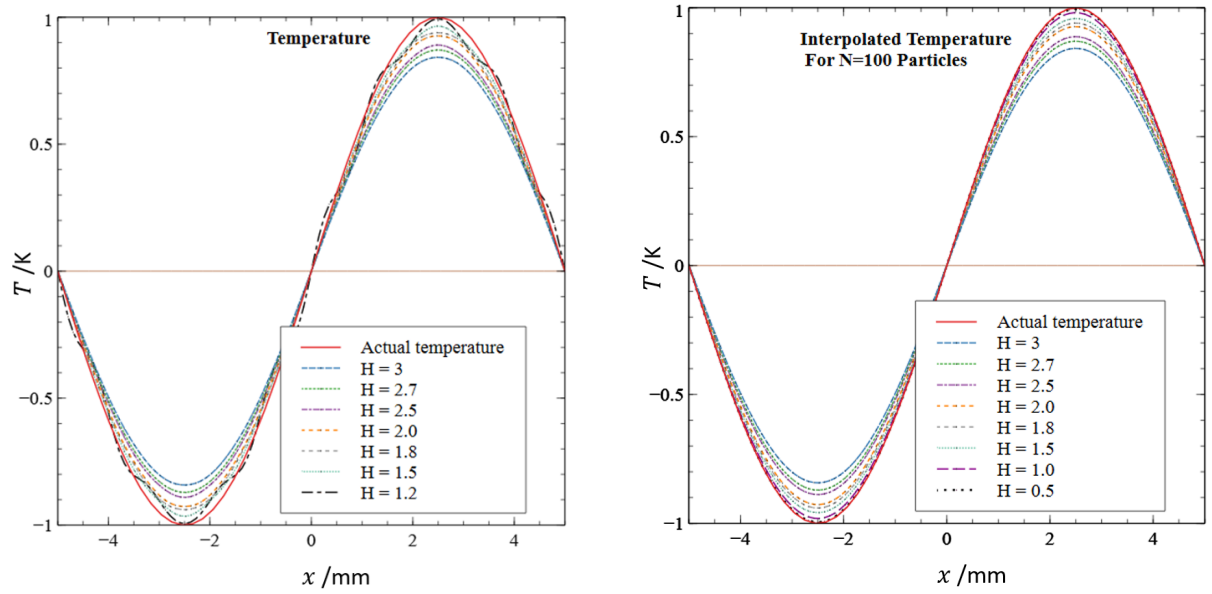

Figure 2.9: The SPAM interpolated temperature vs the expected temperature for $\lambda = 10$mm, $A = 1$K. Left with $N = 10$ particles. Right with $N = 100$ particles. Both shown for a range of smoothing length.

A more comprehensive view of how smoothing lengths effect the interpolation curves for $N = 10$ and $N = 100$ particles is presented in Fig.2.9. It can be seen that the error appears proportional to the smoothing length H. It has already been noted that the error is significantly reduced for

the longer wavelength $\lambda = 100$mm. It has been shown that insufficient particles included in the smoothing length $H < 2\Delta_P$ causes poor interpolation. It is therefore beneficial to seek a simulation constraint from the relation between H, λ, Δ_P and the interpolation error.

The interpolation test is run for a range of values $H = 0.1 \rightarrow 3$mm, $\lambda = 10 \rightarrow 100$mm, $\Delta_P = 0.1 \rightarrow 1$mm and $A = 1, 10, 100, 1000, 10000$K. The error in the peak value is insufficient to properly quantify this test due to the oscillations seen at low H in Fig.2.7. The results for this test are therefore quantified using the residual error in temperature U_T calculated here as:

$$U_T^2 = \frac{1}{N_{r_i}} \sum_{i}^{N_{r_i}} \left(Asin(\frac{2\pi x_{r_i}}{\lambda}) - T(x_{r_i}) \right)^2 \tag{2.14}$$

It is important to note that N_{r_i} here defines the number of *interpolation* values defined by positions r_i, not the particle points used N. For every test $N_{r_i} = 100$ is used but the number of particle points is dependent on spacing and wave length $N = \lambda/\Delta_P$. The full final data for this test is contained in Fig.2.10. The data consists of $15,000$ results where the reduced error is shown by normalising by the signal amplitude A. This confirms that the error in calculation is simply scaled by amplitude A which is to be expected. The error is plotted against the smoothing length per wavelength H/λ which can be considered the 'sample space' as it is proportional to the percentage of the entire function sampled by each interpolation point. The relative smoothing length defined as the smoothing length per particle spacing H/Δ_P is used to colour the data points.

The significance of Fig.2.10 is several fold. It suggests that the interpolation error scales with signal amplitude A. It can be inferred that the relative error depends directly on the sample space H/λ, with smaller sample spaces giving better interpolation of the underlying function. This is often referred to as the smoothing error. However it is very clear that there is a limit to this improvement in interpolation. Once the relative smoothing length is reduced beyond $H/\Delta_P < 1$, that is to say it includes less than an average of 1.5 nearest neighbour particles in each direction, the error diverges. This divergence is referred to as the discretisation error. The discretisation error gives rise to the first restraint on all SPAM simulations completed within this work. It is required at *minimum* that:

$$\left(\frac{H}{\Delta_P} \right)_{Min} \geq 1.5 \tag{2.15}$$

It is therefore beneficial to remove all the data where Eq.2.15 is not met and examine the remaining data. These results are shown in Fig.2.10. It can be seen through the now shifted colour grading that the error reduction diverges from the clear underlying relation for relative smoothing lengths of approximately $H/\Delta_P < 3$ even though the relative error is still reduced within the range $1.5 < H/\Delta_P < 3$.

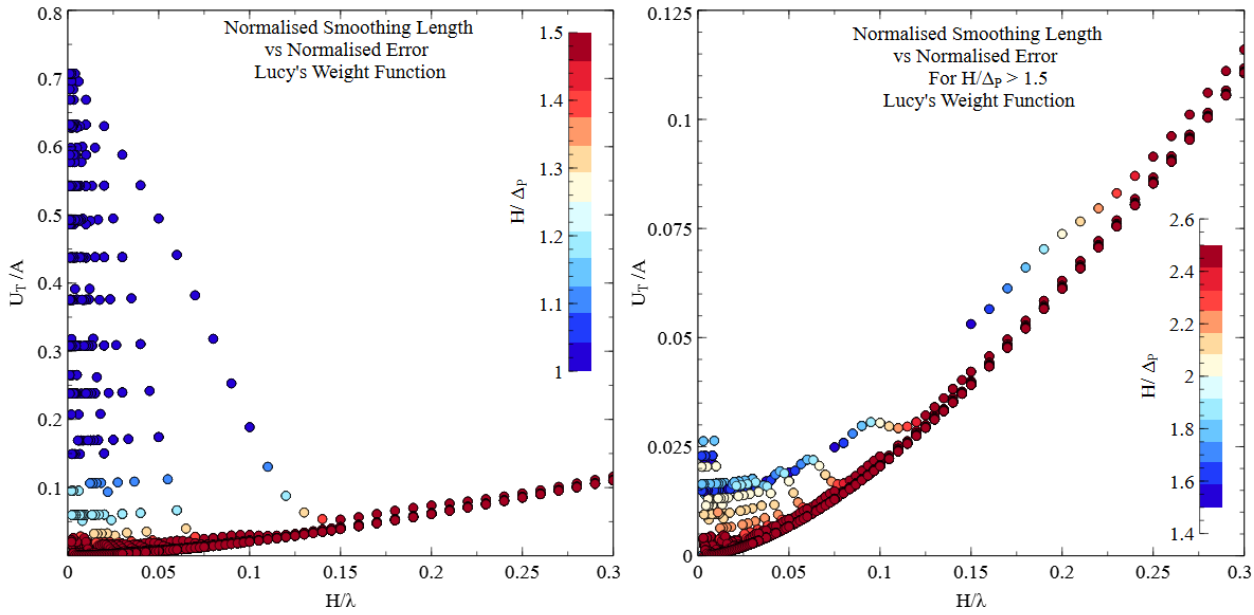

Figure 2.10: The SPAM interpolated temperature reduced error vs the smoothing length per wavelength of the underlying function to be interpolated. The colouring highlights the relative smoothing length (per particle spacing), set to highlight points within the range $1 < H/\Delta_P < 1.5$ left and $1.5 < H/\Delta_P < 2.5$ right where all point $1.5 > H/\Delta_P$ are removed. Values less than this are shown in dark blue, values more in dark red. The test is completed for Lucy's weight function.

Further exploration of these ideas are given in Fig.2.11. Once all values $H/\Delta_P < 3.0$ are removed it becomes clear that the smoothing error is given by the sample space H/λ. A simple fit for terms of up to second order in sample space is shown to demonstrate this, however it suggests that higher order terms are necessary to fully describe the error relation.

To further understand restrictions on the particle spacing and smoothing length the SPAM interpolated derivative is examined. The temperature gradient in one dimension within SPAM is calculated as follows:

$$\nabla T = \frac{dT}{dx} = \sum_j m_{ij} \left[T_j - T_i\right] \nabla_x w_{ij} / \rho_{ij} \tag{2.16}$$

The expected derivative for the sine wave temperature is easily calculated as:

$$\frac{dT}{dx} = \frac{2\pi A}{\lambda} cos(\frac{2\pi x}{\lambda}) \tag{2.17}$$

The error in the temperature gradient can then be calculated as:

$$U^2_{\nabla T} = \frac{1}{N_{r_i}} \sum_i^{N_{r_i}} \left(\frac{2\pi A}{\lambda} cos(\frac{2\pi x}{\lambda}) - \nabla T_{r_i} \right)^2 \tag{2.18}$$

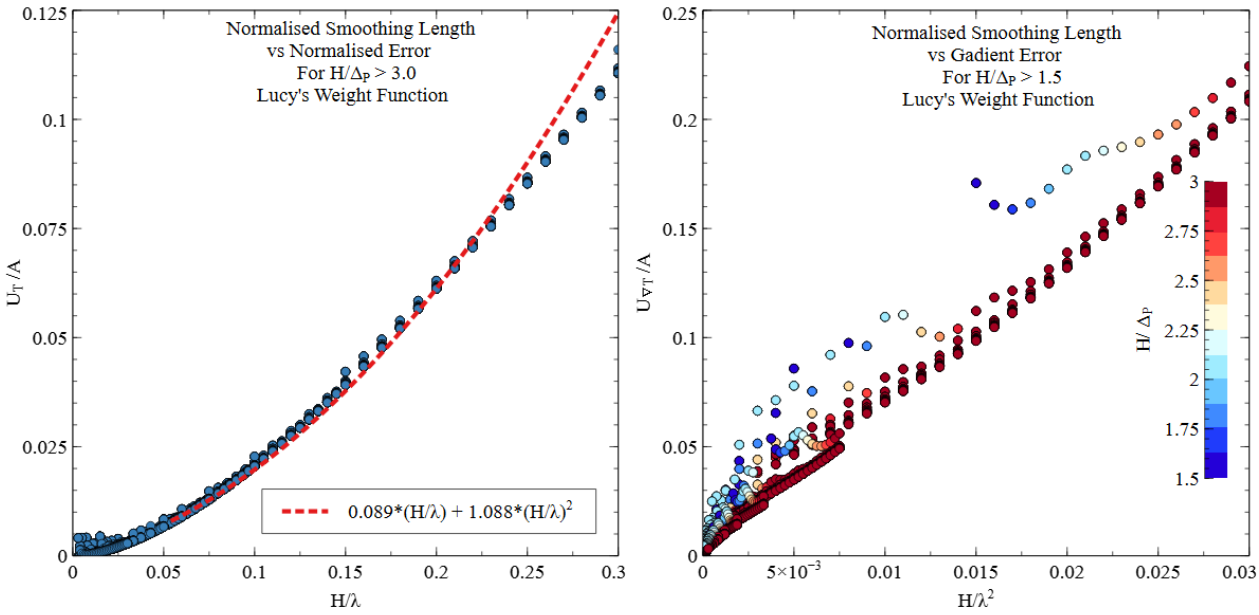

Figure 2.11: The SPAM interpolated temperature reduced error (shown left) and temperature gradient reduced error (shown right) vs the smoothing length per wavelength of the underlying function to be interpolated. Left is restricted to only show values of $3.0 < H/\Delta_P$. Right the colouring highlights the relative smoothing length (per particle spacing), set to highlight points within the range $1.5 < H/\Delta_P < 2.5$. Values more than this are shown in dark red. The test is completed for Lucy's weight function.

The results for the error in the SPAM temperature gradient are shown in Fig.2.11 for a restricted relative smoothing length of $1.5 < H/\Delta_P$ such that most of the discretisation error is removed. The smoothing error this time is found to be a function of H/λ^2. The data suggests that the discretisation error occurs for higher values of relative smoothing length. This is because the gradient requires pairs of particle points to be calculated. A more strict condition is therefore adhered to within this work:

$$\left(\frac{H}{\Delta_P}\right)_{Min} \geq 2.7 \tag{2.19}$$

This is a minimum limit. Throughout this work however the value of H will usually determined by the condition:

$$H = 3\Delta_P \tag{2.20}$$

It is common practice in many SPAM simulations to employ the use of a variable smoothing length [63]. This is beneficial for systems which undergo large-scale deformations causing the distance between neighbouring particles to shift significantly during simulations. This is not required for the simulations presented within this thesis, however may become important within microstructural simulations within future work. For now a constant smoothing length is sufficient. With this condition chosen, the value of H must be minimised by minimising the particle spacing (equivalent to maximising the number of particle points N used to construct the simulation). This must

be balanced with computational cost. SPAM uses sums over particle pairs therefore without optimisation SPAM computational time grow proportional to the square of the particle number (shown in big O notation):

$$Computation\ \ time \propto O(N^2) \tag{2.21}$$

In fact the convergence of SPAM codes under these conditions was studied more extensively within the work of Lind and Stansby [64]. The convergence was shown to improve with the use of higher order weight functions which allow for a faster reduction in the discretisation error. Convergence studies have been applied to SPAM equation requiring the Laplace operator due to the effect on the smoothing and discretisation errors [65]. This particular study demonstrated the convergence of the heat equation among others for again careful choices of weight function with regard to minimising the discretisation error. The most recent work within SPAM has achieved an increase in the order of convergence of simulations form an expected theoretical optimal convergence of 2^{nd} order up to 4^{th} order [66]. The work presented in this thesis achieves between 1^{st} order and 2^{nd} order convergence however a full review of techniques for improving convergence can be found [67]

All these tests were completed on Lucy's weight function. For completeness we include the results for Monaghan's weight function in Fig.2.12. It is seen that the same behaviour is exhibited with respect to the relative smoothing length and sample space.

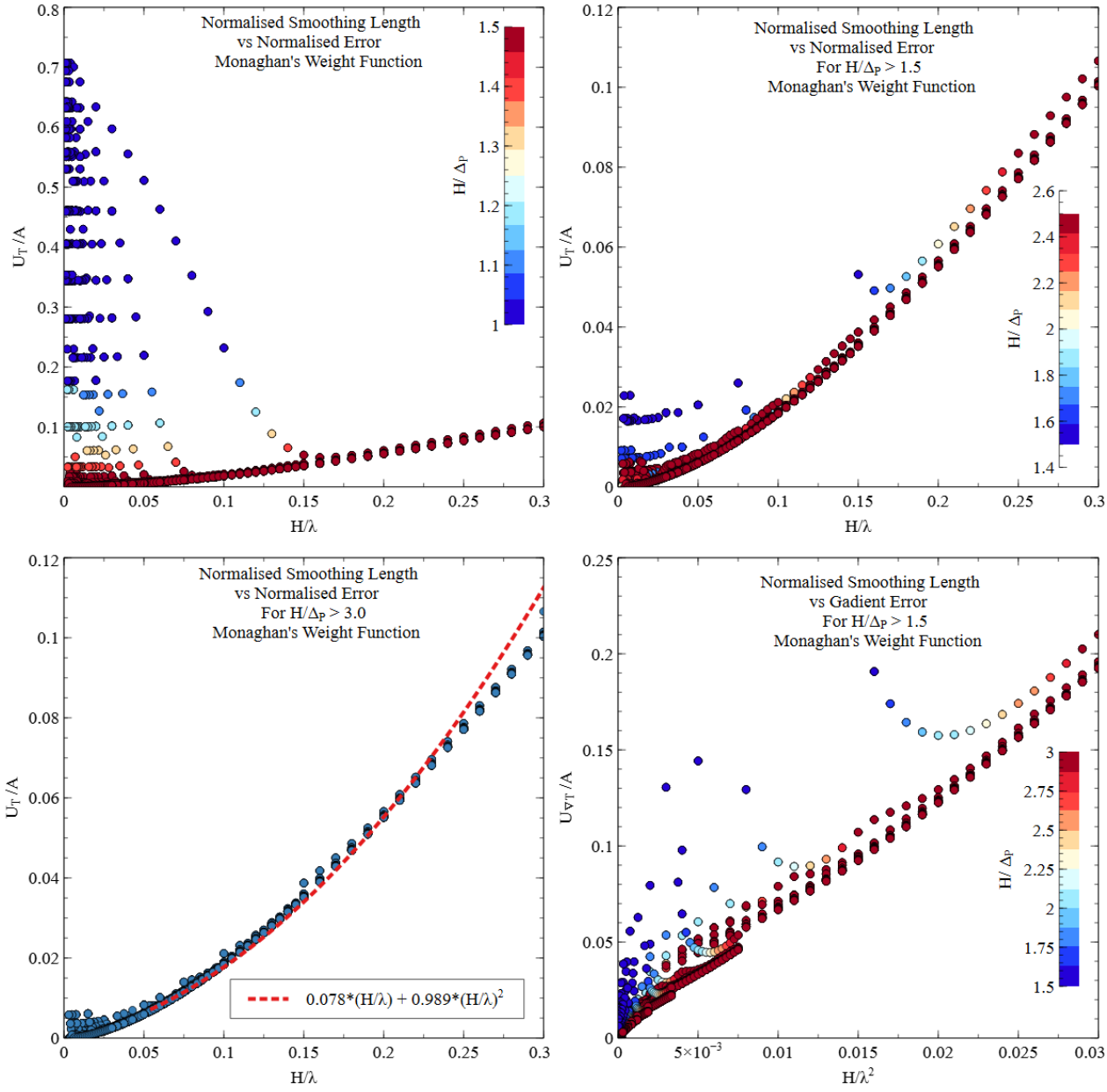

Figure 2.12: The SPAM interpolated temperature reduced error vs the smoothing length per wavelength of the underlying function to be interpolated. The colouring highlights the relative smoothing length (per particle spacing), set to highlight points within a reduced range range. Values more than this are shown in dark red, less in dark blue. The tests are completed for Monaghan's weight function. Bottom right shows the error for the gradient of temperature.

2.3 Smoothed Particle Discretisation

Smoothed particle methods discritise the domain of interest into a set of points. To understand this idea it is best to first consider the Dirac delta function $\delta(x - x_i)$, acting on some smoothed

continuous function $f(x)$:

$$\int_{-\infty}^{\infty} f(x)\delta(x - x_j)dx = f(x_i) \tag{2.22}$$

where x_i is some arbitrary position. This is a well established definition. It is noted that the Dirac delta function is considered a special case of a Gaussian function for which the width, lets call this width $2H$, is minimal. Let us denote some arbitrary Gaussian function as w, it can then be said that our continuous function f at a point x_j can be described as:

$$\lim_{2H\to 0} \int_{-\infty}^{\infty} f(x)w(x - x_j, H)dx = f(x_i) \tag{2.23}$$

Now suppose instead of a complete function $f(x)$ we have instead a discrete set of N sample points along the function which we denote f_i. We can use the Riemann sum to approximate the integral. This requires the function $f(x)$ be split into a set of discrete rectangles of width Δx_i and a mid point f_i. This gives the discrete approximation:

$$\lim_{2H\to 0} \sum_{i}^{N} f_i \Delta x_i w(x_i - x_j, H) \approx f(x_j) \tag{2.24}$$

There exists a problem with this expression. In the limit that $2H \to 0$ the function w will not sample enough space to include any discrete points f_j. The approximation must therefore have a finite width $H \neq 0$:

$$f(x_j) \approx \sum_{j}^{N} f_i \Delta x_i w(x_i - x_j, H) \tag{2.25}$$

A more rigorous argument can be found in Monaghans review of SPAM [51] and alternatively Violeau's book [68]. It is important to note here however that a key assumption has been made. The function f is assumed to be continuous. The implications of this will be explored, however it is beneficial to examine the nature of the continuum equations with the SPAM approximation applied.

2.3.1 Derivation of Smoothed Particle Density

The idea of discretisation by a Gaussian like function given by Eq.2.25 is insufficient. To arrive at the fundamental density equation of SPAM we must consider a continuous function f operating in three dimensional space with position described by $\mathbf{r}$. To the segment length Δx_i then becomes a volume V_i. The subscript j is no longer necessary as $\mathbf{r}$ describes an arbitrary point, and although not specifically noted the weight function still depends on the smoothing length. This gives:

$$f(\mathbf{r}) \approx \sum_{i}^{N} f_i V_i w(\mathbf{r} - \mathbf{r}_i) \tag{2.26}$$

The volume occupied by each particle point in our SPAM particle arrangement has an undefined volume unlike for the case of finite elements. Each point is however assigned a mass m_i such that the total system M is defined:

$$M = \sum_{i}^{N} m_i \tag{2.27}$$

If it is assumed that each particle point has some density value ρ_i, it must therefore be true that the total system volume is given by:

$$V = \sum_i^N \frac{m_i}{\rho_i} = \sum_i^N V_i \tag{2.28}$$

With these assumptions the particle volume V_i can be substituted with the mass per density $\frac{m_i}{\rho_i}$. From here the final step to retrieve the SPAM density equation is to substitute in the function for the density anywhere within the material by assuming it is continuous $f(\mathbf{r}) = \rho(\mathbf{r})$. This gives:

$$\rho(\mathbf{r}) \approx \sum_i^N \rho_i \frac{m_i}{\rho_i} w(\mathbf{r} - \mathbf{r}_i) \tag{2.29}$$

This gives the smoothed particle approximation of density which is used as a definition within the formulation of SPAM and is thus quoted as exact as in Eq.2.1. This also gives the interpolation function for any continuous function $f(\mathbf{r})$:

$$f(\mathbf{r}) = \sum_i^N f_i \frac{m_i}{\rho_i} w(\mathbf{r} - \mathbf{r}_i) \tag{2.30}$$

This interpolation is used to give the temperature for Eq.2.13. A clear distinction must be made. The continuum function does not return the particle values $T(\mathbf{r}) \neq T_i$ under these assumptions. However for the case of density we define it such that $\rho(\mathbf{r}) = \rho_i$ by Eq.2.1.

2.3.2 Derivatives from the Smoothed Particle Approximation

Considering the derivative of some continuous field variable $f(\mathbf{r})$ within SPAM shows one major advantage over alternative modelling methods. The derivative operator now only acts on the weight function. Using Eq.2.30 the derivative becomes:

$$\nabla f(\mathbf{r}) = \sum_i^N f_i \frac{m_i}{\rho_i} \nabla_{\mathbf{r}} w(\mathbf{r} - \mathbf{r}_i) \tag{2.31}$$

As already shown in Fig.2.3, the derivative of the weight function is calculated before hand and so calculations of derivatives within SPAM are extremely efficient. It is noted however by Hoover [54] that by substituting the identity $f(\mathbf{r}) \equiv g(\mathbf{r})\rho^n(\mathbf{r})$, where n can take any integer value, it is possible to arrive at any number of minor variations of the derivative. Two important examples are:

$$\nabla(f(\mathbf{r})\rho(\mathbf{r})) = \sum_i^N f_i m_i \nabla_{\mathbf{r}} w(\mathbf{r} - \mathbf{r}_i) \tag{2.32}$$

$$\nabla\left(\frac{f(\mathbf{r})}{\rho(\mathbf{r})}\right) = \sum_i^N \frac{f_i m_i}{\rho_i^2} \nabla_{\mathbf{r}} w(\mathbf{r} - \mathbf{r}_i) \tag{2.33}$$

The same substitutions give different forms of the smoothed particle interpolation function as:

$$f(\mathbf{r})\rho(\mathbf{r}) = \sum_i^N f_i m_i w(\mathbf{r} - \mathbf{r}_i) \tag{2.34}$$

$$\frac{f(\mathbf{r})}{\rho(\mathbf{r})} = \sum_i^N \frac{f_i m_i}{\rho_i^2} w(\mathbf{r} - \mathbf{r}_i) \tag{2.35}$$

With these algorithms defined it is now possible to derive the SPAM continuum equations.

2.3.3 Derivation of SPAM Continuity Equation

The continuity equation states that the rate of change of density and at any point is given by the rate at which the material diverges at that point:

$$\dot{\rho} = -\rho \nabla \cdot \mathbf{v} \tag{2.36}$$

Consider the right-hand side of the equation. The following identity can be used:

$$\nabla \cdot (\rho \mathbf{v}) = \rho \nabla \cdot \mathbf{v} + \mathbf{v} \cdot \nabla \rho \tag{2.37}$$

This allows the continuum equation to be written as:

$$\dot{\rho} = \mathbf{v} \cdot \nabla \rho - \nabla \cdot (\rho \mathbf{v}) \tag{2.38}$$

The smoothed particle approximation to the first term on the right hand side using Eq.2.31 is now:

$$\mathbf{v}_i \cdot (\nabla \rho)_i = \mathbf{v}_i \cdot \sum_j^N m_j \nabla_i w(\mathbf{r}_i - \mathbf{r}_j) \tag{2.39}$$

Similarly using Eq.2.34 the second term can be approximated as:

$$[\nabla \cdot (\rho \mathbf{v})]_i = \nabla_i \cdot \sum_j^N \mathbf{v}_j m_j w(\mathbf{r}_j - \mathbf{r}_i) \tag{2.40}$$

Combining these gives the smoothed particle continuum equation of motion:

$$\dot{\rho}_i = \sum_j^N (\mathbf{v}_i - \mathbf{v}_j) m_j \cdot \nabla_i w(\mathbf{r}_i - \mathbf{r}_j) \tag{2.41}$$

This equation offers an alternative calculation of density within SPAM simulations. Rather than sum the density at every time step using Eq.2.1 the density can be evolved through each time step.

It should be noted here that the weight function only actually depends on the magnitude of the distance $w(|\mathbf{r}_i - \mathbf{r}_j|)$. The gradient of the weight function can thus be calculated as:

$$\nabla_i w = \frac{\partial w(|\mathbf{r}_i - \mathbf{r}_j|)}{\partial |\mathbf{r}_i - \mathbf{r}_j|} \frac{\partial |\mathbf{r}_i - \mathbf{r}_j|}{\partial \mathbf{r}_i} \hat{\mathbf{r}}_{ij} = w' \hat{\mathbf{r}}_{ij} \tag{2.42}$$

Here w' is the first derivative of the weight function and $\hat{r}_{ij}$ is the unit vector in the direction r_{ij}.

2.3.4 Derivation of SPAM Equation of Motion

In the absence of any body forces continuum equation of motion states that the acceleration at a point is given by diverging pressure at that point per unit density:

$$\rho \ddot{r} = \rho \dot{\mathbf{v}} = -\nabla \cdot P \tag{2.43}$$

again we can use an identity for the right hand side:

$$\nabla \cdot \left(\frac{P}{\rho} \right) = \frac{1}{\rho} \nabla \cdot P - \left(\frac{P}{\rho^2} \right) \cdot \nabla \rho \tag{2.44}$$

This gives the acceleration as:

$$\dot{v} = -\left(\frac{P}{\rho^2}\right) \cdot \nabla\rho - \nabla \cdot \left(\frac{P}{\rho}\right) \tag{2.45}$$

Considering the first term of the right hand side, the smoothed particle approximation is given by Eq.2.31 as:

$$\left(\frac{P}{\rho^2}\right)_i \cdot \nabla_i \rho_i = \left(\frac{P}{\rho^2}\right)_i \cdot \sum_j^N m_j \nabla_i w(\mathbf{r}_i - \mathbf{r}_j) \tag{2.46}$$

Similarly using Eq.2.35 the second term is given by:

$$\nabla_i \cdot \left(\frac{P}{\rho}\right)_i = \sum_j^N m_j \left(\frac{P}{\rho^2}\right)_j \cdot \nabla_i w(\mathbf{r}_i - \mathbf{r}_j) \tag{2.47}$$

Combining these gives the smoothed particle approximation of the acceleration:

$$\dot{\mathbf{v}}_i = \sum_j^N m_j \left[\left(\frac{P}{\rho^2}\right)_i + \left(\frac{P}{\rho^2}\right)_j\right] \cdot \nabla_i w(\mathbf{r}_i - \mathbf{r}_j) \tag{2.48}$$

This equation allows the particle positions to be updated in time.

2.3.5 Derivation of SPAM Equation of Energy

The continuum equation of energy describes how the addition of work done at a point as well as the heat flowing into that point describe its internal energy e. Here Q denotes the heat flux. In the absence of heat sources and sinks:

$$\rho\dot{e} = -P : \nabla v - \nabla \cdot Q \tag{2.49}$$

The second term in this equation is analogous to Eq.2.43. It follows that the smoothed particle approximation for the diverging heat flux must be calculated as:

$$-\left(\frac{1}{\rho}\right)_i \nabla \cdot Q_i = \sum_j^N m_j \left[\left(\frac{Q}{\rho^2}\right)_i + \left(\frac{Q}{\rho^2}\right)_j\right] \cdot \nabla_i w(\mathbf{r}_i - \mathbf{r}_j) \tag{2.50}$$

Considering the first term we can use the identity:

$$\nabla(\mathbf{v}\rho) = \rho\nabla\mathbf{v} + \mathbf{v}\nabla\rho \tag{2.51}$$

Using the same methods as previously combined with the approximations of Eq.2.32 and Eq.2.31, it can be shown:

$$\rho_i \nabla \mathbf{v}_i = \sum_j^N (\mathbf{v}_i - \mathbf{v}_j) m_j \nabla w(\mathbf{r}_i - \mathbf{r}_j) \tag{2.52}$$

This expression is used to evaluate the temperature gradient in Eq.2.16. For its use here, it should be noted that the expression for internal energy can be re-written as:

$$\dot{e}_i = -\left[\frac{P}{\rho^2} : \rho\nabla\mathbf{v}\right]_i - \left(\frac{1}{\rho}\right)_i \nabla \cdot Q_i \tag{2.53}$$

The operator : acts as $P : \nabla \mathbf{v} = \sum_{\alpha,\beta} P_{\alpha\beta} \nabla_\beta v_\alpha$ across dimensions α, β. The symmetric pressure P_{ij} is used to ensure conservation of energy [54]:

$$\left(\frac{P}{\rho}\right)_{ij} = \frac{1}{2}\left[\left(\frac{P}{\rho}\right)_i + \left(\frac{P}{\rho}\right)_j\right] \tag{2.54}$$

This gives the SPAM energy equation as:

$$\begin{aligned}\dot{e}_i = &-\sum_j^N m_j \frac{1}{2}\left[\left(\frac{P}{\rho}\right)_i + \left(\frac{P}{\rho}\right)_j\right] : (\mathbf{v}_i - \mathbf{v}_j)\nabla w(\mathbf{r}_i - \mathbf{r}_j) \\ &-\sum_j^N m_j \left[\left(\frac{Q}{\rho^2}\right)_i + \left(\frac{Q}{\rho^2}\right)_j\right] \cdot \nabla_i w(\mathbf{r}_i - \mathbf{r}_j)\end{aligned} \tag{2.55}$$

The SPAM approximation is not limited to the continuum equations presented within this work. The standard procedure of discretization shown here can be applied to any equation which describes the time evolution of continuous quantities within the system, such as those describing magnetism [69]. This may present an opportunity to attempt a SPAM description of the phase field equations (which present material phases as a continuum) within future work.

2.3.6 Conservation of Energy and Linear Momentum

The total momentum Mv for the SPAM system can be calculated as:

$$Mv = \sum_i^N m_i \mathbf{v}_i \tag{2.56}$$

It is required that the equations conserve momentum to be able to simulate problems with SPAM without significant error introduced, therefore it is must be confirmed that:

$$\frac{d(Mv)}{dt} = \sum_i^N m_i \dot{\mathbf{v}}_i = 0 \tag{2.57}$$

The acceleration $\dot{\mathbf{v}}_i$ is given by Eq.2.48. This gives the rate of change of the total system momentum as:

$$M\frac{dv}{dt} = \sum_i^N \sum_j^N m_i m_j \left[\left(\frac{P}{\rho^2}\right)_i + \left(\frac{P}{\rho^2}\right)_j\right] \cdot \nabla_i w(\mathbf{r}_i - \mathbf{r}_j) \tag{2.58}$$

The simplest way to demonstrate conservation here is to consider contributions from pairs of particles i, j. The contribution from particle i due to j, denoted $\Delta_j(m\mathbf{v}_i)$, is:

$$\Delta_j(m\mathbf{v}_i) = m_i m_j \left[\left(\frac{P}{\rho^2}\right)_i + \left(\frac{P}{\rho^2}\right)_j\right] \cdot \nabla_i w(\mathbf{r}_i - \mathbf{r}_j) \tag{2.59}$$

Observing the opposite contribution, particle j due to i, it can be seen that:

$$\Delta_i(m\mathbf{v}_j) = m_i m_j \left[\left(\frac{P}{\rho^2}\right)_i + \left(\frac{P}{\rho^2}\right)_j\right] \cdot \nabla_j w(\mathbf{r}_i - \mathbf{r}_j) \tag{2.60}$$

The gradient term for the $\Delta_j(m\mathbf{v}_i)$ contribution is given by Eq.2.61. For the opposite contribution:

$$\nabla_j w = \frac{\partial w(|\mathbf{r}_i - \mathbf{r}_j|)}{\partial |\mathbf{r}_i - \mathbf{r}_j|} \frac{\partial |\mathbf{r}_i - \mathbf{r}_j|}{\partial \mathbf{r}_j} \hat{\mathbf{r}}_{ij} = -w' \hat{\mathbf{r}}_{ij} \tag{2.61}$$

For each pair of particles (i, j) the contributions are therefore equal and opposite and thus momentum is conserved. The same principle follows to show that the heat flux contributions to the energy equation cancel. This shows the total thermal energy E_T is conserved:

$$\frac{dE_T}{dt} = \sum_i^N \sum_j^N m_i m_j \left[\left(\frac{Q}{\rho^2} \right)_i + \left(\frac{Q}{\rho^2} \right)_j \right] \cdot \nabla_i w(\mathbf{r}_i - \mathbf{r}_j) = 0 \tag{2.62}$$

To show the conservation of total energy E it is necessary to consider the change in linear momentum in the direction of motion (the rate of change in the total kinetic energy E_K):

$$\sum_i^N m_i \dot{\mathbf{v}}_i \cdot \mathbf{v}_i = \sum_i^N m_i \left[\sum_j^N m_j \left[\left(\frac{P}{\rho^2} \right)_i + \left(\frac{P}{\rho^2} \right)_j \right] \cdot \nabla_i w(\mathbf{r}_i - \mathbf{r}_j) \right] \cdot \mathbf{v}_i \tag{2.63}$$

This can be written as:

$$\dot{E}_K = \sum_i^N \sum_j^N m_i m_j \left[\left(\frac{P}{\rho^2} \right)_i + \left(\frac{P}{\rho^2} \right)_j \right] w' \hat{\mathbf{r}}_{ij} \cdot \mathbf{v}_i \tag{2.64}$$

Now consider the rate of change of the total potential energy E_P given by the first term in Eq.2.55:

$$\dot{E}_P = -\sum_i^N \sum_j^N m_i m_j \frac{1}{2} \left[\left(\frac{P}{\rho} \right)_i + \left(\frac{P}{\rho} \right)_j \right] : (\mathbf{v}_i - \mathbf{v}_j) w' \hat{\mathbf{r}}_{ij} \tag{2.65}$$

Again considering pairs of particles i, j the kinetic energy will have terms:

$$\dot{E}_{K_{(ij+ji)}} = m_i m_j \left[\left(\frac{P}{\rho^2} \right)_i + \left(\frac{P}{\rho^2} \right)_j \right] \left(w' \hat{\mathbf{r}}_{ij} \cdot \mathbf{v}_i - w' \hat{\mathbf{r}}_{ij} \cdot \mathbf{v}_j \right) \tag{2.66}$$

Similarly for the potential energy:

$$\dot{E}_{P_{(ij+ji)}} = -m_i m_j \left[\left(\frac{P}{\rho} \right)_i + \left(\frac{P}{\rho} \right)_j \right] \left(\frac{1}{2} (\mathbf{v}_i - \mathbf{v}_j) w' \hat{\mathbf{r}}_{ij} + \frac{1}{2} (\mathbf{v}_i - \mathbf{v}_j) w' \hat{\mathbf{r}}_{ij} \right) \tag{2.67}$$

Considering the sum of these two rates of change of energy it becomes clear that:

$$\dot{E}_K + \dot{E}_P = 0 \tag{2.68}$$

Therefore energy is conserved through the SPAM approximations as given here.

2.4 Limitations of Smoothed Particle Methods

There are many limitations of the SPAM interpolation scheme described above. There have been five 'grand challenges' identified that require significant research to overcome some of these limitations [70], these are: convergence, consistency and stability; boundary conditions; adaptivity; coupling to other methods and applicability to industry. It is hoped that this thesis will contribute towards this final challenge. Within these challenges the main issues and methods impacting upon this work are outlined and discussed below. Each issue will be discussed within the relevant simulations in the following chapters.

2.4.1 Conservation of Angular Momentum and Density

Angular momentum is not conserved within the formulation given. The notation for the stress tensor is used in the place of the pressure $P = -\sigma$. It is shown by Hoover [54] that the contribution to the rate of change of angular momentum $\dot{L}$ for a pair of particles in 2D i, j is non zero:

$$\begin{aligned}\dot{L}_{ij} = \left(\frac{mw'xy}{r}\right)_{ij} \left[\left(\frac{\sigma_{yy}}{\rho^2}\right)_i + \left(\frac{\sigma_{yy}}{\rho^2}\right)_j - \left(\frac{\sigma_{xx}}{\rho^2}\right)_i - \left(\frac{\sigma_{xx}}{\rho^2}\right)_j\right] \\ + \left(mw'\frac{x^2-y^2}{r}\right)_{ij} \left[\left(\frac{\sigma_{xy}}{\rho^2}\right)_i + \left(\frac{\sigma_{xy}}{\rho^2}\right)_j\right] \neq 0\end{aligned} \tag{2.69}$$

The off-diagonal terms of the stress tensor cause a non-zero rate of change for a rotating body. The work by Bonet and Lok [71] alternatively uses the variational principle to explore conservation within SPAM. It is found that through the use of velocity smoothing, outlined in Sec.2.4.4 and kernel correction explored in Sec.2.4.2 that these effects can be mitigated.

A more important key finding of Bonet and Lok is that for simulations which use the alternative route of density evolution (Eq.2.41) instead of the more traditional sum density (Eq.2.1) to update the simulations, an alternative equation of motion is proposed to ensure the equations used are variationally consistent:

$$F_i = m_i\dot{\mathbf{v}}_i = \sum_j^N V_i V_j \left[P_i + P_j\right] \cdot \nabla_i w(\mathbf{r}_i - \mathbf{r}_j) \tag{2.70}$$

2.4.2 Boundary Deficiency and Kernel Corrections

The weight function (or kernel) used is normalised so that integration over the kernel support gives 1. The SPAM method is however discretised, therefore it is not guaranteed that the sum over all particles that lie within range H is 1. For there to be no error introduced it is required that the following hold true everywhere within the SPAM system of domain space Ω:

$$\sum_i^N w(\mathbf{r} - \mathbf{r}_i) = 1 \qquad \forall \mathbf{r} \in \Omega \tag{2.71}$$

At simulation boundaries the issue of kernel consistency becomes most evident. At the physical boundary of an SPAM simulation the smoothing function begins to encounter empty space if no

boundary particles are provided. This causes the function to incorrectly estimate the smoothed continuum values and thus cause boundary deficiencies. This is due to the definition and normalisation of the kernel function [73], for example in 1D:

$$\lim_{H\to 0}\int_0^B w(x-x',H)dx' = 1 \tag{2.72}$$

Here $0, B$ represent the boundaries of the simulation. The normalisation of the weight function (kernel) W is chosen to be 1. This always holds true in the limit where $H \to 0$. However in practice the smoothing length H is finite due to the compact support of the kernel of the simulation. Therefore it is true that:

$$\lim_{x\to B}\left[\lim_{H\to 0}\int_0^B w(x-x',H)dx'\right] = \frac{1}{2} \tag{2.73}$$

This means that for calculations done on positions at the boundary B, half of the kernel lies out side of the simulation and thus the normalisation condition causes the estimate to be half of the volume expected. Fig.2.13 illustrates how insufficient particles are included within the smoothing length for points which approach the system boundary. This causes deficiencies in the values calculated at the boundaries if untreated. An example is given in Fig.2.14 which shows interpolated densities within a $1D$ system with as much as a 30% error approaching the system boundary.

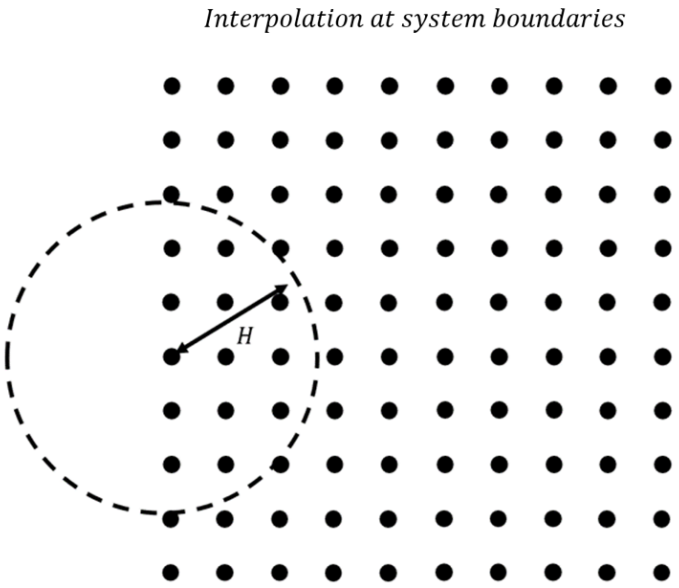

Figure 2.13: An illustration of the deficient number of particle points within a range H of particles approaching the boundary

One method to mitigate against this issue is to introduce boundary particles. By adding additional particles outside of the domain of interest it can be ensured that the sum of the weight function within the domain approaches unity. Boundary conditions are one of the main foci of the next chapter, and so will be discussed in more depth then. However more advanced boundary conditions have been proposed [74] and in-depth analysis of the accuracy and stability completed [75]. In

addition to this, methods of using corrective factors for the kernels specific to the boundaries have been proposed [76], as well as more advanced corrections accounting for material interfaces [77].

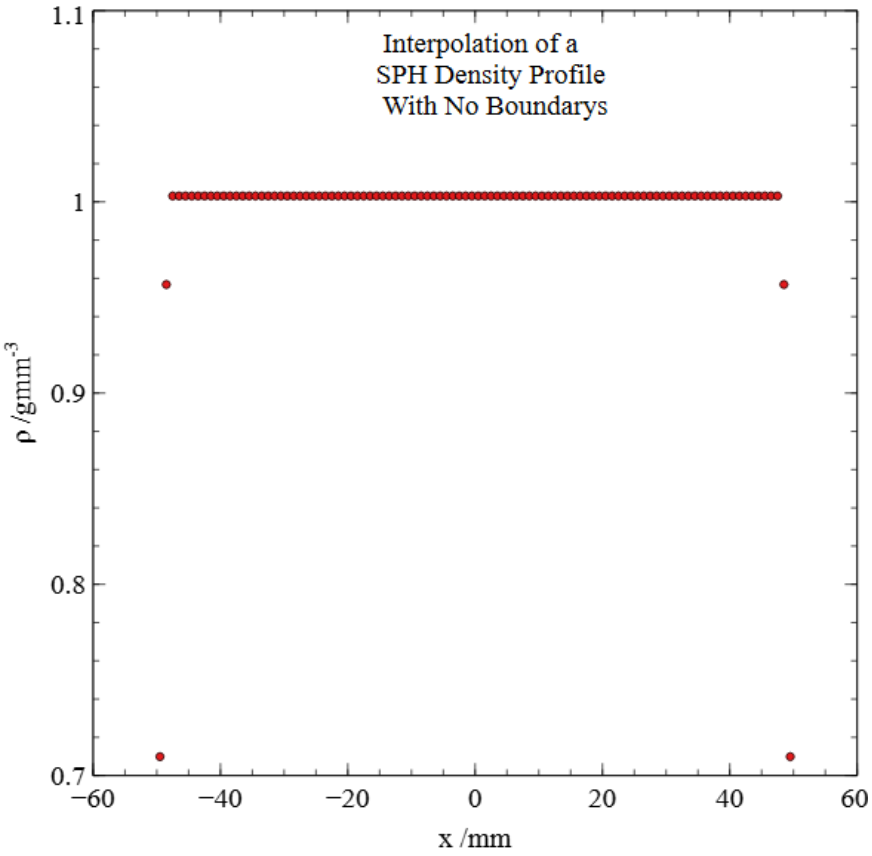

Figure 2.14: The interpolated density profile for an SPAM material with no boundary conditions enforced. The system is composed of $N = 100$ particles with unit mass and grid spacing such that the expected density is $\rho_0 = 1\text{g/mm}^3$

Research has also been completed which suggests that the chosen kernels used within SPAM simulations have a direct effect on the convergence of the simulations [78]. More importantly, as first noted, the kernels can suffer from inconsistency across the simulation. If the particle configuration is disordered the kernel estimate will vary across the simulation due to inconsistency in the number of evaluated neighbour particles (just as at the boundary). Methods exist which combat this issue with a variable smoothing length [79]. These are calculated such that the smoothing length always includes the required number of particles. An alternative method, which will be briefly explored in this work, involve kernel corrections and kernel gradient corrections.

The Corrective Smoothed-Particle Method (CSPM) was first proposed to help mitigate the tensile instability [80]. The correction is based around the idea of truncated Taylor expansions of the kernel estimated functions within the SPAM simulation. In standard 1D SPAM, any arbitrary function f is said to be given (before discretization where x_i simply notes an arbitrary position) by:

$$f(x_i) = \int f(x)w(x_i - x)dx \tag{2.74}$$

The integral is calculated across the whole domain defined by the smoothing length H. By examining a Taylor expansion of the function f on the right hand side of this equation, the proposed corrective factor can be derived:

$$\int f(x)w(x_i - x)dx = f(x_i)\int w(x_i - x)dx + f'(x_i)\int (x - x_i)w(x_i - x)dx + ... \tag{2.75}$$

By truncating all the derivatives and rearranging we obtain the approximation:

$$f(x_i) \approx \frac{\int f(x)w(x_i - x)dx}{\int w(x_i - x)dx} \tag{2.76}$$

This is the simplest form or correction. The physical interpretation of this equation is that if the value of the kernel (the denominator) differs from the expected normalisation of 1, then the value of the function is re-scaled accordingly by this factor. It is evident that higher order corrections may be included by truncating the Taylor series at a higher order. Similarly gradients of functions maybe corrected in the same way by first taking the gradient of the above SPAM approximation of a function. For 1D this is:

$$f(x_i) = \int f(x)w'(x_i - x)dx \tag{2.77}$$

Then the Taylor expansion has the form:

$$\int f(x)w'(x_i - x)dx = f(x_i)\int w'(x_i - x)dx + f'(x_i)\int (x - x_i)w'(x_i - x)dx + ... \tag{2.78}$$

Discarding all terms higher than those given here gives the approximation:

$$f'(x_i) \approx \frac{\int [f(x) - f(x_i)]w'(x_i - x)dx}{\int (x - x_i)w'(x_i - x)dx} \tag{2.79}$$

This corrective method is one of many which have since been derived [78]. There are far more studies and reformulations of SPAM to deal with deficiencies close to the system boundaries which are not explored in this work, these include enhancements to the Laplace approximation [81] and the δ-SPH formulation [82].

2.4.3 Discontinuities

There are many cases where discontinuities occur naturally such as across phase boundaries, during formation of cracks within materials or when shock waves are formed. SPAM is however poorly suited to handle these discontinuities as derived here. This is because the functions are assumed to be continuous. Fig.2.15 shows the SPAM interpolated temperature and temperature gradient for a discontinuous piecewise temperature profile. It shows that the SPAM calculated temperature gradient diverges around the discontinuity. This is to be expected as the gradient of a function at a discontinuous point is by its very definition not well-defined.

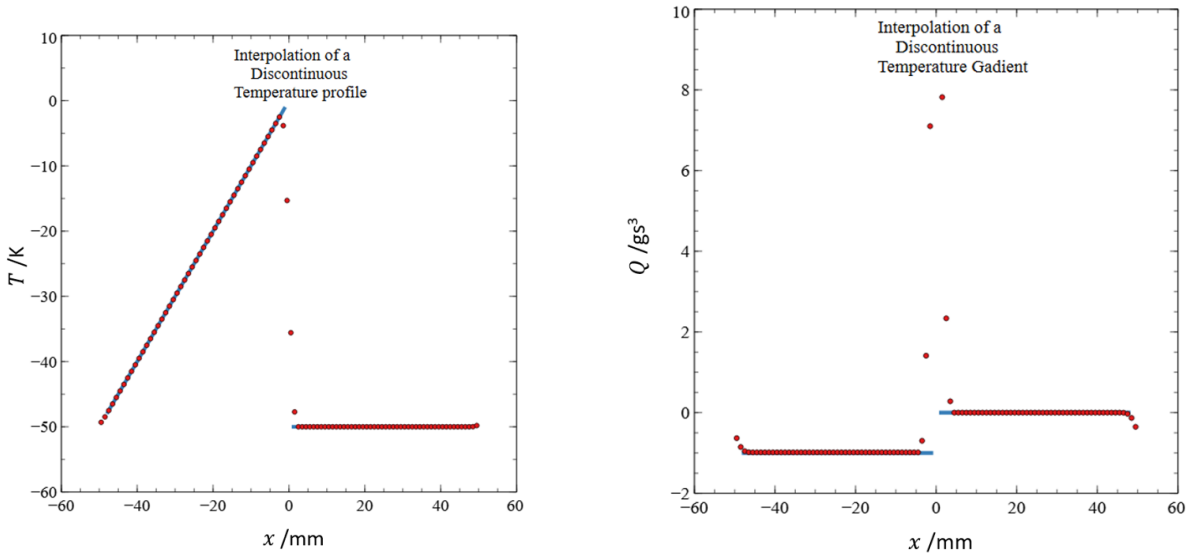

Figure 2.15: A discontinuous piece wise temperature profile given by $T = x : -50 < x < 0$ and $T = -50 : 0 < x < 50$ is interpolated at 100 points with Eq.2.13, shown left. The negative of the interpolated temperature gradient calculated with Eq.2.16 is shown right. The interpolated values are shown in red, the expected profile in blue. $N = 100$ SPAM particle points and periodic boundary conditions are used.

The often used method to deal with this in the literature is with 'artificial' (dissipative) terms. These terms can be considered discontinuity smoothing. They calculate diverging points within the properties they are assigned to and add terms to the calculation to reduce the divergence. These terms will be explored in full in the following chapter. This method is acceptable for shocks or single point discontinuities however far more complex cases can arise from the mixing of material phases or wide spread cracking.

Alternative formulations such as those of of Parshikov [83, 84] deal with this issue by introducing contact algorithms between the particles based on Riemann solvers. Parshikov demonstrates that this removes the need for artificial terms entirely, however this adds to the complexity of the computation and implementation of the method.

More studies not explored within this report, will be important to future SPAM nuclear fuel models. One feature explored in the literature is multi-phase simulations [85]. SPAM has been applied to problems of phase change [58], liquid solid interfaces [86] and solid particles moving within fluid flows [87,88] to name just a few. Within nuclear fuel pellets we see fission gas produced which causes bubble formation and pellet swelling. Multi-phase simulations will be important to account for these processes. However, the large density gradients between solid gas interfaces can cause problems with the kernel estimates of the continuum values. A methodology involving more advanced kernel gradient corrections has already been proposed to deal with this issue [89].

Bubble formation within nuclear fuel pellets is responsible for micro crack initiation. Again many varied approaches toward damage modelling within SPAM exist. For simplicity within the simulations presented in this report damage is controlled by the tensile and yield strengths, as in Hoover's tension tests [54] (explored in a later chapter). More advanced damage models have been proposed

however. A two scale damage concept [90] developed for continuum descriptions was applied with great success within SPAM simulations of fracturing metal rings [91]. The main challenge with this more complex description of damage is that more precise knowledge of neighbouring particles is required so that damage between nearest neighbour particles can affect the forces between next nearest neighbours. The method used to achieve this is referred to as 'Total Lagrangian' SPAM, which consists of storing a neighbour list for each particle from initialisation with the appropriate form to calculate how damage should effect each neighbour list. Although effective, this methodology is computationally expensive and limits the ability of a material to flow, therefore it has not been used within simulations presented within this report.

SPAM is built on the underlying assumption that all functions are continuous [92]. However more complex formulations of SPAM have been proposed which address this are able to directly deal with discontinuous function [93]. This method uses the kernel corrections of CSPM but divides the domains by the material interface. The whole domain is then considered as normal in CSPM but a corrective factor is added considering just one of the sub-domains to adjust for the influence of discontinuity. This method is particularly appealing as it treats the system as a whole, thus the SPAM code has the same basic form, however the interface is still treated using the idea of corrective factors, making the method relatively easy to implement. The disadvantage of this method is that it requires two domains to be defined for the discontinuity, therefore it cannot replace artificial terms in dissipating discontinuities that arise within the simulation.

2.4.4 The Tensile Instability

The tensile instability refers to the tendency of SPAM particles to clump together in an un-physical way when under tension. Tension is characterised by a negative pressure state $-P$ for the particles. Consider Eq.2.48, if P is assumed to varies slowly in time and space, the particle accelerations will become:

$$\dot{\mathbf{v}}_i \propto -\sum \nabla w(\mathbf{r}) \tag{2.80}$$

This takes the same form as a molecular dynamics potential. It can be seen that in the near field the derivative of the weight function is negative. This means that the closest particle pair will accelerate towards each other in a purely tensile regime.

A large amount of research has already been dedicated to attempts to mitigate this issue. Solid mechanics modelling with SPAM was explored early on by Hoover [54]. Hoover successfully implemented test simulations of the tension test and ball and plate penetration for arbitrary materials and compared these with SPAM-like molecular dynamics simulations of the same nature. The methods used to overcome challenges are far simpler when compared with recent research developments, and show successful results in mitigating instabilities. Two examples of these methods to mitigate instability in solids under tension are core potentials and velocity averaging. Core potentials take the form:

$$\Phi_{core} = 100 \sum_{i<j} [1 - (r_{ij}^2/\sigma^2)]^4; r_{ij}^2 < \sigma^2 \tag{2.81}$$

Here i and j are particle indices and r the distance between them. For a given 'core size' σ, the potential acts to force particles to separate when their 'cores' overlap. This prevents particles from clumping together under tension and thus mitigates the instability. In SPAM there is a danger however that such parameters will simply be fitted to obtain the desired results which does little to validate the underlying physical equations.

The method of velocity averaging was originally proposed by Monaghan [94]. Often called XSPH, the method was developed to prevent particle penetration at material interfaces but has been shown to reduce the tensile instability [95]. The idea is to average velocities locally with equations of the form:

$$\langle v \rangle_i = v_i + \sum_j (v_j - v_i) w_{ij} / \rho_{ij} \tag{2.82}$$

Here v are particle velocities, ρ density and w represents the smoothing function of SPAM. The concept aims to modify local velocities to be nearly identical which reduces random variations in movement which are only applicable at the molecular scale. Velocity averaging also becomes very important for modelling material interfaces. The weight function of SPAM acts to spread the influence of particles in space. At material interfaces this has the effect of causing inter particle penetration of the surfaces beyond that expected from molecular diffusion or force driven penetration. Unfortunately Hoover notes (without explicit detail) that combining velocity averaging with the viscous damping forces used can result in instability and so is not favourable. This report will aim to confirm this among other methods. The damping forces used by Hoover are of the form:

$$F_{drag} = -v/\tau \tag{2.83}$$

Here τ is an arbitrary value chosen by Hoover to allow dissipation which would normally take place at the atomic length scales. An alternative to this method of dissipation is the more commonly used artificial viscosity first proposed by Lucy [96]. This is an example of the discontinuity capturing terms mentioned in Sec.2.4.3. To implement artificial viscosity, an extra term is added to the equation of motion:

$$\Pi_{ab} = -\alpha h c / \rho_{ab} \left(\frac{v_{ab} \dot{r}_{ab}}{r_{ab}^2 + \epsilon h^2} \right) \tag{2.84}$$

Here c is the sound speed, $\epsilon \approx 0.001$ a factor to prevent singularities, and alpha an adjustable parameter. This form of viscosity, although artificial, can be likened to true viscosity, however the difference is the scale considered. True viscosity would be ineffective as the particle size represents a section of continuous matter and not true particles, which would be at a much smaller scale. The artificial terms aim to compound the true viscosity into a force which can act as expected to slow particle motion. The effectiveness of this method has been demonstrated [97], and more advanced descriptions of artificial viscosity based on the ideas of Riemann solvers have been developed [98].

2.5 Boundary Conditions

Boundary conditions are important in simulations, not only for correcting calculations (such as that for the weight function deficiency close to the boundary), but also for the implementation of non-equilibrium thermodynamics and mechanics. For example by prescribing different temperature profiles at opposing boundaries, a flow of heat can be generated across the system which allows for the study of more complex physical systems such as that of a nuclear fuel rod.

2.5.1 Periodic Boundary Conditions

There are three widely used methods which form the basis the implementation of of most boundary conditions. The first and most easily implemented of these is known as periodic boundary conditions. Periodic boundaries are implemented by effectively tiling the simulated system in infinite

space. That is to say that the left-most side of the system is allowed to see and interact with the right-most side and the same between the upper and lower boundaries. Fig.2.16 illustrates this.

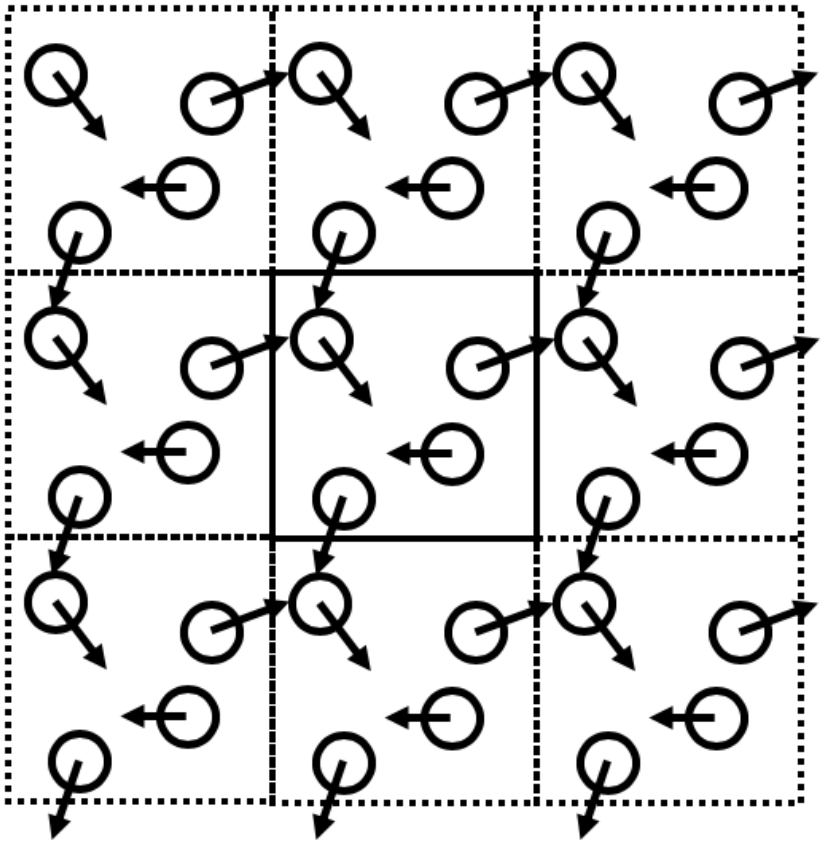

Figure 2.16: An example of the 'tile like' nature of periodic boundary conditions. Only one square is simulated however this small subsection acts as if in the bulk of a much larger system through the use of periodicity.

Periodic boundaries, although easily implemented, are very restrictive on the simulation. Interaction lengths of particles (characterised by the cut off length H for SPAM simulations) are restricted to be the minimum of half the length or width of the simulation size so that no particle may re-interact with itself. It is very difficult (but not impossible) to implement non-equilibrium conditions for the case of periodic boundary conditions as the boundary properties are predefined by the opposing system side so non-equilibrium situations cause nonphysical discontinuities within the system if not carefully implemented. Despite this periodic boundaries have seen wide spread use. Hoover demonstrated their use in a non-equilibrium simulation of Rayleigh-Bernard flow, in which periodic boundaries where implemented across the x-axis of a 2D simulation, while the y-axis is examined under both fixed and mirror boundaries.

2.5.2 Fixed Boundary Conditions

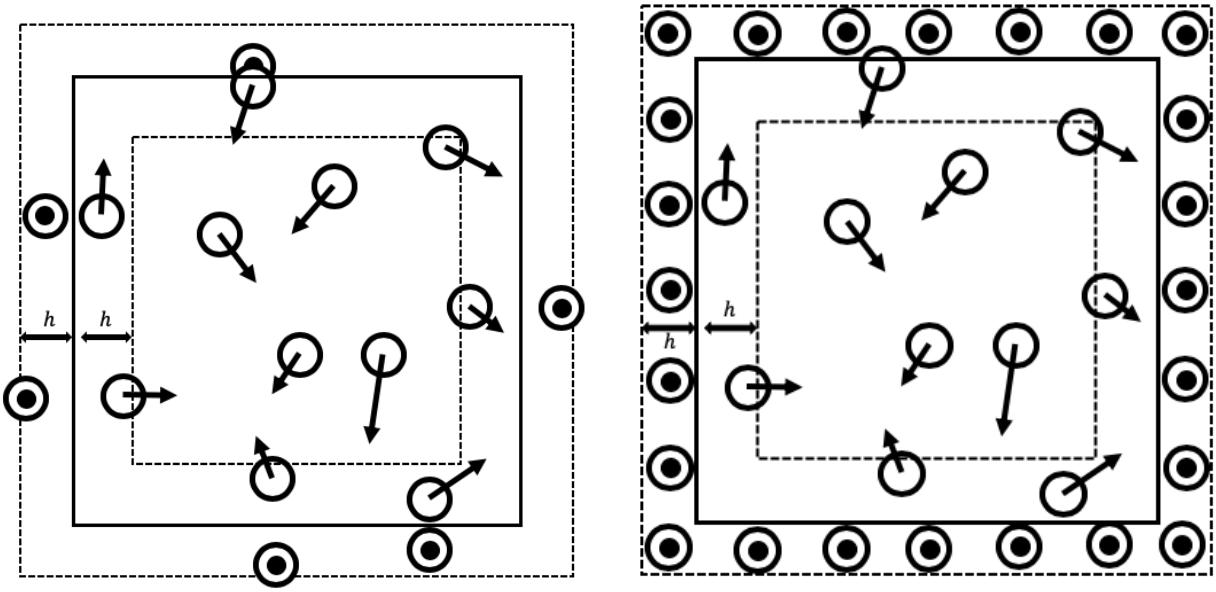

Figure 2.17: Visualisation of fixed boundary conditions. The fixed particle method has multiple different methods of assigning particle locations; for all methods values assigned to velocity and temperature are fixed and determined by the boundary associated with each particle. Particle positions may be assigned relative to system particles close to the boundary (Left) or in a regular lattice (Right).

Fixed boundary methods can be used to create non-equilibrium simulations. The particle locations may be assigned by methods such as mirroring particle locations across the boundary, as shown in Fig.2.17, by methods used to initialise the particle system (e.g regular lattices, random distributions, or relaxation methods) or by more complex algorithms designed to optimise particle density along more complex boundaries [68]. The important factor in the method is that quantities such as velocities, temperatures, heat fluxes etc., are predefined before the simulation as fixed values appropriate to the system being modelled. The main issue with this method is that the values of these fixed properties calculated *on* the system boundaries are not equal to the fixed values. Furthermore, the boundaries in no way react to the system evolution and thus small errors are introduced into the system for properties calculated close to the boundaries. Despite this fixed boundary methods are widely used and very robust, being able to be applied to more complex boundary shapes than periodic and mirror boundaries.

2.5.3 Mirror Boundary Conditions

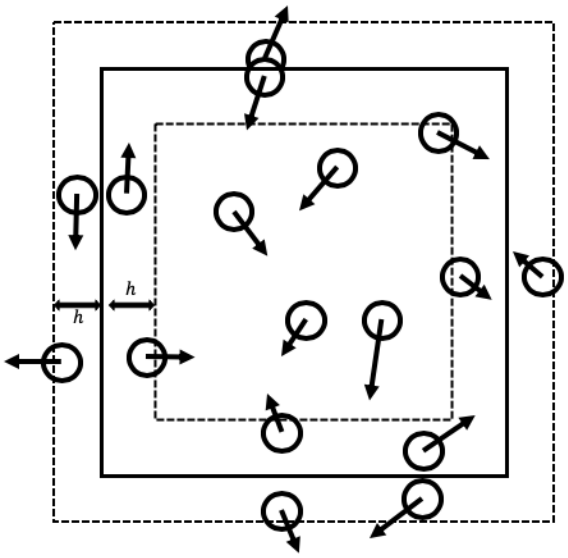

Figure 2.18: Visualisation of mirror boundary conditions. The mirror particle positions are defined by system particles close to the boundary and their properties by relations that define exact values *on* the system boundary.

Mirror (or dynamical) boundary conditions assign boundary particle locations based on the locations of system particles close to the boundary. As can be seen in Fig.2.18 the boundary particle properties are assigned relative to their mirror particles in such a way as to create exact values of properties *on* the system boundary. For example, as shown in the figure, if it is desirable to have no particles pass the system boundary, then mirrored particles are prescribed negative velocity, such that the net velocity on the boundary is zero $v_i + v_{i'} = 0$. This minimises the error introduced into system properties calculated on the boundary.

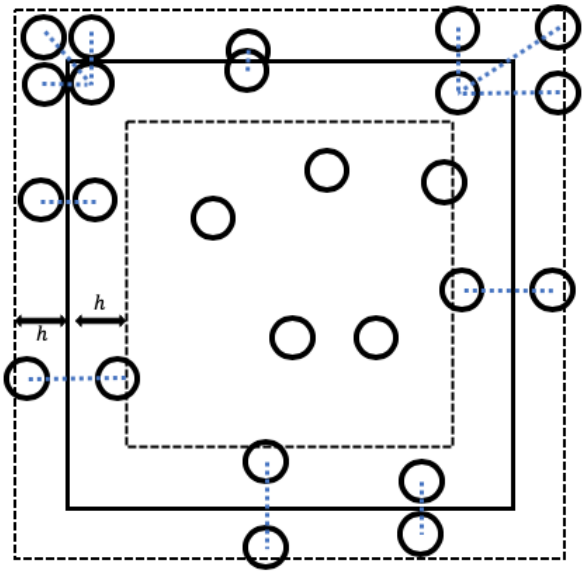

Figure 2.19: Visualisation placement of mirror boundary particles. Extra care and consideration is required when dealing with system corners to achieve the desired properties on the boundaries.

Mirror boundary conditions suffer however with the geometry of the boundary used. For a simple square case such as the one shown in Fig.2.19 it can be seen that special consideration must be given to the system corners. This will be discussed in more detail in the 2D example case. As well as this property calculations over curved system boundaries suffer from density issues. The nature of a curved boundary causes a greater number of particles to be required on the outside of the curve than the inside [72]. This means that for simple mirror boundaries too few particles are mirrored on the outside of the curve which causes the value of density and other properties to be in accurately interpolated.

2.5.4 Alternative Boundary Conditions

The boundary conditions so far presented are by no means exhaustive. Here we include a few alternative methods for implementation of boundary conditions. The first of these is through the use of potential boundaries. The particle behaviour at the simulation edges does not need to be constrained by the inclusion of more particles and can instead simply be constrained numerically [73]. A similar method calculates numerical adjustments based on line segments for a wall boundary [99]. This formulation can be difficult to generalise and therefore attempts have been made to introduce potentials through the use of particles [100]. This methodology was further complicated to include calculations of the exact correction factors for the boundary deficiency. The particles are used to calculate the sum of the weight function at the simulation surface which is then equated to the gradient by use of Gauss's theorem. This value is then used as a more accurate numerical factor to adjust the values calculated near the boundary [101]. Methods have also been proposed which create repulsive forces to emulate virtual particle boundaries for use with complex geometry [102]

More complex variations based on the idea of particle mirroring have also been proposed. Dynamic boundaries can be generated per particle at each time step based on a set of boundary points [103].

These particles can be considered 'ghost' or virtual particles as they are never truly stored and do not interact with all system particles. The virtual particle method (VPM) has been extended and shown to handle fluid flows with reasonable effectiveness [104]. More recently a method for the dynamical update of fixed boundary particles was created under the name modified dynamic boundary conditions (mDBC) [105]. This has also shown improvements in reducing the non-physical behaviour of particles at the boundaries. Full exploration of these methods are left to future work on this project. For now, the effect of the boundary implementation is best described when using boundaries for which the introduced error is more easily understood. These more complicated methods introduce more complicated distributions of error into the boundaries which although improve the simulations make the demonstration of the boundary effects more complicated than was desired for this work.

2.6 Time Integration Algorithms

The governing equations of motion for SPAM, such as Eq.2.48, Eq.2.55, give a value for the rate of change of particle properties. To use this value to update particle properties to the next time step, a time integration algorithm is required. Many different time integration schemes exist, each with its own advantages and disadvantages. The two important measures of these schemes however are the speed of the calculation within the code and the order of the errors introduced by the algorithm. To show this, three different schemes are demonstrated. These schemes are tested using a simple methodology shown by Hoover [106]. These are Euler's method, the Euler modified method (also known as Heun's method) and the Runge-Kutta method. In all cases the differential equation to be solved is noted as:

$$\dot{x} = f(x(t), t) \tag{2.85}$$

The Taylor expansion of this equation is the basis of all three schemes. Truncation to first order gives the Euler's method of time integration, with errors of order dt^2:

$$x_{n+1} = x_n + \dot{x}dt = x_n + dtf(x_n, t_n) \tag{2.86}$$

Here the subscript n refers to discretization in time where the nth time step is at time $t_0 + ndt$.

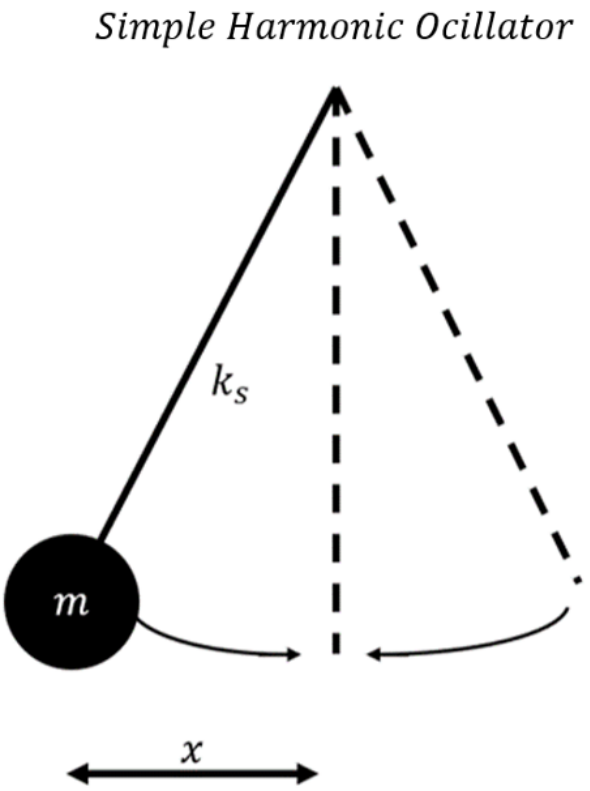

Figure 2.20: An example of a simple harmonic oscillator is the pendulum shown here. The acceleration experience by the pendulum is proportional to its distance from the centre line x and always acts towards the centre line. It is assumed no drag forces act on the pendulum.

To visualise the error introduced by each time integration scheme, each of the algorithms discussed in this section will be run for a simple differential equation, the simple harmonic oscillator. It is assumed that no drag forces act on the system therefore if the time integration algorithm introduces no error then the system should oscillate back and forth forever. A visualisation of this model would be a pendulum for small displacements is shown in Fig.2.20. The acceleration for this simple case is given by:

$$\ddot{x} = -\frac{k_s x}{m} \tag{2.87}$$

where k_s is the spring constant. The model has no resistive forces, therefore the total energy of the system is constant with perfect exchange of kinetic and potential energy. It is also expected that the coordinate and momenta of the system should form a perfect elliptical plot, as the imagined pendulum returns to the same extreme positions with each cycle. To clearly demonstrate the error of each method a large time step $dt = 1$s is used.

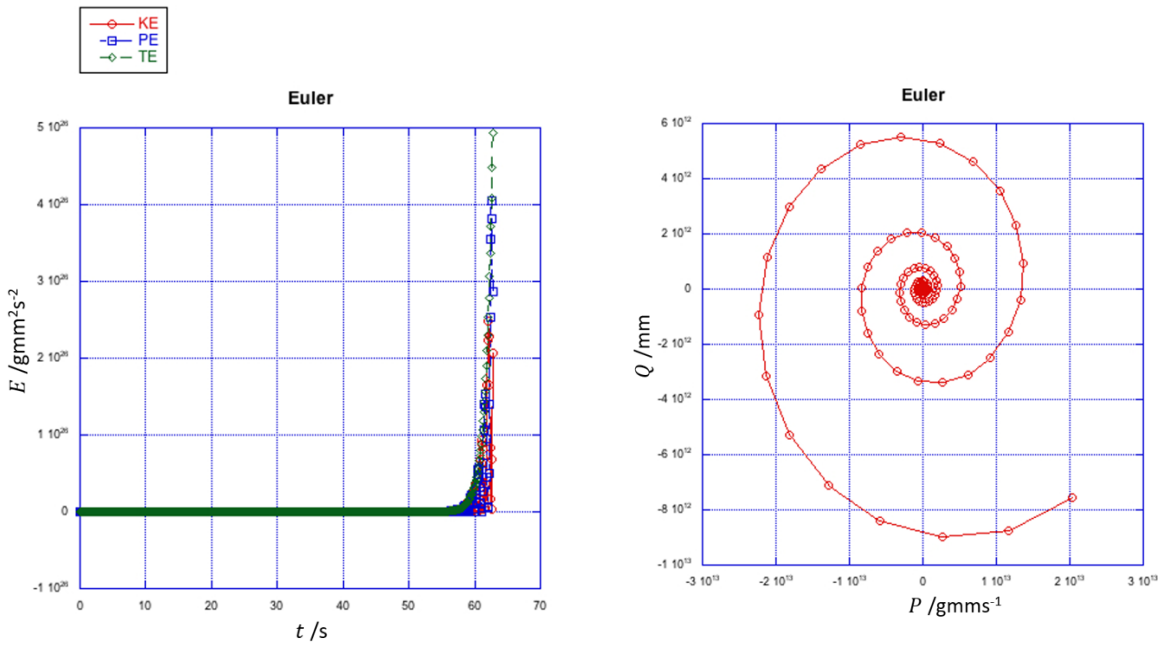

Figure 2.21: Euler's time integration scheme for the example of a simple harmonic oscillator run for approximately 3 periods of motion. Here Q is the space coordinate, P momentum. The system energy (Left) and phase space (right).

Fig.2.21 shows that the integration scheme does not conserve energy over extended periods of time for the chosen time step. Clearly the system energy is not conserved and the phase space is thus unstable. This makes it insufficient for use in SPAM simulations as a significantly reduced time step is required, resulting in far longer computation times. The simplest improvement on the Euler method is called the Heun (Euler modified) method, based on second order Taylor truncation. This involves a modification of the form:

$$\tilde{x}_{n+1} = x_n + \dot{x}dt \tag{2.88}$$

$$x_{n+1} = x_n + \frac{dt}{2}\left(f(x_n, t_n) + f(\tilde{x}_{n+1}, t_{n+1})\right) \tag{2.89}$$

This two step modification uses an average of the rate of change of the variable evaluated at two positions. This gives accurate time integration to second order in the time step, giving errors of dt^3. The effect of this can be seen in Fig.2.22. The system energy is still not conserved and the phase space unstable however the final estimated system energy is on the same order of magnitude as the true system energy, being over 10^{20} orders of magnitude closer than the Euler estimate. It is important to note that this increased accuracy comes at a cost. The equations of motion (denoted by function f) must be evaluated twice for each time-step of this algorithm, thus the computational run time of SPAM simulations would be doubled by its use over the Euler scheme, this is offset by the reduced time steps required.

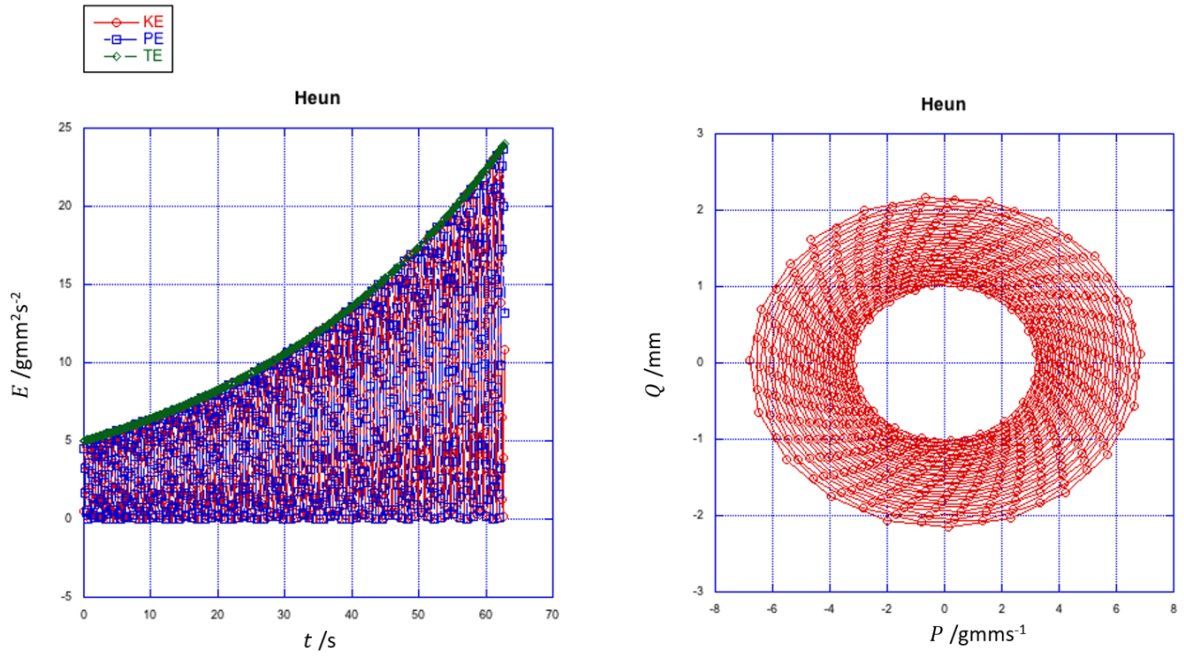

Figure 2.22: Heun's time integration scheme for the example of a simple harmonic oscillator run for approximately 3 periods of motion. Here Q is coordinate, P momentum. The system energy (Left) and phase space (right).

The same two-step modification shown in the Heun method may be extended to an arbitrary number of steps, each achieving an order of magnitude of error reduction in the time-step. The 4th order Runge-Kutta algorithm uses a four-step modification represented by:

$$\begin{aligned} c_1 &= f\left(x_n, t_n\right) \\ c_2 &= f\left(x_n + \frac{dt}{2}c_1, t_n + \frac{dt}{2}\right) \\ c_3 &= f\left(x_n + \frac{dt}{2}c_2, t_n + \frac{dt}{2}\right) \\ c_4 &= f\left(x_n + dtc_4, t_n + dt\right) \end{aligned} \tag{2.90}$$

$$x_{n+1} = x_n + \frac{dt}{6}\left(c_1 + 2c_2 + 2c_3 + c_4\right) \tag{2.91}$$

The averaging applied by the Runge-Kutta method when visualised is effectively the famous 'Trapezium rule' for approximating integrals. The modification ensures the algorithm has errors on the order of dt^5 The benefits of which can be seem in comparison to the Euler and Euler modified scheme in Fig.2.23. The system energy shows a minor decrease and the phase space thus approximately stable for the time period shown. This is due to the Runge-Kutta method being accurate to the order of dt^4 .

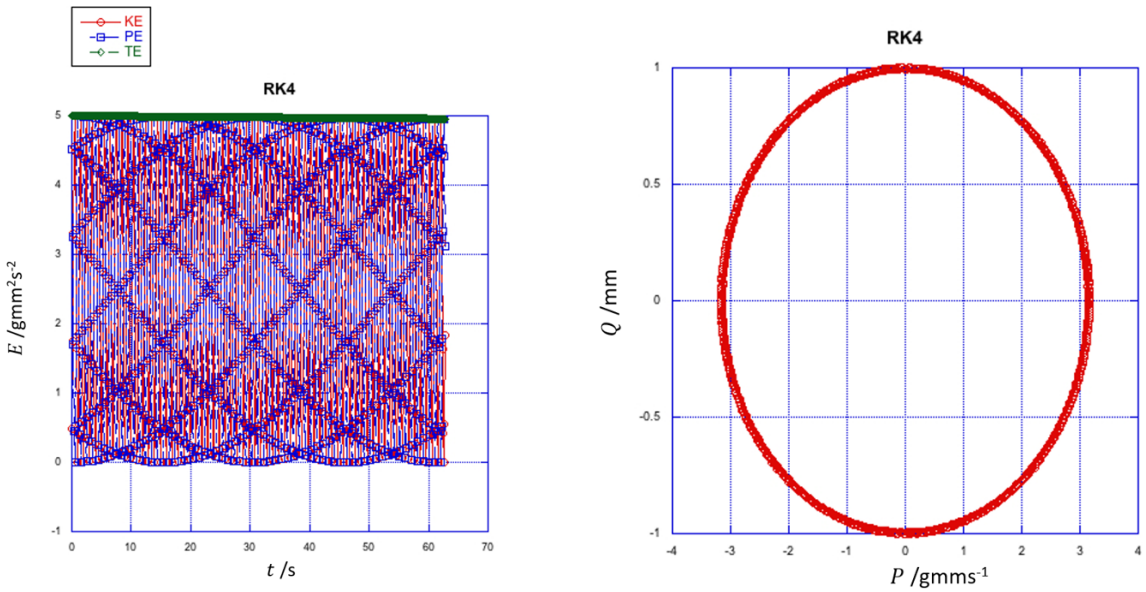

Figure 2.23: Runge-Kutta time integration scheme for the example of a simple harmonic oscillator run for approximately 3 periods of motion. Here Q is coordinate, P momentum. The system energy (Left) and the phase space (right)

Clearly a comparison of Fig.2.21,2.22,2.23 identifies that the Runge-Kutta time integration scheme offers a significant reduction in error with calculations than its counter parts, allowing far larger time steps to be taken. The computational cost of the Runge-Kutta method must however be considered. As discussed with the Heun method, the Runge-Kutta algorithm requires the equations of motion be evaluated 4 times at 4 separate locations for each time-step in the simulation. As stated higher orders of Taylor truncation can be achieved however more function evaluations are required at each time step. As we will see within the investigative sections to follow the time step must be restricted by other factors such as sound speed propagation within the material. It is therefore sufficient to dedicate greater computational time through the restriction of smaller time-steps than by the inclusion of higher order accuracy within the time integration scheme.

Other algorithms exist such as the Verlet and Gear predictor corrector [107]. Again each has drawbacks. For example the Verlet algorithm is not self starting. Balancing all these factors the Runge-Kutta 4th order algorithm has been deemed the most appropriate. The algorithm has therefore be used for all the following simulations.

2.7 Cell Division of Particles

As seen throughout the derivations given in sec.2.3, the SPAM equations call for algorithms which loop over particle pairs. This means without optimisation, for a system with N particles, the algorithm must check the distance between $N^2/2$ particle pairs. A method of cell division is therefore implemented for $2D$ simulations shown within this work.

The system domain is divided into smaller cells each of dimension H so that the full $N^2/2$ list is replaced by a smaller sum over particles within each cell plus particles in nearest neighbour cells

provided $r_{ij} < H$. Clearly no less than 3 cells can be employed along each edge to achieve this, therefore if H becomes too large relative to the system size this method is no longer useful.

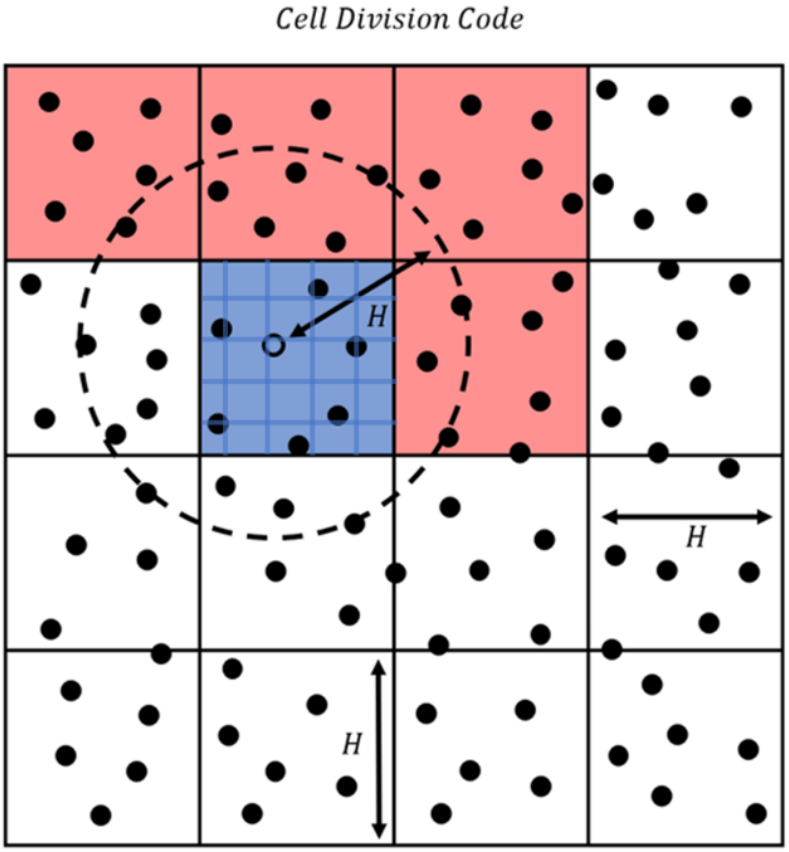

Figure 2.24: Illustration of how the cell division code splits the domain into cells of length and width H to allow for faster computation of pairs within range H.

Using the example shown in Fig.2.24 the point of interest is displayed within the blue cell. To find all its pairs, first the distance is checked between all particle within the blue (hatch marked) cell. Then all particles within the red (solid colour) cells are looped over. The red cells make up exactly half of all the 8 neighbouring cells of the blue cell. It is only necessary to check half the neighbouring cells within this repeating pattern as this prevents pairs from being counted twice.

This method allows a complete list of particle pairs within range H to be stored where each pair is included once. This can then be looped over with contributions included for both particles within the pair. If the particles are in motion the cell division can be repeated between time steps to recalculate the pairs list. This algorithm roughly scales as $O(NlogN)$ which allows larger systems of particles to be simulated within reasonable time scales.

2.8 Conclusion

This chapter has derived the basic equations of motion for SPAM and has demonstrated how the discretisation and smoothing errors can affect these calculations. An algorithm for time integration

has been selected as well as a suitable algorithm to generate the pair list. The boundary conditions to be explored within this work have also been outlined. This sets the stage for simulations to be carried out exploring further the effect of boundary conditions and choice of evolution equations within SPAM simulations of heat flow.

This chapter also highlights a great deal more work which has been completed within the field of smoothed particle modelling. Most of this research is beyond the scope of this PhD however the scope of the literature included gives great confidence that many of the limitations for the simulation of nuclear fuel carried out within this work can be overcome with future research.

Chapter 3

Heat flow within SPAM

3.1 Introduction

In this chapter only problems involving heat flow are considered. Mechanical deformation will be explored in later chapters. Boundary conditions will be a particular focus in this chapter as physical boundaries are required to drive non-equilibrium heat flow, as occurs in the case of a fuel rod. Boundary conditions are still considered one of the 'grand challenges' within SPAM [70]. Research has been done to establish the various disadvantages of the currently proposed boundary methods, however no general consensus of the best method has yet been reached. In this chapter results from heat flow with various boundary methods will be compared using well-defined analytical solutions to quantify their accuracy and their usefulness to SPAM and the fuel pin conceptual model.

The models presented here are well established test models which have been used in previous SPAM studies of heat conduction [108–110]. This work aims to compare different methods of implementation of the governing temperature equation as well and demonstrate the effect of boundary conditions on the simulations. From this work a widely unused methodology proposed by Hoover [54] is the simplest implementation and achieves the best accuracy against analytical results for both the transient and steady state cases.

3.2 Heat flow in a 1D periodic chain

The examination of SPAM begins with a computationally simple and physically intuitive model: Fourier's ring model [111]. The physical interpretation of this model would be a circular wire of uniform and negligible thickness, given some initial and non-uniform temperature distribution. A diagram of the model is shown in Fig.3.1.

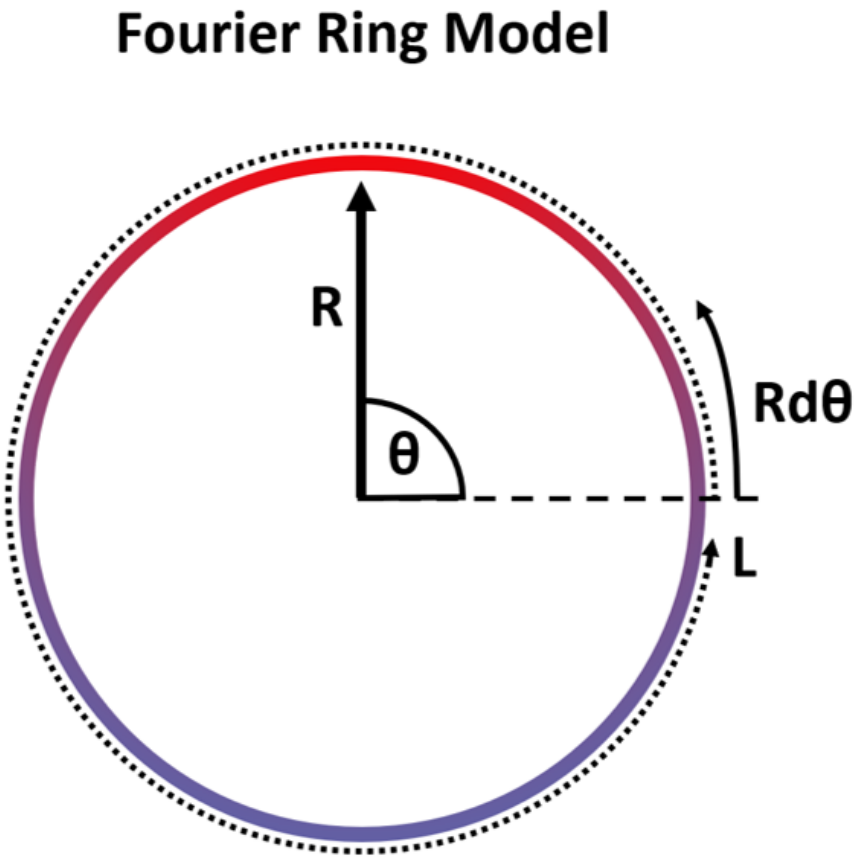

Figure 3.1: Fourier's ring model. The radius R is fixed and the temperature around the circumference of the system is only a function of the angle $T(\theta)$, thus the system can be modelled as 1D.

The temperature anywhere along the Fourier ring is described by the heat diffusion equation considered in polar co-ordinates:

$$\frac{\partial T(r,\theta)}{\partial t} = D_T \nabla^2 T(r,\theta) \tag{3.1}$$

where r is the radial position and θ is the angular position in polar co-ordinates. Here D_T represents the thermal diffusivity. Consider the assumption that temperature does not vary with radius (equivalent to the system having constant radius R). We then have:

$$\frac{\partial T(r,\theta)}{\partial r} = 0 \tag{3.2}$$

This means temperature is only a function of angle $T(r,\theta) = T(\theta)$ and reduces to the Laplacian:

$$\nabla^2 T(r,\theta) = \frac{\partial^2 T}{\partial r^2} + \frac{1}{r}\frac{\partial T}{\partial r} + \frac{1}{r^2}\frac{\partial^2 T}{\partial \theta^2} = \frac{1}{R^2}\frac{\partial^2 T}{\partial \theta^2} \tag{3.3}$$

For a simplified case where we choose to substitute variable $(R\theta) = x$:

$$\nabla^2 T(r,\theta)|_{r=R} = \frac{1}{R^2}\frac{\partial^2 T}{\partial \theta^2} = \frac{\partial^2 T}{\partial (R\theta)^2} = \frac{\partial^2 T}{\partial x^2} \tag{3.4}$$

This demonstrates that the Fourier ring model can be considered a 1D heat flow problem. Before the analytical solution can be derived we need to consider the initial and boundary conditions. The ring can be considered periodic. This means it loops back round, and thus if we describe the circumference of the ring as length L we must have $T(x,t)$ be periodic in x as:

$$\begin{aligned} T\left(-\frac{L}{2},t\right) &= T\left(\frac{L}{2},t\right) \\ \frac{\partial T\left(-\frac{L}{2},t\right)}{\partial x} &= \frac{\partial T\left(\frac{L}{2},t\right)}{\partial x} \end{aligned} \tag{3.5}$$

Here we assume $-\frac{L}{2} < x < \frac{L}{2}$. We can assume the initial condition as a general function of the distance around the ring $T(x,0) = f(x)$ where only the boundary condition need be satisfied by $f(x)$.

3.2.1 Fourier's ring analytical solution

As shown, the analytical solution to the Fourier ring model requires we solve:

$$\frac{\partial T(x,t)}{\partial t} = D_T \frac{\partial^2 T(x,t)}{\partial x^2} \tag{3.6}$$

We first assume a separable solution of the form $T(x,t) = X(x)E(t)$. This leads to the separation of the heat conduction equation as:

$$\frac{X''(x)}{X(x)} = \frac{\dot{E}(t)}{D_T E(t)} = -\lambda^2 \tag{3.7}$$

where λ is the separation constant, which we know must exist as the functions $E(t)$ and $X(x)$ are assumed independent. Consider first the time dependent function. The general solution for $E(t)$ must take the form:

$$E(t) = Ce^{-\lambda^2 D_T t} \tag{3.8}$$

Here C is some constant of integration. To find the nontrivial values of λ the position dependant solution is examined:

$$X''(x) + \lambda^2 X(x) = 0 \tag{3.9}$$

The general solution of this 2nd-order ODE is:

$$X(x) = Asin(\lambda x) + Bcos(\lambda x) \tag{3.10}$$

Again A, B represent constants of integration. Substituting the boundary conditions into $X(x)$ constrains the value λ:

$$X(-L/2) = Asin(-\lambda L/2) + Bcos(-\lambda L/2) = Asin(\lambda L/2) + Bcos(\lambda L/2) = X(L/2) \tag{3.11}$$

We use the symmetry of the trig functions $cos(x) = cos(-x)$ and $sin(x) = -sin(-x)$ to show:

$$2Asin(\lambda L/2) = 0 \tag{3.12}$$

Similarly, if we consider the derivative $X'(x)$, we get the constraint:

$$2B\lambda sin(\lambda L/2) = 0 \tag{3.13}$$

Therefore the non-trivial solution is defined by the set of λ_n:

$$\frac{\lambda_n L}{2} = (n\pi) \qquad\qquad where \quad n \ \epsilon \ \mathbb{N} \tag{3.14}$$

The full solution can then be shown to be:

$$T(x) = \sum_{n=0}^{\infty} [A_n sin(2n\pi x/L) + B_n cos(2n\pi x/L)] \tag{3.15}$$

We choose one of the simplest initial temperature distributions to explore:

$$T(x,0) = Asin(2n\pi x/L) \tag{3.16}$$

This gives the analytical solution for the temperature decay as:

$$T(x,t) = Asin(2n\pi x/L)e^{-\left(\frac{2n\pi}{L}\right)^2 D_t t} \tag{3.17}$$

Then using Fourier's law for the heat flux $Q = -\kappa\nabla T$, we can describe the time dependence:

$$Q(x,t) = -\kappa\frac{\partial T}{\partial x} = -\frac{\kappa 2\pi A}{L} cos(2n\pi x/L)e^{-\left(\frac{2n\pi}{L}\right)^2 D_t t} \tag{3.18}$$

3.2.2 Fourier's ring SPAM Solution

The 1D periodic system (analogue to the Fourier ring model) is a logical starting point to explore heat flow via SPAM. For this we consider a set of point masses (particles) with unit spacing along the x axis and $\rho_0 = 1\text{g/mm}^3$, see Fig.3.2. The particle positions are fixed throughout this chapter. This means the mass dependence in the SPAM equations can effectively be ignored as they are all unity.

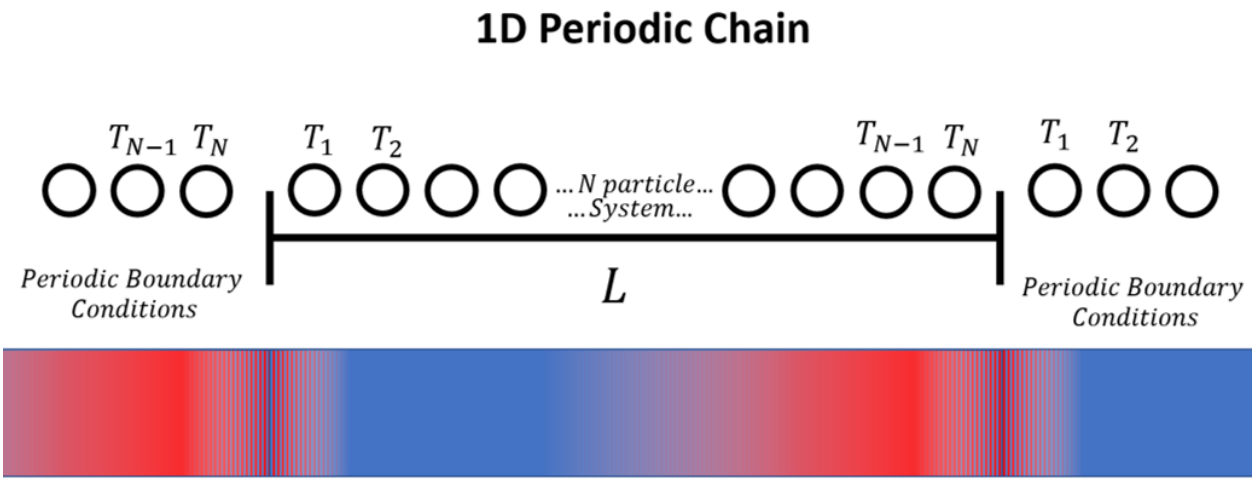

Figure 3.2: A chain of 1D system particles with unit spacing $\Delta x_p = 1\text{mm}$ and thus $\rho_0 = 1\text{g/mm}^3$, used to initialise the SPAM solution to the Fourier ring model. The chain of particles is length L with periodic boundaries enforced at $x = \pm\frac{L}{2}$

The static particle arrangement means only the SPAM approximation of the heat diffusion equation, Eq.3.6 needs to be considered. As shown in chapter 2, the evolution energy equation can be considered in two stages in terms of the heat fluxes. Ignoring the the momentum dependence, we recognise that the evolution of the temperature at a point depends on the energy evolution through the specific heat at constant volume as $\dot{e} = c_v \dot{T}$. The energy evolution therefore reduces to:

$$\dot{T}_i = \frac{-1}{c_v} \sum_j \left[Q_i + Q_j\right] \frac{x_{ij}}{|x_{ij}|} w'(|x_{ij}|) \tag{3.19}$$

where the heat flux at particle positions can be calculated from the smoothed particle sum of temperature differences via:

$$Q_i = -\kappa \sum_j \left[T_j - T_i\right] \frac{x_{ij}}{|x_{ij}|} w'(|x_{ij}|) \tag{3.20}$$

where κ is the thermal conductivity. The SPAM simulation of heat flow proceeds by assigning initial temperatures to each particle and then evolving them over time. Each time step dt consists of evaluating the set of values $\{Q_i\}$ from Eq.3.20. $\{Q_i\}$ is then used to evaluate the right-hand side of Eq.3.19. The first order ODE for temperature evolution is then solved using the 4th-order Runge-Kutta algorithm.

The rate of propagation of heat is finite and constant [112]. We therefore constrain the time step by considering the continuum decay time τ within the exponential of the temperature solution given

in Eq.3.17. The largest contribution $n = 1$ gives:

$$e^{-\left(\frac{2n\pi}{L}\right)^2 D_T t} = e^{-\frac{t}{\tau}} \tag{3.21}$$

This gives:

$$\frac{1}{\tau} = \frac{4\pi^2 D_T}{L^2} \tag{3.22}$$

We therefore constrain the size of the time step as:

$$dt < \frac{1}{\tau} = \frac{4\pi^2 D_T}{L^2} \tag{3.23}$$

We can also consider the particle spacing. It is expected that the characteristic diffusion length Δx of a temperature perturbation over time dt is given by:

$$\Delta x \approx \sqrt{D_t dt} \tag{3.24}$$

We can therefore ensure that the thermal energy diffuses no more than a single particle spacing every time step by enforcing:

$$dt < \frac{\Delta x_p^2}{D_T} \tag{3.25}$$

By choosing dt to satisfy both equations we ensure that the SPAM algorithm will have an appropriate step size over which to approximate the derivatives. For the weight function we use Lucy's choice, which with normalisation for 1D is given by:

$$w(z) = \frac{5}{4h}(1-z)^3(1+3z) \qquad where \quad z = x/H \tag{3.26}$$

The first derivative is:

$$w'(z) = \frac{-60}{4H^2} z(1-z)^2 \tag{3.27}$$

Finally we enforce the initial condition given by Eq.3.28 on the system particles as:

$$T_i(x_i) = Asin(2\pi x_i/L) \tag{3.28}$$

As stated this condition is compatible with the periodic boundary conditions with the system centre at $x = 0$ and the temperature vanishing at $x = \pm L/2$. We choose the case $A = 1$.

3.2.3 1D Periodic Results

For each SPAM simulation, interpolated values are calculated for $0, 1$ and 10 half lives. The first simulation was run for a thermal conductivity of unity $\kappa = 1gmm/s^3K^1$, an initial density of $\rho_0 = 1\text{g/mm}^3$ and specific heat of unity $C_p = 1\text{mm}^2/\text{s}^2\text{K}$. This gives the thermal diffusivity as:

$$D_T = \frac{\kappa}{\rho C_p} = 1mm^2/s \tag{3.29}$$

This gives the expected time to m half lives as:

$$t_m = \frac{mL^2 ln(2)}{4\pi^2 D_T} \tag{3.30}$$

We would therefore expect $t_0 = 0s$, $t_1 \approx 175.576s$ and $t_1 \approx 1755.762s$. The results for the SPAM simulation for $\kappa = 1\text{gmm/s}^3\text{K}$ are shown in Fig.3.3. The results give good agreement to the analytical solution with an error deviation of less than 1%.

Since $t_m \propto D_T^{-1}$, it is advantageous to use a larger thermal conductivity. Fig.3.3 shows the results from an SPAM simulation using $\kappa = 10\text{gmm/s}^3\text{K}$. Since the discrepancy is still low, the shorter simulation time mean henceforth, the remaining simulations will use $\kappa = 10$.

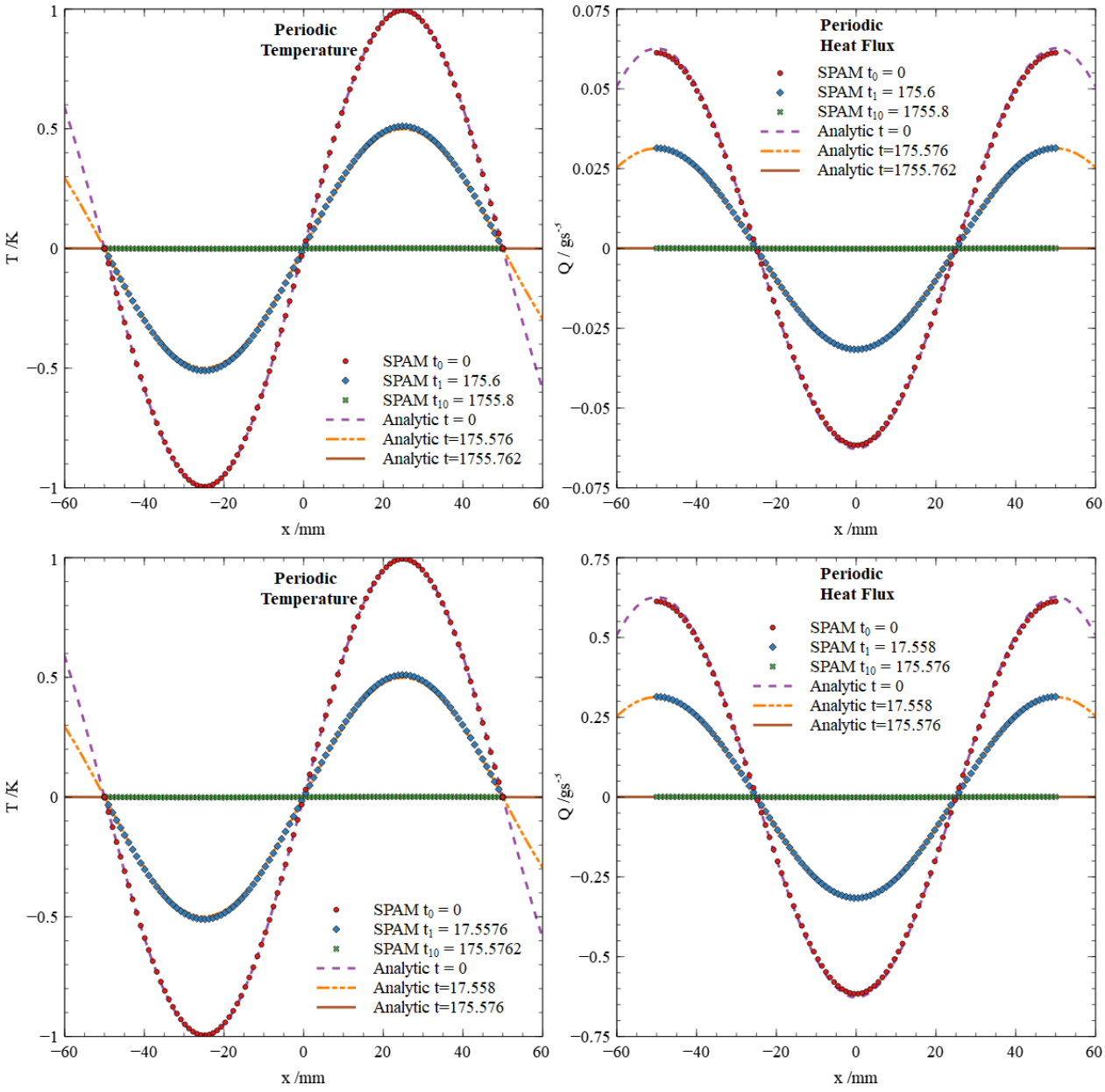

Figure 3.3: SPAM results vs analytical results for the Fourier ring model. Left shows temperature plot, right shows heat flux. Top shows thermal conductivity $\kappa = 1\text{gmm/s}^3\text{K}$, bottom $\kappa = 10\text{gmm/s}^3\text{K}$. All SPAM values shown are calculated as the smoothed interpolated values. Each is shown for a decay time of $0, 1$ and 10 half lives. All times are given in seconds.

Although these results appear promising, it is necessary that we must examine a hidden weakness of the temperature evolution given in Eq.3.19. The evolution calculates differences in particles temperature for the heat flux and then differences of heat flux for the rate of change of the temperature. This gives rise to an even-odd instability between the nodes which causes each particle to only be effected by its second nearest neighbour and become decoupled from its nearest. This is easily demonstrated if we add a small perturbation to each particle temperature of the form:

$$\begin{aligned} T_{odd} &= T + dT \\ T_{even} &= T - dT \end{aligned} \tag{3.31}$$

where *odd* represents the $1^{st}, 3^{rd}, 5^{th}, ...$ particles from the counting from the left simulation boundary and *even* represents particles $2, 4, 6, ...$ Here we take $dt = 0.01s$, which gives an initial temperature profile shown by the particle values in Fig.3.4. It is immediately obvious that calculation of the heat flux given by Eq.3.20 means that the perturbations cancel out, giving rise to a smoothed heat flux across the system shown in the lower half of Fig.3.4.

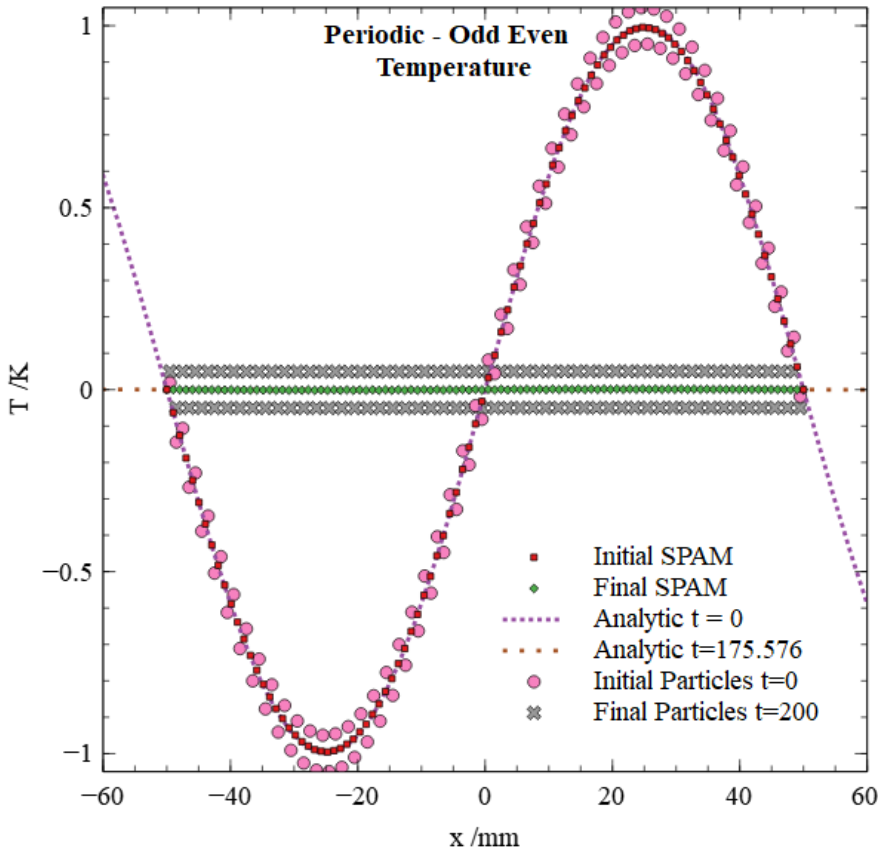

Figure 3.4: SPAM temperature results vs analytical results for the Fourier ring model for thermal conductivity $\kappa = 10\text{gmm/s}^3\text{K}$. The 'odd-even' instability is shown by the initial and final particle temperatures for which the small perturbation never decays. All SPAM curves shown are calculated as the smoothed interpolated values. Each is shown for a decay time of $0, 1$ and 10 half lives. These curves show the smoothed observation by SPAM interpolation of the non-smoothed particle values.

This means such perturbations cannot be removed and will persist indefinitely. In the fully periodic

system, this is of no consequence and indeed we do not observe any such spike of oscillation in our simulations. However once physical boundaries are used it can become a problem as we will show.

3.3 1D Boundary Driven Heat Flow

There are many possibilities to model physical boundaries including fixed particles, mirrors and potential barriers. Each has advantages and disadvantages. The method used depends on whether matter and/or energy is required to flow through the boundary, as well as the computational efficiency, simplicity and accuracy of the method.

For our present purposes we require boundaries that permit transfer of heat and give agreement with analytical solutions of the heat conduction equation. We will explore several options and critically appraise them. We retain some aspects of the previous model but now consider a more challenging set of initial and boundary conditions. If we begin with $T(x,0) = T_0$, some non-zero constant, but we require the ends to be at constant zero temperature, then our system begins with a discontinuity.

The constant initial function can be written in terms of an infinite sum of sine functions to satisfy the conditions on the diffusion equation. This means the analytical solution takes the form:

$$T(x,t) = \frac{4T_0}{\pi} \sum_{m=1}^{\infty} \frac{(-1)^{(m-1)}}{2m-1} cos\left(\frac{(2m-1)\pi x}{L}\right) exp\left[\frac{-(2m-1)^2\pi^2\kappa t}{L^2}\right] \tag{3.32}$$

With the heat flux derived as:

$$Q(x,t) = -\frac{4T_0\kappa}{L} \sum_{m=1}^{\infty} (-1)^m sin\left(\frac{(2m-1)\pi x}{L}\right) exp\left[\frac{-(2m-1)^2\pi^2\kappa t}{L^2}\right] \tag{3.33}$$

The full derivation of these solutions can be found in the work by Carslaw and Jaeger [114]. This model has already been used by Monaghan to demonstrate the effectiveness of his form of temperature evolution in isolation [108]. We aim to show through comparison of the various proposed forms of evolution here that a superior alternative exists for this work.

3.3.1 Smoothed Particle Boundary Enforcement

Fixed boundary methods are the simplest to implement within non-equilibrium simulations. One drawback is that fixed properties calculated *on* the system boundaries are not equal to the fixed values. Furthermore the boundaries in no way react to the system evolution and thus small errors are introduced into the system for properties calculated close to the boundaries due to discontinuities.

We can enforce our 1D fixed boundary conditions by populating the space outside of L with the same evenly spaced particles but prevent the particle values in this region from evolving. This however causes discontinuous field variables and will thus drive spurious oscillations within the SPAM solution Eq.(3.19) and thus introduce errors. Here we test the fixed boundary method and quantify this error before exploring the proposed adaptations.

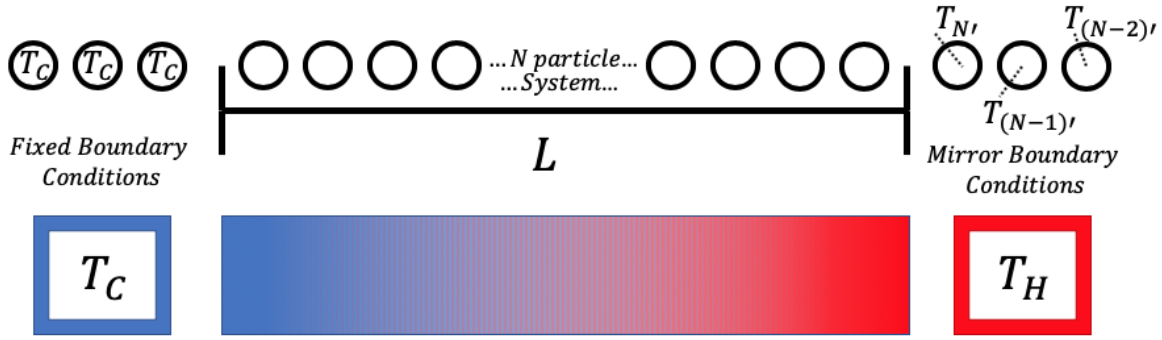

Figure 3.5: An outline of how fixed and mirror system boundaries can be enforced in a 1D smoothed particle simulation. The simplified 1D material is represented as a chain of N particle points with initial temperatures T_i. Each end of the system is placed in contact with an effectively infinite heat bath. In the fixed case this is modelled as constant particle temperatures, shown as T_C. For mirror conditions we enforce temperature *at* the boundary by calculating the boundary particle temperature $T_{i'} = 2T_H - T_i$ at each time step. For our model we take the simplified case $T_C = T_H = 0K$.

3.3.2 1D Fixed Boundary Results

The results for SPAM simulations with initial temperature distribution $T_0 = 1$s and fixed boundary temperatures $T_i = 0$s are shown in Fig.3.6. It is immediately evident that there is a significant error introduced into the simulation. We can calculate the residual error U between the analytical and SPAM temperature distributions:

$$U^2 = \frac{1}{n}\sum_{i}^{n} \left(T_{Analytic}(i) - T_{SPAM}(i)\right)^2 \tag{3.34}$$

where i represents each of the $n = 100$ interpolation points. The analytical temperature is calculated with frequencies up to $m = 100$ included. This number is chosen as $m = 100$ still exhibits significant deviations at $x = \pm\frac{L}{2}$. Using this residual error calculation we obtain the results $u_0 \approx 0.0032$K, $u_1 \approx 0.0035$K and $u_{10} \approx 0.0033$K. Therefore the fixed boundaries used in this simulation ensure the average error in predicted temperature exceeds 3%.

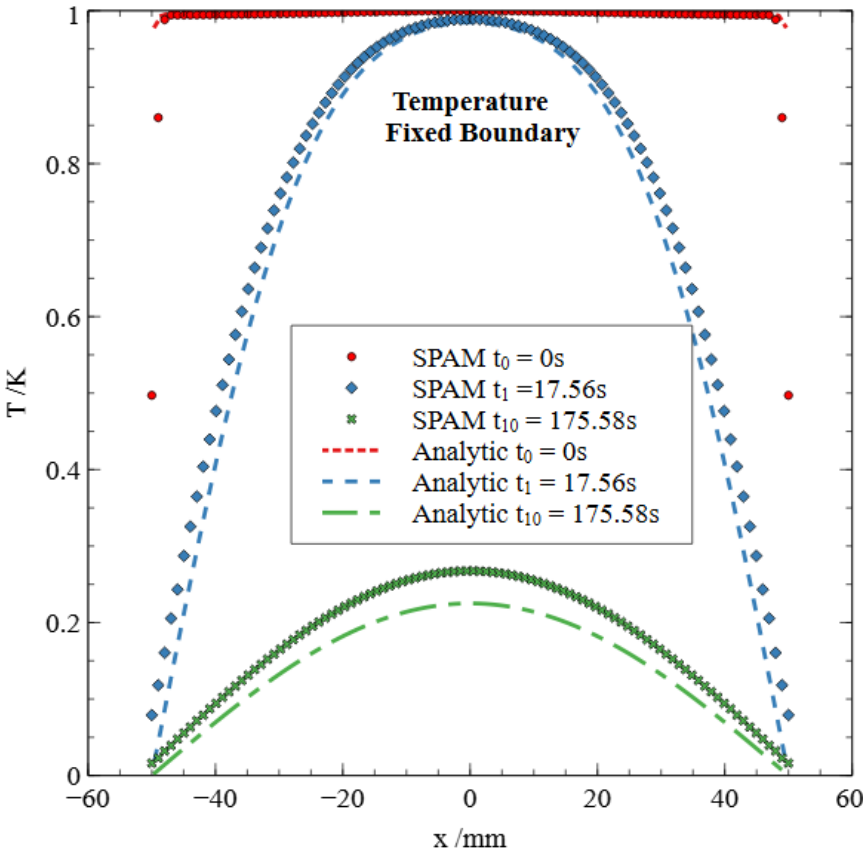

Figure 3.6: SPAM results vs analytical results for 1D fixed boundaries for thermal conductivity $\kappa = 10\text{gmm/s}^3\text{K}$. The initial function used is $T = 1K$. The temperature is shown here. All SPAM curves shown are calculated as the smoothed interpolated values. Each is shown for a decay time of $0, 1$ and 10 half lives. The residual error between the curves is maximally $\approx 4\%$.

Similar results are obtained for the heat flux curves shown in Fig.3.7. The error is due to fixed boundary temperatures. This is because there is a rate of change for the boundary particles exerted by the system. This boundary evolution is discarded and thus the system energy has a small error introduced. There are several proposed methods within the literature to address this, the most obvious of these is to allow the boundary particle temperatures to evolve in a restricted way. We will explore one such method next, mirror boundaries.

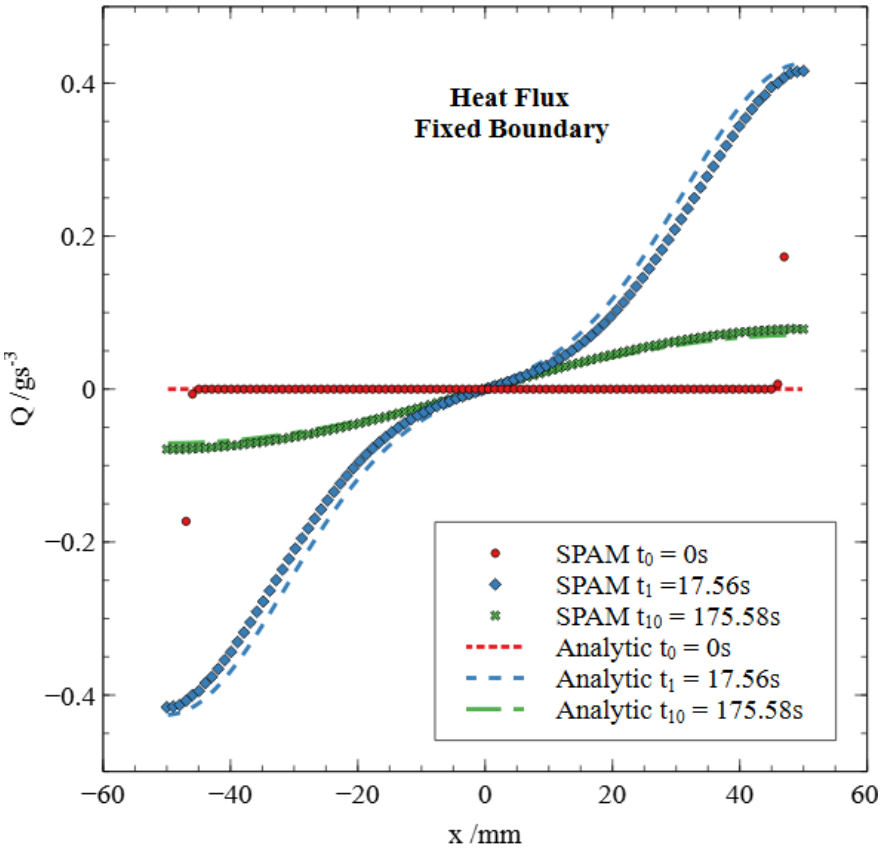

Figure 3.7: SPAM results vs analytical results for 1D fixed boundaries for thermal conductivity $\kappa = 10\text{gmm/s}^3\text{K}$. The initial function used is $T = 1K$. The heat flux is shown here. All SPAM curves shown are calculated as the smoothed interpolated values. Each is shown for a decay time of $0, 1$ and 10 half lives. The residual error between the curves is maximally $\approx 4\%$.

3.3.3 Mirror Boundaries

We will examine the effectiveness of dynamic boundaries in creating continuous system boundaries and thus mitigating the errors so far demonstrated. For the 1D case dynamic boundary conditions are specified with a set of more complex conditions than that of fixed. Let r denote the particle positions. For a particle within range of the boundary $r_B - r_i < h$, a mirror particle is calculated at location:

$$r_{i'} = 2r_B - r_i \tag{3.35}$$

The temperature assigned to the mirror is given by two factors, the required boundary temperature T_B (this is either T_H or T_C for the 1D case) and the temperature of the particle it is a mirror of T_i:

$$T_{i'} = 2T_B - T_i \tag{3.36}$$

This relation for dynamically assigned temperatures ensures that the value of T on the system boundary is always given by T_B. This is clearly not the case for the fixed boundary conditions. For the fixed boundary simulations the heat flux Q is actually calculated within the SPAM similar to the system particles. For the mirror case however the heat fluxes are assigned to be the same

as the particle which they are a reflection of, this ensures the heat flow is continuous across the boundary:

$$Q_{i'} = Q_i \tag{3.37}$$

3.3.4 1D Mirror Boundary Results

Here the SPAM simulation was run with $n = 100$, $L = 100mm$, $\kappa = 10\text{gmm/s}^3\text{K}$. The results obtained are shown in Fig.3.8 and Fig.3.9. The residual error between the analytical results and those obtained with the SPAM mirror boundaries is maximal for the curves of t_{10} half lives. This error is calculated as:

$$U_{Mirror,t_{10}} = 0.0087K \tag{3.38}$$

This suggests that mirror boundaries are significantly better at handling the discontinuous driving boundary conditions required to simulate transient heat flow than fixed boundaries. However, as previously discussed dynamic boundaries quickly become complex in nature as spatial dimensions and geometric complexity increases.

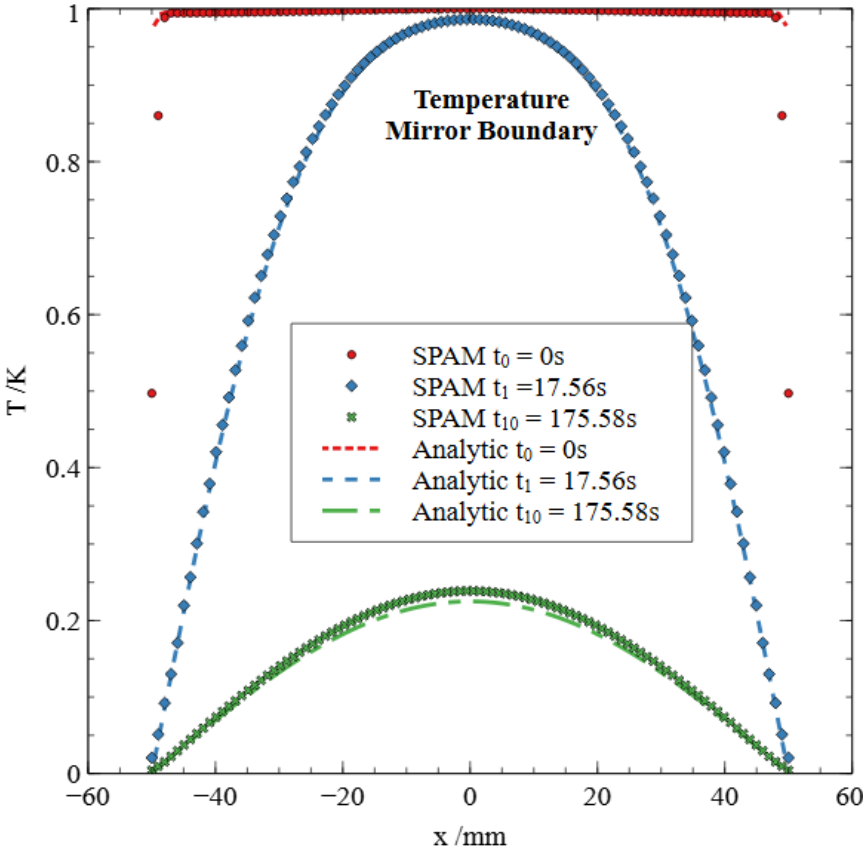

Figure 3.8: SPAM results vs analytical results for 1D mirror boundaries for thermal conductivity $\kappa = 10\text{gmm/s}^3\text{K}$. The initial function used is $\{T_i\} = 1\text{K}$. Temperature plot shown here. All SPAM curves shown are calculated as the smoothed interpolated values. Each is shown for a decay time of $0, 1$ and 10 half lives. The residual error between the curves is maximally $< 1\%$.

One way to increase the accuracy of simulations under fixed boundary conditions is to introduce

corrective factors into the SPAM algorithm. We will therefore quantify the effectiveness of some of the more widely used methods proposed in the literature against the use of mirror boundaries as well as testing if they further increase the accuracy of mirror boundaries.

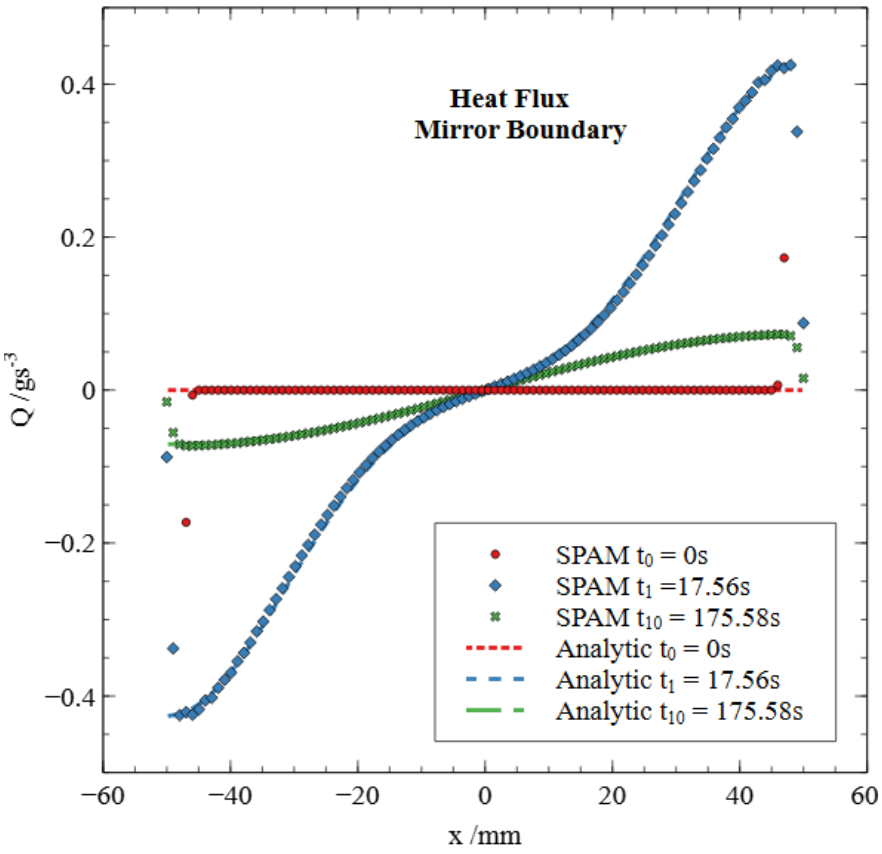

Figure 3.9: SPAM heat flux results vs analytical results for 1D mirror boundaries for thermal conductivity $\kappa = 10\text{gmm/s}^3\text{K}$. The initial function used is $\{T_i\} = 1\text{K}$. All SPAM curves shown are calculated as the smoothed interpolated values. Each is shown for a decay time of $0, 1$ and 10 half lives. The residual error between the curves is maximally $< 1\%$.

3.3.5 Corrective methods

There are several commonly used corrective methods given throughout the SPAM literature. This includes the use of artificial terms such as conductivity and viscosity; first order and higher correction terms to the kernel and kernel gradient; velocity smoothing (irrelevant for systems without motion but will later be explored) and alternative formulation of the evolution SPAM equations. An outline of one method of implementation of each of these follows, then the results are explored for the non-equilibrium temperature simulation, giving direct comparison of the residual errors from the analytical equations.

Artificial Terms

One common method to overcome these unstable build ups of matter and energy within the simulation is to add artificial dissipation to the method for each conserved quantity. Within the

simulations in this chapter the only conserved quantity of interest is the energy leading to the need for artificial terms in the thermal conductivity, although these method were first derived with respect to matter and artificial viscosity [115] which will be explore later.

Artificial conductivity is added as an extra term to the energy evolution equation as:

$$\dot{T}_i = \frac{-1}{c_v} \sum_j \left[Q_i + Q_j + \Pi_{T,ij} \right] \frac{x_{ij}}{|x_{ij}|} w'(|x_{ij}|) \tag{3.39}$$

Several different formulations for the extra term $\Pi_{T,ij}$ are in use in the literature. One of the most promising forms for artificial terms is derived based on Riemann solvers [98] as:

$$\Pi_{T,ij} = \frac{\beta v_{sig,ij}}{\bar{\rho}_{ij}} (T_i - T_j) \tag{3.40}$$

Here β is the coefficient of dissipation which is evolved per particle through time. v_{sig} represents the signal velocity and is commonly given as:

$$v_{sig,ij} = \frac{1}{2} [c_i + c_j - 2 v_{ij} \cdot r_{ij}] \tag{3.41}$$

where c represents the respective particle sound speeds. However Price [116] offers a more general derivation of artificial dissipation terms for any conserved quantity f as:

$$\left(\frac{df_i}{dt} \right)_{diss} = \sum_j m_j \frac{\beta_f v^f_{sig,ij}}{\bar{\rho_{ij}}} (f_i - f_j) \frac{r_{ij}}{|r_{ij}|} w'(|r_{ij}|) \tag{3.42}$$

This is identical to the previous description, however the generalisation points out that an independent signal velocity v_{sig} should be considered for each conserved quantity f. The signal velocity given by Eq.3.41, is constructed by considering shock waves. In the case of the 1D thermal non-equilibrium simulations presented here, no shocks are expected. Instead the discontinuities which the artificial terms are designed to capture arise from discontinuities at the system boundary, these are fundamentally the same however in practice they are without significant velocity differences. With this in mind, an alternative form for signal velocity based on pressure differences has been proposed by Price:

$$v^T_{sig} = \sqrt{\frac{P_i - P_j}{\bar{\rho}_{ij}}} \tag{3.43}$$

Since current simulations do not involve pressure we propose an alternative signal velocity based on differences of local heat fluxes:

$$v^T_{sig} = \sqrt{\frac{Q_i - Q_j}{D_T \bar{m}_{ij}}} \tag{3.44}$$

The motivation for such a choice is based on the fact that we expect all heat fluxes to be equal at steady state and thus the signal velocity would then vanish. The vanishing nature of dissipative artificial terms is further ensured by the time evolution of the coefficient of dissipation β^f as:

$$\frac{d\beta^f_i}{dt} = -\frac{\beta^f_i - \beta^f_{min}}{\tau_i} + S_i \tag{3.45}$$

Here τ_i represents the timescale of decay and Price suggests this value as $\tau_i = 10H/v_{sig}$ where v_{sig} is the maximum signal velocity calculated for particle i. The final term is the source term and

again this should be selected based on the conserved quantity f. For the case of thermal energy the source term is suggested by Price to be:

$$S_i^T = \frac{H|\nabla^2 T|_i}{\sqrt{T_i + \epsilon}} \tag{3.46}$$

where ϵ is some small number to prevent singularities within the calculation. Initial results for the fixed boundary case simulations with artificial conductivity are shown in Fig.3.10. The heat flux results are shown in Fig.3.11. All residual errors are less than those of the fixed boundary case alone, however the residual error can be seen to increase with time and therefore the use of artificial terms may effect the rate of decay and thus introduce errors into the exploration of transient heat-flow results.

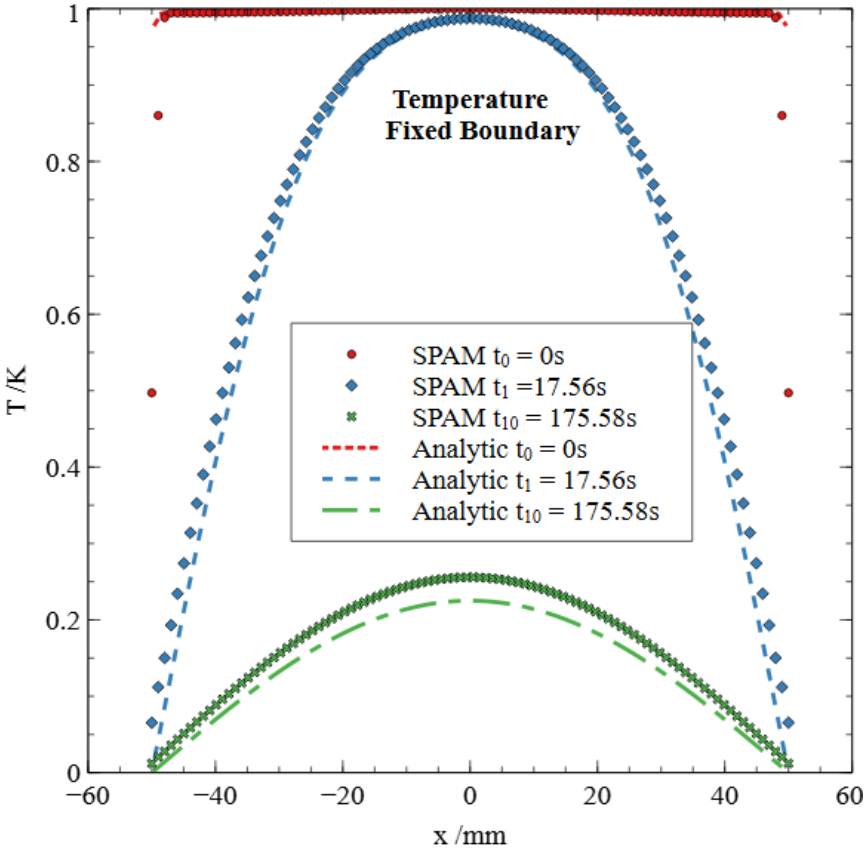

Figure 3.10: Temperature distributions for the model set out in Sec.3.3 with initial temperatures $\{T_i\} = 1$K, thermal conductivity $\kappa = 10$gmm/s^{3}K. The residual error between the curves is maximally $< 2.4\%$.

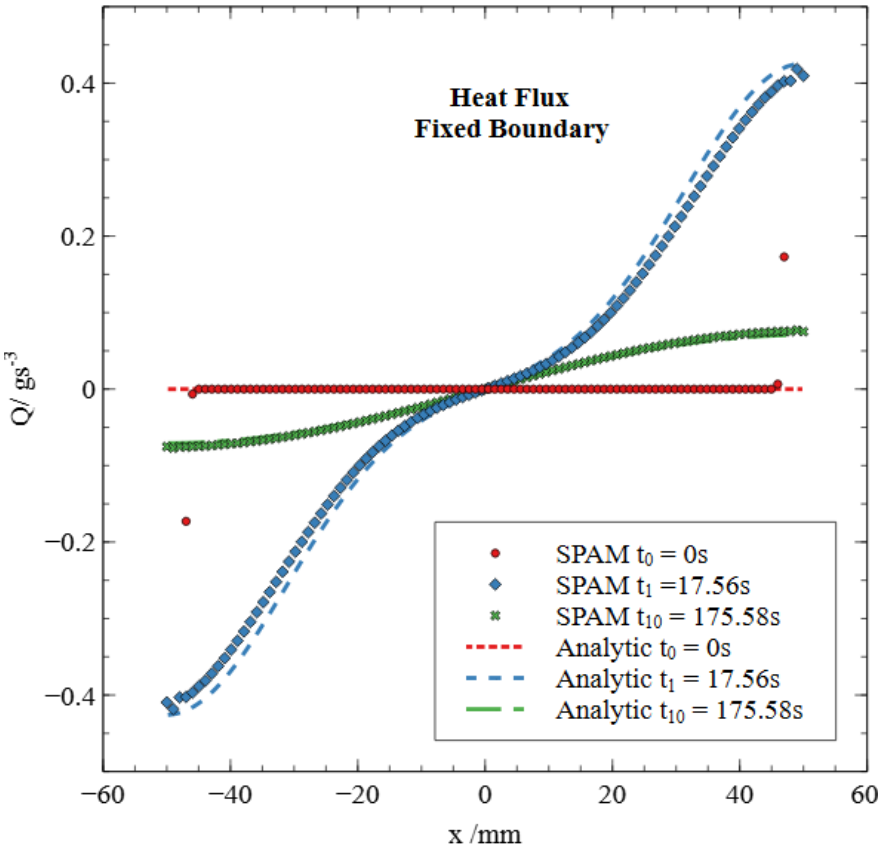

Figure 3.11: Heat flux distributions for the model set out in Sec.3.3 with initial temperatures $\{T_i\} =$ 1K, thermal conductivity $\kappa = 10\text{gmm/s}^3\text{K}$. The residual error between the curves is maximally $< 2.4\%$.

Kernel and Gradient Corrections

Corrections to the kernel and its gradient are found by considering the Taylor expansion of the weight function with some function $f(x)$ about x, this is shown in full detail in Sec.2.4.2. The result for the kernel correction is given as:

$$f_i \simeq \frac{\sum_j m_j f_j W(x_{ij})/\rho_j}{\sum_j m_j W(x_{ij})/\rho_j} \tag{3.47}$$

Results for simulations with 1D kernel corrections are shown in Fig.3.12 with the accompanying heat flux given in Fig.3.13. It is immediately obvious that the use of corrections introduced large errors into the time dependence of the simulation. This result was not supported in the literature so it should be assumed that there is likely an undiscovered error or that more testing is required to validate this. For now it is sufficient that corrective methods are omitted from the simulations that follow within this chapter. The same results are found for the case of kernel gradient corrections, due to the clear indication that there is an error in the implementation these are not included. The corrections were not found to have any significant effect on the steady state solutions.

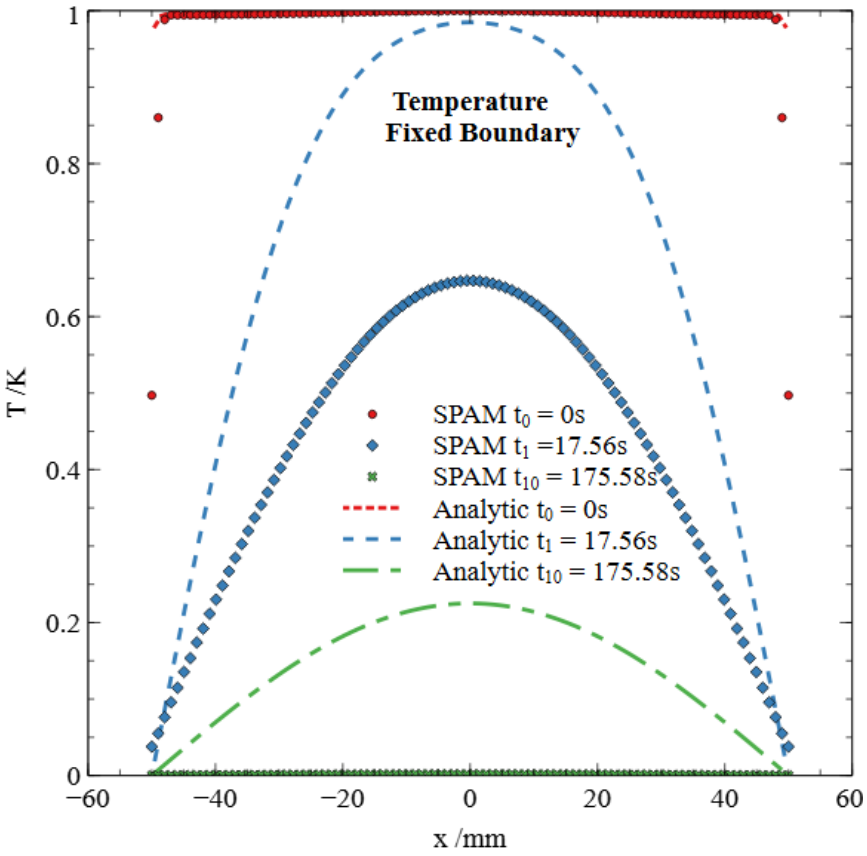

Figure 3.12: SPAM results vs analytical results for 1D fixed boundaries for thermal conductivity $\kappa = 10\text{gmm/s}^3\text{K}$. First order 1D kernel corrections have been included in the SPAM simulation. The initial function used is $T = 1K$. Temperature plot shown here. All SPAM curves shown are calculated as the smoothed interpolated values. Each is shown for a decay time of $0, 1$ and 10 half lives. The residual error between the curves is large, however the steady state solution converges with reduced errors.

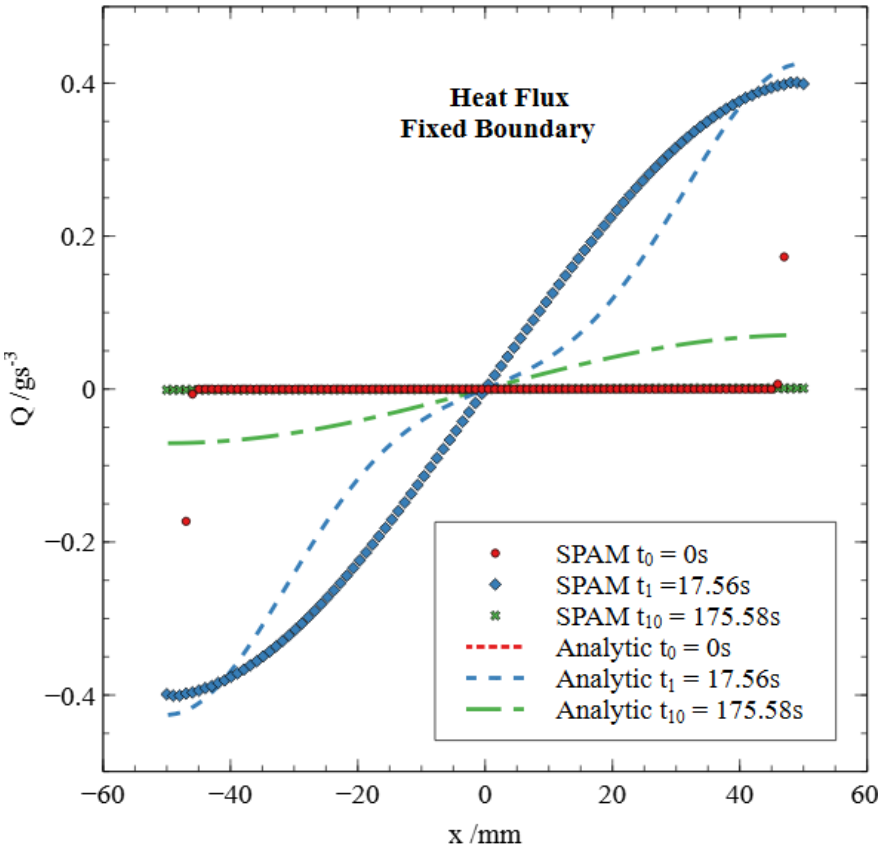

Figure 3.13: SPAM results vs analytical results for 1D fixed boundaries for thermal conductivity $\kappa = 10\text{gmm/s}^3\text{K}$. First order 1D kernel corrections have been included in the SPAM simulation. The initial function used is $T = 1K$. Heat flux plot shown here. All SPAM curves shown are calculated as the smoothed interpolated values. Each is shown for a decay time of $0, 1$ and 10 half lives. The residual error between the curves is large, however the steady state solution converges with reduced errors

Alternate Forms of Temperature Evolution

It is desirable to remove problems such as the instability outlined in Fig.3.4 more directly by reformulating the temperature evolution equations. Monaghan suggested an alternative temperature evolution based on the first derivative of the weight function and particle temperature differences [108]:

$$c_{p,i}\frac{dT_i}{dt} = \sum_j \frac{m_j}{\rho_i\rho_j}\frac{4\kappa_i\kappa_j}{(\kappa_i+\kappa_j)}(T_i - T_j)\frac{dW_{i,j}}{dr_{ij}}\frac{1}{|r_{ij}|} \tag{3.48}$$

This formulation allows for particles to have different thermal conductivities κ_i, κ_j. The more complex form of the thermal conductivity ensures that the heat flux remains continuous across large jumps in material properties. This will become important when considering fissile materials undergoing damage due to irradiation. Results for this alternative evolution are shown in Fig.3.14. The results for this method are far more promising, with a clear reduction in the error for the fixed boundary case.

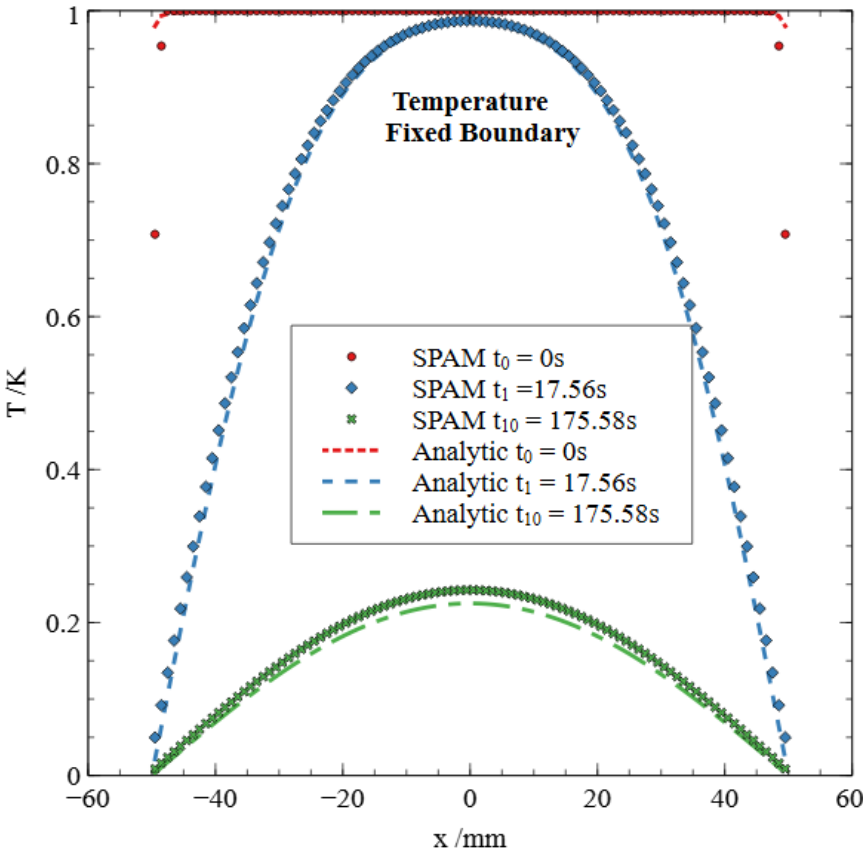

Figure 3.14: SPAM temperature results vs analytical results for 1D fixed boundaries for thermal conductivity $\kappa = 10\text{gmm/s}^3\text{K}$. The SPAM simulation is run with Monaghan's alternative description of temperature evolution 3.48. The initial function used is $T = 1K$. All SPAM curves shown are calculated as the smoothed interpolated values. Each is shown for a decay time of $0, 1$ and 10 half lives.

An alternative method of evolving temperature was proposed by Hoover [54]. This avoids the need to compute kernel gradient or heat fluxes:

$$\frac{dT_i}{dt} = C \sum_j (T_j - T_i) W(r_{ij}) \tag{3.49}$$

where C is a constant of proportionality which can be chosen to match the macroscopic heat equation:

$$C = \frac{D_T}{\sum \frac{x^2 w(x)}{2}} \tag{3.50}$$

The explanation given by Hoover depends on substituting an approximation of the temperature as a cosine function. Instead here a full derivation of this temperature dependence is attempted. The derivation begins from the 1D heat equation:

$$\dot{T}(x) = D_T T''(x) \tag{3.51}$$

If an expression for $\dot{T}(x) = f(x)$ can be derived then the smoothed particle approximation Eq.3.52 can used to give:

$$\dot{T}(x) = \sum_{i}^{N} \dot{T}(x_i) \frac{m_i}{\rho_i} w(x - x_i) \tag{3.52}$$

The second derivative can be approximated by the derivative definition:

$$T''(x) = \lim_{a \to 0} \frac{-T(x+a) + 2T(x) - T(x-a)}{a^2} \tag{3.53}$$

Considering the SPAM approximation, the smallest possible range $a = x - x_i$ where x_i is the closest possible point. This consideration reduces the second derivative to:

$$T''(x) = \lim_{x \to x_i} \frac{2(T(x) - T(x_i))}{(x_i - x)^2} \tag{3.54}$$

The limit used in this definition means that the smoothed particle approximation can be considered as the limit of the function $(x - x_i)^2/2$:

$$\lim_{x \to x_i} \frac{(x_i - x)^2}{2} = \lim_{x \to x_i} \lim_{H \to 0} \int_{-\infty}^{\infty} \frac{(x_i - x)^2}{2} w(H) dx \tag{3.55}$$

This can be converted to summation form:

$$\lim_{x \to x_i} \frac{(x_i - x)^2}{2} = \lim_{x \to x_i} \lim_{H \to 0} \sum_{i}^{N} \frac{(x_i - x)^2}{2} \frac{m_i}{\rho_i} w(H) \tag{3.56}$$

At this point it is noted that due to the smoothed particle approximation the limit is unobtainable, instead all particles x_i within the finite range H are considered:

$$\lim_{x \to x_i} \frac{(x_i - x)^2}{2} \approx \sum_{i}^{N} \frac{(x_i - x)^2}{2} \frac{m_i}{\rho_i} w \tag{3.57}$$

This is used to approximate Eq.3.54. For convenience of notation the index is changed $i \to j$:

$$T''(x) = \frac{T(x) - T(x_j)}{\sum_{j}^{N} \frac{(x_j - x)^2}{2} \frac{m_j}{\rho_j} w} \tag{3.58}$$

Now using the heat Eq.3.51 the desired function for $\dot{T}(x)$ is obtained:

$$\dot{T}(x) = D_T \frac{T(x) - T(x_j)}{\sum_{j}^{N} \frac{(x_j - x)^2}{2} \frac{m_j}{\rho_j} w} \tag{3.59}$$

Using the SPAM approximation given in Eq.3.52 the final SPAM interpolation of the rate of change of temperature, as originally given by Hoover, becomes:

$$\dot{T}(x) = D_T \sum_{i} \frac{(T_i - T_j) \frac{m_j}{\rho_j} w}{\sum_{j}^{N} \frac{(x_j - x_i)^2}{2} \frac{m_j}{\rho_j} w} \tag{3.60}$$

Of interest is that the final form for this evolution is similar to the extension of the kernel correction method derived by Sibilla [117] which is also based on Taylor series expansions. This suggests that

the methodology used here may be expanded to estimate derivatives of functions as is achieved for the corrections outlined by Sibilla. It is also interesting to note that Hoover's evolution eliminates the use of the gradient of the weight function. The total elimination of this was achieved by the Kernel Gradient Free (KGF) methodology [118] which all showed a dramatic increase in the accuracy of the SPAM algorithm.

The reason for the full derivation given here becomes obvious when examining the 2D form later in this chapter. Results for this evolution are given in Fig.3.15. The error is significantly less than the standard evolution for the fixed case with no requirement for artificial terms or calculation of the kernel gradient. Full comparison of these errors follows in the next section however the spatial distribution of error is given for this case in Fig.3.16. It can be seen that the error is greatest for the heat flux calculated at the simulation boundaries which is expected due to the fixed boundary conditions failing to provide a smooth heat flux. Conversely, the calculated error in temperatures is greatest at the centre of the simulation where the temperature peaks. This is likely due to the centre of the simulation being furthest from the driving conditions at the boundary and thus having the most significant time delay for the boundary effects.

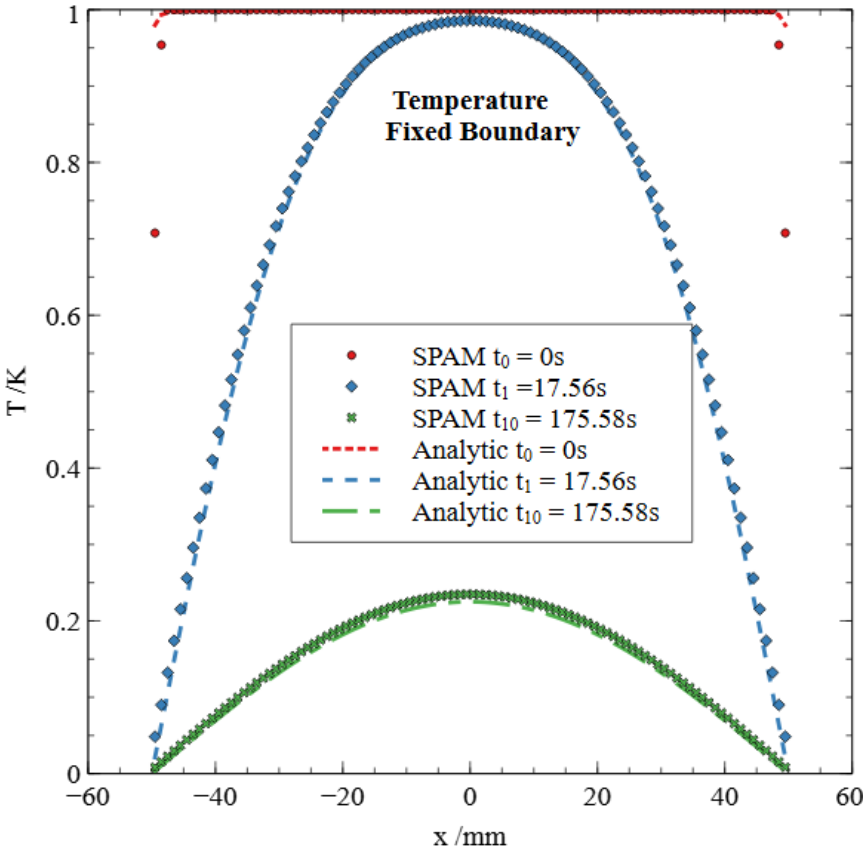

Figure 3.15: SPAM results vs analytical results for 1D fixed boundaries for thermal conductivity $\kappa = 10\text{gmm/s}^3\text{K}$. The SPAM simulation is run with Hoover's alternative description of temperature evolution Eq.3.60. The initial function used is $T = 1K$. Temperature plot shown here. All SPAM curves shown are calculated as the smoothed interpolated values. Each is shown for a decay time of $0, 1$ and 10 half lives.

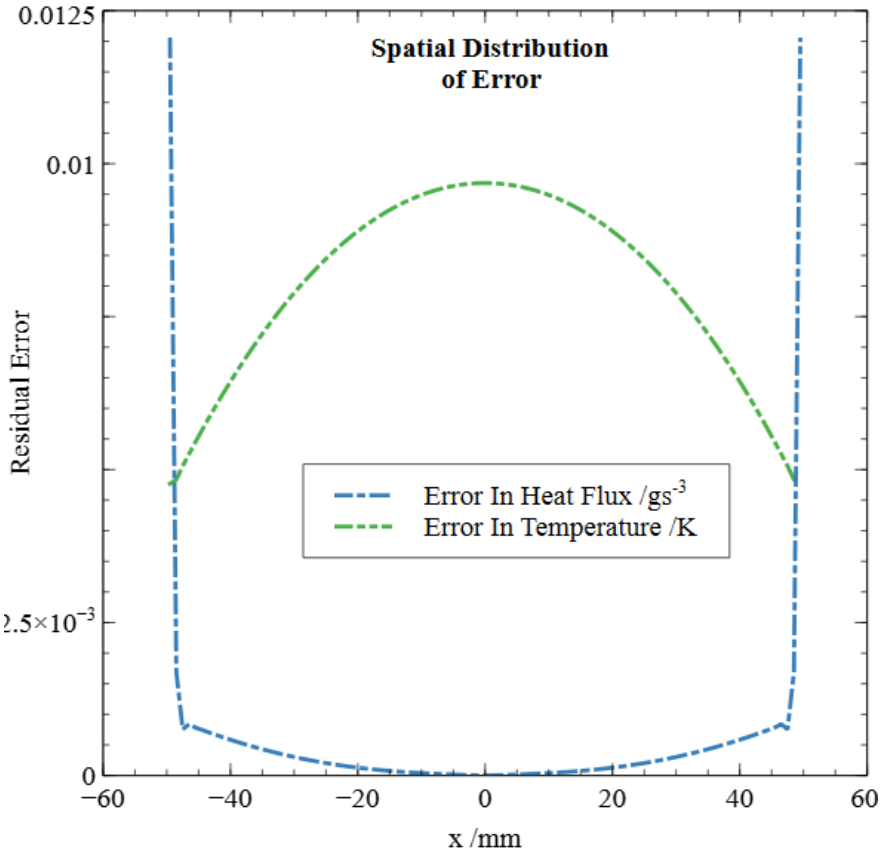

Figure 3.16: The spatial distribution of the error for SPAM results vs analytical results for 1D fixed boundaries for thermal conductivity $\kappa = 10\text{gmm/s}^3\text{K}$. The SPAM simulation is run with Hoover's alternative description of temperature evolution Eq.3.60. The results are shown for both temperature and heat flux and are calculated for a decay time of 10 half lives.

Results for Various Corrections in 1D

As stated before all the corrective methods outline above have been examined for fixed boundary cases. Their effect on the mirror boundary case has also been quantified through the use of residual errors calculated as in Eq.3.101. A direct comparison of the residual errors is given in Fig.3.17 with the error in heat flux in Fig.3.18. The error in the method of kernel correction is removed here as it allows for better comparison of the remaining methods which have significantly less error. The residual error for each result is calculated within the bounds $-45\text{mm} < x < 45\text{mm}$ to remove the contribution of the boundary error.

Clearly the least useful method tested here is the standard evolution proposed given by Eq.3.19. The use of artificial terms improves these results as well as combating the discontinuous heat flux. Examining all forms of evolution it is clear that the use of mirror boundaries is still superior for its natural smoothing of discontinuities at the boundary.

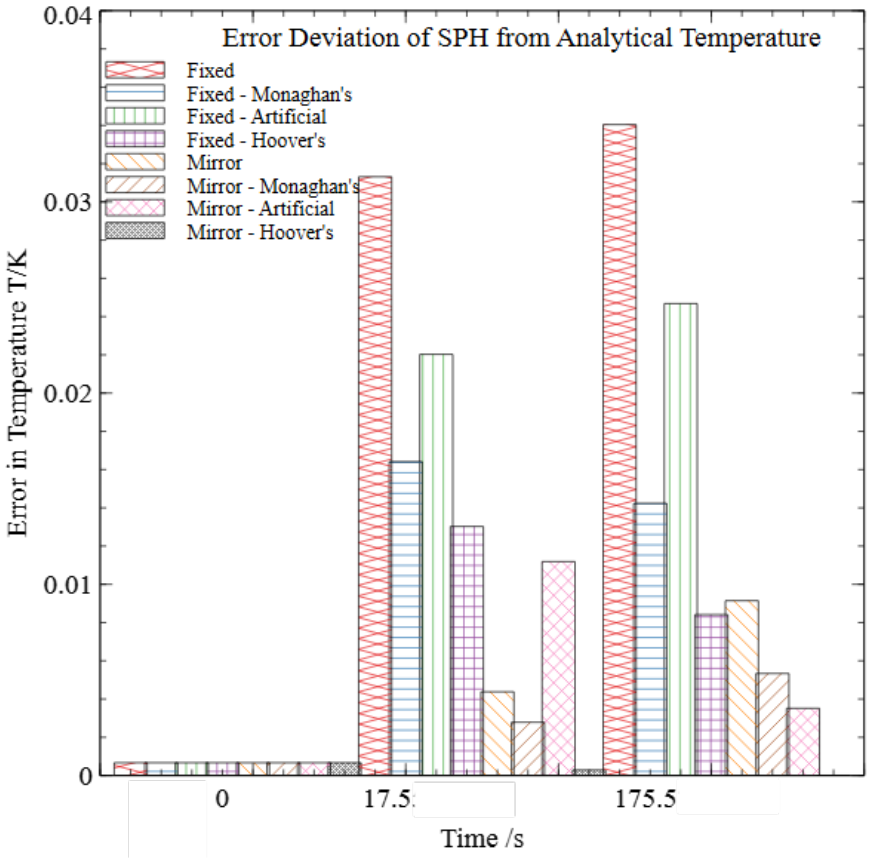

Figure 3.17: SPAM results vs analytical results for 1D corrective methods for thermal conductivity $\kappa = 10\text{gmm/s}^3\text{K}$. The SPAM simulation is run for fixed and mirror boundaries. In each case the simulation is also run with artificial conductivity as well as each alternative description of temperature evolution Eq.3.48 and Eq.3.60. The initial function used is $T = 1K$. Above shows the residual errors in the temperature plot. All SPAM values are calculated as the smoothed interpolated values. Each is shown for a decay time of $0, 1$ and 10 half lives.

The most promising result is that given by Hoover's temperature formulation Eq.3.60. The error for the fixed case in the absence of artificial conductivity is the lowest of all choices. Although not included here, no improvement was found for the addition of artificial terms to Hoover's formulation. The best results are produced by Hoover's evolution with mirror boundaries. The error calculated for $t = 175s$ is $U_T \approx 1 \times 10^{-5}K$.

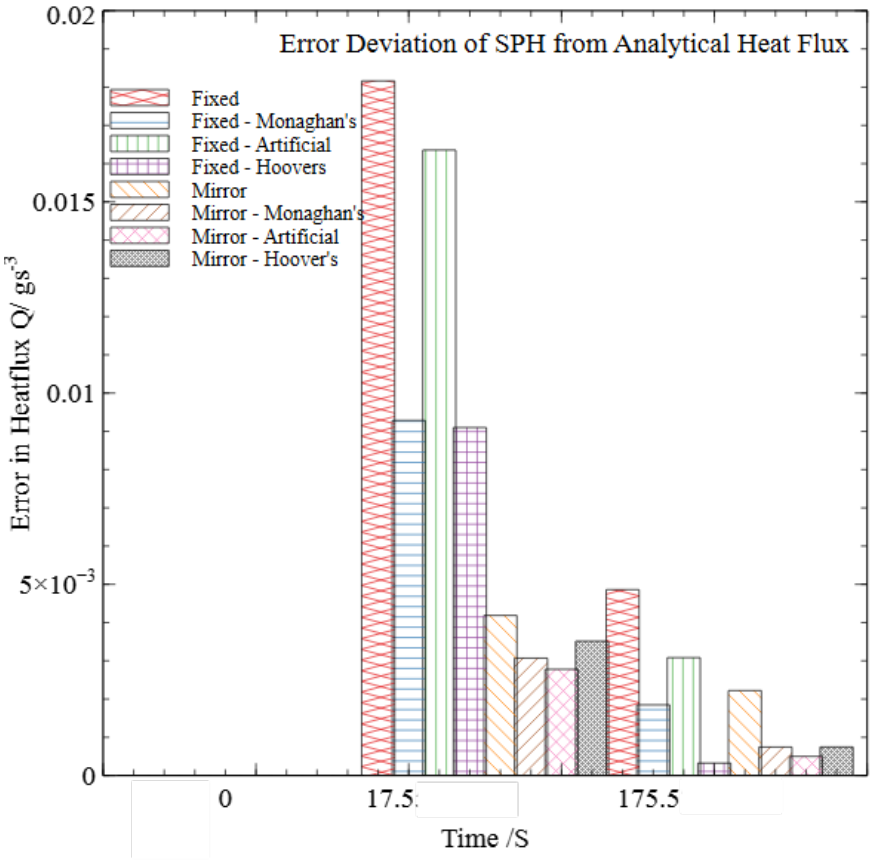

Figure 3.18: SPAM results vs analytical results for 1D corrective methods for thermal conductivity $\kappa = 10\text{gmm/s}^3\text{K}$. The SPAM simulation is run for fixed and mirror boundaries. In each case the simulation is also run with artificial conductivity as well as each alternative description of temperature evolution Eq.3.48 and Eq.3.60. The initial function used is $T = 1K$. Above shows the residual errors in the heat flux plot. All SPAM values are calculated as the smoothed interpolated values. Each is shown for a decay time of $0, 1$ and 10 half lives.

3.4 Transient 2D Heat Flow

The generalisation of the three SPAM temperature evolution equations given to higher dimensions is non trivial. In particular Eq.3.60 is only offered briefly in the literature and only in one dimension. It is therefore important to confirm that the correct decay times are maintained in two dimensions. This is achieved using the derivation of Eq.3.60 provided in the previous section. A model is therefore selected for 2D heat flow with analytical solutions for the transient case. This model is used by various other studies [108–110] which demonstrate the effectiveness of SPAM to model heat conduction. Here we use the model to compare the methods for temperature evolution and show that there is a difference in accuracy for each method.

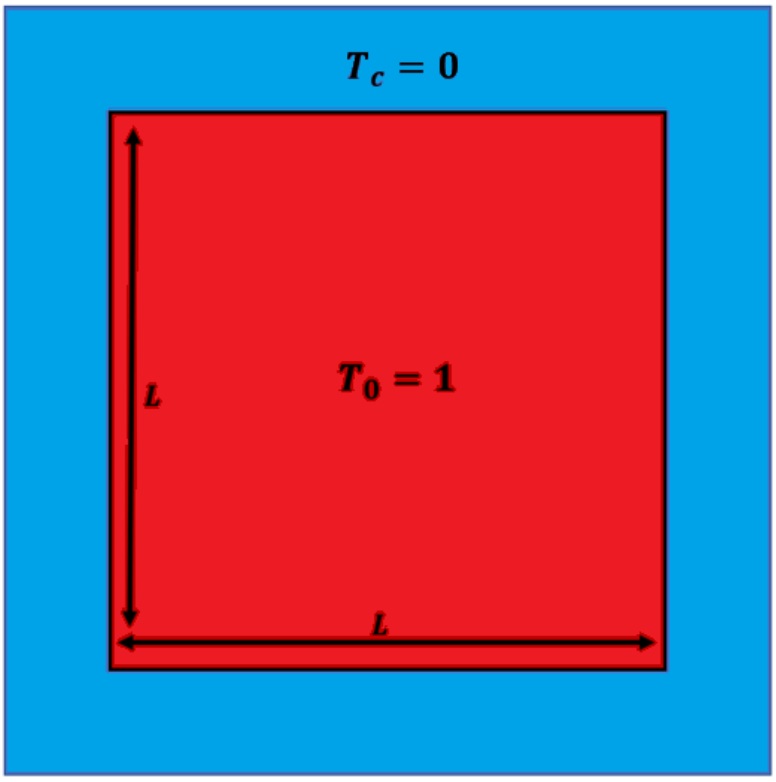

Figure 3.19: A visualisation of the transient 2D heat flow model. A square of length L is released from an initial temperature $T_0 = 1K$. All system boundaries are held at a constant temperature $T_c = 0K$

The PDE used is well established and can be found detailed in Carslaw & Jaeger [114]. Transient solutions are complex to derive in 2D, therefore the model is restricted to a simplified case. A 2D square of length L is considered. If all boundaries are assumed to be at temperature $T_c = 0K$ and the system initial state assumed to be $T_0 = 1K$ then the solution is a product of the transient solution in each dimension separately:

$$T(x, y, t) = \phi(x, t)\phi(y, t) \tag{3.61}$$

The solution ϕ is given by Eq.3.32:

$$\phi(x, t) = \frac{4}{\pi} \sum_{m=1}^{\infty} \frac{(-1)^{m-1}}{2m-1} cos\left(\frac{(2m-1)\pi x}{L}\right) \exp\left(\frac{-(2m-1)^2\pi^2 D_T t}{L^2}\right) \tag{3.62}$$

3.4.1 Restricted Solution

To allow for direct comparison of the results as in the 1D heat flow models, the solution is restricted to a single slice of the 2D model. This is obtained by arbitrarily selecting $y = 0$. This gives the

expected temperature profile within the region as:

$$T(x, y=0, t) = \frac{16}{\pi^2}\left[\sum_{n=1}^{\infty}\sum_{m=1}^{\infty}\frac{(-1)^{m-1}}{2m-1}cos\left(\frac{(2m-1)\pi x}{L}\right)\exp\left(\frac{-(2m-1)^2\pi^2 D_T t}{L^2}\right)\right. \\ \left.\cdot\frac{(-1)^{n-1}}{2n-1}\exp\left(\frac{-(2n-1)^2\pi^2 D_T t}{L^2}\right)\right] \tag{3.63}$$

Eq.3.63 is plotted in Fig.3.20 for a system length of $L = 50$ where $-L/2 < x < L/2$. Several times are shown in powers of 10.

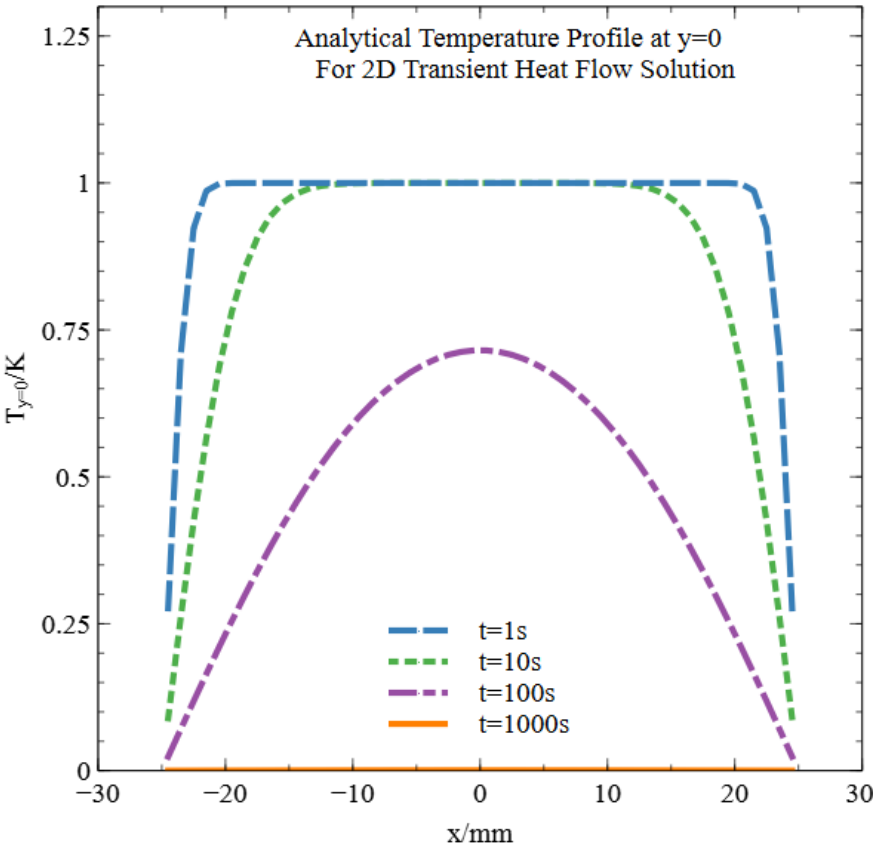

Figure 3.20: The analytical solution for the transient heat flow in a slab as shown in Fig.3.19 is plotted for the slice $y = 0$ as given by Eq.3.63. Time steps are given in powers of 10.

3.4.2 2D SPAM Temperature Evolution

The standard temperature evolution depends on the dot product of particle heat flux sums with the gradient of the weight function. This is well documented and takes the form:

$$\dot{T}_i = \frac{-1}{\rho c_p}\sum_j\left[\left(\frac{Q}{\rho^2}\right)_i + \left(\frac{Q}{\rho^2}\right)_j\right]\cdot\nabla_i w\left(r_{ij}\right) \tag{3.64}$$

where the heat flux is now calculated as:

$$Q_i = -\kappa\sum_j\frac{m_j}{\rho_j}\left[T_j - T_i\right]\cdot\nabla_i w\left(r_{ij}\right) \tag{3.65}$$

Monaghan's temperature evolution is already noted in a form for implementation in 2D by Eq.3.48. The case of Hoover's evolution is not as clear. The temperature evolution can be expressed as:

$$\dot{T}_i = C \sum_i (T_i - T_j) \frac{m_j}{\rho_j} w \tag{3.66}$$

The value C can then be obtained by considering the 2 separate spatial dimensions x, y of the vector $\mathbf{r}$. From the earlier derivation, it can be seen that in two dimensions the factor $T''(y)$ must be considered:

$$T''(y) = \frac{T(y) - T(y_j)}{\sum_j^N \frac{(y_j - y)^2}{2} \frac{m_j}{\rho_j} w} \tag{3.67}$$

The summation of the two factors can be considered as:

$$\nabla^2 T(x,y) = [T(x,y) - T(x_j, y_j)] \left(\frac{2}{\sum_j^N (x_j - x)^2 \frac{m_j}{\rho_j} w} + \frac{2}{\sum_j^N (y_j - y)^2 \frac{m_j}{\rho_j} w} \right) \tag{3.68}$$

This gives a new constant C in 2D as:

$$C_{2D} = 2D_T \left(\frac{1}{\sum_j^N (x_j - x)^2 \frac{m_j}{\rho_j} w} + \frac{1}{\sum_j^N (y_j - y)^2 \frac{m_j}{\rho_j} w} \right) \tag{3.69}$$

Derivation using a test function as Hoover does for the 1D case [54] suggests that a factor of 2 is all that is required when simply using inter particle distances, therefore excellent results can be obtained from:

$$C_{2D} = \frac{4D_T}{\sum_j^N r_{ij}^2 \frac{m_j}{\rho_j} w} \tag{3.70}$$

where R_{ij} is the scalar distance between particles i, j. It is believed this holds due to the symmetric nature of the particle arrangement in the x, y directions and that the factor of 2 can be found by considering the two summations over x, y to be equal. The effectiveness of each of these methods is demonstrated in the following section.

3.4.3 SPAM Results

For all SPAM simulations of 2D transient heat flow the simplest boundary enforcement of fixed particles is used. The particle arrangement is shown in Fig.3.21. Boundary particles are included to within the range H to ensure no errors in interpolation.

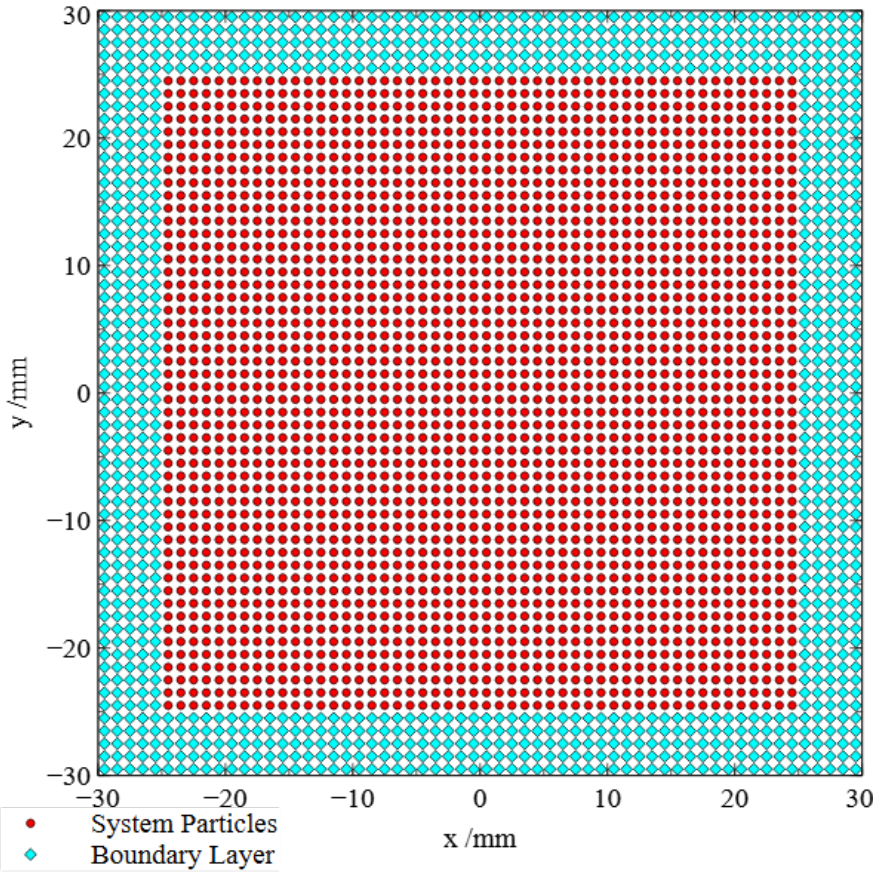

Figure 3.21: The 2D particle arrangement used for SPAM simulations of transient heat flow. The particles shown as red circles are system particles. The particles shown as blue diamonds are the fixed boundary particles, restricted from evolving in time.

The SPAM is run with a time step of $dt = 0.05s$ and the particle arrangement uses unit grid spaced unit mass particles with $\rho_0 = 1\text{g/mm}^3$. The results for the standard temperature evolution given by Eq.3.92 can be seen in Fig.3.22. For this test the artificial terms were included as they presented a slight improvement on the standard method in the 1D case.

The SPAM temperature distribution is systematically higher at all times and becomes worse as time progresses. The error for the $T = 100K$ curve is $\approx 8\%$ at the peak value.

The results for Monaghan's alternative temperature evolution (Eq.3.48) are shown in Fig.3.22. Again artificial terms are included as they were found to reduce the error in the 1D case. The evolution given by Monaghan again shows improvement over the error of the standard evolution. Its ability to handle discontinuities makes it seem appealing and steady state conditions have been shown to be reproducible with the method.

Finally the results for the two presented methods of Hoover's temperature evolution in $2D$ are given in Fig.3.22. Artificial terms were not included. Both calculations of C with either Eq.3.70 or Eq.3.69 are seen to give identical results. Considering the error improvement given in Table.3.1 this method of temperature evolution appears therefore to be the superior choice. To fully confirm this, a final 2D test will be explored with more complex boundary conditions.

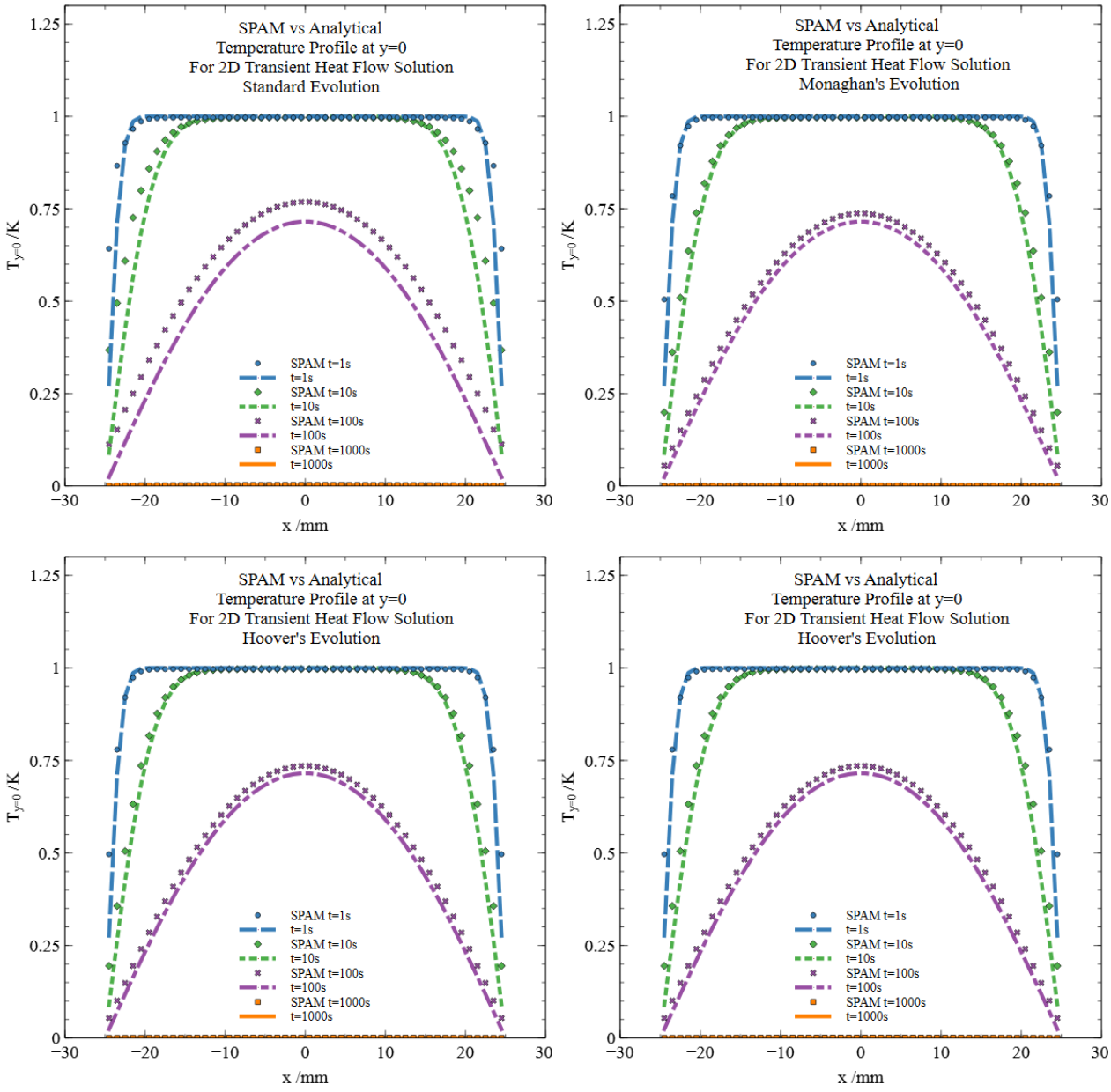

Figure 3.22: Analytical solution to 2D transient heat flow given by Eq.3.63 is compared with SPAM solution. Top left given by Eq.3.92. Top right given by Eq.3.48. Both have artificial terms included. Bottom given by Hoover's evolution Eq.3.66. Two variations on the calculation of C are presented here and are found to give identical results. Bottom Left is calculated with Eq.3.70, right with Eq.3.69. Artificial terms are NOT included.

Method	Residual Error for t=100s (2D)
Standard	0.0722
Monaghan's	0.0283
Hoover's	0.0260

Table 3.1: Residual error calculated for each method of SPAM evolution tested on the 2D transient heat flow problem for time $T = 100K$

The spatial distribution of the error for both the case of Monaghan's and Hoover's evolution equations are highlighted within Fig.3.23 for $t = 100s$. The distribution of error for each method is shown to follow the same general shape, being maximal close to but not on the boundary. A clear deviation occurs at the system boundary and the minimum error occurs at the peak of the temperature value within the slice $y = 0$. Most importantly the error is seen to be less at all points within the distribution for Hoover's formulation, again supporting it as the superior choice.

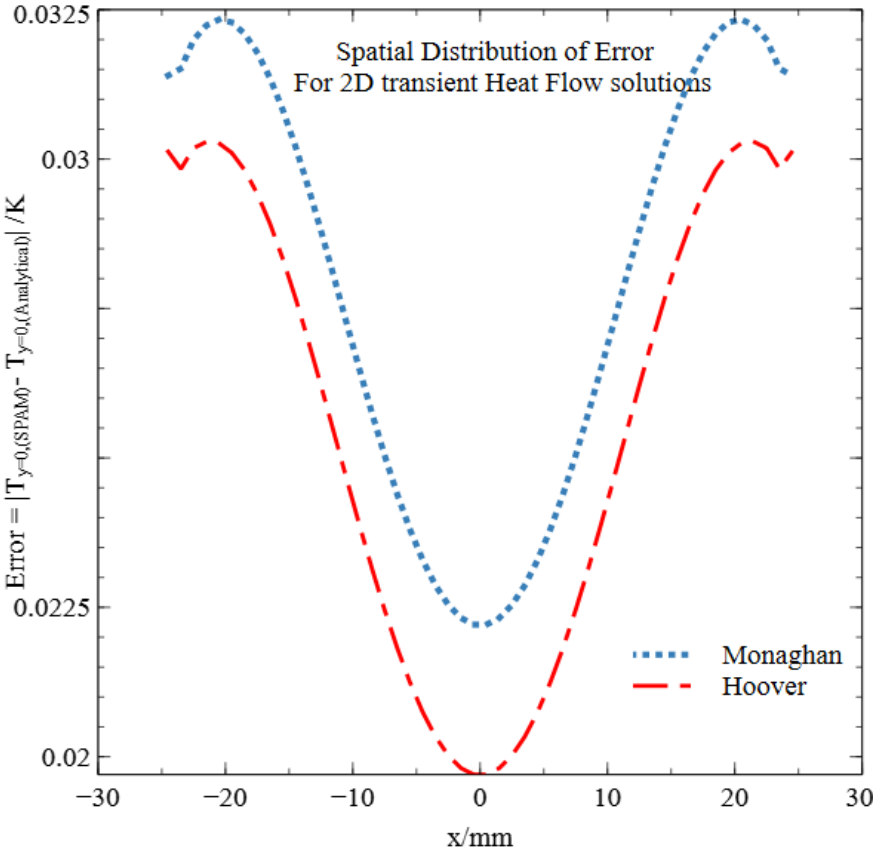

Figure 3.23: The a comparison for the spatial distribution of error between the SPAM and analytical is given for the 2D transient heat flow problem. Errors are shown for the formulation given by Hoover's evolution Eq.3.66 and Monaghan's Eq.3.48. Results are shown for $t = 100s$.

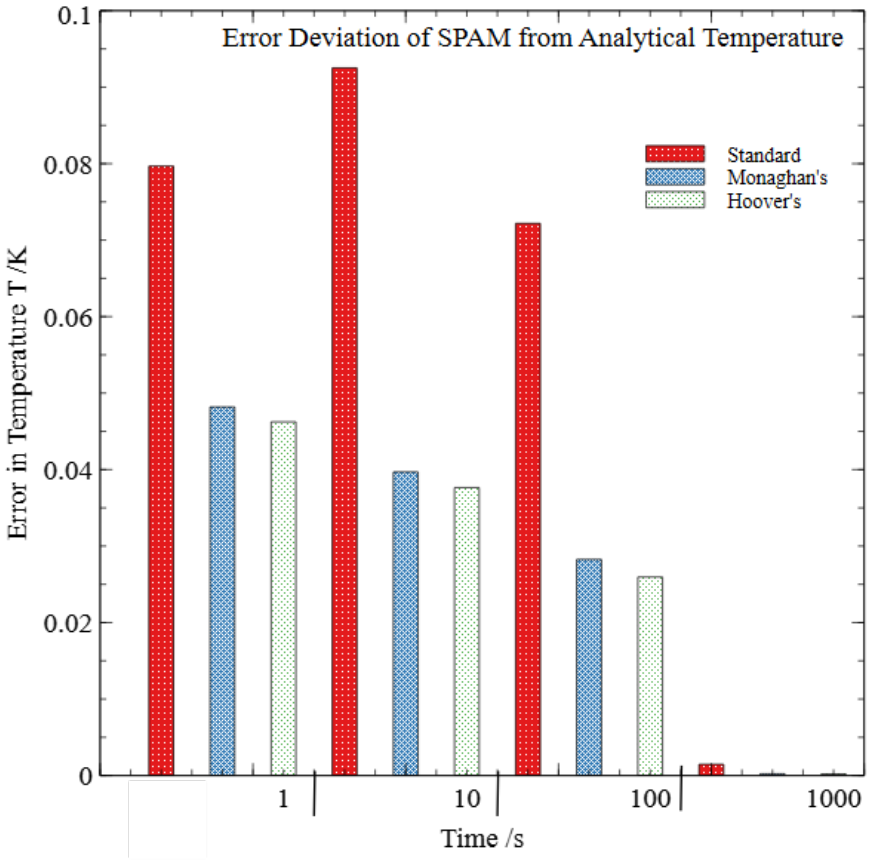

Figure 3.24: The residual error is given for each of the 3 methods of time evolution in SPAM for the 4 time steps shown.

3.5 More Challenging Boundary Conditions - 2D Heated Tile

Any method of temperature evolution by an SPAM model must not only be consistent in time but be robust in its ability to handle complex boundary value problems. A more complex 2D model will therefore be explored with full discussion of the advantages and disadvantages surrounding various methods of boundary modelling within SPAM.

Consider a square of side lengths L, centred on the origin. Boundary conditions are enforced to drive the system toward a steady state as:

$$T = \begin{cases} T_H & : y = L/2, -L/2 < x < L/2 \\ T_C & : y < -L/2, x < -L/2, x > L/2 \end{cases} \tag{3.71}$$

Both T_H and T_C are constant temperatures. A visualisation of the model is given in Fig.3.25. The model is chosen with the knowledge that a steady state analytical solution exists.

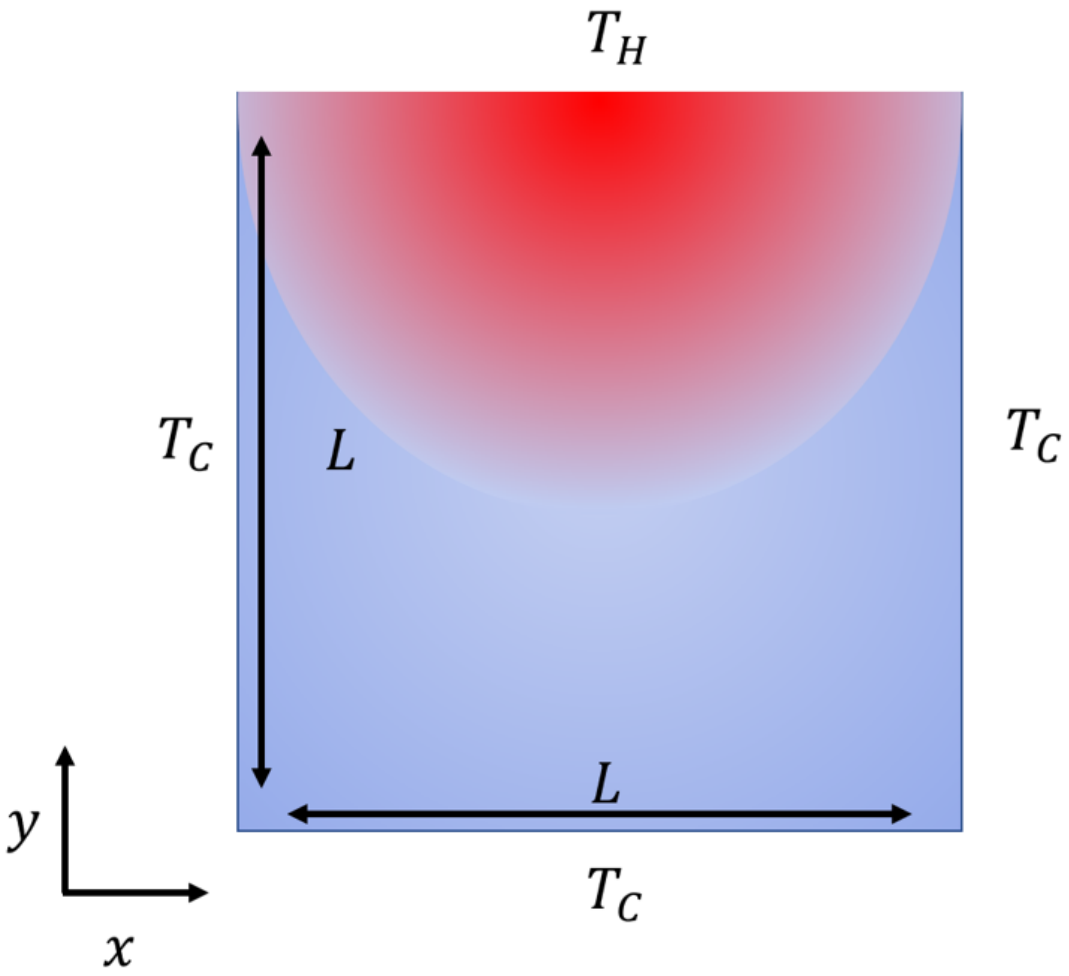

Figure 3.25: A visual representation of the 2D problem being studied. 3 sides are kept at temperature T_C, the other side at T_H.

3.5.1 Analytical Solution

Again we choose a model which permits an analytical solution; the steady state flow of heat on a rectangular region of space is well documented [119]. For the condition of steady state in two dimensions with no source terms and constant thermal conductivity the heat diffusion equation becomes:

$$0 = \frac{\partial T}{\partial t} = D_T \left(\frac{\partial^2 T}{\partial x^2} + \frac{\partial^2 T}{\partial y^2} \right) \tag{3.72}$$

By substituting the variables with the following the derivation of the solution becomes simplified:

$$T^* = T - T_C \tag{3.73}$$

$$x^* = x + \frac{L}{2} \tag{3.74}$$

$$y^* = y + \frac{L}{2} \tag{3.75}$$

This gives the modified boundary problem as:

$$T^* = \begin{cases} T_H - T_C & : y^* = L, 0 < x^* < L \\ 0 & : y < 0, x < 0, x > L \end{cases} \tag{3.76}$$

Now it can be assumed that the solution is separable:

$$T^*(x^*, y^*) = X(x^*)Y(y^*) \tag{3.77}$$

Then through separation it can be shown that:

$$\frac{d^2X}{dx^{*2}} + \lambda^2 X = 0 \tag{3.78}$$

$$\frac{d^2Y}{dy^{*2}} - \lambda^2 Y = 0 \tag{3.79}$$

where λ^2 is the separation constant. The constant value on the upper boundary can be written as an infinite sum of sine functions:

$$T_H - T_C = \sum_{n=1}^{\infty} a_n sin\left(\frac{n\pi x^*}{L}\right) \tag{3.80}$$

For this reason it is ideal to examine solutions in the range $\lambda^2 > 0$ which take the general form:

$$T* = (C_1 cos(\lambda x^*) + C_2 sin(\lambda x^*))\left(C_3 e^{-\lambda y^*} + C_4 e^{\lambda y^*}\right) \tag{3.81}$$

Now the boundary conditions given by Eq.3.76 can be applied to give the conditions:

$$\begin{aligned} C_1 &= 0 \\ C_3 &= -C_4 \\ C_2 C_3 sin(\lambda L)\left(e^{-\lambda y^*} + e^{\lambda y^*}\right) &= 0 \end{aligned} \tag{3.82}$$

This final condition given above implies that $sin(\lambda L) = 0$. The root of this non-linear equation are given by:

$$\lambda_n = \frac{n\pi}{L} \tag{3.83}$$

The temperature solution then becomes a sum of these infinite solutions:

$$T^* = \sum_{n}^{\infty} C_n sin(\frac{n\pi x^*}{L})\left(e^{\frac{-n\pi y^*}{L}} - e^{\frac{n\pi y^*}{L}}\right) \tag{3.84}$$

This contains the hyperbolic function. The upper boundary condition now gives:

$$T_H - T_C = \sum_{n}^{\infty} C_n sin(\frac{n\pi x^*}{L}) sinh(n\pi) \tag{3.85}$$

This is a variation of the condition assumed in Eq.3.80 and thus can be used to obtain the values of C_n:

$$C_n = \frac{2}{\pi}(T_H - T_C)\frac{1}{sinh(n\pi)}\frac{(-1)^{n+1} + 1}{n} \tag{3.86}$$

This gives the full expression for the temperature as:

$$T^* = (T_H - T_C)\frac{2}{\pi}\sum_n^\infty \frac{(-1)^{n+1}+1}{n} sin(\frac{n\pi x^*}{L})\frac{sinh(n\pi y^*/L)}{sinh(n\pi)} \tag{3.87}$$

This equation can then be transposed back to T, x, y to give the desired co-ordinate system for the model:

$$T = (T_H - T_C)\frac{2}{\pi}\sum_n^\infty \frac{(-1)^{n+1}+1}{n} sin\left(\frac{n\pi(x+L/2)}{L}\right)\frac{sinh(n\pi(y/L+1/2))}{sinh(n\pi)} + T_C \tag{3.88}$$

This allows the steady state temperature to be calculated anywhere on the square. The heat flux follows from Fourier's law:

$$\begin{aligned} Q_x &= (T_H - T_C)\frac{2}{L}\sum_n^\infty [(-1)^{n+1}+1] cos\left(\frac{n\pi(x+L/2)}{L}\right)\frac{sinh(n\pi(y/L+1/2))}{sinh(n\pi)} \\ Q_y &= (T_H - T_C)\frac{2}{L}\sum_n^\infty [(-1)^{n+1}+1] sin\left(\frac{n\pi(x+L/2)}{L}\right)\frac{cosh(n\pi(y/L+1/2))}{sinh(n\pi)} \end{aligned} \tag{3.89}$$

Finally by considering $y = 0$ the equation of a single slice through the centre of this model can be calculated as:

$$T = (T_H - T_C)\frac{2}{\pi}\sum_n^\infty \frac{(-1)^{n+1}+1}{n} sin\left(\frac{n\pi(x+L/2)}{L}\right)\frac{sinh(n\pi/2)}{sinh(n\pi)} + T_C \tag{3.90}$$

3.5.2 Analytical results

For the case studied here we set $L = 50$mm, $T_C = 1$K and $T_H = 2$K. The analytical solutions were calculated including frequencies up to $n = 100$ to give smoothed temperature and heat flux profiles as seen in Fig.3.27. It is important to note that this solution is actually discontinuous at the corners of the system despite the well-defined analytical solutions. This makes it a good further case study for the stability of the SPAM algorithms with complex boundaries. The 1D dimensional slice through the system at $y = 0$mm is given in Fig.3.26.

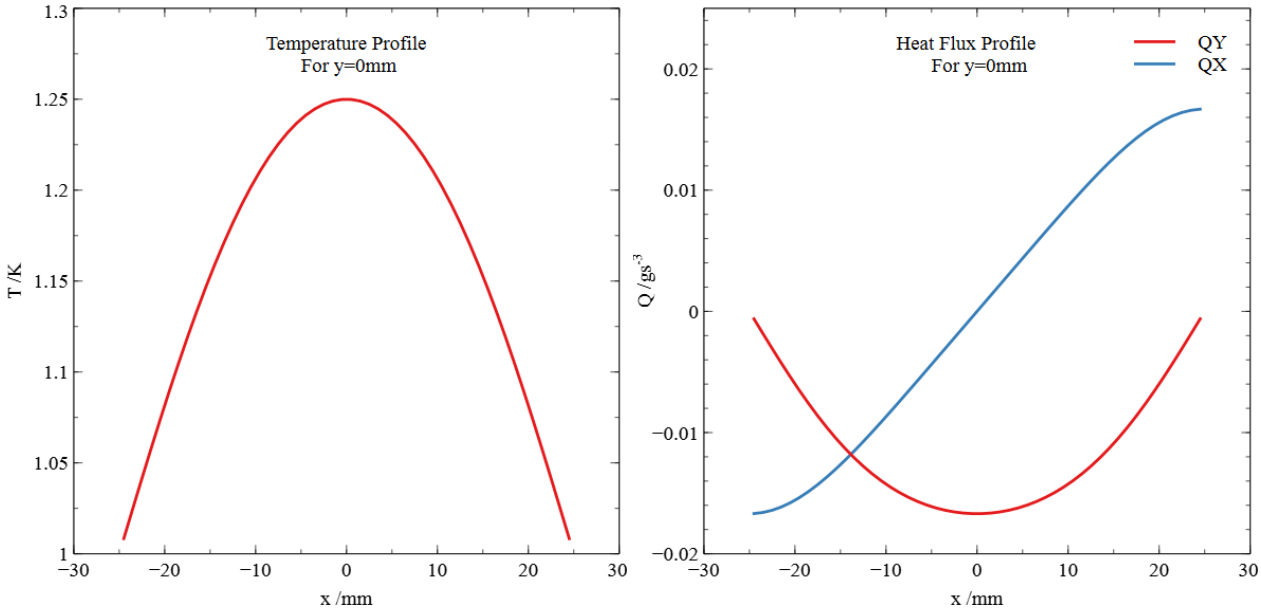

Figure 3.26: The solutions of Eq.3.90 for temperature as well as its counterpart heat flux equations in both the x and y directions for the 1D slice through the system at $y = 0$mm. The solutions were generated using the first $n \leq 100$ frequencies to create a smoothed map.

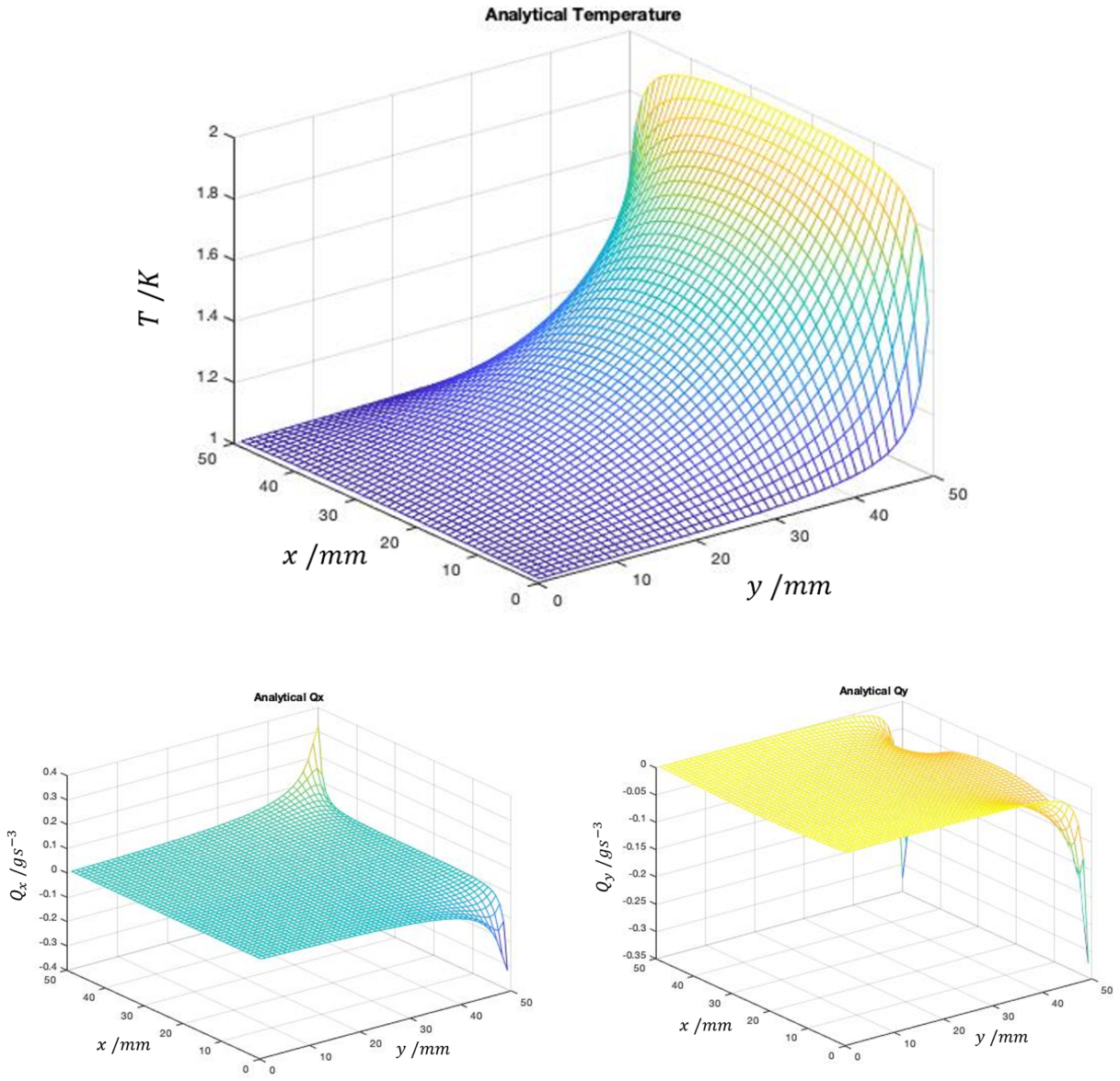

Figure 3.27: The solutions of Eq.3.88 for temperature as well as its counterpart heat flux equations in both the x and y directions. The solutions were generated using the first $n \leq 100$ frequencies to create a smoothed map

3.5.3 SPAM Solution with Fixed Boundaries

The fixed boundary solution to the 2D heat tile problem with SPAM is the simplest of those presented here, however it has the potential to introduce the most error. The particle arrangement used for these simulations is identical to Fig.3.21. The only difference is in the assignment of temperatures to the boundary particles. All fixed boundary particles are given one of two temperature

values based on:

$$\begin{aligned} T_i &= 2 \quad : x_i > 25 \\ T_i &= 1 \quad : x_i < 25 \end{aligned} \tag{3.91}$$

The boundary particle values are then restricted from being updated, however values such as heat fluxes are still calculated at each time step. The discontinuity exists clearly within the fixed boundary particles and so it is expected that the heat flux will diverge. The heat flux is calculated using Eq.3.65. The temperature evolution is shown here calculated with two of the explored methods. The first is using standard evolution with artificial terms expressed as:

$$\dot{T}_i = \frac{-1}{\rho c_p} \sum_j \left[\left(\frac{Q}{\rho^2} \right)_i + \left(\frac{Q}{\rho^2} \right)_j + \Pi_{T,ij} \right] \cdot \nabla_i w \left(r_{ij} \right) \tag{3.92}$$

where the artificial conductivity is given by Eq.3.40. This is used in an attempt to tame the diverging heat flux effects on the steady state results. The other method used will be Hoover's evolution given by Eq.3.66 with C given by Eq.3.70. This does not depend on the heat flux and so should be able to handle the the discontinuities without modification.

3.5.4 SPAM Fixed Boundary Results

The SPAM simulations are run in 2D with the smoothed interpolated profiles given for $y = 0$mm. A time step of $dt = 0.05s$ is used. The smoothing length is $H = 3$mm. Results for the standard evolution with artificial terms is presented is Fig.3.28. Errors introduced by the fixed boundary conditions can clearly be seen. The heat flux is reduced at the boundaries due to the incorrect boundary temperature enforced by the fixed particles. Furthermore the temperature figure clearly shows the boundary temperature is interpolated as greater than the desired $T_C = 1$K. For standard evolution to work with fixed boundary conditions it is noted that the particle heat flux must be calculated for the fixed boundary particles.

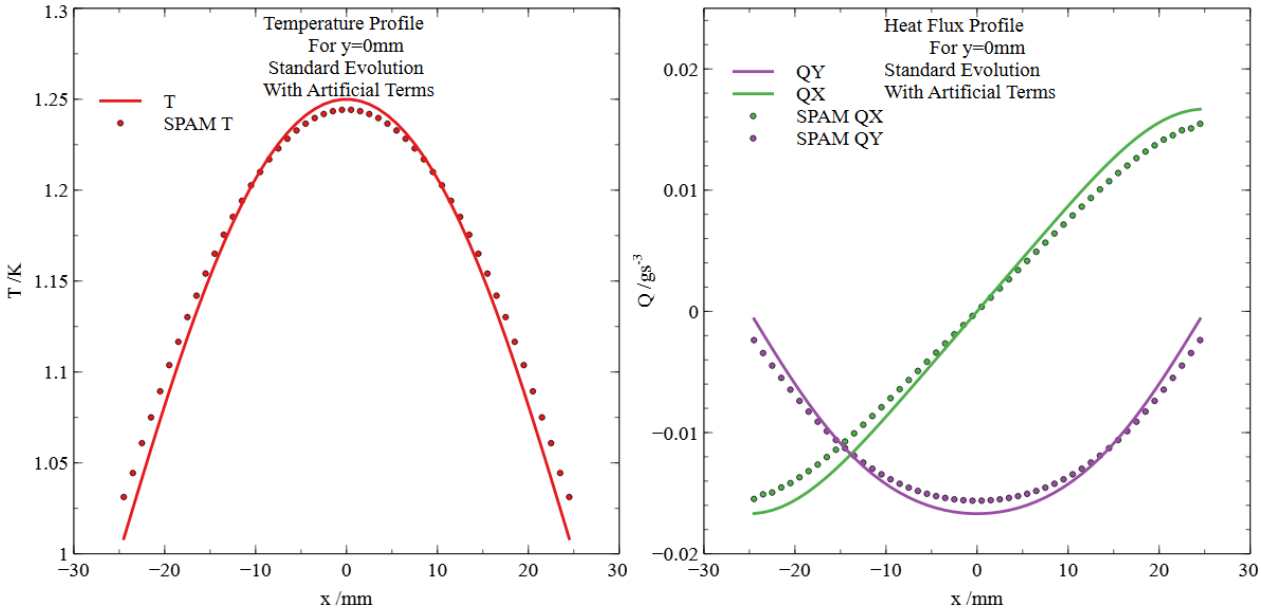

Figure 3.28: The SPAM solutions of the 2D heat tile problem shown in Fig.3.25 for temperature shown left and heat flux both the x and y directions shown right for the 1D slice through the system at $y = 0$mm. The solutions were generated using fixed boundary conditions with standard evolution with artificial terms given by Eq.3.92

The same boundary error is evident in the case of Hoover's evolution given in Fig.3.29, however the overall error is significantly reduced compared to the case of standard evolution. This error can be reduced further by considering dynamic boundary conditions instead.

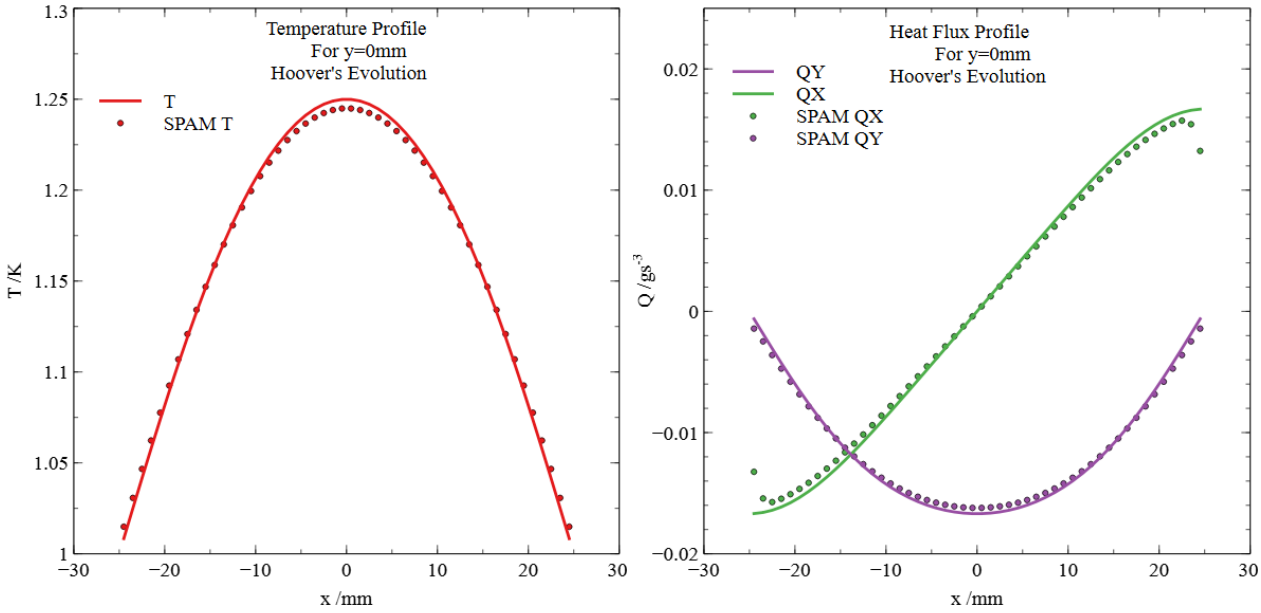

Figure 3.29: The SPAM solutions of the 2D heat tile problem shown in Fig.3.25 for temperature shown left and heat flux both the x and y directions shown right for the 1D slice through the system at $y = 0$mm. The solutions were generated using fixed boundary conditions with Hoover's evolution given by Eq.3.66 with factor Eq.3.70

3.5.5 SPAM Solution with Dynamic Mirror Boundaries

Before examining the results for dynamic boundaries we first need to examine the issue of assigning mirror or 'ghost' particles across the system corners. For this problem the upper corners of the tile represent a discontinuous temperature distribution, with the instantaneous jump from the hot to cold boundary. This may not seem problematic at a point but the area beyond the corner is not trivially a point and the assignment of dynamic particles within this area from their own discontinuity if the point from which they are assigned is discontinuous. This idea is represented in Fig.3.30.

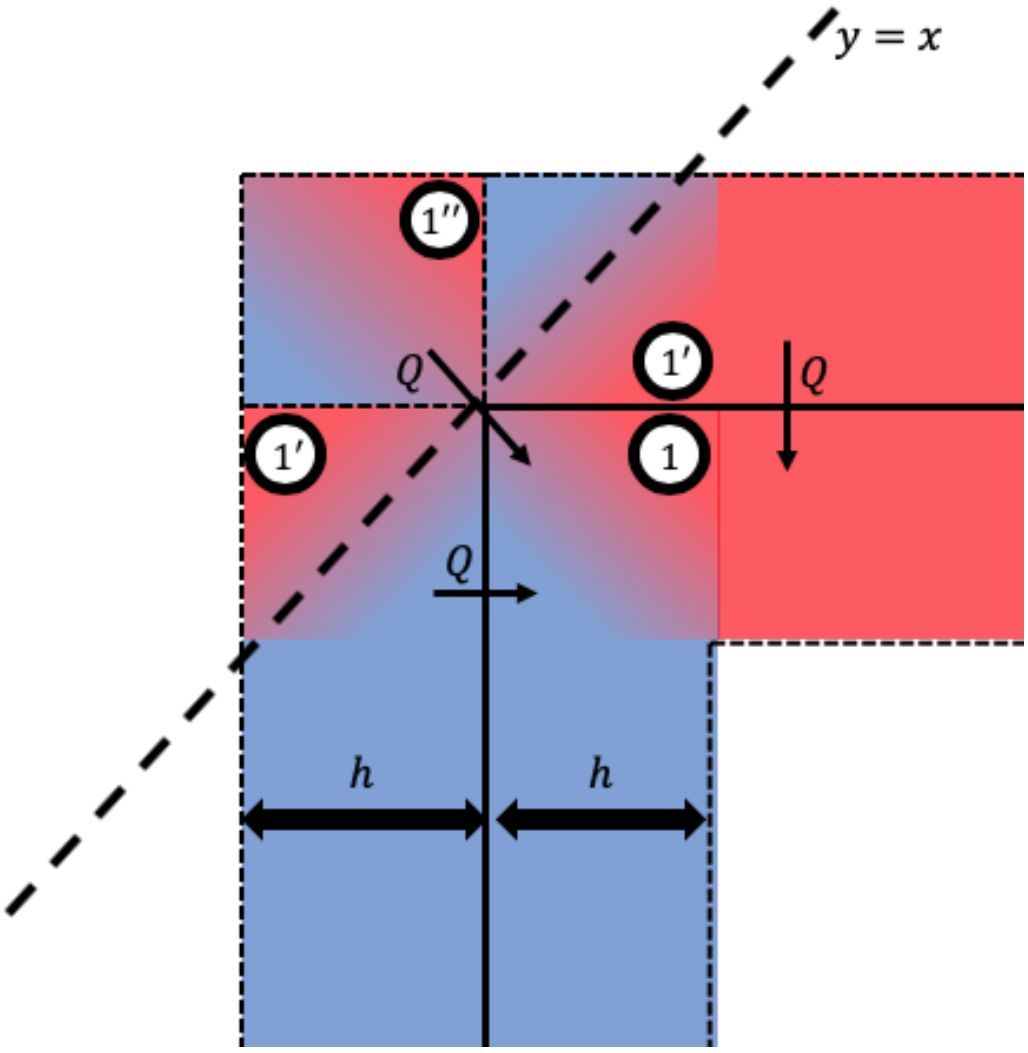

Figure 3.30: A visualisation of the way in which mirror particles across the SPAM simulation corners are assigned their position. As is demonstrated by the colour profile of the particles, such a reflection preserves the expected temperature profile of the physically real case. The reflection is adapted to be in the line $y = -x$ for the alternative corners.

Mirror particle positions are assigned as before but again a more complex relation is required to assign particle positions at the system corners:

$$\begin{aligned} x_{i'} &= -y_i + x_B + y_B \\ y_{i'} &= -x_i + x_B + y_B \end{aligned} \tag{3.93}$$

To understand the geometry of such a relation Fig.3.30 shows how such a reflection appears. These equations demonstrate a reflection in the line $y = x$ or $y = -x$ dependent upon the simulation corner. Such a reflection is chosen to maintain an appropriate temperature profile in the mirror particles. The normal boundary reflections of particle 1 are represented by $1'$. The corner reflected particle is $1''$. As can be seen from the figure, a reflection of the form $y = x$ preserves the expected temperature profile in the corner as it progresses from hot to cold. It does however form

a discontinuity with the mirrored sections given by $1'$. To combat this, restrictions on the mirrored particle heat flux are created so that heat may only ever flow perpendicular to the boundary. For the corner case heat flux is restricted to flow only perpendicular to the line of reflection, as can be seen in the below figure. Such a restrictions for a $y = x$ reflection take the form:

$$\begin{aligned} Q_{x'} &= -Q_y \\ Q_{y'} &= -Q_x \end{aligned} \tag{3.94}$$

For a $y = -x$ reflection take the form:

$$\begin{aligned} Q_{x'} &= Q_y \\ Q_{y'} &= Q_x \end{aligned} \tag{3.95}$$

With reflections perpendicular to the x-axis controlled by:

$$\begin{aligned} Q_{x'} &= -Q_x \\ Q_{y'} &= Q_y \end{aligned} \tag{3.96}$$

Reflections perpendicular to the y-axis:

$$\begin{aligned} Q_{x'} &= Q_x \\ Q_{y'} &= -Q_y \end{aligned} \tag{3.97}$$

It already becomes clear that generalising such algorithms to three dimensions with arbitrary boundary shapes is complex and inefficient. Fig.3.31 shows the particle temperatures and heat fluxes for standard SPAM evolution with artificial terms evolved using these boundary conditions. It is evident immediately that (as shown by Fig.3.30) the enforced boundary temperatures are still discontinuous and so generate an unstable solution.

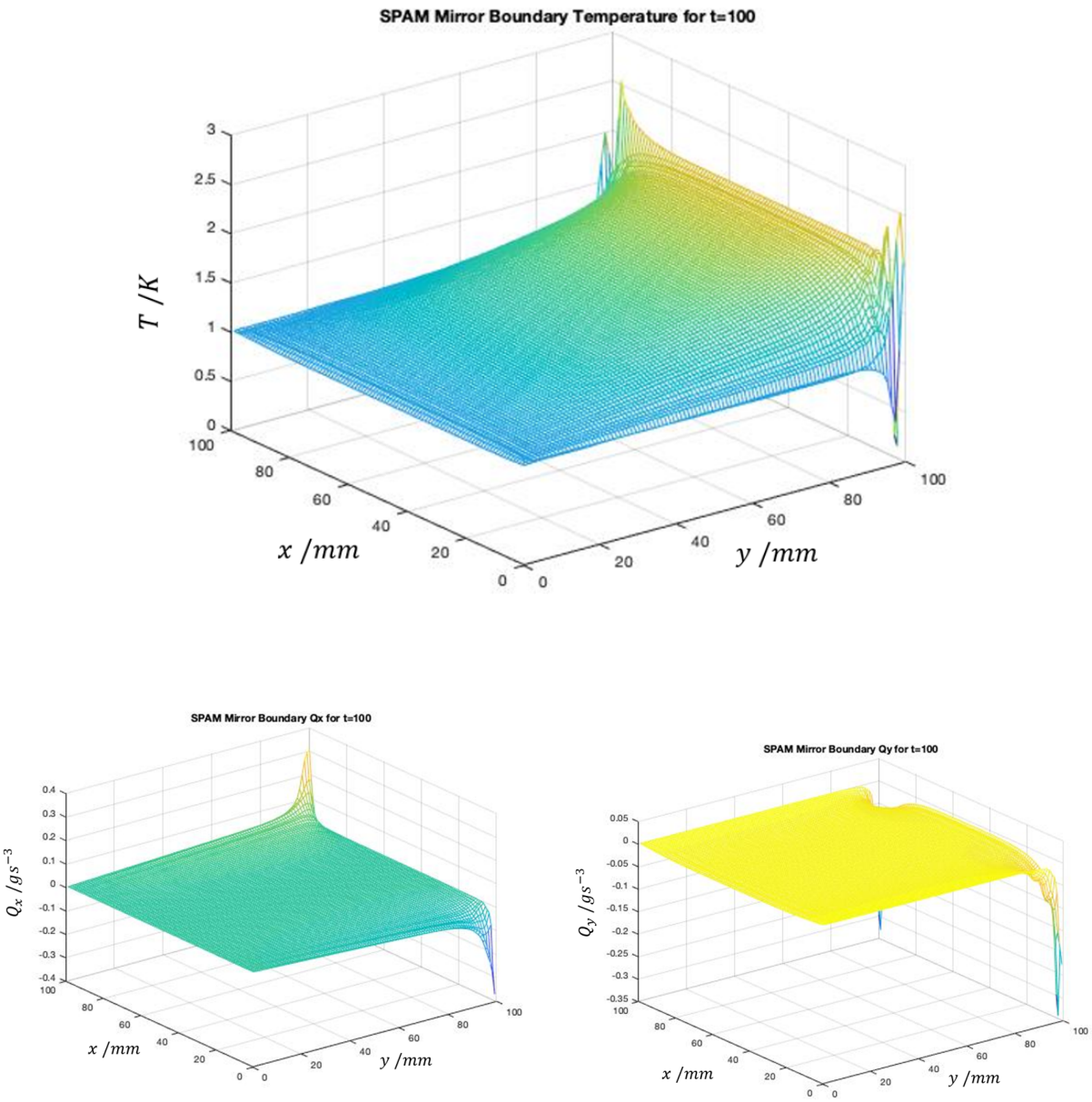

Figure 3.31: The SPAM solution Eq.3.48 for the 2D heated tile problem under mirror boundary conditions as defined above. Particle final temperatures as well as particle heat flux in both the x and y directions for $T = 100K$.

Without a generalised boundary algorithm to over come this, dynamic boundary conditions appear unsuitable for further simulations. A generalised method based on particle positions instead of direct geometric calculations is therefore proposed.

3.5.6 Generalised Geometry for the Mirror Algorithm

For mirror boundary conditions to be general to all geometry and easily implemented within SPAM algorithms it is beneficial that they be based on particle points instead of geometry, as with the main SPAM algorithm. The method given here therefore uses a particle arrangement of boundary points as can be seen within Fig.3.32. The boundary is populated by particle of zero mass $m_B = 0$ with particle spacing equivalent to the system. These particles define the shape of the boundary but are not included within the evolution algorithms by design as they have no mass.

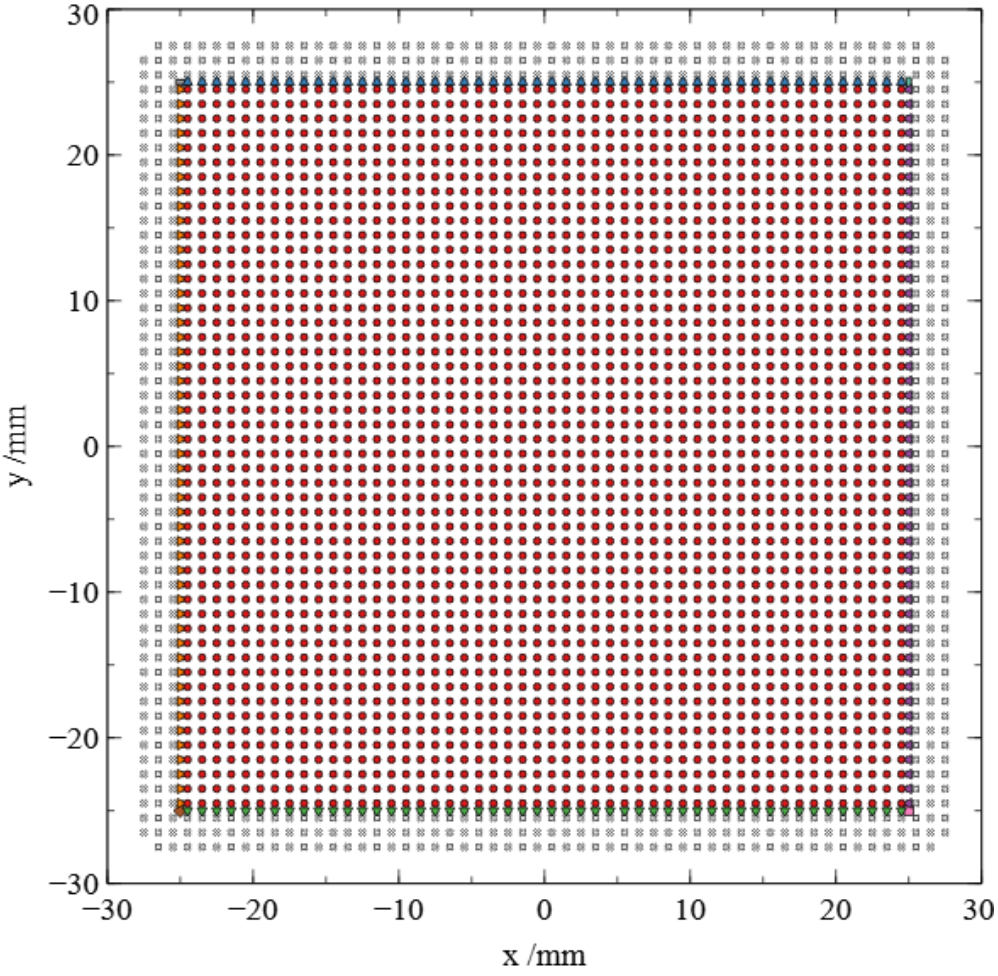

Figure 3.32: The particle distribution for the generalised mirror algorithm is shown above. The system particles are represented in red. The 'ghost' particles created by the algorithm are shown as white crosses. The boundary particles are given unit spacing along the boundary with no mass $m_B = 0$ and are shown in 8 different colours and symbols to represent the 8 different boundary sections.

The boundary particles are separated into separate groups for each distinct piece of the boundary over which particles will be mirrored, in this case there are 8, shown by the different colours and symbols. The 4 sides are considered independently as well as the 4 corners. An array of the closest boundary particle to each system particle is then created by looping though all system pairs. A

distinct array is created for each boundary piece. Therefore information for any system particle i is known such that the the closest 8 boundary particles, one from each distinct section, is stored and retrievable. For a moving boundary this can simply be recalculated as often as needed.

From here the final stage is the creation of mirror particles. The boundary particles are assigned temperatures as well as positions. For each closest pair within range H a particle is created at position:

$$\mathbf{r}_{i'} = 2\mathbf{r}_B - \mathbf{r}_i \tag{3.98}$$

Again the temperature and heat flux are simply assigned as:

$$\begin{aligned} T_{i'} &= 2T_B - T_i \\ Q_{i'} &= Q_i \end{aligned} \tag{3.99}$$

Although not used here, it is noted that for curved boundaries the radius of curvature of the boundary can be used to adjust the mirrored particle mass to ensure the density is maintained. Similarly for fast moving system particles such as in a fluid the boundary particle spacing can be decreased so that particle reflections approach the boundary normal. The boundary method outlined within this section is similar in nature to the method proposed by Ferrari et al [103]. The key difference between these methods is that for this method all system particles can see all mirror particles generated by the method. The method proposed by Ferrari instead generates a reduced set of mirror particles in isolation for each system particle. This may cause system particles close to the boundary to react to non-symmetric forces however the results shown by their method are still promising.

3.5.7 SPAM Mirror Boundary Results

The results of the generalised mirror boundary simulation are presented here again for standard evolution with artificial terms as well as Hoover's evolution. The simulation is run in full 2D, with the smoothed interpolation calculated for the slice $y = 0$mm. The time step used is $dt = 0.05$s for 20000 steps. The smoothing length used is $H = 3$mm. The results for the standard evolution are presented in Fig.3.33. Similarly the results for Hoover's evolution are shown in Fig.3.34. Both results show excellent agreement and stability. A small error is evident in both temperature profiles however the analysis of interpolation given in the previous chapter suggests that this error is reduced with particle number. This along with other features of the particle arrangement will be explored in greater detail in the next chapter.

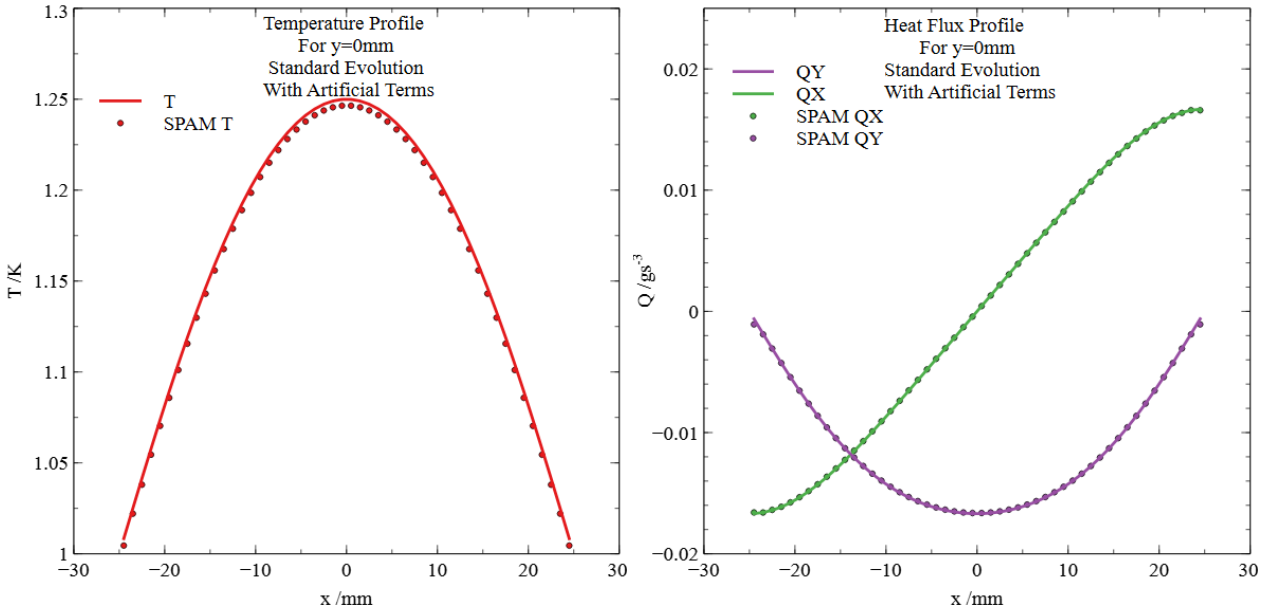

Figure 3.33: The SPAM solutions of the 2D heat tile problem shown in Fig.3.25 for temperature shown left and heat flux both the x and y directions shown right for the 1D slice through the system at $y = 0$. The solutions were generated using generalised mirror boundary conditions with standard evolution with artificial terms given by Eq.3.92

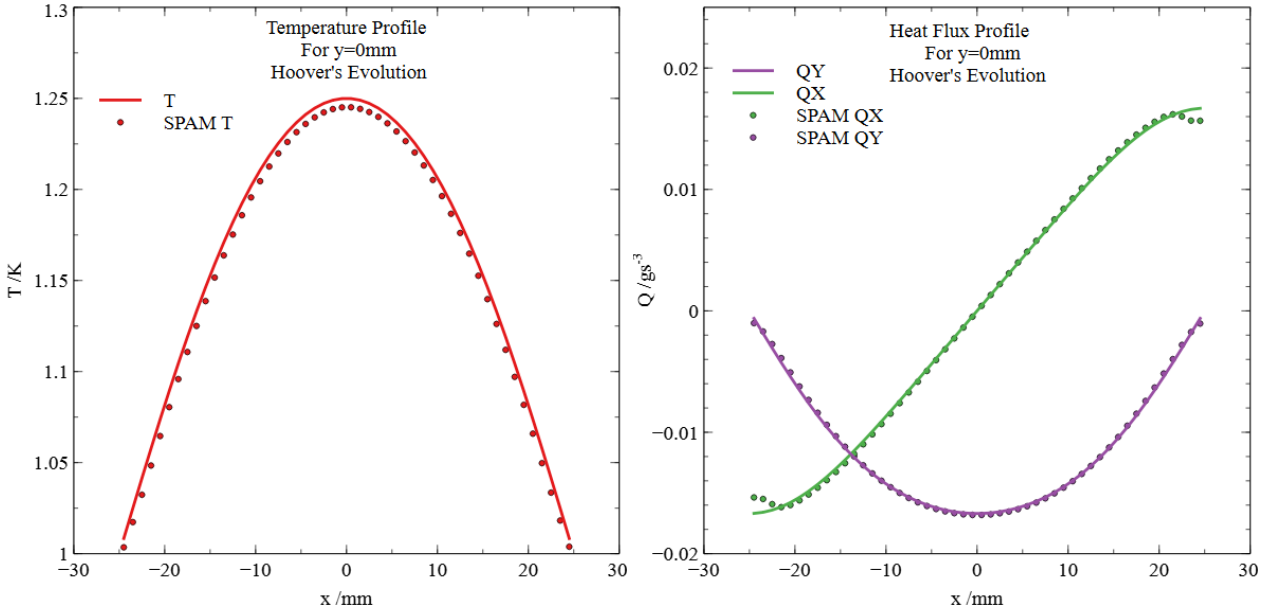

Figure 3.34: The SPAM solutions of the 2D heat tile problem shown in Fig.3.25 for temperature shown left and heat flux both the x and y directions shown right for the 1D slice through the system at $y = 0$. The solutions were generated using generalised mirror boundary conditions with Hoover's evolution given by Eq.3.66 with factor Eq.3.70

3.5.8 FEM Solution

It is important when examining novel modelling methods to compare results not only with well-defined analytical solutions but also with the industry standards for currently available modelling software. ANSYS represents a standard and widely-used software within corporations and university research and so its results will be used as an error benchmark for the acceptable error of the model from the analytical solution.

FEM is the standard method used within Fuel Performance Codes (FPCs) however they are independently created models and software that is purpose built. ANSYS is instead widely used for thermal and stress analysis in fields such as structural engineering and aviation. The underlying FEM methods are of the same standards however and so it provides a good comparison.

The ANSYS output was corrected to the required co-ordinate system and the slice at $y = 0$ is presented for comparison with the analytical solution in Fig.3.35. Clearly the error in the FEM results is significantly less than the SPAM. The methodology of smoothing length refinement through decreased particle spacing and increased particle numbers should reduce this discrepancy. This idea will be explored in greater detail in the following chapter.

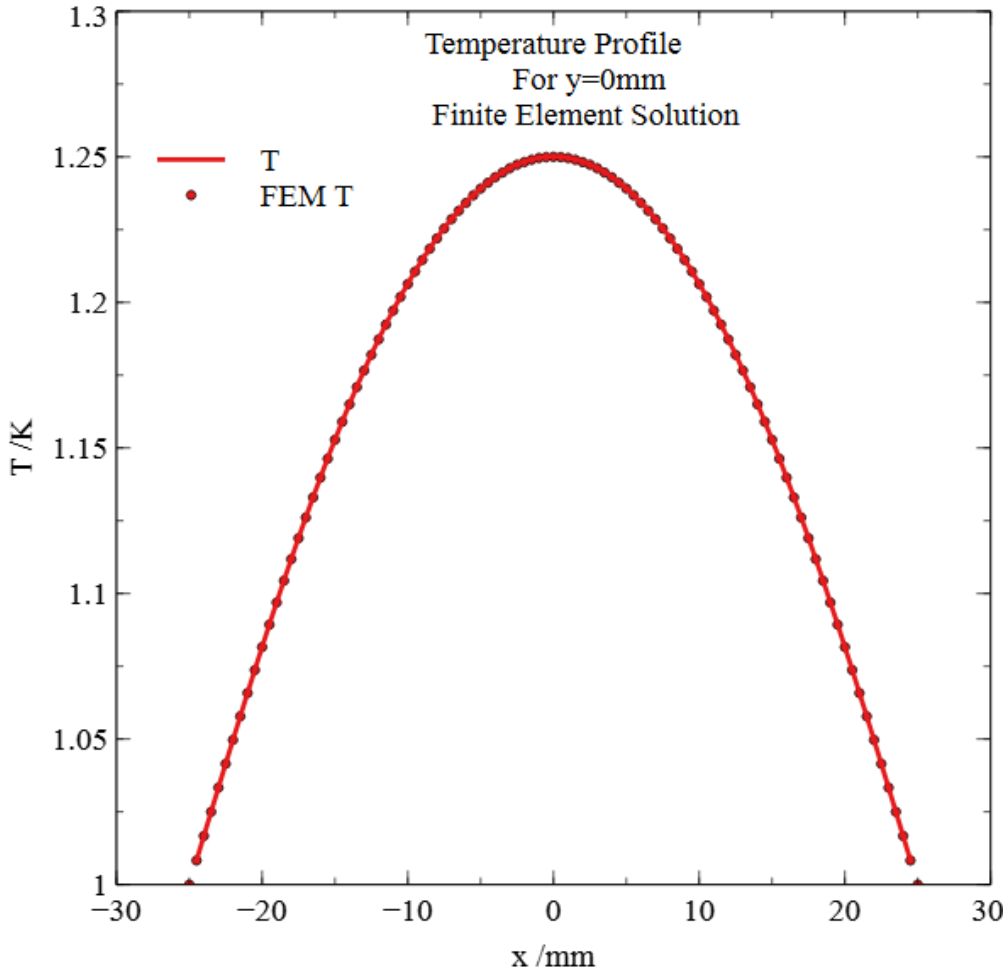

Figure 3.35: Temperature profile of the ANSYS result for the system slice $y = 0$mm. FEM solution to the 2D heated tile problem represented in Fig.3.25

3.5.9 Error Comparison

All of the results given for the 2D heat tile simulations are compared here along with those for the alternative temperature evolutions explored in earlier sections but not shown for the 2D heat tile. The error is calculated with the residual temperature error with the FEM result included for completeness.

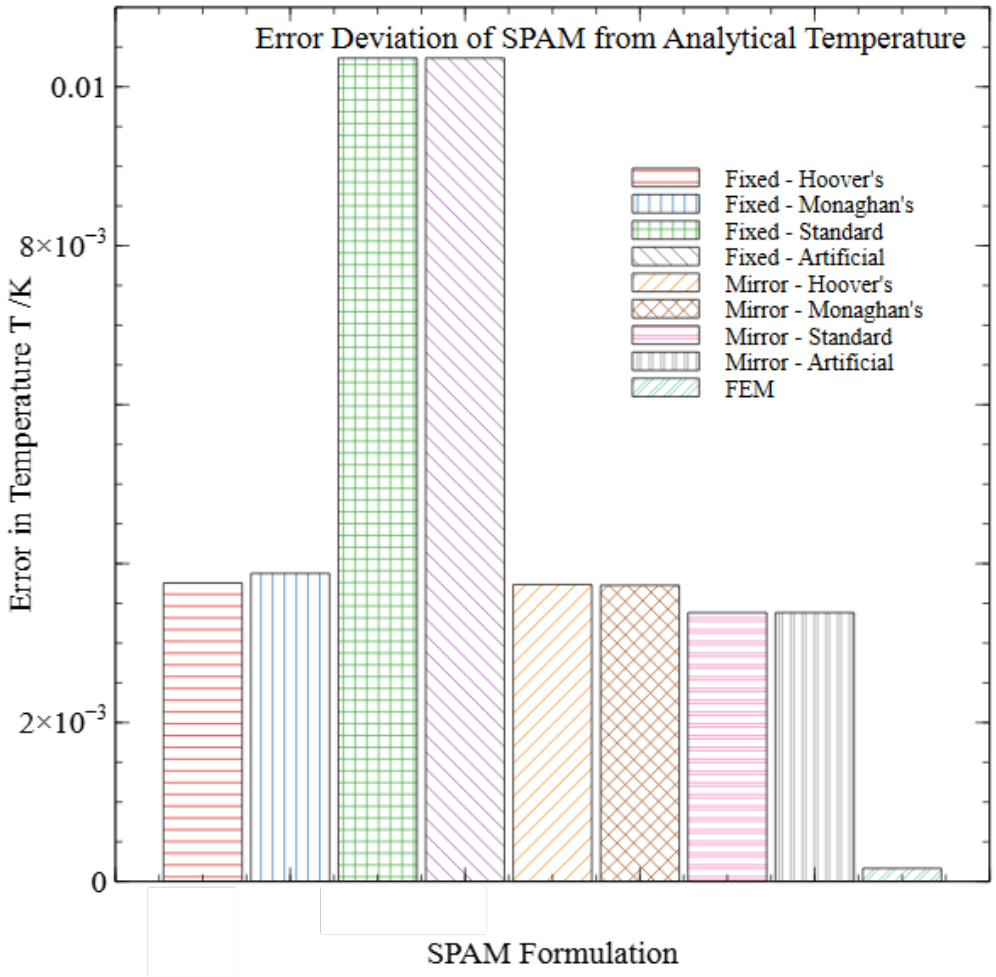

Figure 3.36: Comparison of the various residual errors in approaches to the solution of the 2D heated tile problem represented in Fig.3.25. The 'artificial' simulations are run with the standard evolution formulation.

The results are shown in Fig.3.36. All SPAM results are for $N = 2500$ particles therefore improvement toward the error given by the FEM result may still be achievable with a larger number of particles. Interestingly the standard temperature evolution both with and without artificial terms performs better in the mirror case by a margin despite being worse for fixed boundary particle conditions. The artificial terms also provide no improvement in the steady state solution.
These results suggest that for steady state solutions the choice of evolution used is less important than the choice of boundary conditions however this will likely be application dependant. One final piece of analysis will be shown to demonstrate how the full field data can be used to measure the

accuracy of future simulations. This will be particularly useful for any validation experiments that could be created.

3.5.10 Comparison via Shape Descriptors

The complex computational models discussed in this report are capable of producing a rich amount of data with full field maps of properties such as temperature, strain, heat flux, pressure, etc. In the past validation of simulations of this kind have been completed by comparison of maximum and minimum values or by comparisons of values at specific locations as for the 1D case. Experimental rigs can also be engineered to record specific values such as those used by Miaoa et al. in validating models of the stress peen forming process [120].

Recent developments in experimental techniques however now allow for full field data to be recorded by technology such as thermal imaging cameras, and Digital Image Correlation (DIC). These techniques were initially employed with much the same validation criteria as before but with an extended amount of data. This makes numerical confidence in the model difficult to establish as seen in the validation of welding simulations for thermal stresses [121].

Over the last few years there has been research done on the application of shape descriptors, such as those used in target recognition [122] and finger print recognition [123], to reduce the full field data and thus aid in the validation of solid mechanics models [124]. A full methodology for validating simulations through full field data analysis has been proposed using both Fourier-Tchebichef moments and Fourier-Zernike moments as shape descriptors [125]. This methodology, as detailed in full in the appendix, is applied throughout in this chapter as a measure of the agreement of SPAM results with those of FEM models created in ANSYS and with full field analytical results. This is done as an example of how more complex nuclear fuel models can be validated against experimental results in future work.

The method used here is based on the Fourier transform which is a mathematical formula for the decomposition of a signal into a sum of oscillating functions (sine waves). This idea of decomposing signals is not limited to sums of oscillating functions or to one dimensional signals and in fact can be extended to any number of dimensions and used with any infinite sum of orthogonal functions which appropriately describe the space. For each data set the Tchebichef moments are calculated with a given truncation p, q of the order of Tchebichef polynomials included:

$$[T_{p,q}] \tag{3.100}$$

These moments represent a reduction of the initial data field to data of dimensions p, q. Suppose we have two data sets A, B. For two identical data sets we would expect that for a given p, q that the related moment $T_{A_{p,q}} = T_{B_{p,q}}$ is equal. We can then measure the deviation of the actual moments of the two data sets from the line $T_{A_{p,q}} = T_{B_{p,q}}$. If all values lie within a predetermined error of this line then we can say the two data sets are within error of each other. To better demonstrate this, let us first examine the finite element method solution to the 2D heated tile problem and see how the moments compare with the analytical solution.

The output thermal profile for the system is shown on the left of Fig.3.37. On the right of this figure is the reconstructed image from the shape descriptors (Tchebichef moments). It is important to reconstruct the image in this way to compare with the original data set to ensure that the error in the shape description is not significant. It is immediately obvious that moments up to order

$p, q = 20$ are sufficient to describe the data. The error is estimated as:

$$u^2 = \frac{1}{N^2} \sum_{i,j}^{N^2} \left(\hat{f}(i,j) - f(i,j) \right)^2 \tag{3.101}$$

Here f represents the original data set, $\hat{f}$ the reconstructed data, N the original number of data points. This error is combined with any other error calculated for the simulations and then used to estimate the error bounds for direct moment comparison.

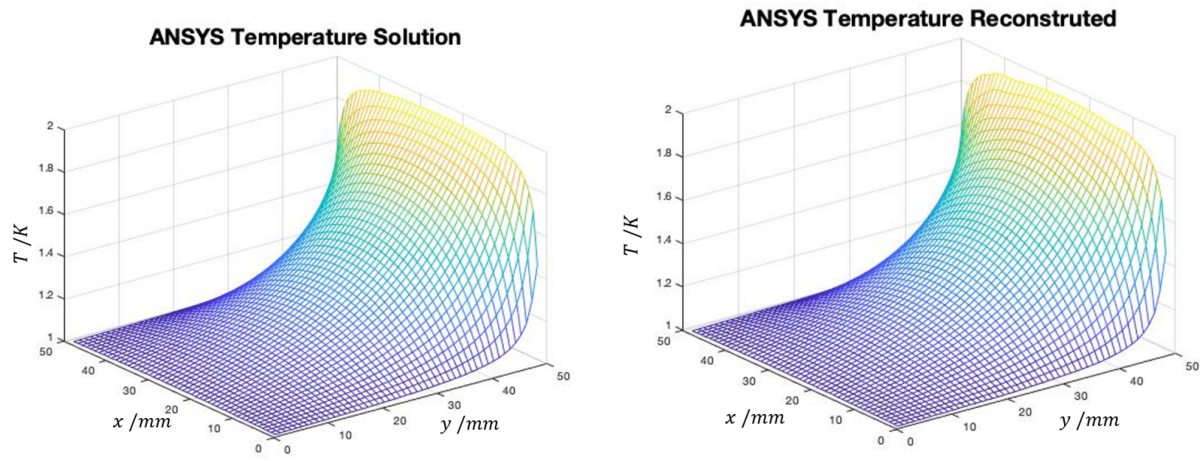

Figure 3.37: Original and reconstructed temperature data taken from the FEM solution to the 2D thermal model at steady state, produced using ANSYS. Data has been decomposed into Fourier-Tchebichef moments up to order 20, and the reconstructed data, shown right, used to estimate the residual error in the moments description of shape.

Analysis of moments between the analytical solution and the ANSYS solution shown in Fig.3.38, demonstrates the desired result for validation. The moments display a tight correlation, demonstrating the agreement of the two independently obtained results. The error for reconstruction is too small to give reasonable error bounds for validation, therefore other sources of error would be required for validation of this (such as the error produced by the ANSYS simulation).

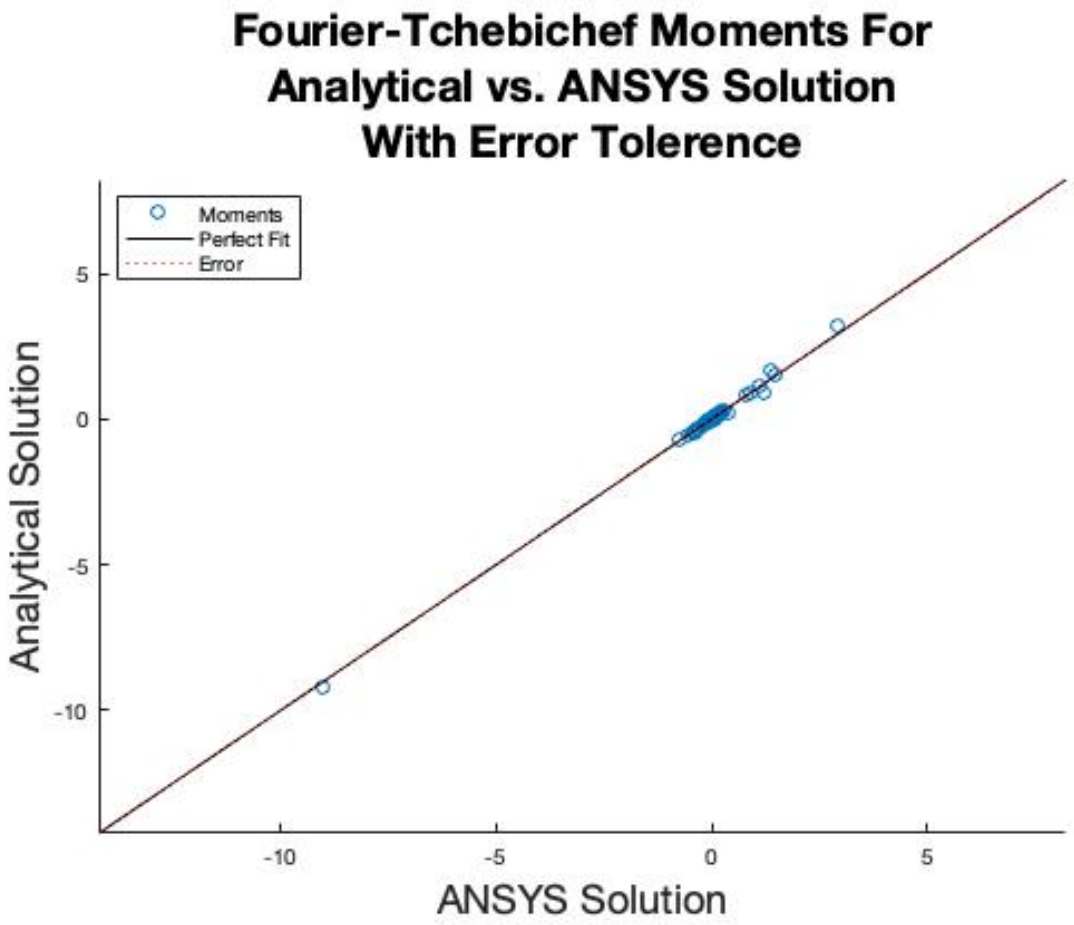

Figure 3.38: Fourier-Tchebichef moments for the ANSYS solution plotted in the x-axis vs the analytical solution's moments in the y-axis. Red dotted lines show the error tolerance for validation given by EQ.3.101 however the error is too small to be seen clearly. The solid black line represents the desired relation of moments for 2 data set with exactly the same shape.

Similar analysis is completed for both the fixed and mirror boundary SPAM solutions. The results for the fixed case simulated with Hoover's temperature evolution are shown in Fig.3.39. These moments show good agreement with little deviation from the centre line however they are not as tightly packed as the FEM moments. This therefore gives a simple visual indicator that the full 2D data result for the FEM simulations are closer to the analytical solution than the full data for the fixed SPAM simulation. The mirror boundary results with Hoover's temperature evolution are also analysed and shown in Fig.3.40. The results are far more similar to those of the fixed results however it can be seen that some of the moments lie closer to the centre line, demonstrating better agreement of the data.

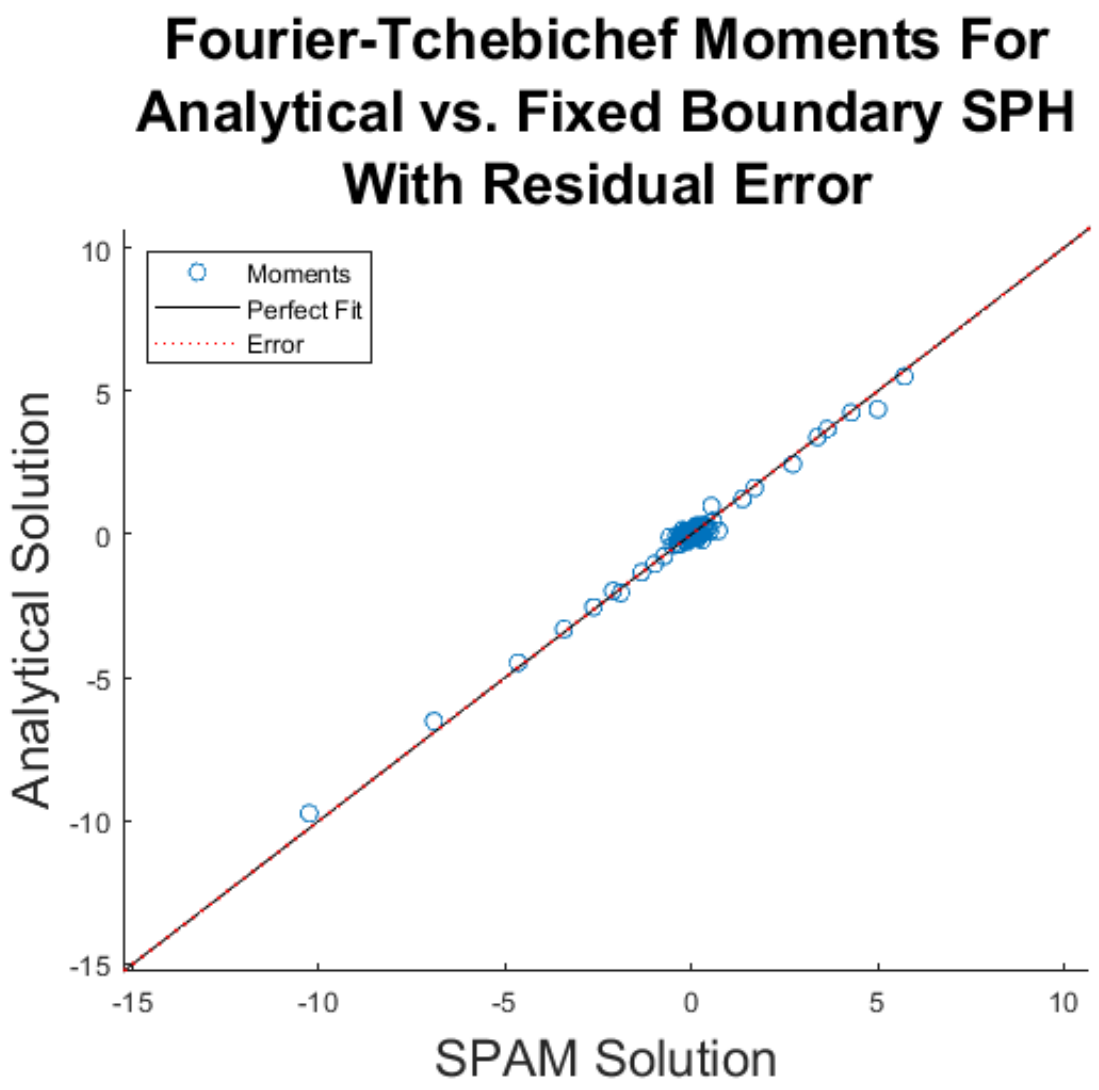

Figure 3.39: Fourier-Tchebichef moments for the SPAM solution with fixed boundaries completed with Hoover's temperature evolution plotted in the x-axis vs the analytical solution's moments in the y-axis. Red dotted lines show the error tolerance for validation given by EQ.3.101 however the error is too small to be seen clearly. The solid black line represents the desired relation of moments for 2 data set with exactly the same shape.

It is important to note here the restrictions of validation by this methodology. Firstly a rejection from this result does not guarantee that acceptance cannot be achieved for the same data with the inclusion of higher order terms. Similarly acceptance by this result does not guarantee the similarity two pieces of data to within the given error bounds, only the shape of that data described up to the given order. The inclusion of higher order terms allows for the description of finer detail within the data but greatly increases computational cost. Questions should also be raised about the use of residuals (calculated in the data space), used as errors in the moment space.

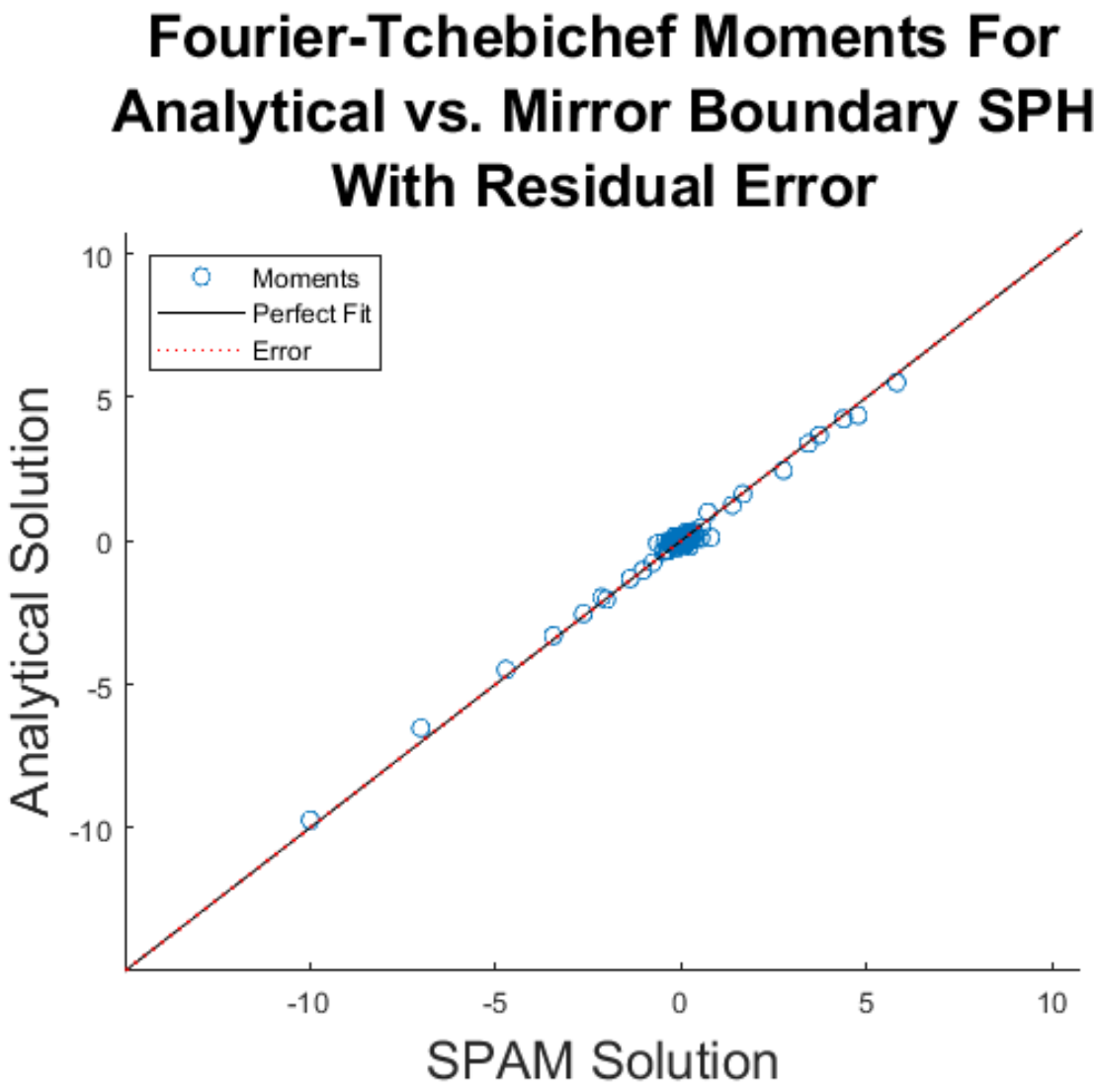

Figure 3.40: Fourier-Tchebichef moments for the SPAM solution with mirror boundaries completed with Hoover's temperature evolution plotted in the x-axis vs the analytical solution's moments in the y-axis. Red dotted lines show the error tolerance for validation given by EQ.3.101 however the error is too small to be seen clearly. The solid black line represents the desired relation of moments for 2 data set with exactly the same shape.

3.5.11 Conclusions

The work presented within this chapter established a few important issues of consideration for any SPAM simulation of nuclear fuel. The first of these is boundary conditions. Mirror boundaries, although more complex are shown by far to be superior to fixed particle boundaries. The second important consideration must be given to the formulation of the SPAM thermal evolution. It is shown that with proper consideration of both corrective methods such as artificial terms and correction factors become less important or beneficial.

Despite this, the results of this chapter suggest that further improvements to the SPAM results are

required for them to reach the accuracy of FEM modelling, the current standard of FPCs. The next chapter will explore therefore if the underlying particle arrangement structure can reduce the remaining errors in thermal simulations with SPAM. Particle structure becomes more important with the circular geometry of fuel pins. With the errors currently demonstrated, any SPAM simulation used for fuel licensing codes would have to show a worthy benefit in model complexity to justify the use of SPAM over FEM.

The results given here demonstrate that there is a difference in accuracy between the various methods of temperature evolution proposed in the literature. Not explored here are more complicated corrective methods such as the use of 'symmetric' SPAM [126] which has been applied to graded structures. Further testing is needed to confirm the superiority of Hoover's evolution for these more complex methods however initial tests are promising and indicate no direct need for further corrections in order to converge.

Chapter 4

Analysis of Annular Particle Arrangements for Solid SPAM

4.1 Introduction

Smoothed particle methods are often referred to as 'mesh-free' methods. It is perfectly reasonable however to consider the particle point configuration within SPAM as a form of Lagrangian mesh. Work has also been done to study SPAM with Eulerian Particle arrangements [113]. Within this work we will adopt the conventional terminology of particle arrangement and these arrangements throughout this chapter and the following are fixed and can therefore be considered Eulerian in nature. Smoothed particle methods are widely used within fluid applications, where greater deformation of particle arrangement is expected and thus the initial configuration has a less measurable effect on the final system configuration. In this work solids are considered therefore the final values calculated within each simulation become far more sensitive to the initial configuration, due to the expected smaller deformations from the initial state.

Straight edge geometry models are considered in the previous chapter, however when considering potential models of a fuel rod cylindrical geometry is required, particularly when considering elements within a fuel assembly such as the cladding which has annular geometry. The previous methods of using grids of particle points as the initial particle arrangement therefore become poor definitions for the desired shape. Considering this and the sensitivity of SPAM results on particle arrangements, this chapter is dedicated to investigating methods of particle structure generation for an annular problem and quantifying the effect on thermodynamic simulation results.

4.2 Radial Heat Flow Model

Consider the cladding on a nuclear fuel rod. The cladding material has an annular cross section. A simplified model of the cladding is presented in this chapter, a 2D slice through the cladding is therefore considered. The heat generated by the nuclear fuel pellet is simplified to a constant internal temperature T_i acting on the 2D annulus. Similarly the convection by the coolant is simplified to a lower constant outer temperature T_o. The internal radius of the considered annulus is noted A, the external radius as B. A visualisation of the model to be used is shown in Fig.4.1.

The model presented to complete the analysis in this section is chosen such that an analytical solution exists. For simplification, only the steady state solution is considered. The 'cladding' material is assumed to be asymmetric and infinite in the z axis such that only radial heat flow occurs.

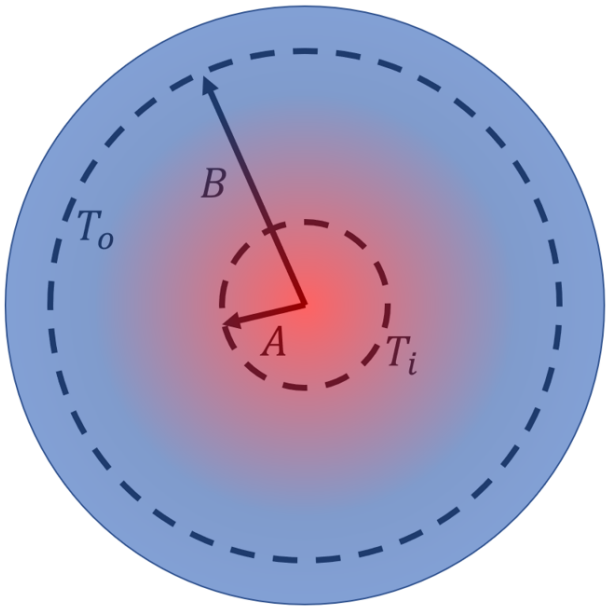

Figure 4.1: Visual representation of the analytical non-equilibrium test model being used. We assume a constant inner and outer temperature T_i, T_o and inner and outer radius A, B respectively

4.3 Analytical Solution

A starting point for determining the exact temperature distribution resulting from heat flow across an annulus, in the absence of heat sources, with inner and outer boundaries maintained at fixed T is the heat conduction equation in cylindrical co-ordinates:

$$\frac{1}{r}\frac{\partial}{\partial r}\left(r\frac{\partial T}{\partial r}\right)+\frac{1}{r^2}\frac{\partial^2 T}{\partial \theta^2}+\frac{\partial^2 T}{\partial z^2}=\frac{1}{D_T}\frac{\partial T}{\partial t} \tag{4.1}$$

A full derivation can be found in standard textbooks [114], but included here for completeness. The boundary conditions for this problem are given as:

$$\begin{aligned} T(A) &= T_i \\ T(B) &= T_o \end{aligned} \tag{4.2}$$

As stated the steady state solution is assumed, this gives:

$$\frac{\partial T}{\partial t}=0 \tag{4.3}$$

If the fuel rod is long compared to its diameter, we can treat it as infinite in z and hence:

$$\frac{\partial^2 T}{\partial z^2}=0 \tag{4.4}$$

Similarly the cladding is assumed to be axisymmetric which gives the simplification:

$$\frac{\partial^2 T}{\partial \theta^2} = 0 \tag{4.5}$$

With these simplifications the heat equation to be solved becomes:

$$\frac{1}{r}\frac{\partial}{\partial r}\left(r\frac{\partial T}{\partial r}\right) = 0 \tag{4.6}$$

Integrating this equation twice gives the general solution:

$$T(r) = C_2 + C_1 ln(r) \tag{4.7}$$

The constants of integration here are C_1, C_2. These can be determined from the boundary conditions Eq.4.2 giving:

$$C_1 = \frac{T_o - T_i}{ln\,(B/A)} \tag{4.8}$$

$$C_2 = \frac{T_i lnB - T_o lnA}{ln\,(B/A)} \tag{4.9}$$

The final steady state temperature distribution through an annulus is therefore:

$$T(r) = \frac{T_i ln(B/r) + T_o ln(r/A)}{ln(B/A)} \tag{4.10}$$

For the model explored in this work the internal temperature is set to $T_i = 2K$ and the external temperature at $T_o = 1K$. This is a simplification which ensures that the internal (fuel) temperature exceeds the external (coolant) temperature $T_i > T_o$. The internal and external radius are set to $A = 8$mm and $B = 20$mm.

4.4 SPAM Solution

All SPAM solutions to the model outlined in Fig.4.1 that are given throughout this chapter are completed with a time step of $dt = 0.05$s. Simulations are run for 20000 time steps with a target arrangement density of unity $\rho_0 = 1\text{g/mm}^3$, unit mass system particles $m_i = 1$g and thus a smoothing length of $H = 3$mm according to $H = 3\Delta_P$ as outlined within the methodology chapter.

Although the solution to this problem is assumed to be axisymetric, the particle arrangement used can cause variation in the angular co-ordinate ($\hat{\theta}$) direction. Two measures will therefore be used throughout this chapter. The first is simply the temperature interpolated along the slice $\theta = 0$. The second is the temperature interpolated along 12 different evenly spaced values of θ This set of interpolation points is shown in Fig.4.2. This increased number of points is used to show the spread of error across the SPAM system due to the particle arrangement.

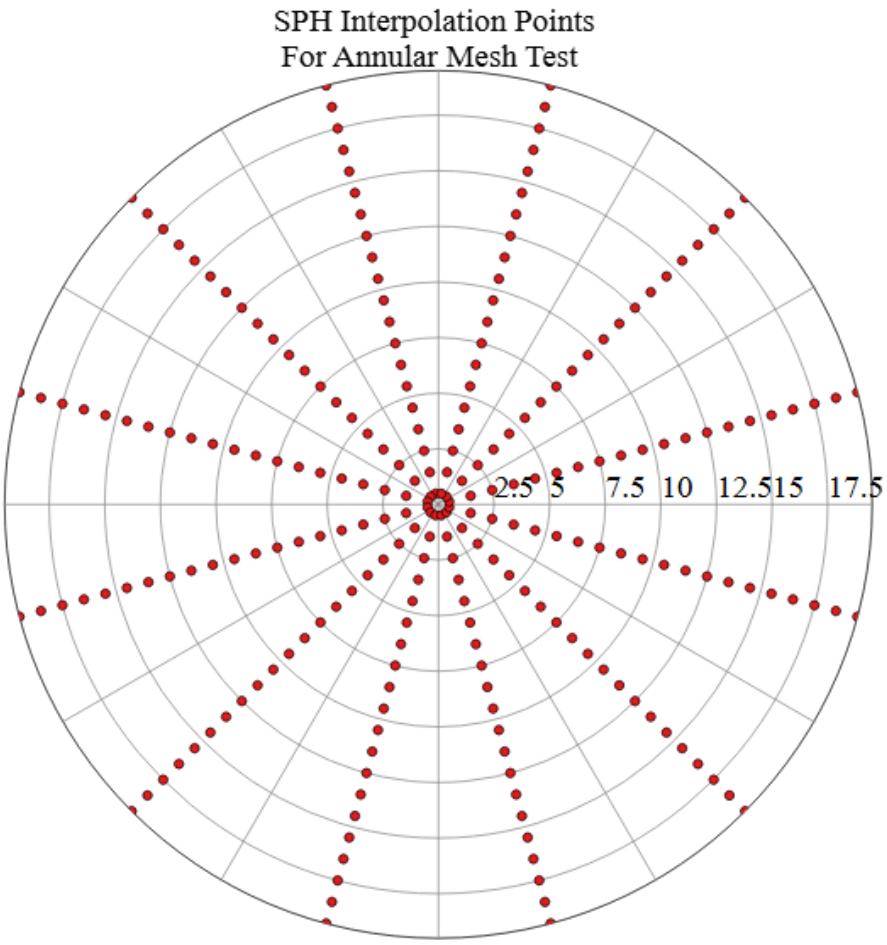

Figure 4.2: SPAM interpolation points used. 20 divisions are used in the radial co-ordinate r, 12 in the angle θ. The co-ordinates here extend out from zero in order to monitor how the density of particles is effected toward the centre however these points are truncated to 8mm$< r <$ 20mm for analysis.

All SPAM simulations are run with Hoover's temperature evolution given by Eq.3.66 with C given by Eq.3.70. This is chosen due to its demonstrated success within the last chapter. Simulations are run for both fixed and mirror boundary formulations however the generalised mirror boundaries require further conditions to deal adequately with curves. All particle points are static, only the temperature evolves not the position.

4.4.1 Curved General Shape Mirror Boundaries

As discussed in the previous chapter, the generalised mirror boundary conditions constructed for the simulations given within this work are based on sets of boundary points. System particles are reflected based on the closest boundary particle. Therefore in order to approach the limit of particles being reflected over boundary normals the number of boundary points must be increased. This becomes more important for a curved geometry where the system particles are not at common distances from the boundary. For this reason a large total number of $N_B = 879$ particles was used

to describe the boundaries. These are shown in Fig.4.3

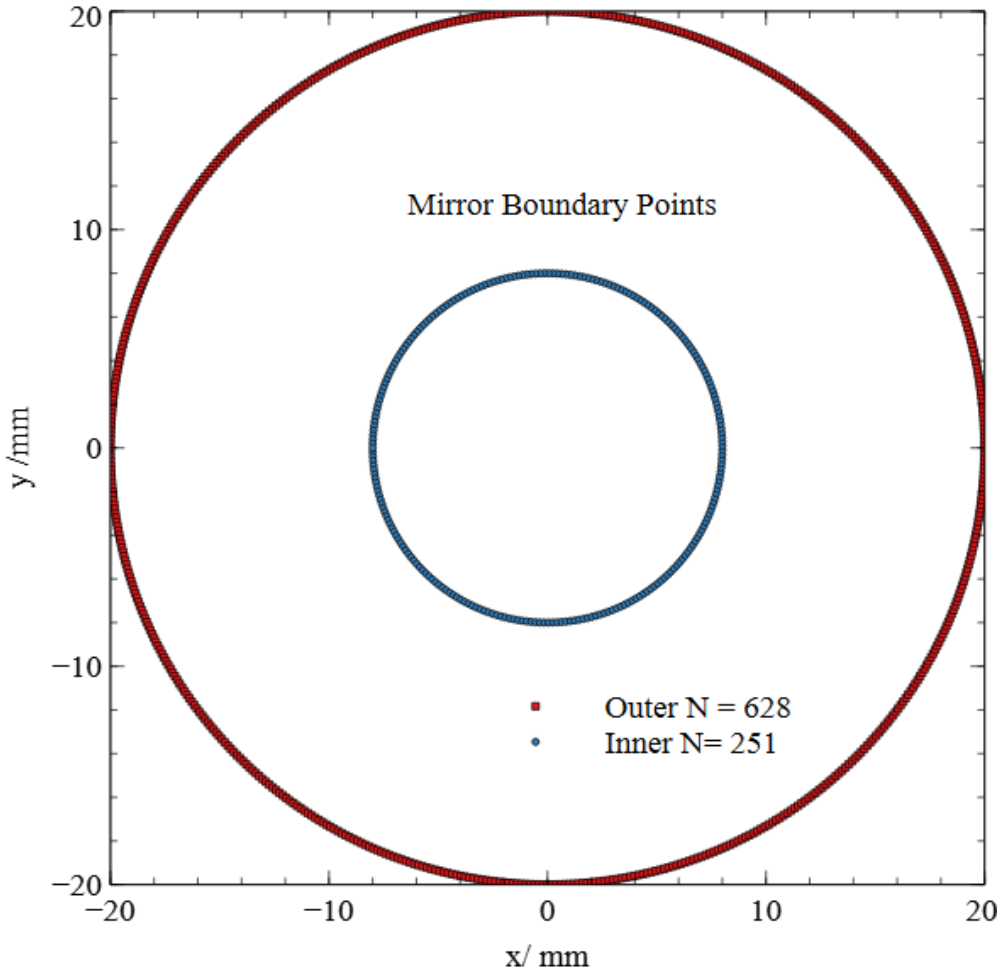

Figure 4.3: The boundary points used for mirror boundary simulations of constant temperature through an annulus. These points are only used for particle reflections.

There are two further important considerations for mirror boundaries to work within curved geometry. Both of these consideration are linked to corrections to the mirror particle masses. As particles are mirrored further away from the boundary they will occupy less space than the original particle from which they are reflected. This idea is illustrated by particles j and j' in Fig.4.4. The average spacing beyond the curved boundary becomes greater than the average system particle spacing of Δ_P. Methods have been proposed to deal with this problem based on using repulsive forces instead of virtual mirror particles [76]. Instead of this, a simple method of mass correction is proposed here. A corrective factor is calculated based on the curvature of the boundary and used to correct the mirrored particles mass to preserve the desired density ρ_0 beyond the boundary. For this consider a boundary with radius of curvature denoted r_c. The ratio of particle mass m_j to mirrored mass $M_{j'}$ is then given by the ratio of particle areas, which is given by the ratio of the circumference at each particle point:

$$\frac{m_j}{m_{j'}} = \frac{2\pi(r_c - R)}{2\pi(r_c + R)} \tag{4.11}$$

where R denotes the distance between the system and boundary particle. Considering this relation leads to the mass curvature correction M_{curv}:

$$M_{curv} = \frac{r_c + R}{r_c - R} \tag{4.12}$$

The final modification is that the curvature for the inner boundary is given as negative, this leads to $M_{curv} < 1$ which reduces the mass for reflection over the opposite direction of curvature. Although not completed within this work for extremely complex boundary shapes it may be possible to estimate the local boundary curvature simple from the boundary particles provided without needing to prescribe it initially as with these simulations.

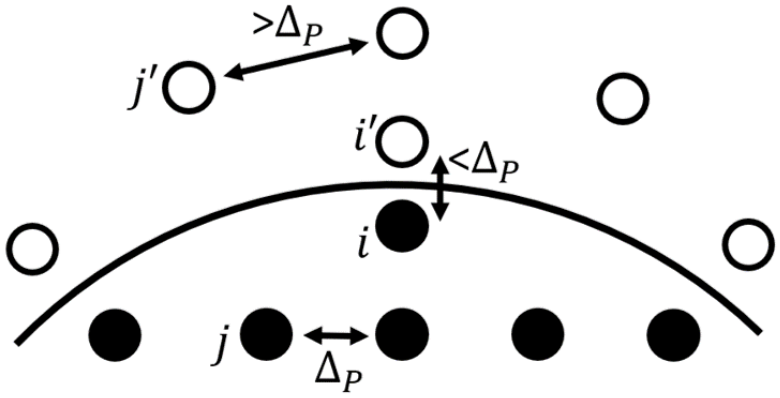

Figure 4.4: Interior particles (shaded) and their mirror image reflections (open circles) across a circular boundary. The effect on particle spacing is shown.

The second mass correction is due to a particle within the range $R < \Delta_P/2$ of the boundary particles. This case is illustrated by particles i and i' in Fig.4.4. As can be seen this leads to too little space being provided for the occupying mass of particles. To correct for this we consider the new space occupied by the two reflected particles in the direction of the boundary normal. On the opposite side of the particle to the boundary (the interior) the spacing Δ_P is preserved. On the boundary side (the exterior) a spacing $2R$ exists. This is compared to standard particle mass spacing for two particles:

$$\frac{2m_i}{m_i + m_{i'}} = \frac{2\Delta_P}{\Delta_P + 2R} \tag{4.13}$$

This rearranges to give the mass closeness correction M_{close}:

$$M_{close} = \frac{2R}{\Delta_P} \tag{4.14}$$

Therefore we have the mirror particle mass given by:

$$m_{i'} = \begin{cases} m_i M_{curv} M_{close} & if \quad R < \Delta_P/2 \\ m_i M_{curv} & otherwise \end{cases} \tag{4.15}$$

4.5 Construction of Particle Arrangement

The simplest methods for initial construction used so far in this work have been regular geometric arrangements. Two examples of this can be seen in Fig.4.5. Both the square and triangular lattices can be used to infinitely tile $2D$ space with perfect uniform particle density and spacing and given a starting point the algorithms for generating such lattices are trivial. The use of such lattices to fit irregular boundary shapes such as curves can be insufficient and cause drops in density due to gaps in the particles along the boundary. However by using a finer particle arrangement you can reduce such errors at the expense of increased CPU and memory requirements.

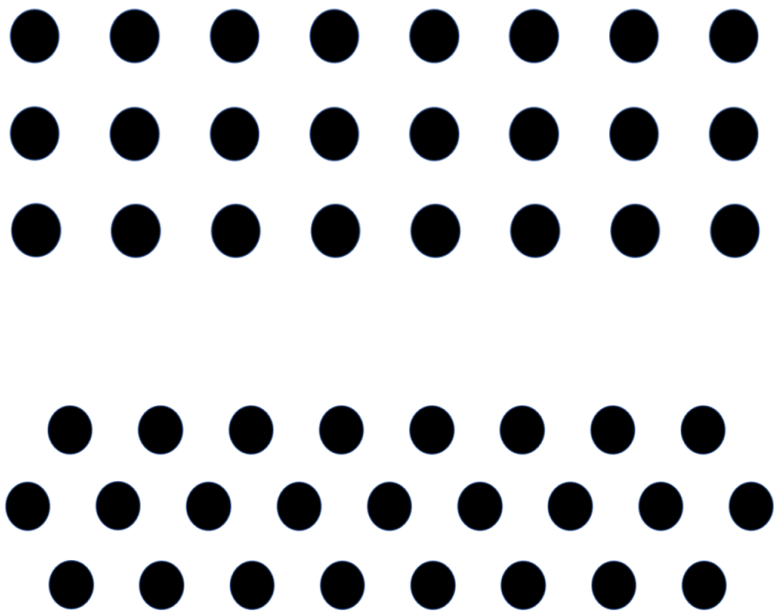

Figure 4.5: Two examples of uniform density lattices which can be infinitely tiled. Top the square lattice, bottom the triangular lattice

Special consideration has to be given to the density in the case of the triangular particle arrangement however. The particle spacing may be assumed as $\Delta_P = 1\text{mm}$ for both lattices. However this causes the density of the triangular lattice to be higher than desired at $\rho_0 \approx 1.15\text{g/mm}^3$ as shown. This can be corrected by modifying the particle spacing.

The unit density particle spacing can be calculated from the unit cell shown in Fig.4.6. The density for this lattice is calculated as:

$$\rho = \frac{2}{\sqrt{3}\Delta x_p^2} \tag{4.16}$$

The correct spacing for unit density is therefore $\Delta x_p = \sqrt{2}/\sqrt[4]{3}$. This produces $\rho_0 = 1\text{g/mm}^3$ however this larger particle spacing may cause effects on the accuracy of the SPAM temperature algorithms as will be shown in the next section.

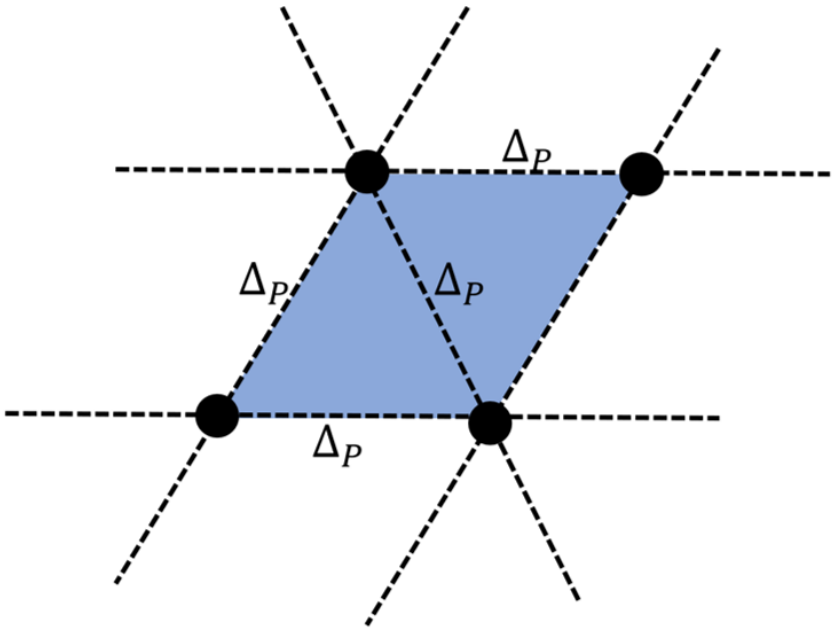

Figure 4.6: The unit cell for the triangular lattice. Each particle included is on a vertex between 4 cells and thus the cell is occupied by only one particle in total.

One final construction technique that is used is concentric rings of particles. The rings are spaced evenly along the radial axis in divisions of the desired particle spacing $\Delta_P = 1\text{mm}$. The number of particles N_r placed on each equal radius r ring is calculated based on the area of the annulus it creates:

$$N_r = 2\pi r \Delta_P \tag{4.17}$$

4.6 Particle Arrangement Relaxation

For complex geometries such as curved geometry the use of square and triangular lattices may be insufficient to evenly tile the space. One method of particle arrangement creation for such shapes is to use relaxation. This begins from some initial construction, which can be ordered such as those depicted in Fig.4.5, however they can also be some random particle distribution. Relaxation of these particle arrangements is then achieved by solving the SPAM equation of motion often in conjunction with special forces designed to steer the system to the desired particle arrangement. Such a method was outlined by Hoover [54] to create a variety of particle arrangements including a 2D tapered bar geometry for tensile test simulations. Since then alternative methods have been proposed which have improved results, key among these is the particle packing algorithm [127]. For the case of Lagrangian meshes the method of particle shifting has been proposed [128] which actively shifts particle positions during the simulation to obtain a more optimal structure. For this work we have chosen to further explore the methods proposed by Hoover in order to demonstrate the effects of particle disorder. The optimal solution reached within this work agrees with those derived through the use of the particle packing algorithm. Hoover's method is therefore sufficient to study the required particle arrangements needed for the study of nuclear fuel rods.

4.6.1 Density Dependence

The key feature of the produced particle arrangement is the particle density. To achieve some desired density ρ_0 within a complex geometry the starting particle configuration can be evolved with density-dependent forces which accelerate each particle toward the desired ρ_0. For this work we use the simple density-dependent forces derived from the embedded atom potential suggested by Hoover [54]:

$$\Phi_{density} = \frac{m_i B_0}{2\rho_0} \sum_i \left[\left(\frac{\rho_i}{\rho_0} \right) - 1 \right]^2 \tag{4.18}$$

where B_0 is the bulk modulus derived from the equation of state at ρ_0. This gives the particle acceleration as:

$$\ddot{r}_i = \frac{m_i B_0}{\rho_0^2} \sum_j \left(2 - \frac{\rho_i}{\rho_0} - \frac{\rho_j}{\rho_0} \right) \nabla_i W_{ij} \tag{4.19}$$

4.6.2 Elastic Boundaries

In order to enforce the required geometry on the particles boundary conditions must be employed. The simplest choice, used in this work, is elastic boundaries. These is defined by the reversal of particle velocities acting at a normal to the boundary as the particle contacts the boundary.

To implement elastic boundaries within the SPAM code it helps to first consider the effect of the time step. After each time step the particle positions are incremented by some unknown amount defined for each particle by:

$$\Delta r_i = dt \cdot v_i \tag{4.20}$$

Considering this we know that the chance of the particle intersecting the boundary exactly at any time step is effectively zero. Instead we therefore employ a check for particles exceeding the boundary after each time step and simply revert them to their previous position before reversing the particle velocity which acts normal to the boundary. This means momentum is not perfectly conserved and can cause particle overlapping, to reduce these effects a small enough time step must chosen. The effect of overlapping is also mitigated by the short range core potential employed.

4.6.3 Damped Particle Motion

For relaxation of the particle arrangement to occur the particle motion must be damped in order to remove the kinetic energy. The damping force used is based on simple Brownian motion, in which the deceleration of the particle is proportional to the particle velocity:

$$F_{i,damp} = -\frac{m_i v_i}{\tau} \tag{4.21}$$

Here τ controls the magnitude of the damping force with the particle deceleration increasing with decreasing τ.

4.6.4 Core Forces

Uniform particle density interpolated *at* the particles does not guarantee uniform density at *all* possible interpolation points within the sample space. To ensure this we not only need uniform particle *density* but also uniform particle *spacing*. This ensures a smoothed continuum uniform density throughout the sample.

The method employed in this work to achieve this is the addition of another potential, called the core potential, again used by Hoover [54]. This takes the general form:

$$\Phi_{core} = \sum_j \epsilon \left[1 - \left(\frac{r_{ij}^2}{\sigma^2}\right)\right]^4 ; |r_{ij}| < \sigma \tag{4.22}$$

Here ϵ represents the energy at zero separation, σ the distance from which the force begins to act between two particles. This gives a force acting on particle i as:

$$m_i \ddot{r}_i = \frac{8\epsilon}{\sigma^2} \sum_j r_{ij} \left[1 - \left(\frac{r_{ij}^2}{\sigma^2}\right)\right]^3 \tag{4.23}$$

4.6.5 Boundary Density Correction

The use of elastic boundaries means that calculation of density near to the boundary is deficient in particles beyond the boundary and therefore the density calculated here is significantly lower than ρ for the desired final particle configuration. To combat this issue we simply employ 0^{th} order corrections to the density calculation as outlined by [71]:

$$\rho_i = \frac{\sum_j m_j W_{ij}}{\sum_j \frac{m_j}{\rho_j} W_{ij}} \tag{4.24}$$

4.6.6 Equilibriated Particle Arrangement

For each of the starting types of particle arrangement given in the results below both 'static' (meaning the initial configuration) and relaxed configurations will be be explored. All particle arrangement relaxation is completed with a damping force defined by:

$$\tau = \frac{t_{total}}{10t} : \tag{4.25}$$

where t is the simulation time-step. We also artificially restrict the initial damping force from being too small by requiring $\tau > 0.5$. This means that the damping force increases with time and thus the particle motion is slowly reduced allowing a local equilibrium position to be found.

The core force used is restricted to act only at a distance less than $\sigma = 0.7$mm with a prefactor of $\epsilon = 1$. This is chosen to prevent particle overlaps at short distances whilst having a minimal effect on the relaxation for particles at or approaching the desired spacing. The density-dependent forces are chosen to achieve uniform density with $\rho_0 = 1\text{g/mm}^3$ and a bulk modulus $B_0 = 1\text{gmm}^{-}1\text{s}^{-}2$.

4.7 Square Particle Arrangement

The configuration of the fixed particle arrangement created from the square lattice and relaxed square lattice can be seen in Fig.4.7. As discussed the boundary is poorly defined by the square shape however the values used for relaxation create a large amount of particle disorder and spaces which leads to a lack of consistency in the density profile, although the boundary has better definition. A range of values was attempted to achieve desirable relaxation, however it is speculated that an improvement on the elastic boundary condition may be able to help this in future tests.

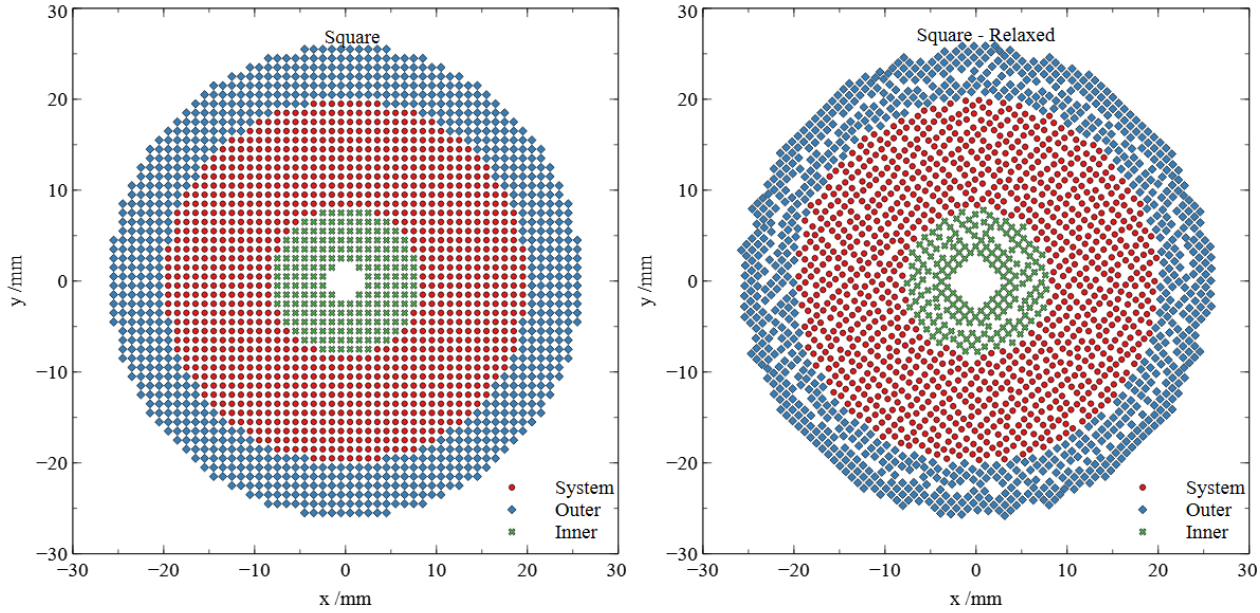

Figure 4.7: Annular particle arrangement geometry from square lattice. The image on the right was created by relaxing an initial system of particles towards a uniform density. The inner and outer fixed particles are shown up to range $2H$

The final steady state temperature profile for these two particle arrangements is shown in Fig.4.8. Immediately it is apparent that the static square lattice gives more consistency than the relaxed square lattice due to the consistent density. Neither case agrees with the analytical solution but the the regular lattice is a better approximation than the relaxed case. The values are seen to spread out for the relaxed case. This is caused by the disorder of the particle positions which causes the density to vary more.

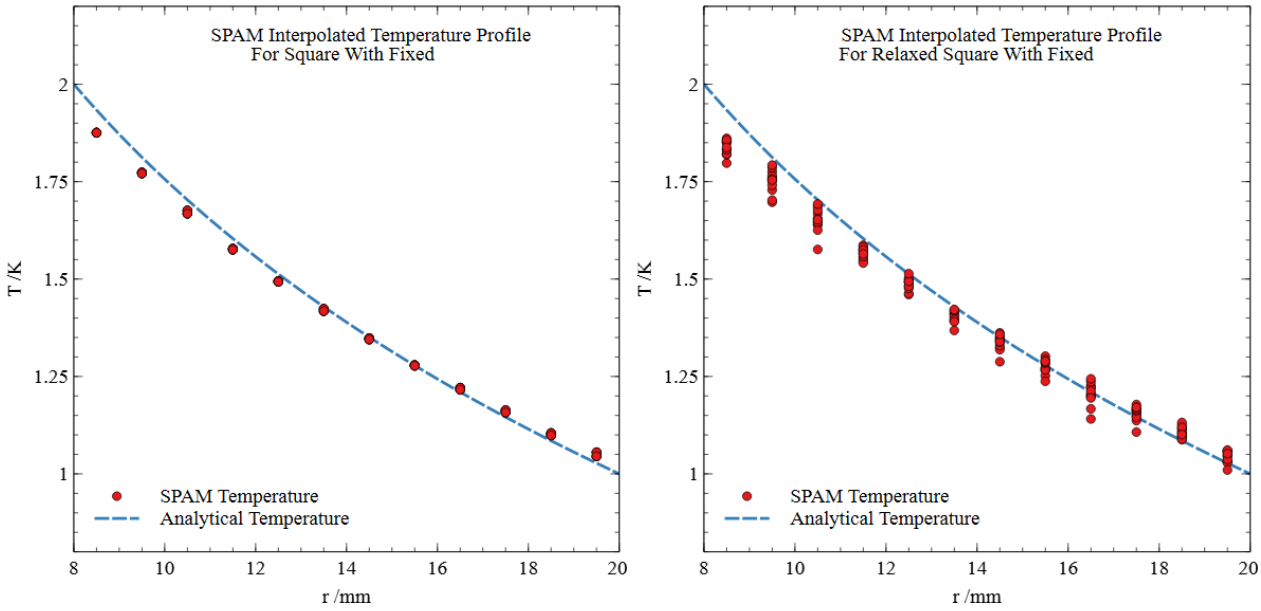

Figure 4.8: The total set of interpolated temperatures for the SPAM solution to the radial heat flow problem in Fig.4.1 with fixed boundaries. Left shows the square lattice results, right shows the relaxed square lattice results.

4.7.1 Square with Mirror Boundaries

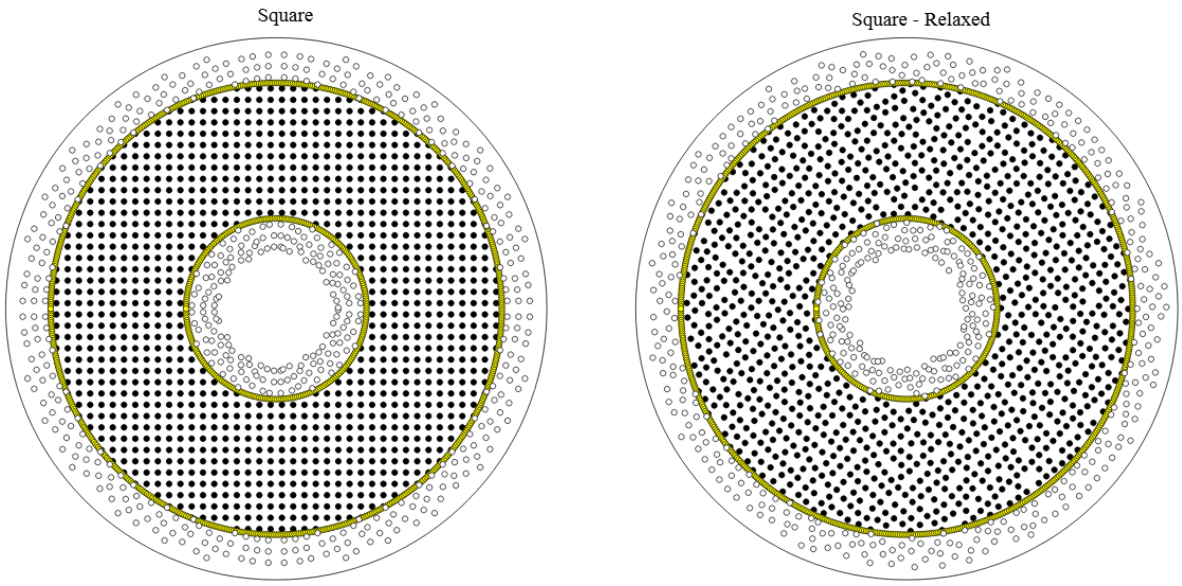

Figure 4.9: Mirror particles created from the square lattice. The right lattice was created by relaxing the square lattice towards a uniform density. The system particles are shown in black and solid and the mirror particles white and outlined. The boundary particles can be seen marked between these layers.

The system particle arrangements are the same for the mirror cases as for the fixed. The configuration of the mirrored ghost particles are shown in Fig.4.9. The spreading of particles as well as those too close to the boundary line can clearly be seen. The creation of mirror particles gives a better representation of the boundary than for the fixed boundary particle case.

The steady state temperature profiles for the mirror case are shown in Fig.4.10. Due to the loss of the regular lattice across the boundary for the static case, the spreading of temperatures occurs. Interestingly, despite the wider spread of results for the relaxed case, the average profile is in better agreement with the spread of error achieving the analytical values at both boundaries.

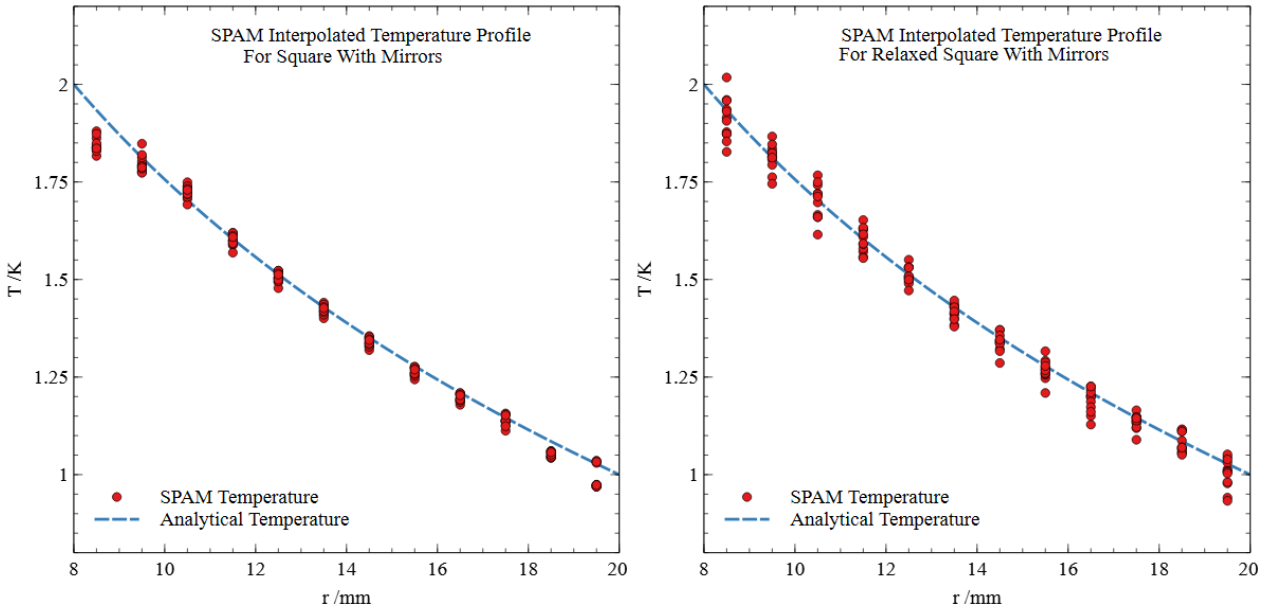

Figure 4.10: The total set of interpolated temperatures for the SPAM solution to the radial heat flow problem in Fig.4.1 with mirror boundaries. Left shows the square lattice results, right shows the relaxed square lattice results.

4.7.2 Square Particle Arrangement Results

The slice at $\theta = 0$ for each of the square particle arrangement simulations are presented in Fig.4.11. The density profile can be seen to oscillate around the desired value to a greater extent for the relaxed particle arrangements. This translates to the temperature values at these points along the slice deviating more from the analytical temperature profile. For this particle arrangement, the error improvements given by the mirror boundaries are not as evident as they were for the square particle arrangements presented in the previous chapter.

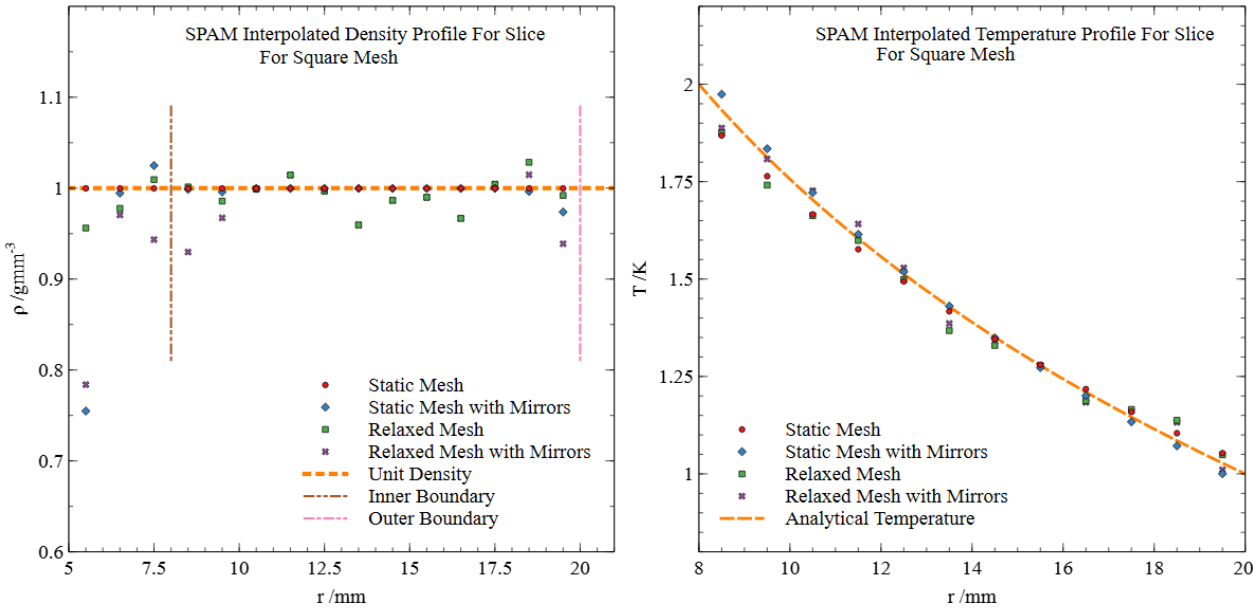

Figure 4.11: Results of the square lattice tests for the slice $\theta = 0$. Left shows comparison of the density profiles, right shows comparison of the temperature profiles.

4.8 Triangular Particle Arrangement

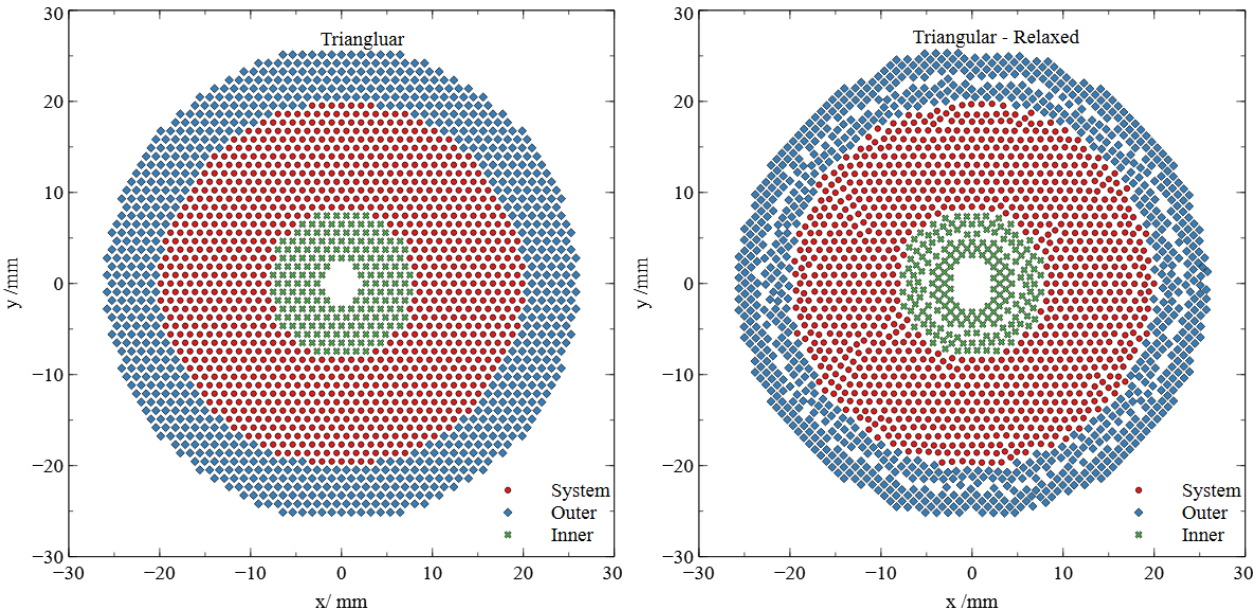

Figure 4.12: Annular particle arrangement geometry from triangular lattice. The right setup is created by relaxing an initial system of particles towards a uniform density. The inner and outer fixed particles are shown up to range $2H$

The fixed triangular particle arrangement, both static and relaxed are shown in Fig.4.12. The triangular particle arrangement is better able to represent the circular boundary. Again the formation of gaps in the relaxed particle arrangement can be seen as well as general particle disorder. It is likely that improvements on the elastic boundaries used, as well as a refinement of the control variables can reduce these gaps.

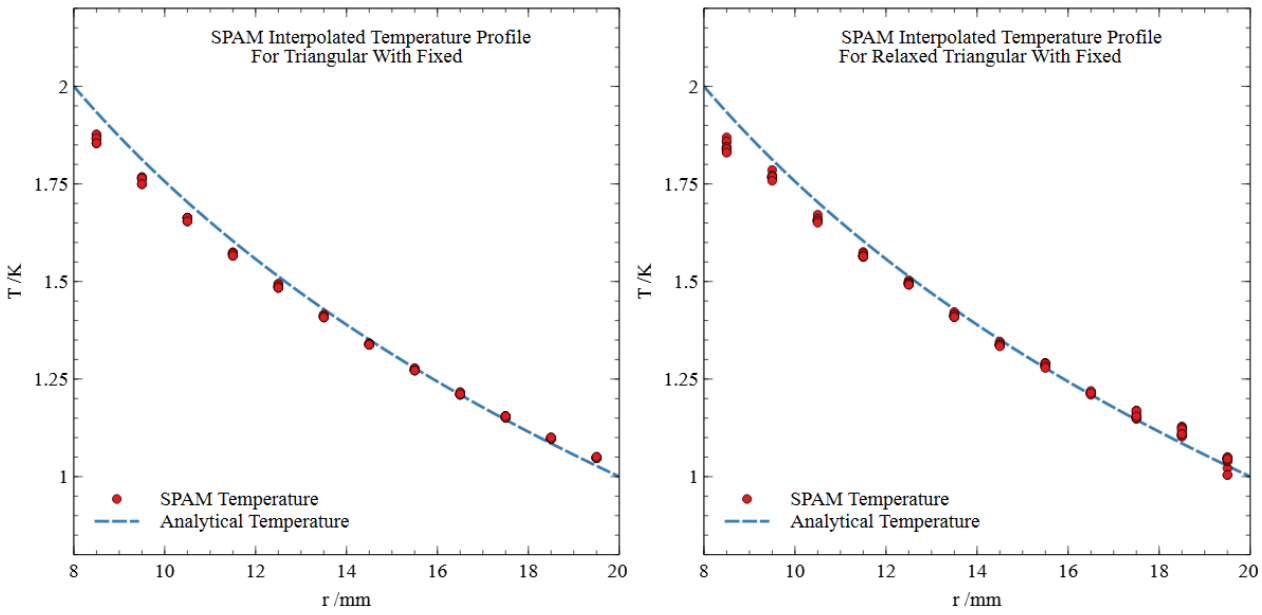

Figure 4.13: The total set of interpolated temperatures for the SPAM solution to the radial heat flow problem in Fig.4.1 with fixed boundaries. Left shows the triangular lattice results, right shows the relaxed triangular lattice results.

The results of these particle arrangements for the constant temperature boundary test are shown in Fig.4.13. The static case shows the same low spread as for the square case due to the well-defined density profile produced by the triangular lattice. The temperature close to the system boundaries diverges from the expected analytical profile. This is due to the boundary temperatures being interpolated differently than the values prescribed to the fixed particle *at* the boundary.

For the relaxed particle arrangement it is observed that very little spreading of interpolated temperatures occurs. This is due to the relaxed particle arrangement achieving a more consistent density. More spreading occurs close to the system boundary however. The interpolated values close to the boundary also suffer from error introduced by the use of fixed boundaries as for the static case.

4.8.1 Triangular with Mirror Boundaries

For an ideal particle arrangement the error introduced by the fixed boundaries should be reduced by the use of mirror boundaries. The resultant ghost particles produced by each particle configuration are shown in Fig.4.14. Both configurations are widely the same. It becomes clear that the greatest effect for relaxation for the triangular particle arrangement is concentrated on the boundary particle sets, leaving the system particles in very similar configurations.

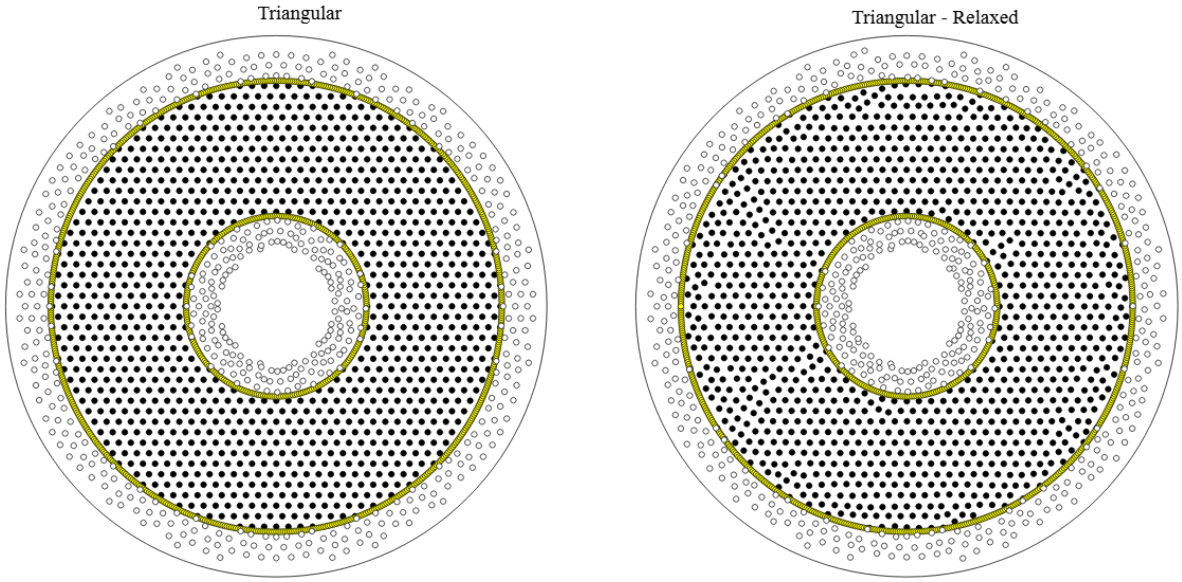

Figure 4.14: Mirror particles created from the triangular lattice. The right lattice was created by relaxing the triangular lattice towards a uniform density. The system particles are shown in black and solid and the mirror particles white and outlined. The boundary particles can be seen marked between these layers.

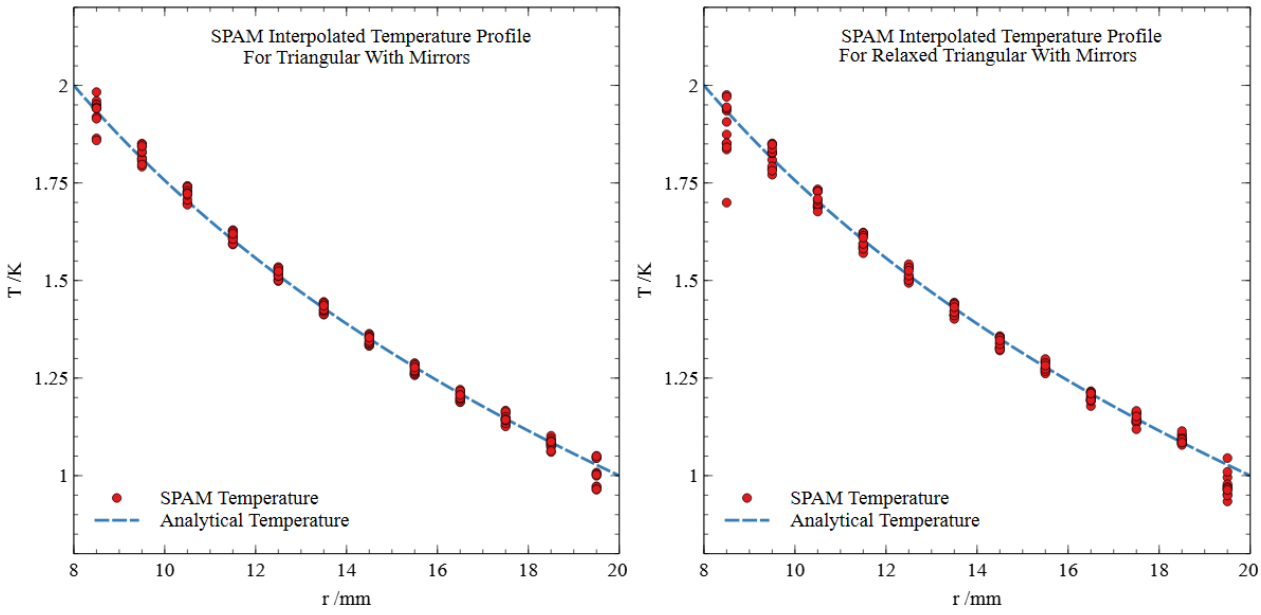

Figure 4.15: The total set of interpolated temperatures for the SPAM solution to the radial heat flow problem in Fig.4.1 with mirror boundaries. Left shows the triangular lattice results, right shows the relaxed triangular lattice results.

The temperature profiles for the resulting mirror test with the triangular particle arrangements is

shown in Fig.4.15. Again the spread of interpolated temperatures is small for both profiles, however it is noticeably larger than for the fixed case alone. This suggest more disorder in particle density is introduced by the mirror boundaries. Reinforcing this idea is the far greater interpolation spread close to the boundaries. This is most pronounced for the relaxed case which again shows that relaxation occurs more towards the outer edges of the particle arrangement.

The temperature deviation toward the boundary of the system that is seen for the fixed case is however removed for the mirror case, instead replaced by interpolation spreading around the analytical value. This reinforces the ideas given in the previous chapter showing the superiority of mirror particles for enforcing boundary values whilst highlighting the complex problem of curved geometry.

4.8.2 Triangular Particle Arrangement Results

Full comparison of the interpolated density and temperature profiles along the slice $\theta = 0$ are presented in Fig.4.16 for the triangular particle arrangements. The profiles suggest that the mirror boundaries are far superior at reducing boundary error in the temperature profile, even in the presence of density errors at the boundary .

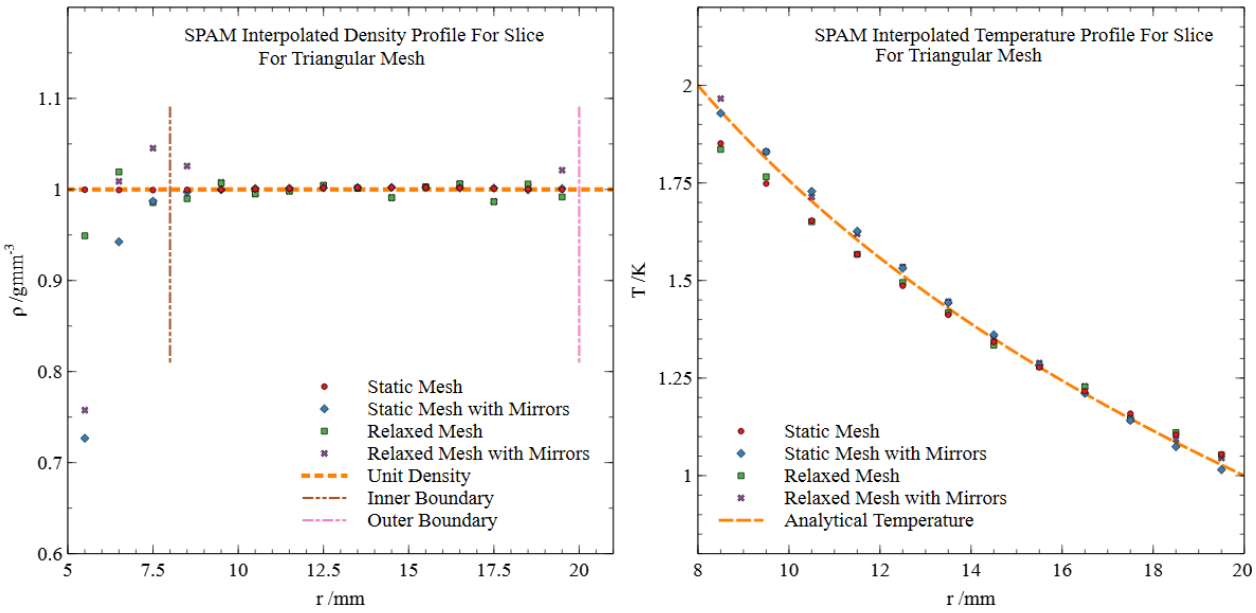

Figure 4.16: Results of the triangular lattice tests for the slice $\theta = 0$. Left shows comparison of the density profiles, right shows comparison of the temperature profiles.

4.9 Alternative Particle Arrangement Configurations

Considering the issues of the above particle arrangements two alternative particle arrangements are explored which seek to address the inefficiencies. Firstly a concentric particle arrangement is used in order to offer better boundary definition. As well as this, a configuration of random particles is relaxed to unit density $\rho_0 = 1\text{gmm}^{-}3$. The random particle arrangement is given a 5% lager number of particles to try and address the gaps seen forming in the relaxed square and triangular lattices due to boundary deficiencies with the elastic boundaries in relaxation.

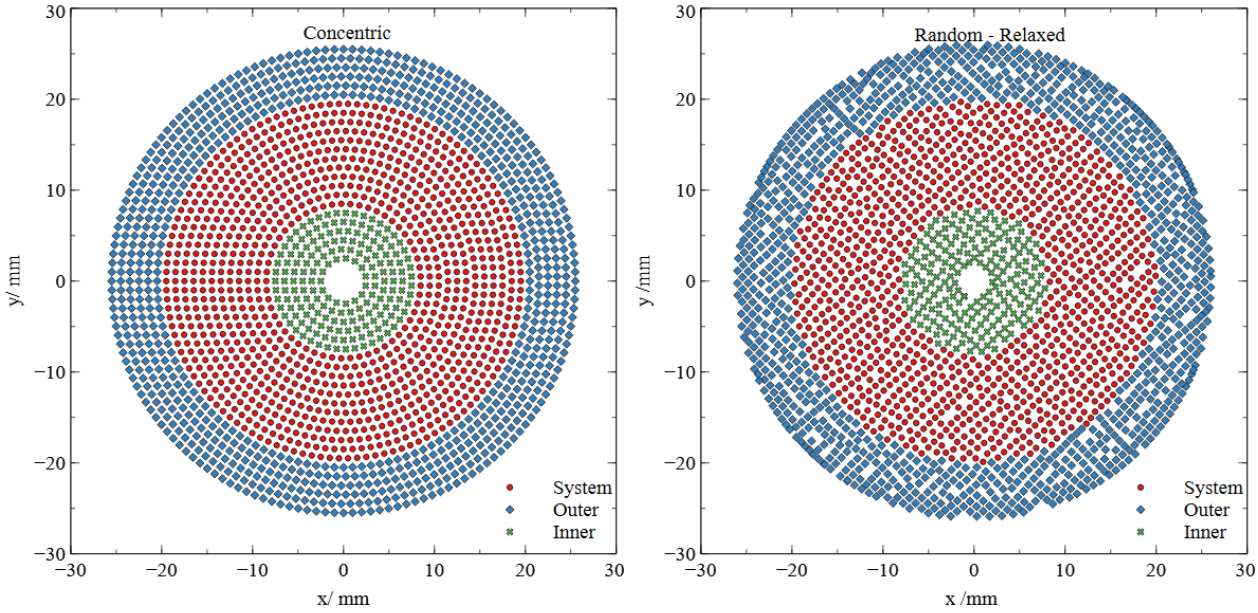

Figure 4.17: Annular particle arrangement geometry from: concentric rings of particles shown left, The right setup is created by relaxing an initial system of particles towards a uniform density. The inner and outer fixed particles are shown up to range $2H$

The alternative particle arrangements to be explored for the fixed case are shown in Fig.4.17. Both show excellent definition of the system boundaries when compared to the square and triangular case. The interpolated temperature profiles produced by each particle arrangement for fixed boundaries is shown in Fig.4.18. It can be seen that the concentric particle arrangement shows no spreading of interpolated values due to its excellent consistency for particle configuration. Still the effects of the error introduced by fixed boundaries shows the discrepancy of the temperature profile from the analytical solution.

Again the random particle arrangement reinforces this offset of interpolated temperatures at the system boundary due to the fixed particles. The profile shows more spreading of interpolated values and disorder due to the configuration of the particles, however this is not as extreme as in the previous cases for relaxed particle arrangements. The ease of construction by relaxation of random particles means that this option, if refined, may therefore still be a promising way of producing SPAM particle arrangements.

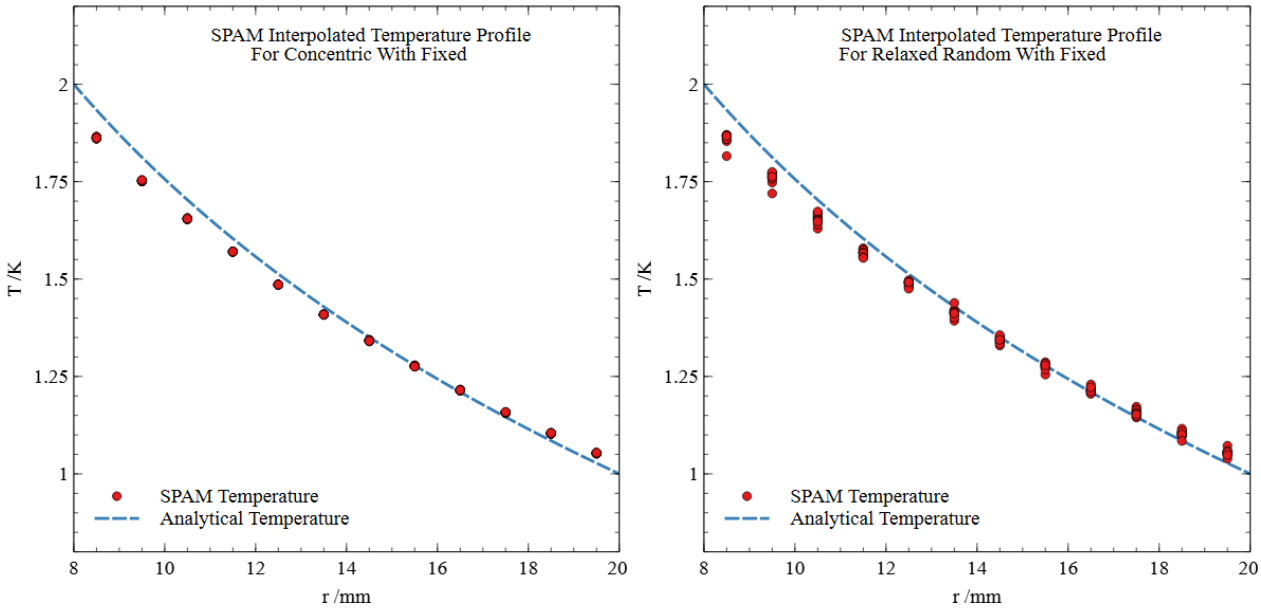

Figure 4.18: The total set of interpolated temperatures for the SPAM solution to the radial heat flow problem in Fig.4.1 with fixed boundaries. Left shows the concentric lattice results, right shows the relaxed random lattice results.

4.9.1 Alternatives with Mirror Boundaries

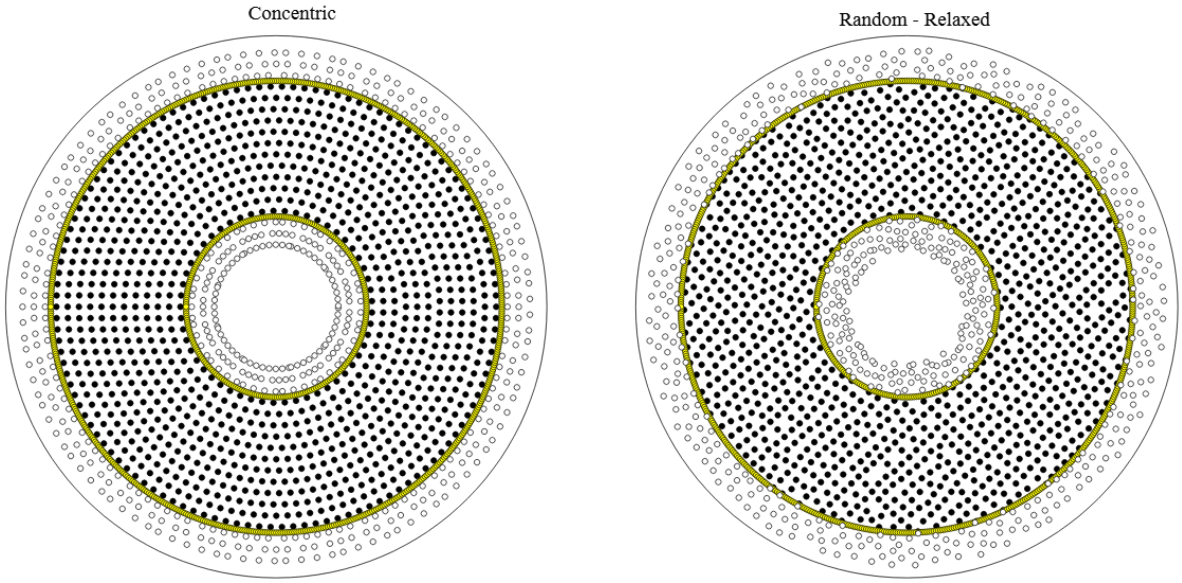

Figure 4.19: Mirror particles created from the concentric lattice shown left. Mirrors for the lattice which was created by relaxing the random lattice towards a uniform density shown right. The system particles are shown in black and solid and the mirror particles white and outlined. The boundary particles can be seen marked between these layers.

The configuration of ghost particles for the concentric and relaxed random particle arrangements are shown in Fig.4.19. The final temperature profiles produced by these alternative particle arrangements is shown in Fig.4.20. It can be seen that the concentric particle arrangement produces excellent agreement with the analytical results with the interpolated temperature values close to the boundary reproducing the expected result with minimal error due to spread for the outer boundary when compared with the other results.

The interpolated temperatures close to the boundary for the relaxed random case show significantly more spread of error, however the underlying analytical profile is reproduced. This suggests with better relaxation the random creation of particle arrangements could be a powerful tool.

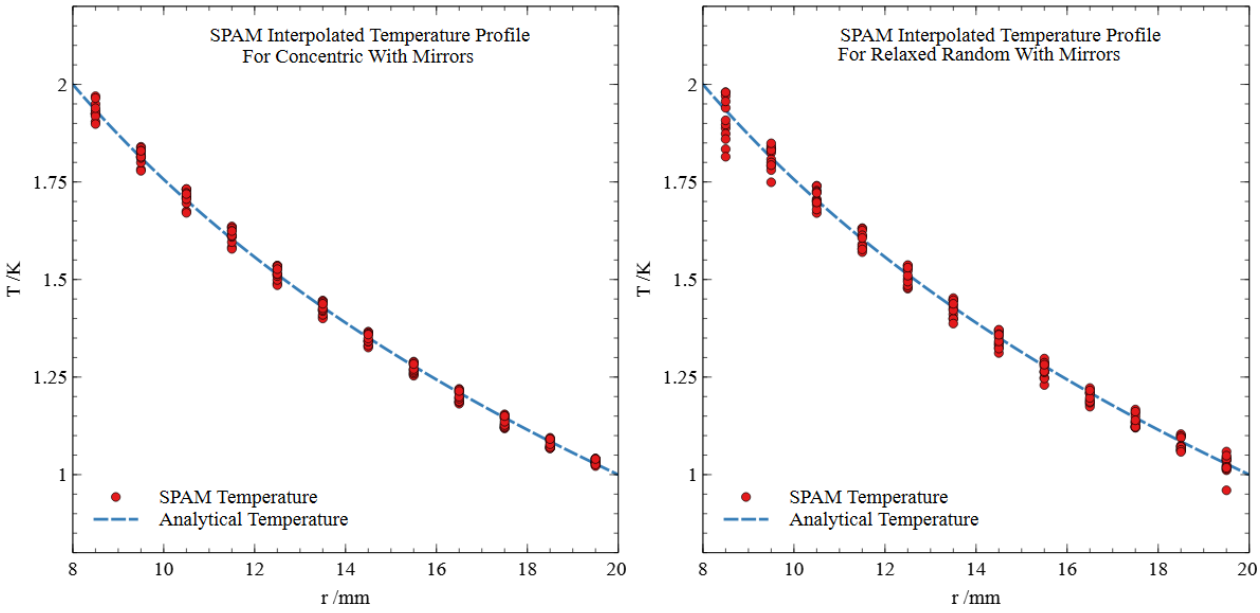

Figure 4.20: The total set of interpolated temperatures for the SPAM solution to the radial heat flow problem in Fig.4.1 with mirror boundaries. Left shows the concentric lattice results, right shows the relaxed random lattice results.

4.9.2 Random Mesh Results

The results for the interpolated slice at $\theta = 0$ through the system are given for the random particle arrangement construction. The static and relaxed particle arrangement results are included for the random configuration for completeness. The random results are given in Fig.4.21. Clearly the density profile for the static case shows that random particle placements are insufficient without relaxation. Interestingly the relaxed density is seen to deviate significantly from the desired profile however the temperature profile does not. This suggests it is consistency and disorder, not simply density that produces the errors seen throughout this section. That is to say uniform density with a systematically incurred error is still capable of reproducing the correct temperature profile.

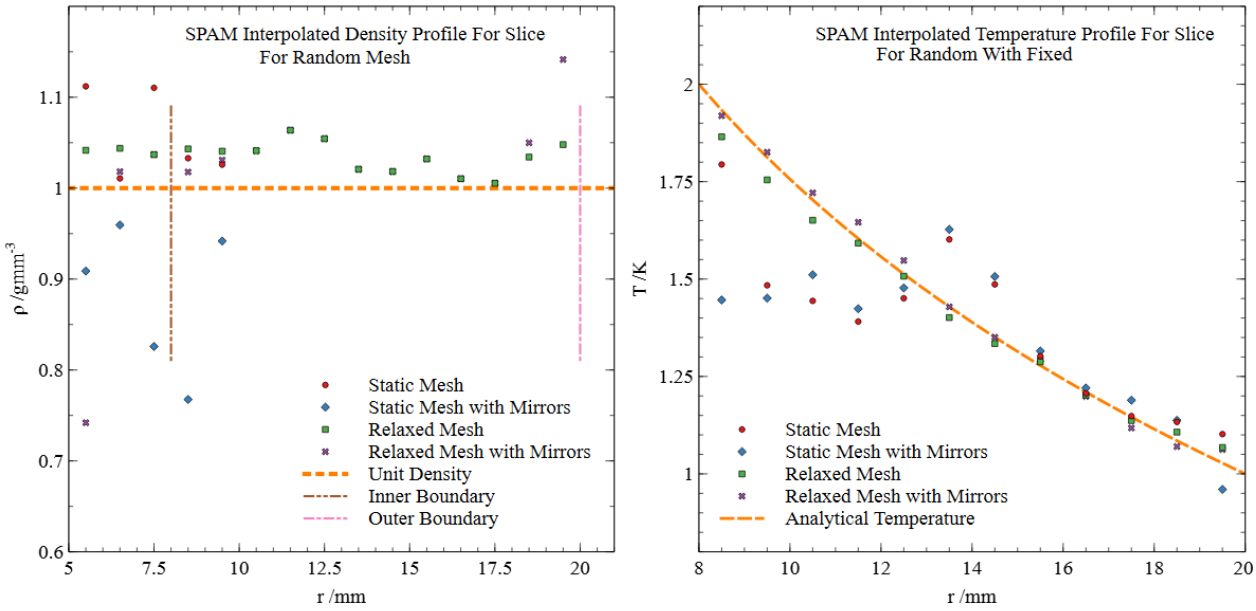

Figure 4.21: Results of the random lattice tests for the slice $\theta = 0$. Left shows comparison of the density profiles, right shows comparison of the temperature profiles.

4.9.3 Concentric Particle Arrangement Results

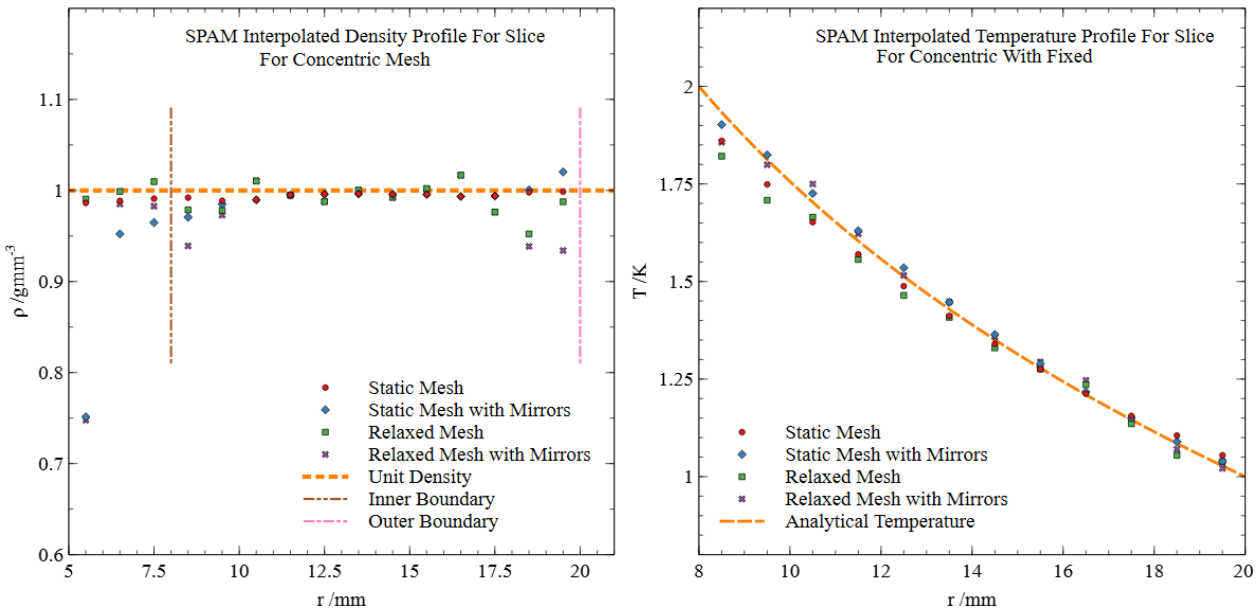

Figure 4.22: Results of the concentric lattice tests for the slice $\theta = 0$. Left shows comparison of the density profiles, right shows comparison of the temperature profiles.

Finally the results for the interpolated slice at $\theta = 0$ through the system are given for the concentric particle construction. The static and relaxed particle arrangement results are included again for

completeness. The concentric results are given in Fig.4.21. The relaxation for the concentric case is seen to incur more error than for the static particle construction. This reinforces the idea that particle order is of high importance for SPAM solid thermal simulation of this kind.

4.10 Particle Arrangement Error Comparison

The total errors for all the particle arrangements presented in this chapter are calculated using the residual error between the SPAM and analytical solutions given as:

$$u_T^2 = \frac{1}{N}\sum_{i}^{N}\left(T_{Analytical} - T_{SPAM}\right)^2 \tag{4.26}$$

The results of this error calculation are shown against the residual density error from $\rho_0 = 1\text{g/mm}^3$ in Fig.4.23. The error in the static random particle arrangement results are seen to clearly exceed those of any other particle arrangement a result that is not surprising, however the inclusion highlights that although disorder rather than density may be a better measure of error introduced, a clear effect can be seen for larger values.

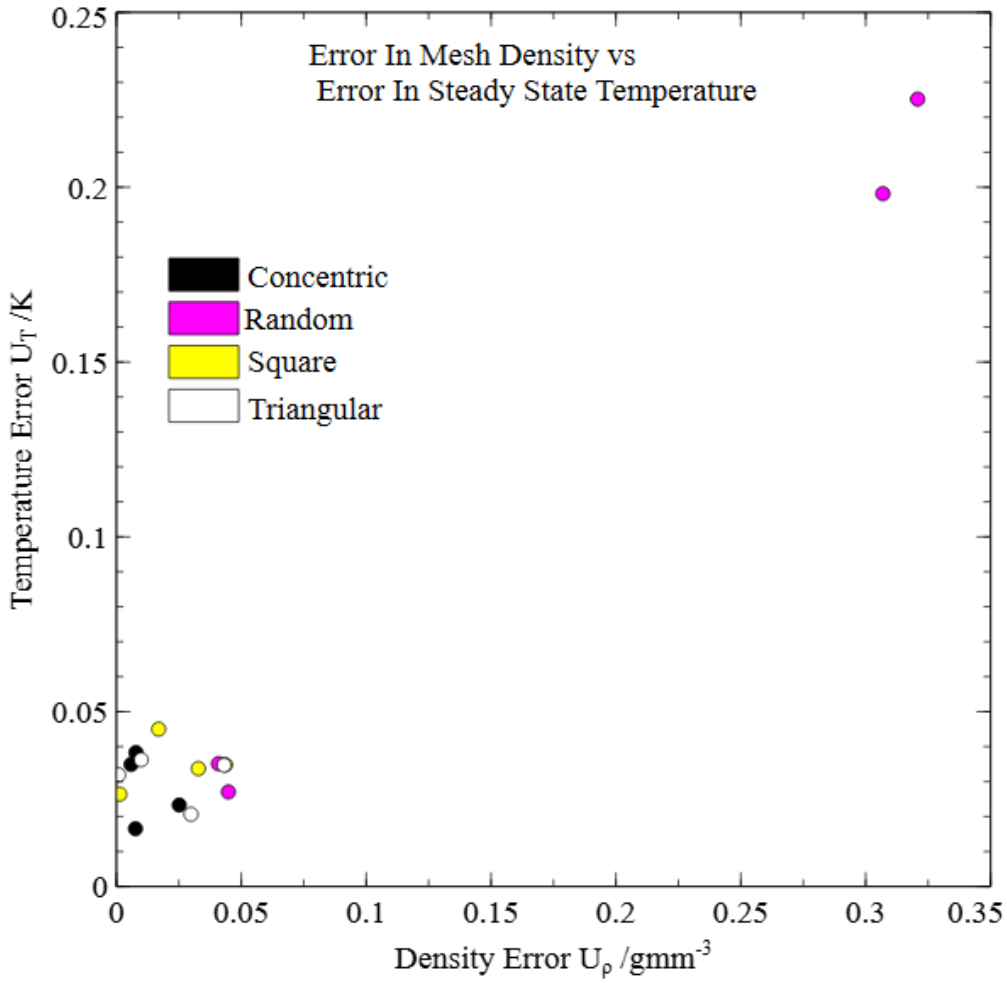

Figure 4.23: Comparison of the residual errors in the steady state temperature profile produced by each variation of particle arrangement configuration compared with the residual error in interpolated density

The results of the residual error calculation are given in Fig.4.24. The static random particle arrangement results are included, however they exceed the error bounds given on the graph. This comparison shows that the superiority of mirror boundary conditions is greatly diminished by the use of a poorly defined set of particle arrangement points. The static concentric and triangular particle arrangements are seen to be the superior choice for radial geometry.

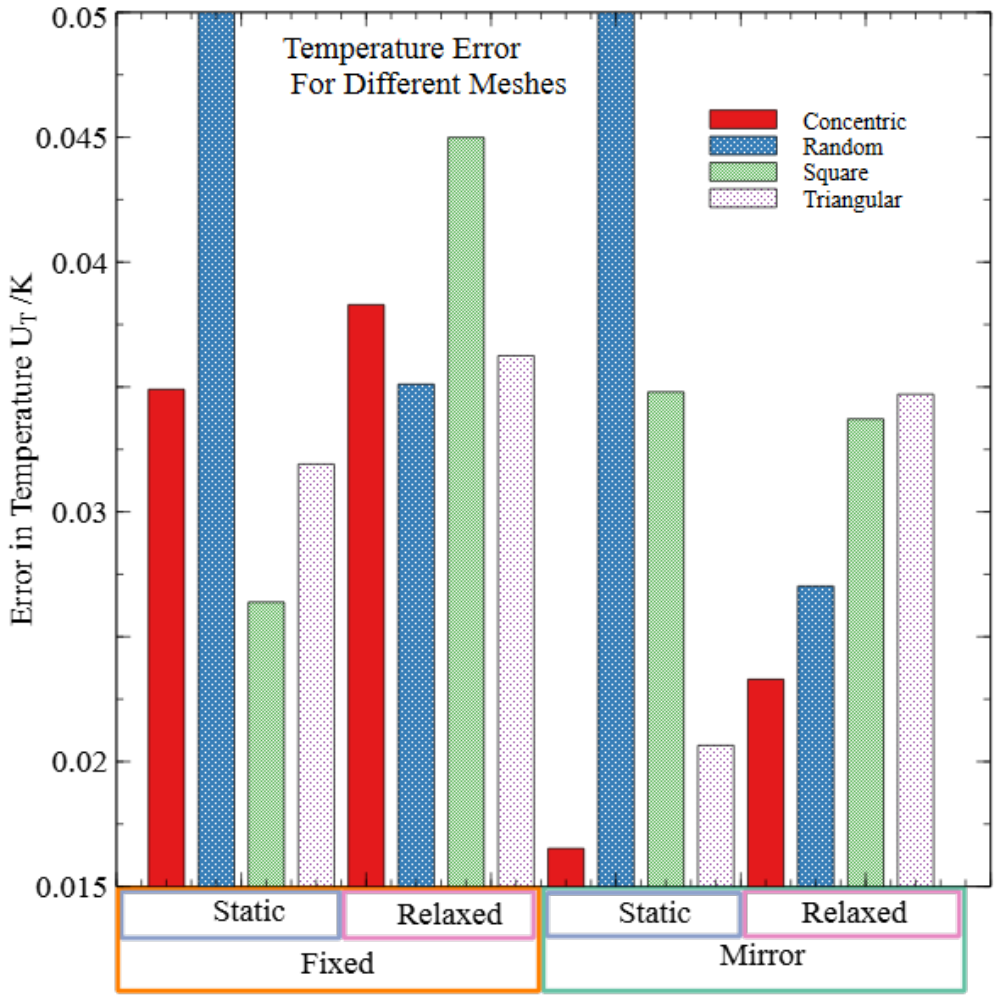

Figure 4.24: Comparison of the residual errors in the steady state temperature profile produced by each variation of particle arrangement configuration

4.11 Refinement of Particle Arrangement

The relations between smoothing length and interpolation error was explored in Sec.2.2.2. It can therefore be assumed that reduction of the smoothing length H will cause the simulation error to reduce. This should cause the simulation, if well formulated, to converge on the analytical solution.

To reduce the smoothing length, as noted in the methodology chapter, the relation $H = 3\Delta_P$ must be maintained to avoid a diverging error. This process can be considered as refinement of particle arrangement. To achieve this, each particle must be replaced by multiple particles which total the same mass. A very basic example of this idea is illustrated in Fig.4.25

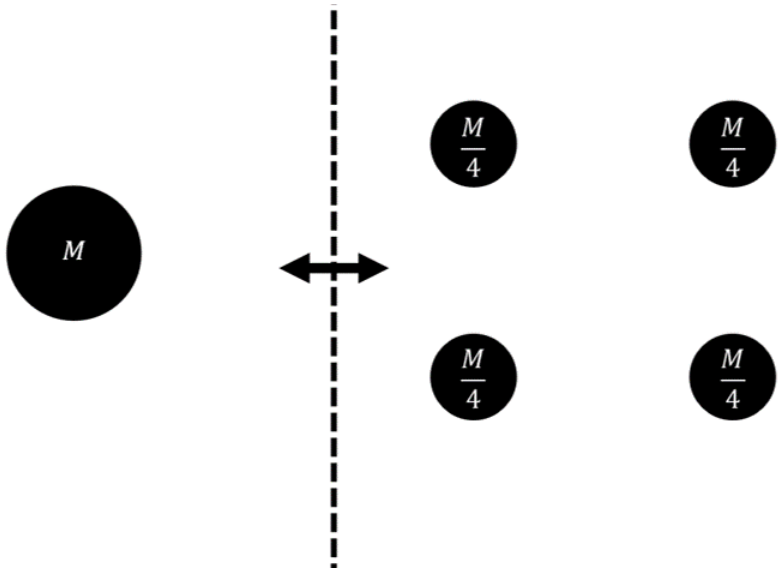

Figure 4.25: Illustration of basic particle arrangement refinement where 4 particles of $m_i = 0.25$ replace one particle of mass $m_i = 1$.

This allows refinement to be carried out on the fly within SPAM, an option that has been explored in other research [129]. For this work however the construction of particle arrangement will simply be altered to adjust the inter-particle Δ_P spacing accordingly. For 2D and unit density $\rho_0 = 1\text{g/mm}^3$ the particle spacing for the desired particle mass m_i is given by:

$$\Delta_P = \sqrt{m_i} \tag{4.27}$$

4.11.1 Convergence Test

A convergence test is carried out on triangular particle arrangements presented to identify the scope for further error reduction. This helps identify the optimal methods and particle arrangements, with an indication of optimal error reduction achievable in the model presented in this chapter.

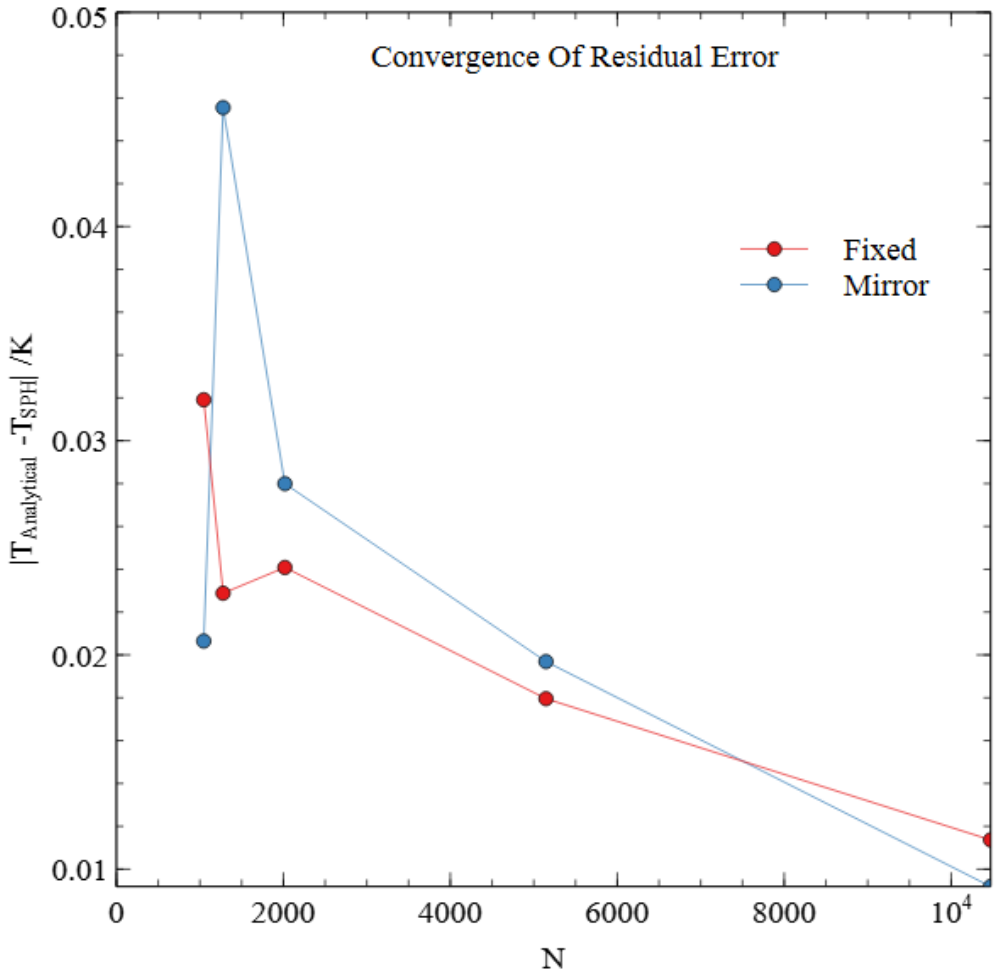

Figure 4.26: Error convergence for increasing particle number within the triangular particle arrangement for both the fixed and mirror boundary simulations.

The results in Fig.4.26 suggest that the particle spacing can cause errors to increase in the curved mirror boundary case if chosen poorly. This is assumed to be due to an increase in particles within range $\Delta_P/2$ of the boundary, causing an increase in particle arrangement disorder. This effect is over taken by the reduction in error achieved for higher particle numbers. For both the fixed and mirror case the error approaches ≈ 0.01 for $N > 10,000$ particles. This suggests that for large systems, acceptable thermodynamic results can be achieved by either boundary conditions in curved geometry. The temperature profile for the $N > 10,000$ mirror simulation with triangular boundaries is presented in Fig.4.27

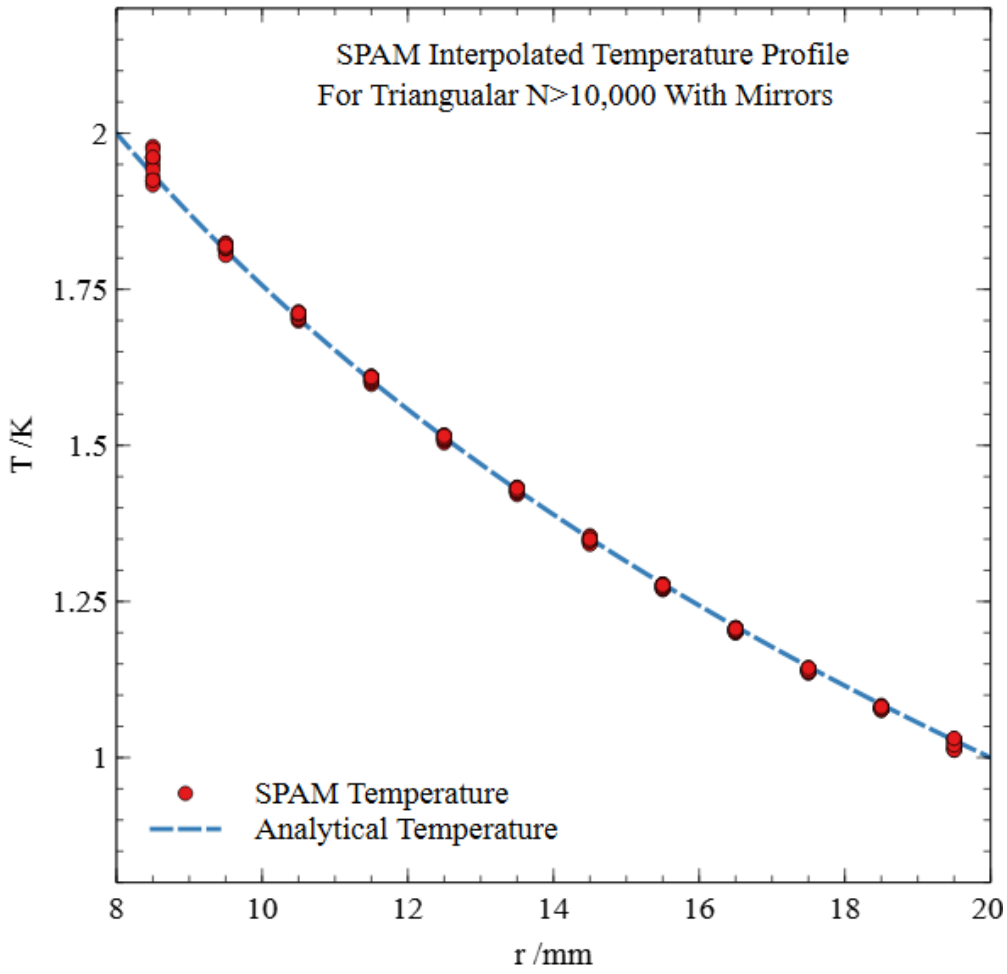

Figure 4.27: SPAM interpolated temperature profile for $N > 10,000$ particle in a triangular particle arrangement formation with mirror boundaries.

4.12 Conclusions

The work presented in this chapter has shown that SPAM thermal simulation within a cylindrical geometry can be constructed with acceptable error bounds, by careful consideration of the chosen particle configuration and number, as well as modification of the mirror boundaries.

The mass modifications to the mirror boundaries, although primitive, show effectiveness in the calculation of material properties close to the boundary. Further improvements could be made to help reduce particle spreading due to a loss of particle symmetry.

The relaxation explored in this chapter shows little benefit for its added complexity. The use of relaxed random particles may still hold future use for simulation exploring very complex geometry such as in initially damaged or grain structural simulations of nuclear fuel. A better methodology such as the particle packing algorithm [127] would overcome the requirement for the determination of the relaxation values however.

The optimal particle arrangement for mirror boundaries was found to be the concentric particle

arrangement, and the optimal for fixed was found to be the square particle arrangement. However the triangular particle arrangement was found to have good consistency for reasonable values across both fixed and mirror boundaries. Work with particle shifting algorithms has demonstrated a tendency to move toward triangular structures [128] which supports their continued use as the structure must minimise density errors to a high degree.

Through refinement of particle arrangement the triangular particle arrangement was shown to be able to produce residual errors on the order of ≈ 0.01 for the temperature profile which considering the constant temperature gap used is an error of 1%. This suggests that SPAM is capable of producing accurate thermal information if used within complex damage simulations for nuclear fuel pellets.

Chapter 5

Dealing with Heat Sources and Convective Boundary Conditions within SPAM

5.1 Introduction

Within a nuclear fuel rod energy is released in the form of heat within the fuel pellet, often UO_2. This heat is usually removed by convection at the cladding surface through the coolant flowing through the fuel assembly. Any FPC developed through SPAM must therefore be able to handle these types of boundary conditions. In this section we explore the simple 1D models for heat source and convective boundary conditions with well-defined analytical solutions. The conditions are implemented within SPAM and direct comparison of results made with analysis of the SPAM error.

Many complex thermal phenomena important to nuclear fuel have already been demonstrated within SPH such as radiation [130], convective current flows [131] and melting and solidification [58]. These will not be explored for the model constructed here but will become important in future work. There are also implementations of heat sources [51], convective boundaries [132] and material interfaces within SPH [108]. These models will be explored and suitable modification to the current problem will be given. In particular for the case of convective boundary conditions an entirely new approach is proposed.

5.2 1D Convection Model

The simplest model for treating a convective boundary condition employs Newton's law of cooling. Equating the heat fluxes at the boundary leads to:

$$\kappa \frac{\partial T(x_B, t)}{\partial x} = -h[T(x_B, t) - T_\infty] \tag{5.1}$$

Here x_B is the position of the convective boundary. T_∞ represents the coolant temperature. The coefficient of convection h controls how much heat is transmitted into the convective boundary at each time step.

To explore the SPAM application of this condition a simple 1D convection model is used. This model has an analytical solution and a visual representation is given in Fig.5.1. Consider an axisymmetric rod, length L, of material with thermal conductivity κ. One end of the material, $x = 0$, is in contact with a constant temperature surface held at T_c as in the previous thermal models. The other end, $x = L$, is in contact with the convective fluid at temperature T_∞. Lateral heat flow can be assumed to be negligible such that the problem is reduced to 1D.

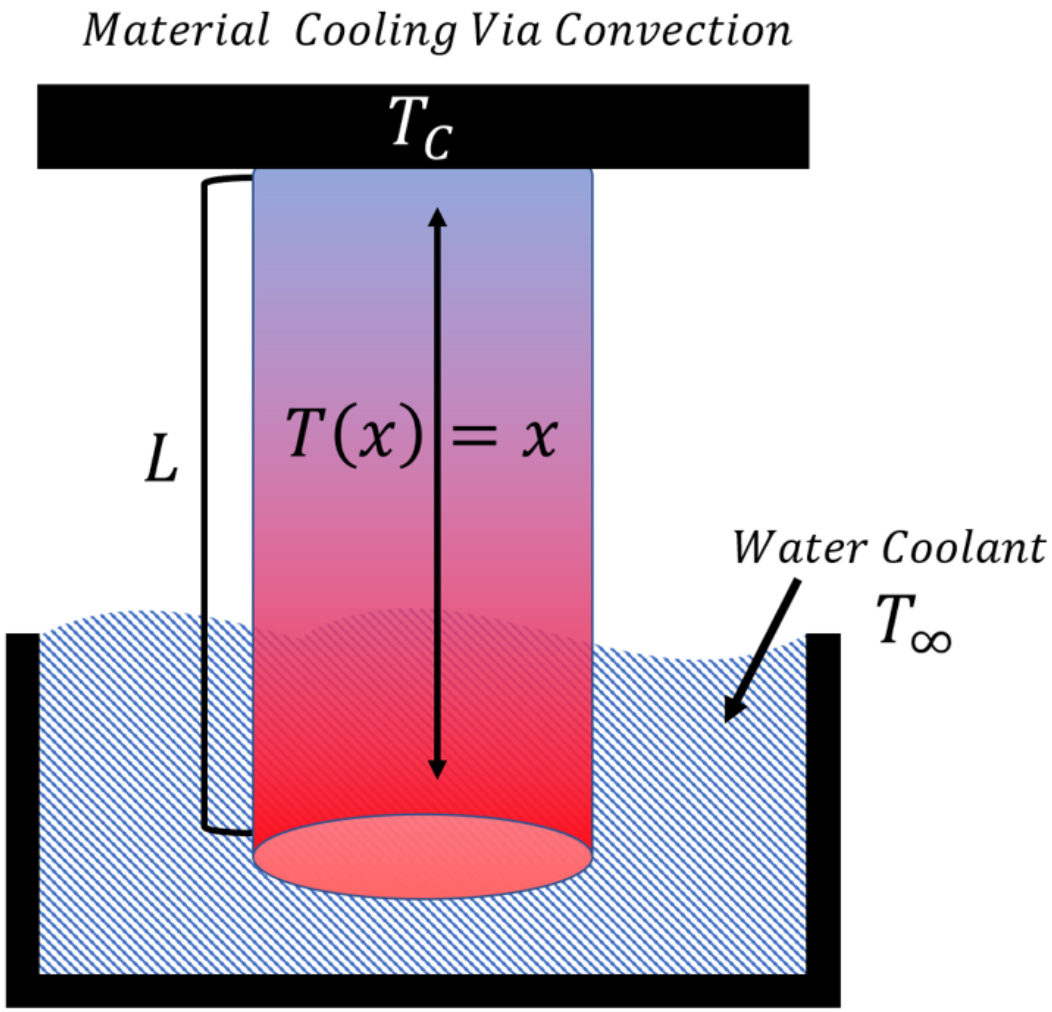

Figure 5.1: An outline of the simple 1D convection model being used. One end of the material (of length L) is held at a constant temperature T_c. The other end is in contact with a fluid at T_∞ and thus undergoes cooling according to Newton's law. The system is given an initial linear temperature profile.

We assume temperature at any point in space and time follows the heat equation:

$$\frac{\partial T(x,t)}{\partial t} = D_T \frac{\partial^2 T(x,t)}{\partial x^2} \tag{5.2}$$

For the analytical solution to this equation we chose the initial condition:

$$T(x,0) = x \qquad\qquad 0 \leq x \leq L \tag{5.3}$$

To simplify the solutions we chose constant temperature boundary at $x = 0$, with $T_C = 0$ such that:

$$T(0,t) = 0 \tag{5.4}$$

A convective boundary at $x = L$, with $T_\infty = 0$ such that:

$$\kappa \frac{\partial T(L,t)}{\partial x} + hT(L,t) = 0 \tag{5.5}$$

Finally we choose $L = 100mm$ and set the specific heat and density to unity $\rho = 1\text{g/mm}^3$,$C_p = 1\text{mm}^2/\text{s}^2\text{K}$ such that the thermal conductivity is given by the thermal diffusivity $D_T = \kappa$. With these values the solution to the heat equation can be calculated for direct comparison with the SPAM solution.

5.2.1 Analytical Solution

The analytical solution to Eq.5.2 maybe obtained by using the method of separation of variables. This is detailed by Farlow [133] among others. The first step involves writing the temperatures as:

$$T(x,t) = X(x)E(t) \tag{5.6}$$

which converts the partial differential equation into two ordinary differential equations:

$$E' + \lambda^2 D_T E = 0 \tag{5.7}$$

$$X'' + \lambda^2 X = 0 \tag{5.8}$$

where $-\lambda^2$ is chosen as the separation constant. These equations have the general solution:

$$E(t) = C_1 exp(-\lambda^2 \kappa t) \tag{5.9}$$

$$X(x) = C_2 sin(\lambda x) + C_3 cos(\lambda x) \tag{5.10}$$

where C represents the constants of integration which combine to give the general temperature solution:

$$T(x,t) = exp(-\lambda^2 \kappa t)[Asin(\lambda x) + Bcos(\lambda x)] \tag{5.11}$$

Using the boundary condition Eq.5.4 it can be shown that $B = 0$. Application of boundary condition Eq.5.5 shows that λ must satisfy:

$$tan(\lambda L) = -\frac{\kappa \lambda}{h} \tag{5.12}$$

There are an infinite number of roots to this transcendental equation, the first three are shown in Fig.5.2. The roots are all real and evenly spaced in intervals of 2π. A numerical scheme can therefore be constructed to find as many roots as required.

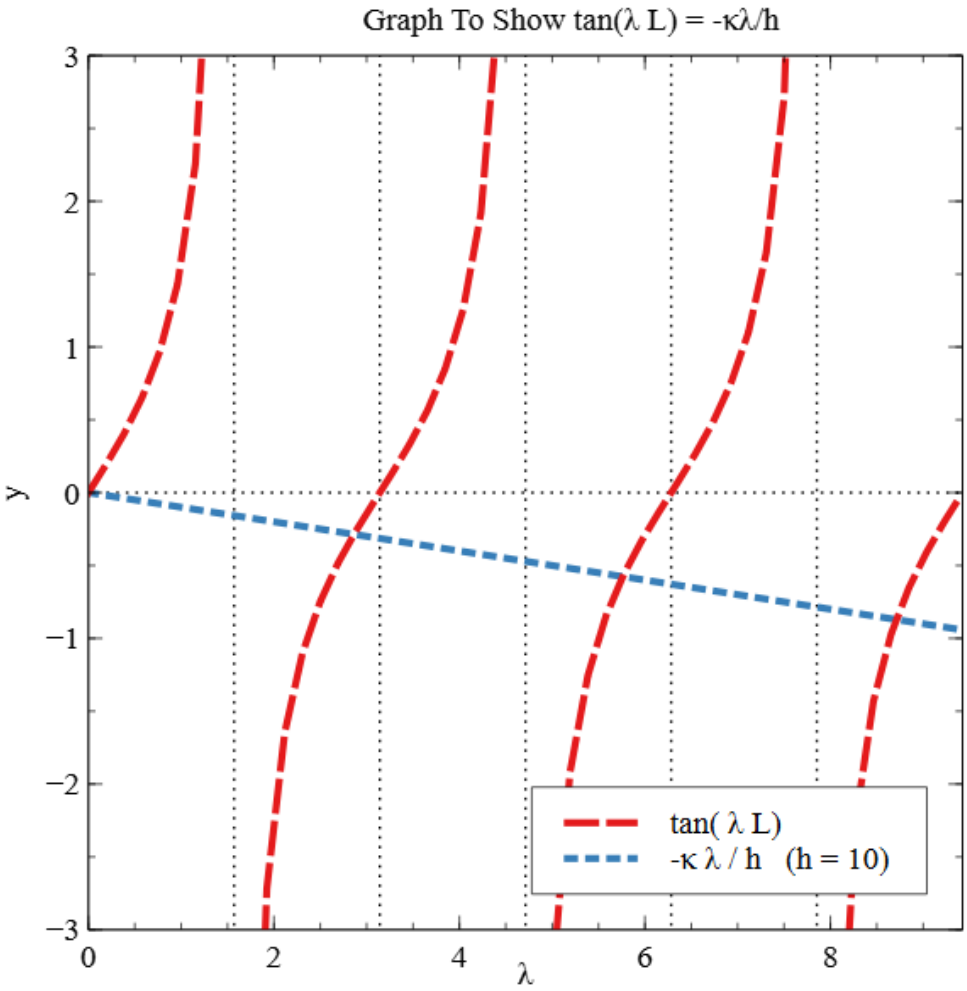

Figure 5.2: The first 3 intersections for the functions $tan(\lambda L)$ and $-\lambda/h$. Shown here with $h = 10$, $L = 1$, $\kappa = 1$. The solutions for the intersection of the functions λ_n can be calculated up to $n = \infty$. The solutions tend toward $\lambda_n = (2n-1)\pi/2L$ due to the asymptotic nature of the tangent function

Due to the linearity of the heat conduction PDE, the general solution is a superposition of all solutions for each λ_n. Thus this suggests that the temperature solution is an infinite sum of solutions to the heat equation based on λ_n. For each value of n a new coefficient A, noted a_n, must be calculated suggesting the complete solution takes the general form:

$$T(x,t) = \sum_{n=1}^{\infty} a_n exp(-\lambda_n^2 \kappa t) sin(\lambda_n x) \tag{5.13}$$

Finally to calculate the coefficients a_n a decomposition of the initial condition (Eq.5.3) must be calculated as a sum of sin functions:

$$T(x,0) = x = \sum_{n=1}^{\infty} a_n sin(\lambda_n x) \tag{5.14}$$

It can therefore be shown that:

$$a_n = \frac{2[sin(\lambda_n L) - \lambda_n L cos(\lambda_n L)]}{\lambda_n [\lambda_n L - sin(\lambda_n L) cos(\lambda_n L)]} \tag{5.15}$$

5.2.2 Roots via Newton's Method

Calculation of the constants λ_n is done using Newton's method with the first guess for each root being selected as $\lambda_n = (2n-1)\pi/2L$. Newton's method is given here as:

$$x_{m+1} = x_m - \frac{f(x_m)}{f'(x_m)} \tag{5.16}$$

where the function f is defined as:

$$f(x) = 0 = tan(xL) + \kappa x/h \tag{5.17}$$

which gives the iterative equation:

$$x_{m+1} = x_m - \frac{tan(x_m L) + \kappa x_m/h}{L/cos^2(x_m L) + \kappa/h} \tag{5.18}$$

We know each solution λ_n must lie within the asymptotes of $tan(\lambda_n)$. We therefore increment the initial guess away from the asympote $(2n-1)\pi/2L$ and restart Newton's method every time the guess x_{m+1} lies outside the predicted root bounds:

$$\frac{(2n-1)\pi}{2L} + \epsilon < \lambda_n < \frac{(2n+1)\pi}{2L} - \epsilon \tag{5.19}$$

Here $\epsilon = 10^{-8}$ is a very small quantity included to avoid the infinite values of the tangent function and possible errors introduced. The first 10 values calculated for $h = 1\text{g/s}^3\text{K}$ are given in Table.5.1

n	λ_n	a_n
1	0.0311	64.2679
2	0.0622	-32.0881
3	0.0933	21.3414
4	0.1244	-15.0881
5	0.1555	12.7089
6	0.1867	-10.5368
7	0.2178	8.9778
8	0.2489	-7.8024
9	0.2800	6.8829
10	0.3111	-6.1431

Table 5.1: Calculated values for λ_n by Newton's method up to $n = 10$ all given to $4dp$. The corresponding values for a_n are given calculated by Eq.5.15. All calculated for $h = 1\text{g/s}^3\text{K}$, $L = 100mm$, $\kappa = 1$

5.2.3 Analytical Results

The analytical solutions are shown here for several decades of time. Up to $n = 100$ frequencies are included in the calculated solution. The thermal conductivity is set to $\kappa = 1\text{gmm/s}^3\text{K}$, and the results here are shown for the case of convection coefficient, $h = 1\text{g/s}^3\text{K}$. The analytical result for the heat flux is also shown.

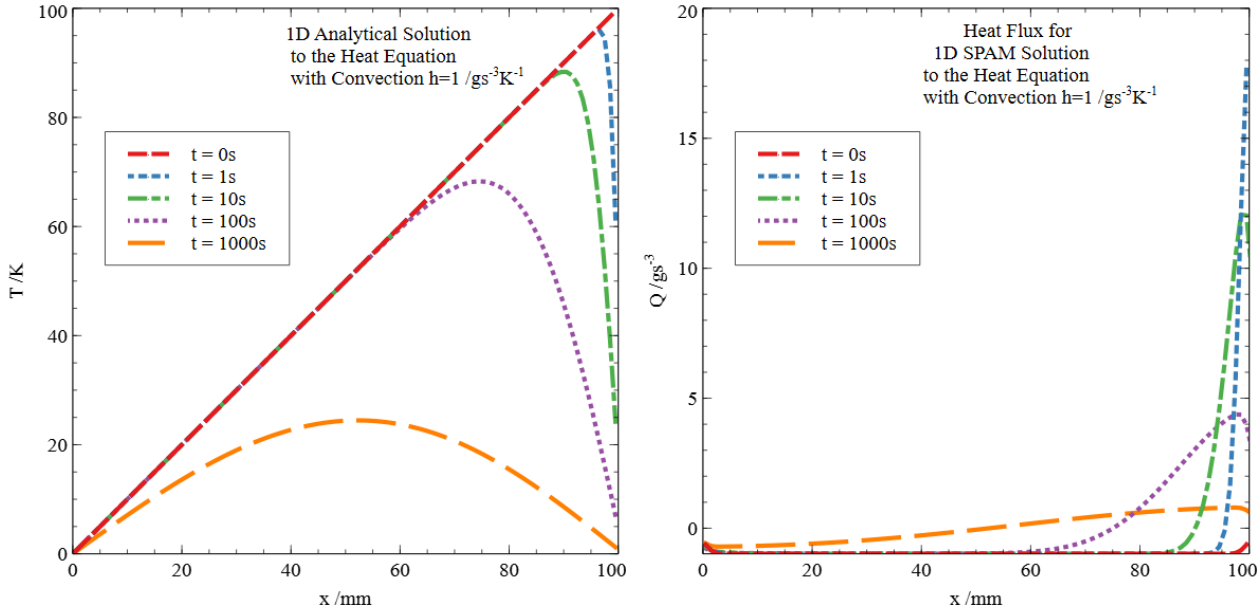

Figure 5.3: Analytical solutions for the 1D convection model shown in Fig.5.1. Up to $n = 100$ frequencies included. Shown here for the value of convection coefficient $h = 1\text{g/s}^3\text{K}$. Left shows the expected temperature profiles, right shows the expected heat flux.

The analytical results show that higher values of convection coefficient h result in faster cooling of the 1D material. We will vary the value h within the SPAM simulations to confirm they follow this behaviour precisely.

5.2.4 Convective BCs within SPAM

Convection has been studied within fluids in SPAM [131], [134]. This work aims instead to investigate convection as a boundary condition. At least one method has been proposed for this within SPAM [132], however this requires the surface area of the particle for which convection occurs. It also requires no external boundary particles be present in order to calculate the surface normal's from the deficiency in the weight function, this is less than ideal as it restricts the model from having further particle driven boundary phenomena enforced such as stresses. In this work a method based only on particle pairs is proposed. The temperature evolution used for these simulations is the Hoover formulation:

$$\frac{dT_i}{dt} = C\sum_j (T_j - T_i)W(r_{ij}) \tag{5.20}$$

where the constant C is calculated by considering the temperature evolution of the long wavelength perturbation $dt \propto cos(2\pi x/\lambda) \approx 1 - (\pi x/2\lambda)^2$:

$$C = \frac{D_T}{\sum \frac{x^2 w(x)}{2}} \tag{5.21}$$

This formulation means that temperature evolution is based directly on particle temperatures. The method for convective boundaries proposed is based on static fixed particle boundaries. The convective boundary condition must therefore assign the boundary particle temperatures at each

time step in a dynamic way such that the temperature evolution reflects the required condition. We require that:

$$\frac{\partial T(x_B, t)}{\partial x} = -\frac{h}{\kappa}[T(x_B, t) - T_\infty] \tag{5.22}$$

To calculate the temperature at the boundary we approximate this function with particle values, starting with the derivative:

$$\frac{\partial T(x_B, t)}{\partial x} = \frac{T_j - T_i}{x_j - x_i} \tag{5.23}$$

Let us assume that particle i is one of the boundary particles in question. We then require particle j to lie on the system side of the boundary in question such that the approximation is the temperature gradient across the boundary. We store the closest system particle to i and choose this to be $j = B_i$. The visual interpretation to this within the 1D SPAM is shown in Fig.5.4. In 1D any choice of boundary particle is assigned the same single system particle T_{B_i} which lies closest to the boundary.

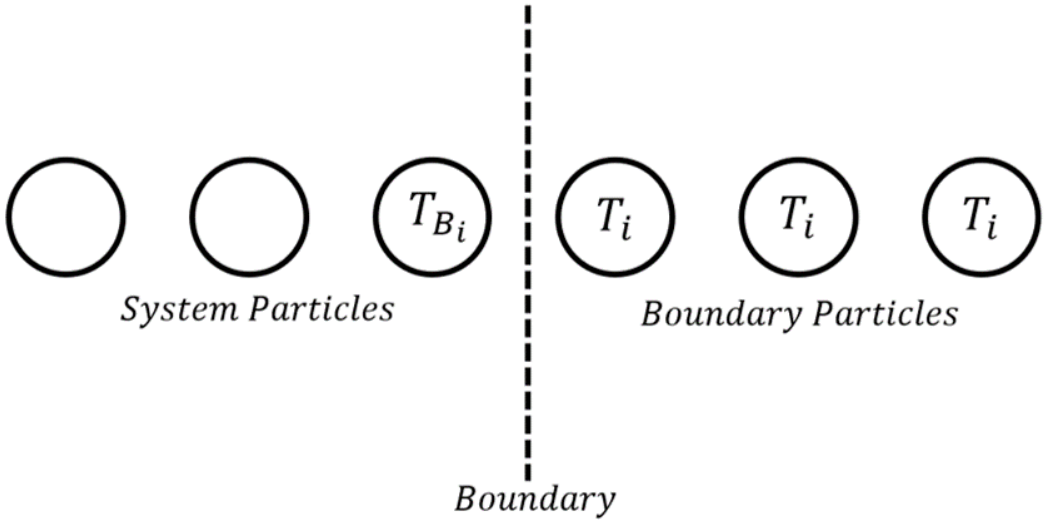

Figure 5.4: Visual interpretation of the chosen system particle B_i for any choice of boundary particle i. In 1D all boundary particles have the same single system particle pair. The use of the closest system particle ensures that the method is easily generalised to 2D and that the used particle B_i is next to the system boundary.

Next the particle T_i is used as the boundary temperature T_B. Newton's law of cooling can then be approximated by the expression:

$$\frac{T_{B_i} - T_i}{x_{B_i} - x_i} = -\frac{h}{\kappa}[T_i - T_\infty] \tag{5.24}$$

We can now rearrange this to create an expression for the temperature of any boundary particle T_i such that Newton's law of cooling is obeyed:

$$T_i = \frac{T_{B_i} - T_\infty F_h}{1 - F_h} \tag{5.25}$$

where the function of convection F_h is defined as:

$$F_h = \frac{h}{\kappa}(x_{B_i} - x_i) \tag{5.26}$$

To demonstrate the validity of this expression for calculating boundary temperatures we examine the limits of this equation. We expect that as the distance from the boundary $R = |x_{B_i} - x_i|$ grows the temperature should approach T_∞:

$$\lim_{R\to\infty} F_h = \infty \tag{5.27}$$

Thus we have:

$$T_i = \frac{T_{B_i}/F_h - T_\infty}{1/F_h - 1} \to T_\infty \tag{5.28}$$

Similarly we expect that for $h = 0$ there should be no heat flux across the boundary:

$$\lim_{h\to 0} F_h = 0 \tag{5.29}$$

Thus we have:

$$T_i = T_{B_i} \tag{5.30}$$

This implies that temperature across the boundary is constant and therefore no heat is transferred. For illustration purposes the boundary temperatures have been calculated within the SPAM simulation beyond the the smoothing length so the the profile can be seen in Fig.5.5.

5.2.5 SPAM Results

Herein, the SPAM simulation was run with Hoover's temperature formulation Eq.5.20. The constant temperature boundary was assigned fixed particles with $T = 0K$ and the convective boundary has particles with the convective temperatures according to Eq.5.25 calculated between each time step. The time step is $dt = 0.01s$. The convective boundary is given the initial temperature of $T = 100K$, to better calculate the initial system temperature profile, and the material temperature of $T_\infty = 0K$. A system of length $L = 100mm$ is used with 100 unit density particle making up the system. A smoothing length of $H = 3$mm is used. The simulation is run for 100000 time-steps and for 4 values of convection coefficient $h = 0.1, 0.5, 1, 10\text{g/s}^3\text{K}$ all with unit thermal conductivity $\kappa = 1\text{gmm/s}^3\text{K}$. We show only two values for $h = 1, 10\text{g/s}^3\text{K}$ here, and the others are included within the error analysis.

The results are shown in Fig.5.5. The final temperature profiles for the SPAM simulation are shown for $0 < x < 120$ so that the convective boundary temperature profile can be shown. Interpolation errors due to reduced particle numbers are apparent around $x \approx 120$. It can be seen that all profiles match the expected shape shown in the analytical model with faster loss of heat for higher values of the convection coefficient h.

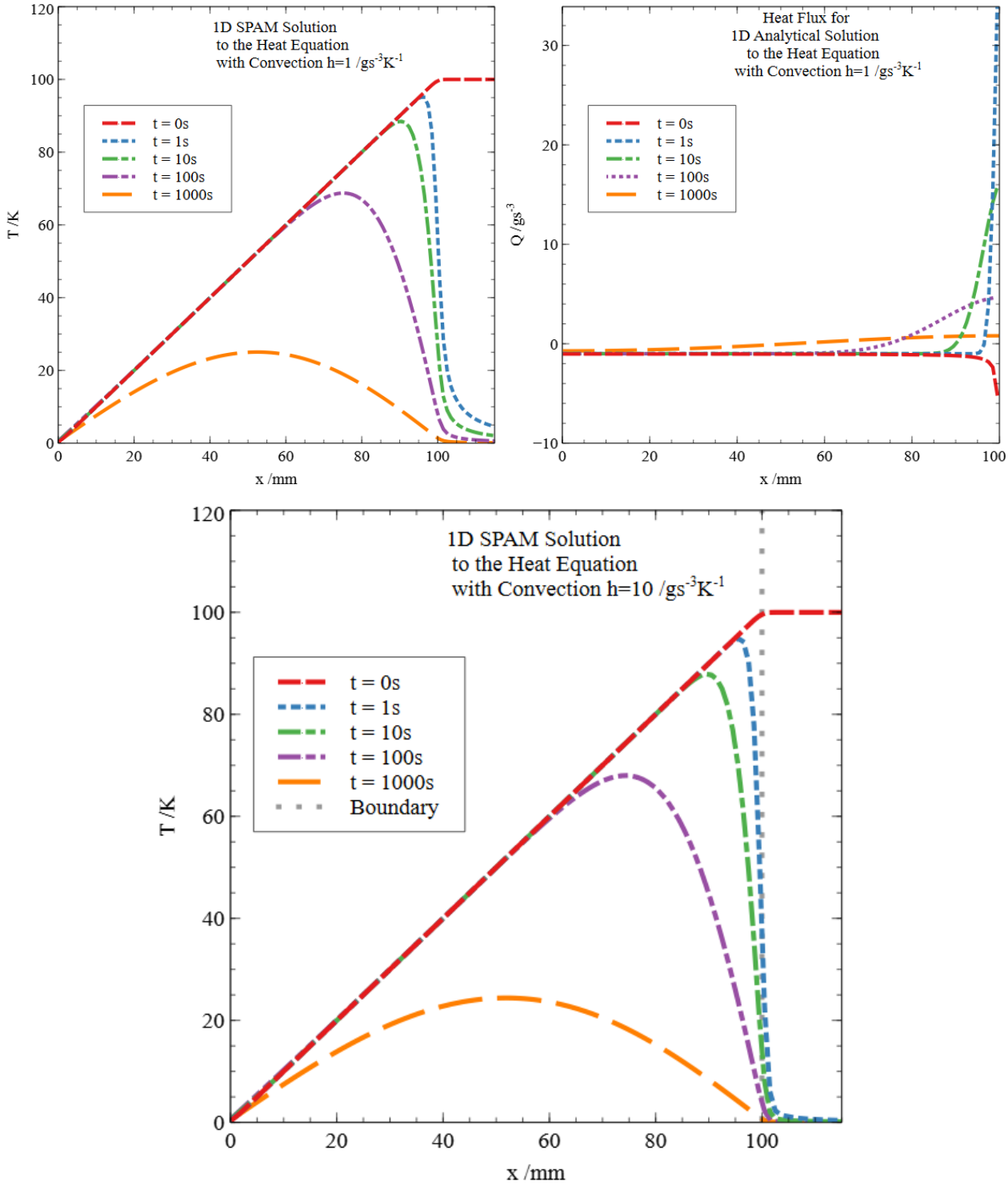

Figure 5.5: SPAM results for the 1D convection model shown in Fig.5.1. The calculated boundary temperatures beyond the convective boundary $L = 100mm$ are shown up to $L = 120mm$ for illustration purposes. Shown here for 2 values of convection coefficient. Top left temperature profile for $h = 1\text{g/s}^3\text{K}$, top right heat flux for $h = 1\text{g/s}^3\text{K}$. Bottom $h = 10\text{g/s}^3\text{K}$.

5.2.6 Behaviour of Residual Error

A direct comparison between the SPAM results and the analytical results for selected times in shown in Fig.5.6-5.7. It is immediately seen that the error in results for the methods used are minimal. Fig.5.8 shows that the SPAM algorithm is capable of reproducing temperature profiles for a range of values of convection coefficient h, with no apparent increase in error.

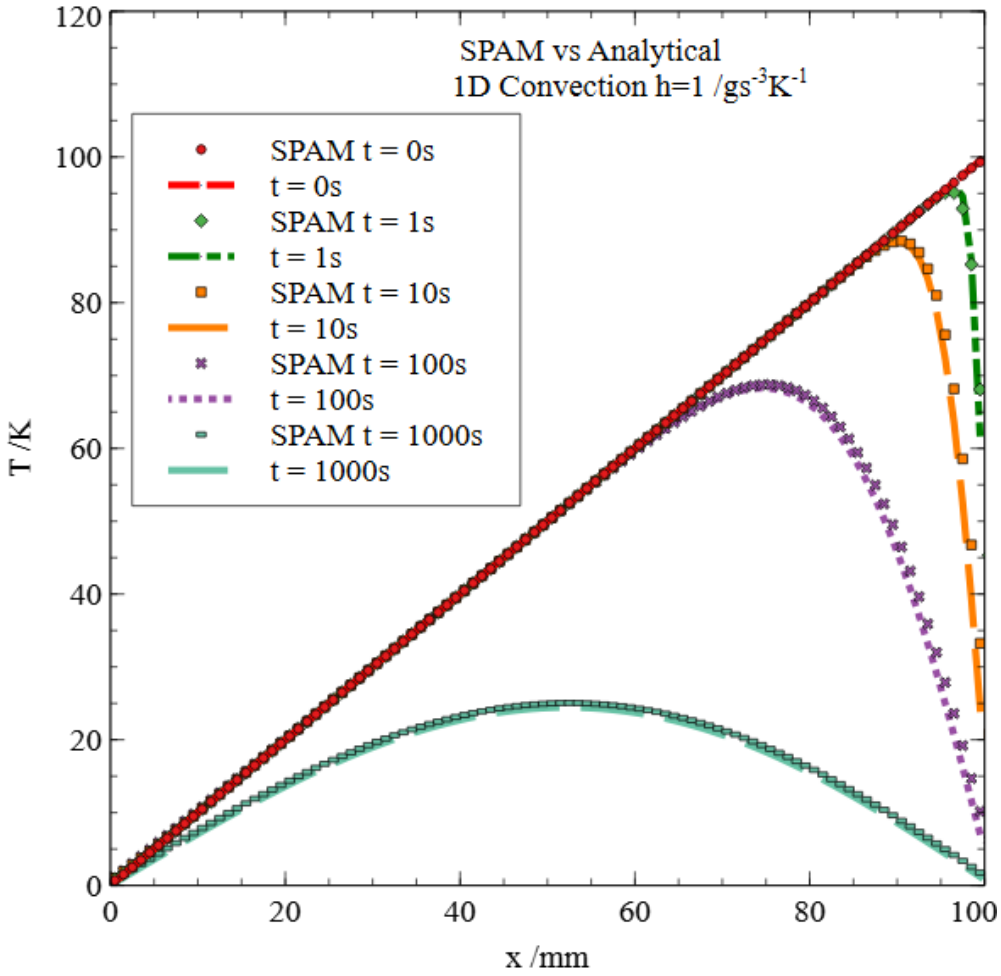

Figure 5.6: Direct comparison of the SPAM results with the analytical solutions for the 1D convection model. Temperature results are shown for $h = 1\text{g/s}^3\text{K}$.

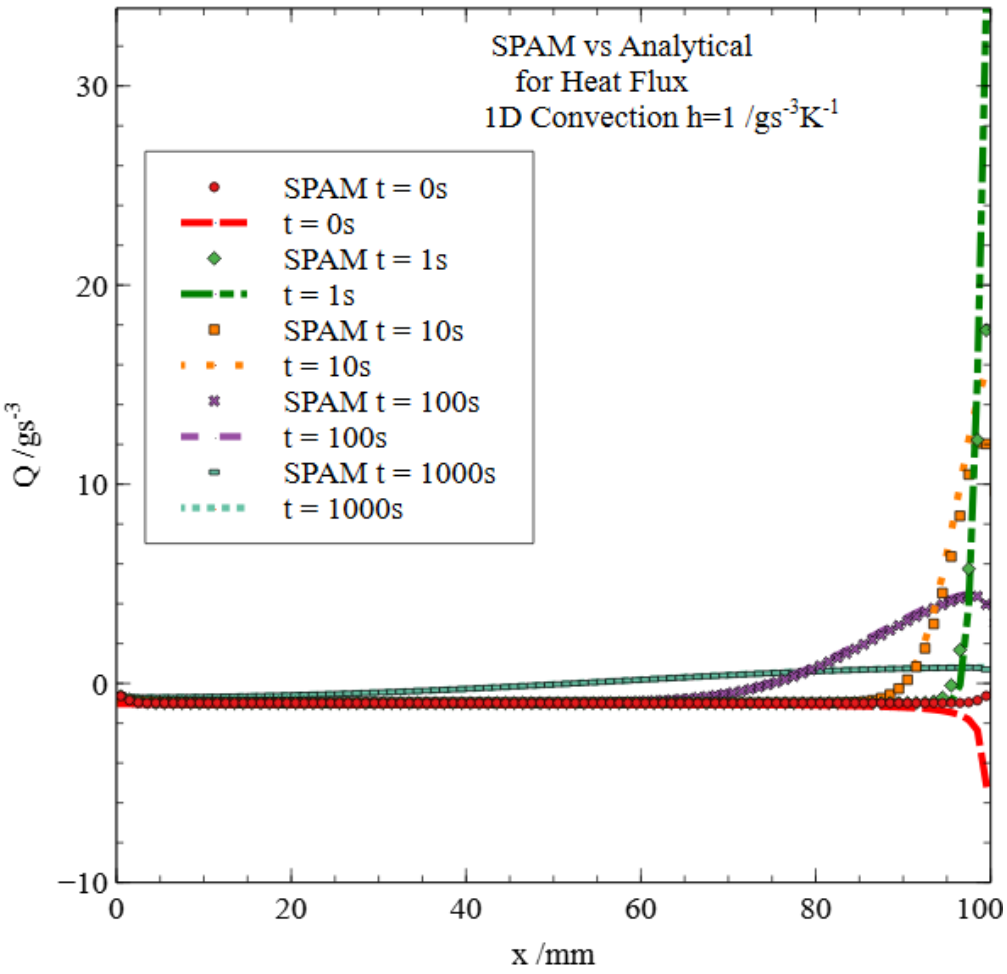

Figure 5.7: Direct comparison of the SPAM results with the analytical solutions for the 1D convection model. Heat flux results are shown for $h = 1\text{g/s}^3\text{K}$.

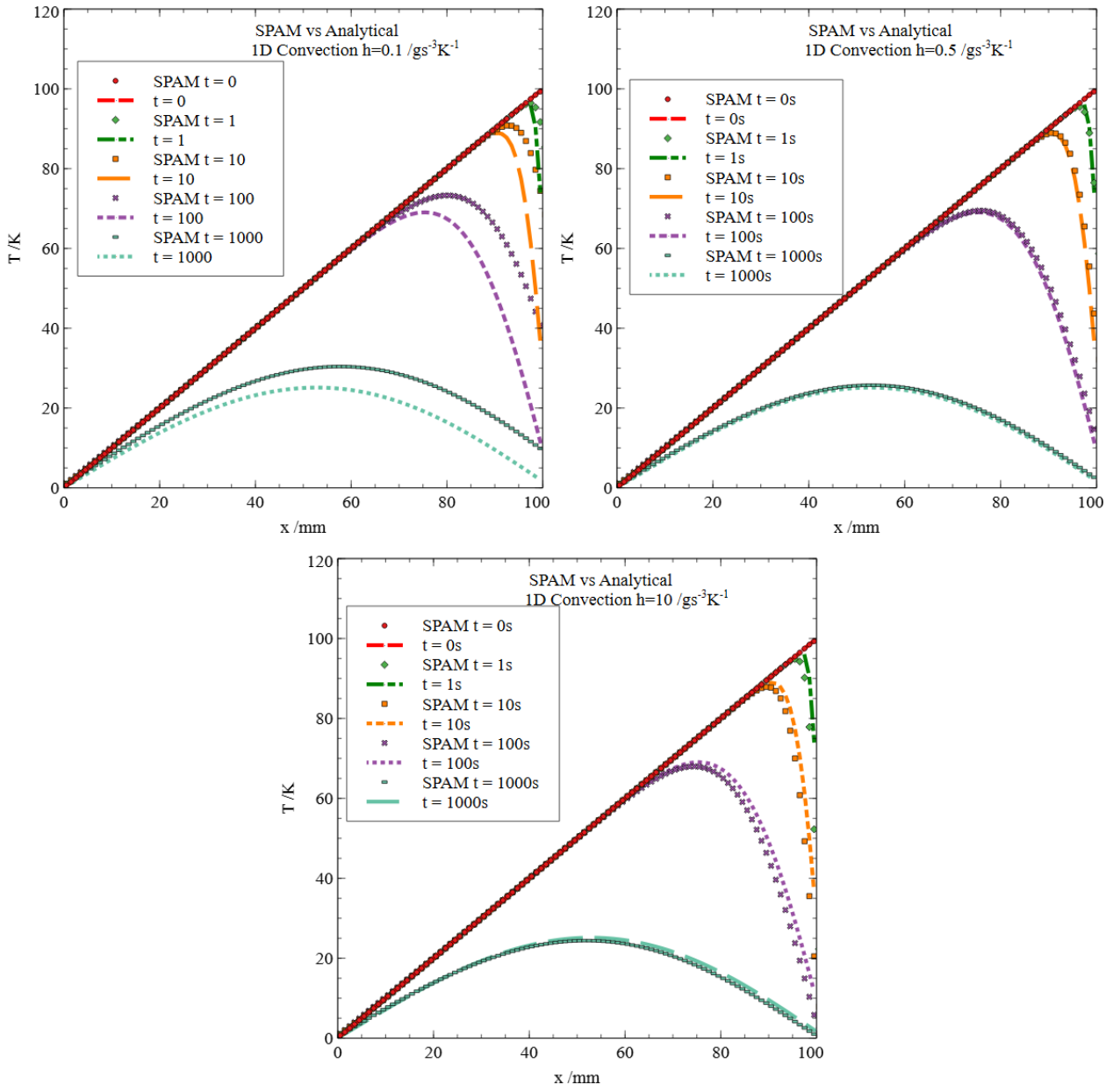

Figure 5.8: Direct comparison of the SPAM results with the analytical solutions for the 1D convection model. Top left $h = 0.1\text{g/s}^3\text{K}$, top right $h = 0.5\text{g/s}^3\text{K}$. Bottom $h = 10\text{g/s}^3\text{K}$.

Discrepancies between the SPAM results and the analytical results have been quantified using the residual error approach described by Eq.4.26. Fig.5.9 shows these residual errors as a function of time for 4 different values of the convection coefficient. The temperature scale for the initial conditions is $dt = 100K$ therefore the residual shows that the SPAM result errors represent $\approx 1\%$ of this range. It is interesting to note also that the errors appear to converge in the long time limit across all values of h.

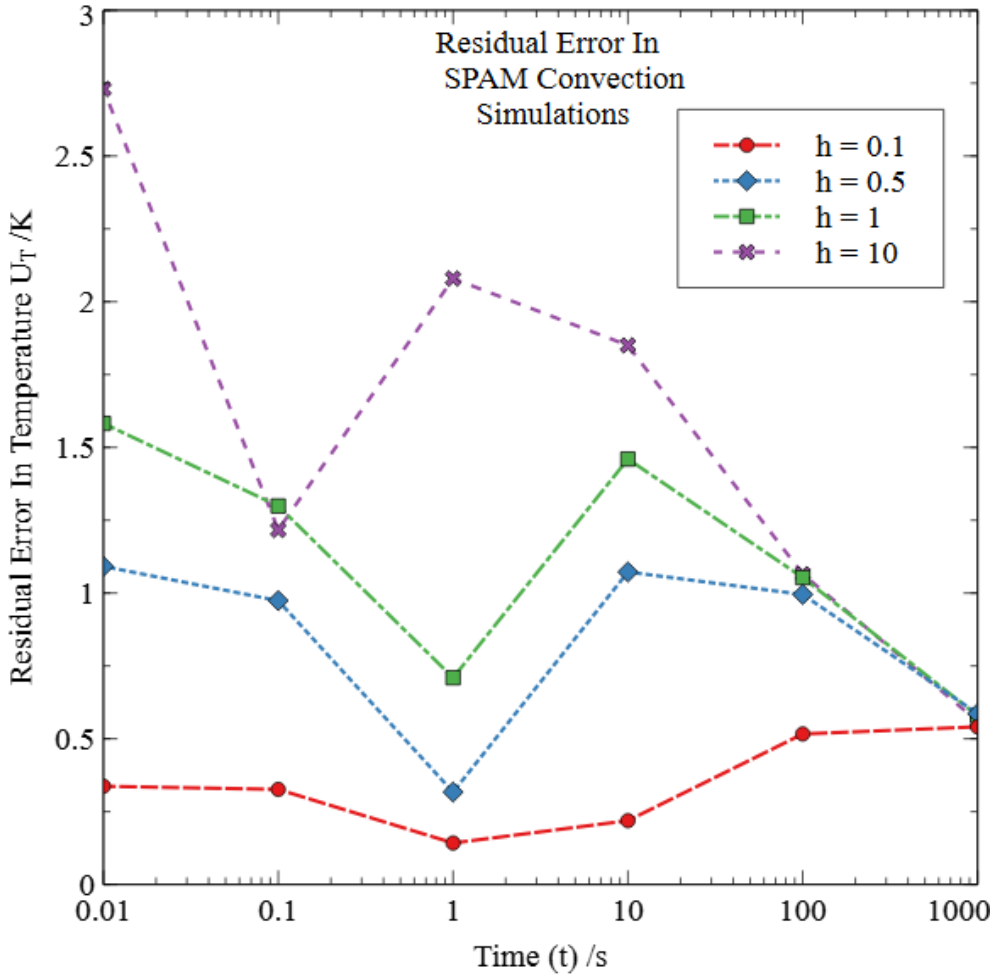

Figure 5.9: Residual error in the SPAM results calculated for the 1D convection model. Calculated for $n = 100$ frequencies of the analytical function. Shown for four values of convection coefficient h (g/s^{3}K) against a logarithmic time scale t

Further testing showed that no extra constraint was required on the time step beyond Eq.3.23, and that using smaller time steps than this had no benefit. Finally, use of boundary particle is required up to within a smoothing length of the boundary $H = 3$mm. Beyond this they have no effect, as expected, but below this threshold interpolation errors are introduced.

5.2.7 Alternative SPAM Convection

Several alternative formulations of the convection boundary conditions were tested for this model and found to have an increased error. This is surprising as both methods are constructed as a refinement of the approximation given in Eq.5.25.

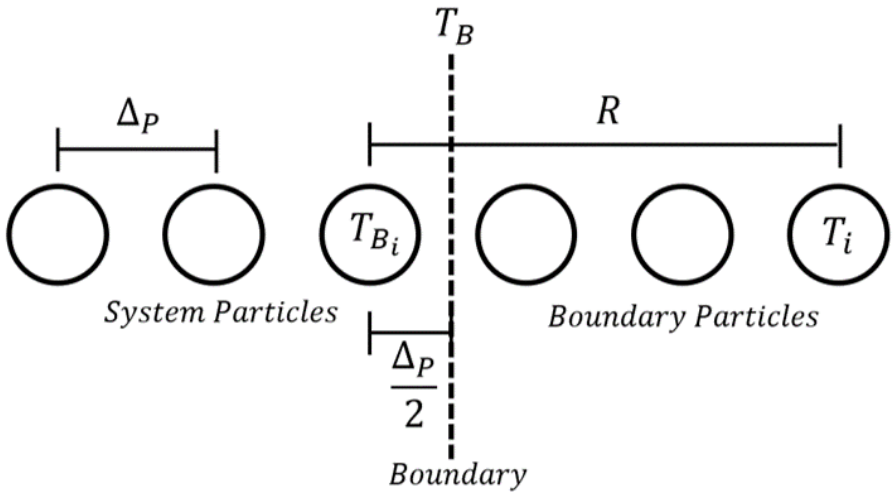

Figure 5.10: Visual interpretation of the inter-particle distances for an improved convective boundary approximation. The use of the closest system particle ensures that the method is easily generalised to 3D and that the used particle B_i is next to the system boundary.

The first refinement is given by accounting for the distance of the boundary particle i from the system boundary B. For this the average particle spacing is required Δ_P. The system boundary temperature is then approximated by the weighted average of the distance of the nearest system particle and the boundary particle. Fig.5.10 is included to illustrate this idea. The system boundary temperature T_B is then approximated as:

$$T_B \approx \frac{\Delta_P}{2R} T_i + \left(1 - \frac{\Delta_P}{2R}\right) T_{B_i} \tag{5.31}$$

With this approximation the boundary particle temperature T_i is then approximated, using the earlier method, as:

$$T_i = \frac{T_N \left(1 - \frac{h}{\kappa}\left(R - \frac{\Delta_P}{2}\right)\right) + T_\infty \frac{h}{\kappa} R}{1 + \frac{h}{\kappa}\frac{\Delta_P}{2}} \tag{5.32}$$

With this approximation made the SPAM simulation is run as before for $h = 10\text{g/s}^3\text{K}$ as this shows the largest visible error. The results are shown in Fig.5.11. Clearly the alternative method introduces an increased amount of error.

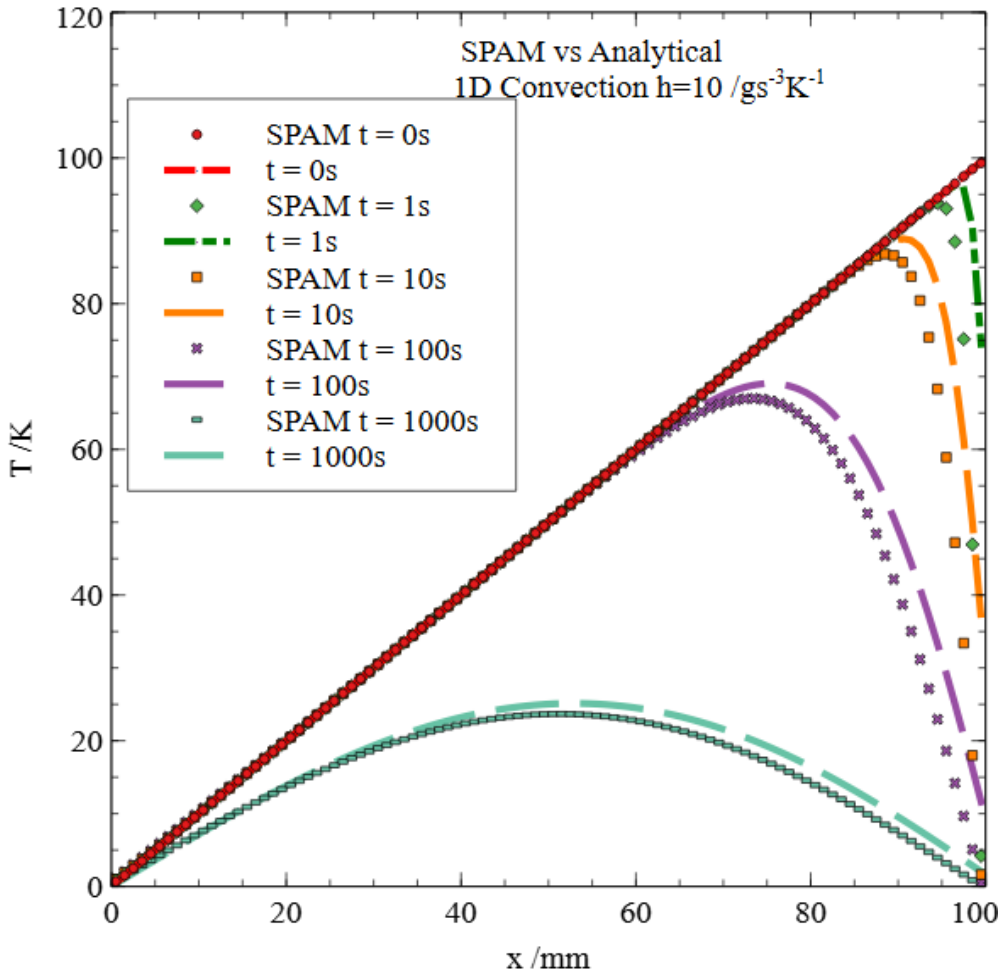

Figure 5.11: Direct comparison of the SPAM results with the analytical solutions for the 1D convection model. Shown here with the alternative convective boundary approximation Eq.5.32. Temperature results are shown for $h = 10\text{g/s}^3\text{K}$.

Another method attempted which is given here is the convective boundary approximation with dynamic (mirror) boundary conditions. Mirror boundary particles are created in pairs about the boundary with each boundary temperature assigned based on a particle now with an equal and opposite distance from the boundary. This idea is shown for one such pair in Fig.5.12. The system particles are now denoted by index i and the mirrors of these particles by i'.

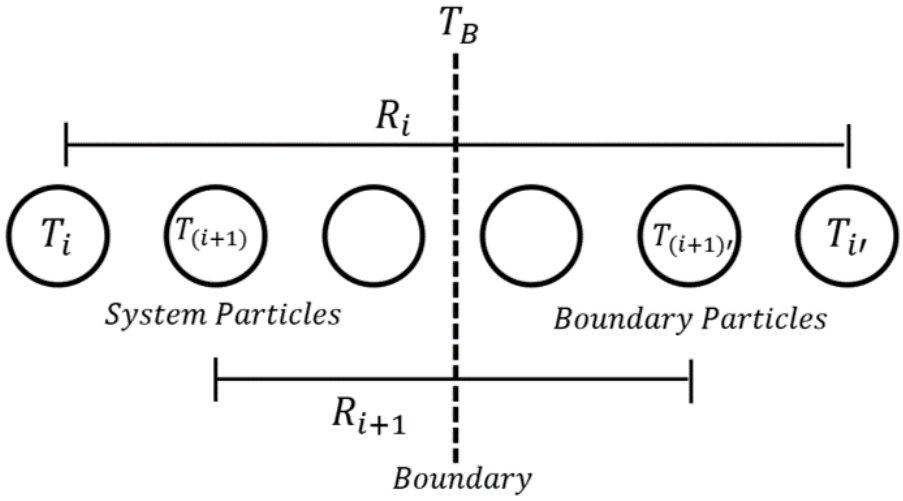

Figure 5.12: Visual interpretation of the inter-particle distances for the mirror convective boundary approximation. Particle pairs for assignment of mirror boundary values are by design equidistant from the system boundary.

For mirror boundary particles the boundary temperature is given by:

$$T_B = \frac{T_i + T_{i'}}{2} \tag{5.33}$$

This time the boundary temperature of interest is noted as $T_{i'}$ and using the same approximations as before to Newton's law of cooling it can be shown that:

$$T_{i'} = \frac{T_i \left(1 + \frac{h}{2\kappa} R\right) - T_\infty \frac{h}{\kappa} R}{1 - \frac{h}{2\kappa} R} \tag{5.34}$$

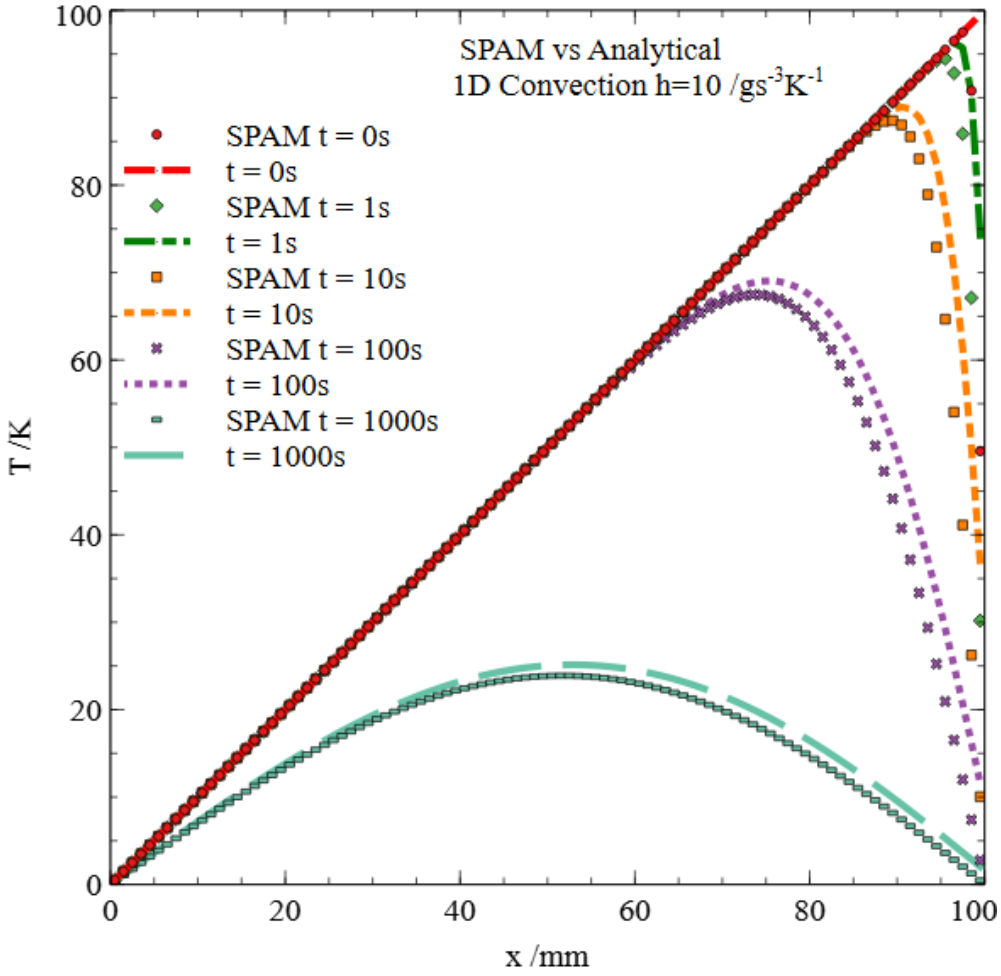

Figure 5.13: Direct comparison of the SPAM results with the analytical solutions for the 1D convection model. Shown here with the mirror convective boundary approximation Eq.5.34. Temperature results are shown for $h = 10\text{g/s}^3\text{K}$.

The results for the mirror convective boundary conditions are shown in Fig.5.13. Again it can be seen that the boundary conditions give an increased error over the standard approximation given first. These result will become important for the 2D problem however so are included here.

5.3 1D Heat Source Model

Any simulation of nuclear fuel material must have some form of heat generation. The heat generated within the nuclear fuel pellet must be removed through the cladding by convection. Having demonstrated the ability of SPAM to deal with convection we now present a simple model for heat generation with well-defined analytical solutions. Heat sources can be included within the heat equation such that a material generating heat at rate $\dot{q}$, per unit volume per unit time, must have a temperature that obeys:

$$\frac{\partial^2 T}{\partial x^2} - \frac{1}{D_T}\frac{\partial T}{\partial t} = -\frac{\dot{q}}{D_T} \tag{5.35}$$

We assume material of length L with each end held at temperature T_C. The material generates heat across its entire length at $\dot{q}$. Again we use $\kappa = D_T = 1\text{mm}^2/\text{s}$. We expect the heat generation to reach a steady state temperature profile where the temperature gradient at either side of the system causes heat to be lost out of the material at the same rate at which it generates heat.

5.3.1 Analytical Solution

To derive the analytical solution to Eq.5.35 we first consider the steady state solution [114]. Let $\partial T/\partial t = 0$. Then through integration:

$$T_{ss}(x) = -\frac{\dot{q}x^2}{2\kappa} + C_1 x + C_2 \tag{5.36}$$

where C_1, C_2 are constants of integration. We have the boundary conditions:

$$T(L/2, t) = T(-L/2, t) = T_c \tag{5.37}$$

The initial condition:

$$T(x, 0) = T_c \tag{5.38}$$

We take $T_c = 0K$. This gives $C_1 = 0$ and $C_2 = \dot{q}L^2/8\kappa$. We therefore have the steady state solution:

$$T_{ss} = \frac{\dot{q}((L/2)^2 - x^2)}{2\kappa} \tag{5.39}$$

To derive the full solution let:

$$T(x, t) = T_{ss} + W(x, t) \tag{5.40}$$

Then $W(x, t)$ must obey the heat equation:

$$\frac{\partial^2 W(x,t)}{\partial x^2} - \frac{1}{D_T}\frac{\partial W(x,t)}{\partial t} = 0 \tag{5.41}$$

The initial condition gives:

$$W(x, 0) = -\frac{\dot{q}((L/2)^2 - x^2)}{2\kappa} \tag{5.42}$$

The use of separation of variable as well as the boundary condition Eq.5.37 gives a solution of the general form:

$$W(x, t) = \sum_{n=1}^{\infty} a_n e^{-\lambda_n^2 D_T t} cos(\lambda_n x) \tag{5.43}$$

where n is odd and $\lambda_n = n\pi/L$. We can use the initial condition Eq.5.42 to calculate the values of a_n. Only the odd terms are non-zero therefore n is denoted by $2n - 1$, thus:

$$a_n = \frac{4\dot{q}L^2}{\kappa\pi^3(2n-1)^3}(-1)^n \tag{5.44}$$

This gives the final temperature solution:

$$T(x, t) = \frac{\dot{q}}{\kappa}\left[\frac{L^2}{8} - \frac{x^2}{2} + \sum_{n=1}^{\infty} \frac{4L^2(-1)^n}{\pi^3(2n-1)^3} e^{-\left(\frac{(2n-1)\pi}{L}\right)^2 D_T t} cos\left(\frac{(2n-1)\pi x}{L}\right)\right] \tag{5.45}$$

The heat flux solution is:

$$Q(x, t) = \dot{q}\left[x + \sum_{n=1}^{\infty} \frac{4L(-1)^n}{\pi^2(2n-1)^2} e^{-\left(\frac{(2n-1)\pi}{L}\right)^2 D_T t} sin\left(\frac{(2n-1)\pi x}{L}\right)\right] \tag{5.46}$$

5.3.2 Analytical Results

The solutions to Eq.5.46 are displayed in Fig.5.14. We set $L = 100mm$. The value of $\dot{q} = 1$ shown.

As expected the results show an increase toward the steady state solution at which time the maximum temperature value is given by:

$$T_{Max} = \frac{\dot{q}L^2}{8\kappa} = 1250K \tag{5.47}$$

The heat flux at the material centre remains zero with heat travelling out from the centre point with a linear profile at steady state.

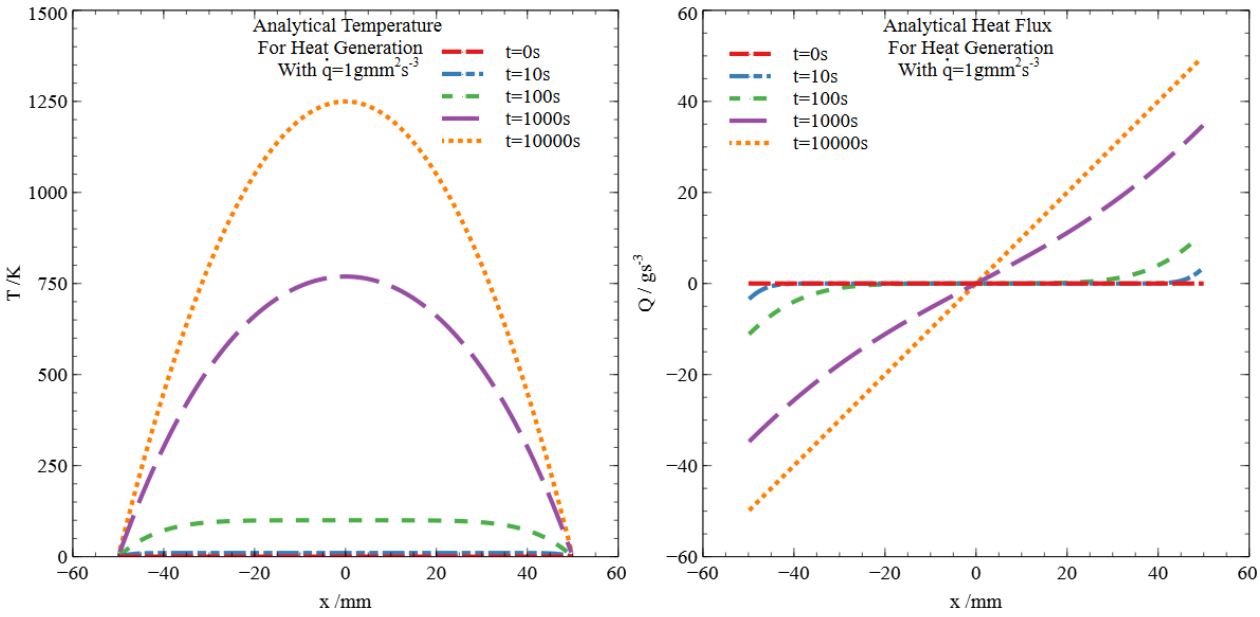

Figure 5.14: Analytical solutions for the 1D heat source model shown in Fig.5.15. Up to $n = 100$ frequencies included. Shown here for heat generation $\dot{q} = 1gmm^2/s^3$. Left the temperature profile, right the heat flux.

5.3.3 Heat Sources within SPAM

The model outline is shown schematically in Fig.5.15. Monaghan offers a method for dealing with heat sources at a point within SPAM [51]. Here a simple method for dealing with heat generation across a material is proposed. We can rearrange the expression for heat generation within the heat equation (Eq.5.35) to give the rate of change of temperature over time. We already have a smoothed particle approximation for the second spatial derivative of the temperature so we simply need to add the heat generation term. Using Eq.5.20 the rate of change of particle temperature T_i becomes:

$$\frac{dT_i}{dt} = C\sum_j (T_j - T_i)W(r_{ij}) + \frac{\dot{q}_i m_i}{\rho_i} \tag{5.48}$$

Here we use the particle volume approximation $V_i = m_i/\rho_i$, and as before C is given by Eq.5.21.

We use fixed boundary condition at $x = -L/2$ and $x = L/2$ to keep the system ends at zero temperature as shown in Fig.5.15.

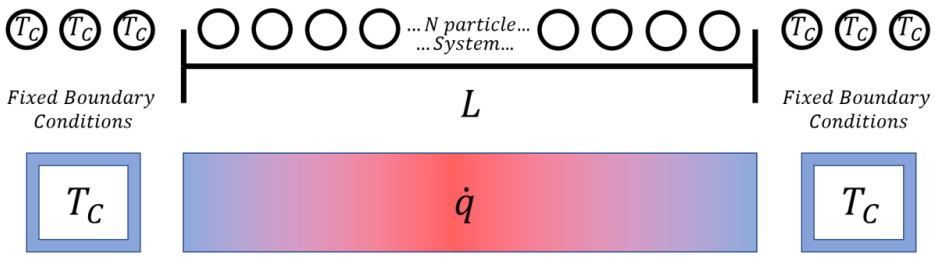

Figure 5.15: Visualisation of the 1D heat generation model. The system produces heat at rate $\dot{q}$. Both ends are held at fixed temperature T_C. A visual representation of the SPAM particle formulation for the model is also shown, with fixed boundary particles at each end. We use centre $x = 0$ such that $-L/2 < x < L/2$.

5.3.4 SPAM Results

For the simulation results shown here we use a smoothing length $H = 3$mm and time step $dt = 0.1s$. The system length is $L = 100mm$. The simulation results are shown in Fig.5.16. The temperature distribution evolves towards a steady state and is stable from $t >\approx 2000$. The final steady state peak temperature has a visible error. The expected steady state peak temperature is $T_{ss}^{SPH} \approx 1275$. Note that the boundary error for the heat flux is due to the fixed particles having $Q = 0$. This has no effect on the temperature evolution but causes the heat flux to have interpolation errors at the boundary.

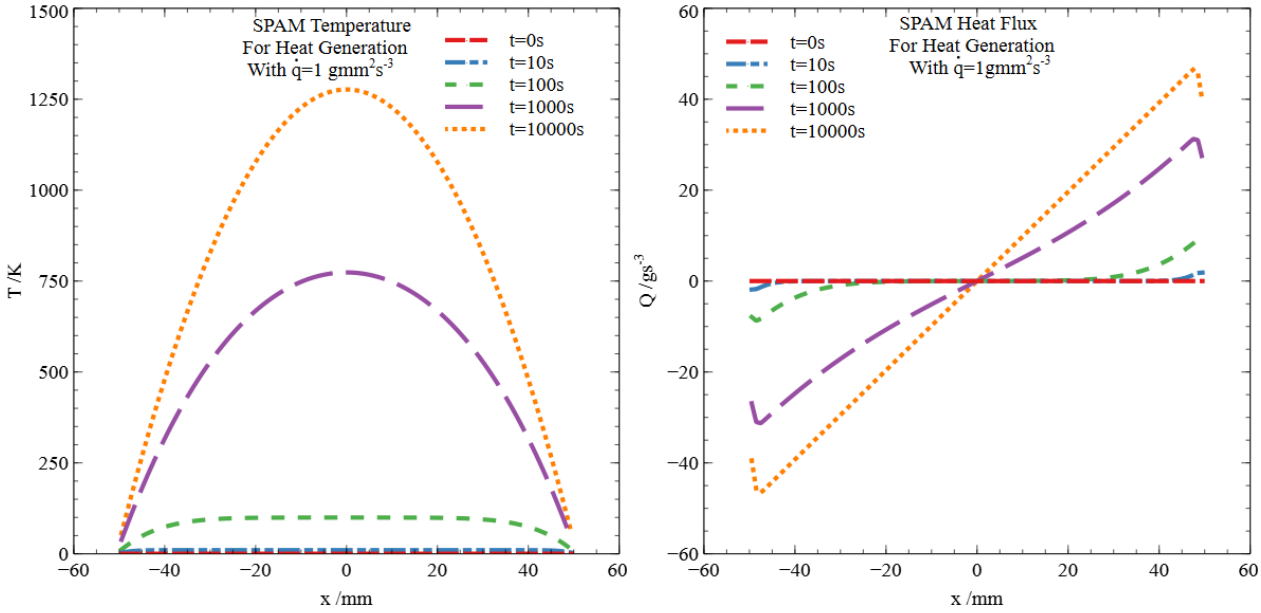

Figure 5.16: SPAM results for the 1D heat source model shown in Fig.5.15. Shown here for heat generation $\dot{q} = 1gmm^2/s^3$. Left temperature profile, right heat flux.

The spatial distribution of the error in the final temperature profile for these results is given in Fig.5.17. The effect of the boundary conditions can be observed by the 'jump' in error at the simulation edges shown by the lack of smoothness in the distribution at the edges. Once again it can be observed that the error is minimal at the centre of the simulation.

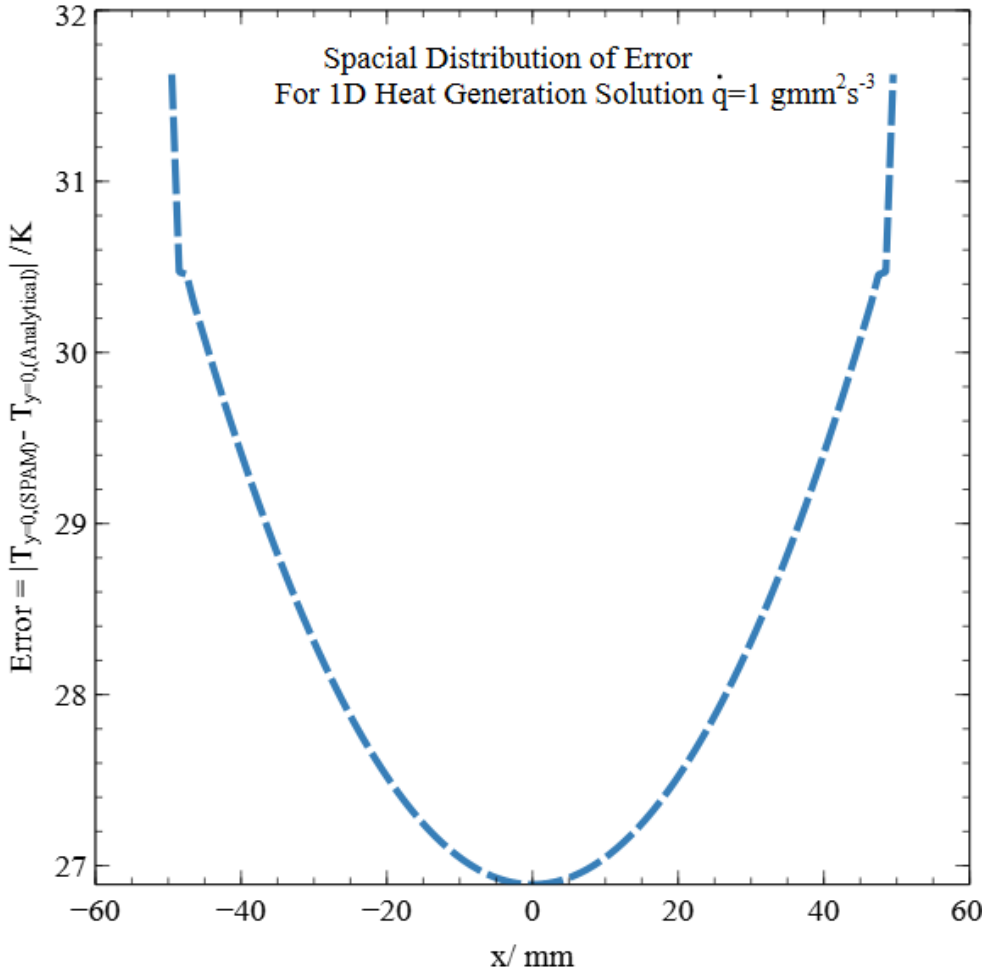

Figure 5.17: Spatial distribution of error for the SPAM results vs the analytical results given by the 1D heat source model shown in Fig.5.15. Shown here for heat generation $\dot{q} = 1gmm^2/s^3$ at $t = 10,000s$.

5.3.5 Behaviour of Residual Error

A direct comparison of the SPAM and analytical results for the 1D heat source model is given in Fig.5.18. The error increases with time for both values of $\dot{q}$. There are several probable reasons for this error. The error is most likely some form of interpolation error. By this it is meant that the values given for the problem are not the expected values once the smoothing function is taken into account. For example one possible error is introduced by the fixed boundaries. The use of boundary particles all with $T_i = 0$K gives a slightly higher boundary interpolation temperature as it is a weighted sum of both boundary *and* system particles close to the boundary.

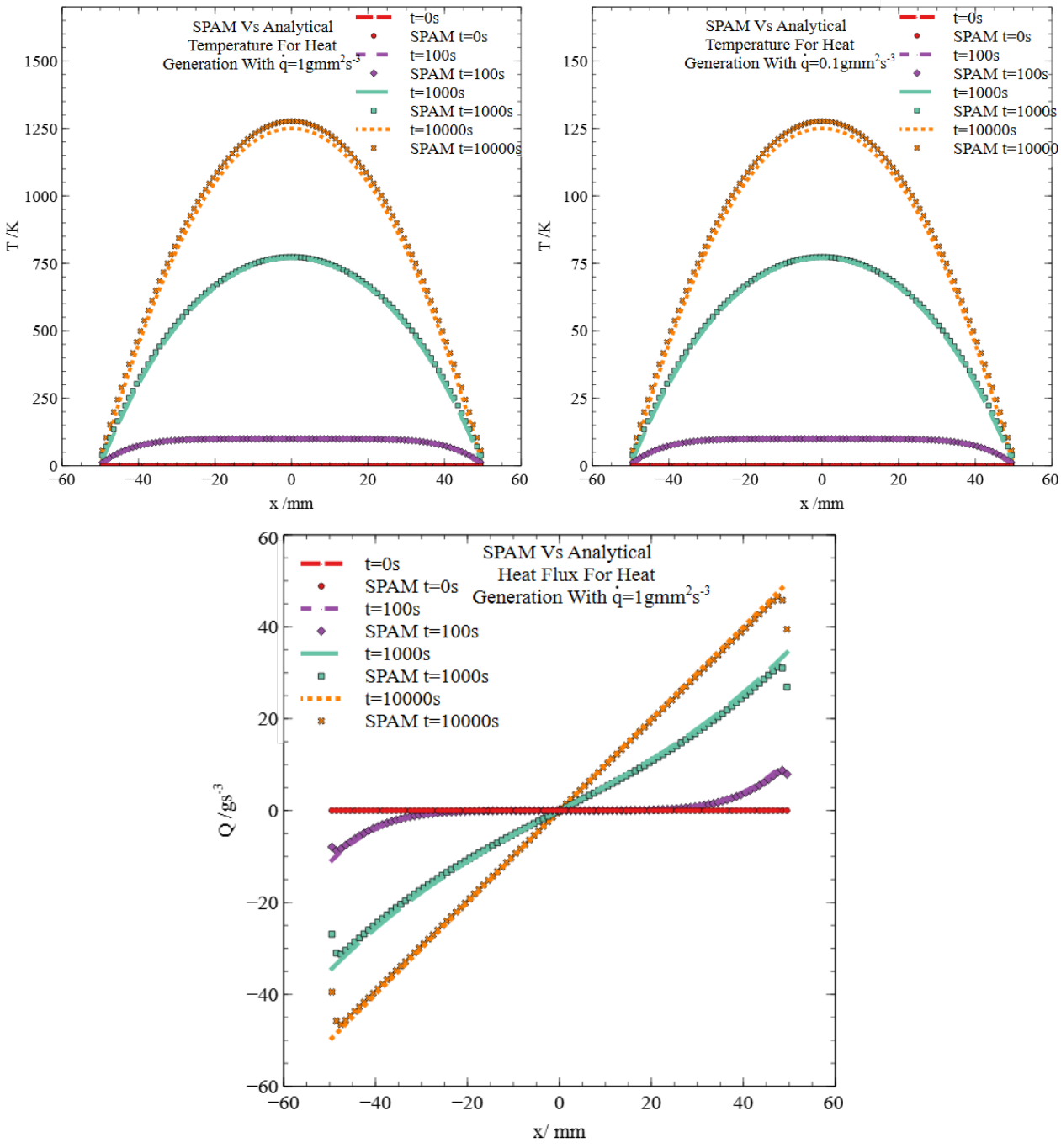

Figure 5.18: SPAM results vs analytical for the 1D heat source model shown in Fig.5.15. Shown here for 2 values of heat generation. Left $\dot{q} = 1\text{gmm}^2/\text{s}^3$, right $\dot{q} = 0.1\text{gmm}^2/\text{s}^3$. Bottom shows a comparison of the heat flux error for $\dot{q} = 1\text{gmm}^2/\text{s}^3$ case.

The residual error in the SPAM is calculated using Eq.3.101. The results are shown in Fig.5.19 with logarithmic scaling. This shows that the error in the simulation grows exponentially with time. This suggests that the error factor is some constant interpolation error as described and that its contribution grows with time integration. It therefore would suggest that the boundary particles

are still credible sources of error.
To better determine the source of error we therefore calculate the interpolated temperature at the boundary $x = 50mm$. The temperature is calculated for the case $\dot{q} = 1\text{gmm}^2/\text{s}^3$ at time steps with orders of magnitude 10^n. These calculated temperatures are shown against the calculated residual errors in Fig.5.20.

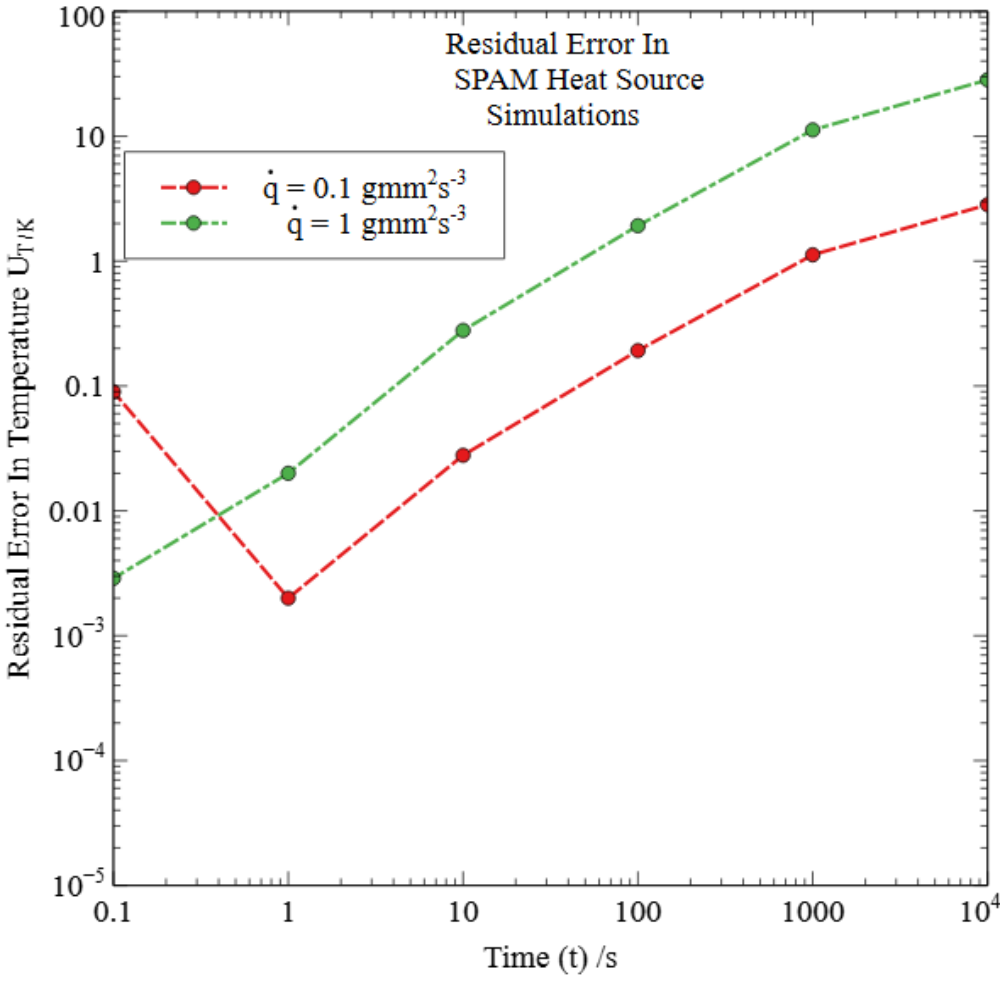

Figure 5.19: Residual error in the SPAM simulation of heat generation compared with the analytical model. Shown here for 2 values of heat generation $\dot{q} = 0.1, 1\text{gmm}^2/\text{s}^3$

It can be seen from Fig.5.20 that at steady state for $\dot{q} = 1\text{gmm}^2/\text{s}^3$ the boundary temperatures for the fixed boundary case are $T \approx 35$K. This is a significant error compared to the desired temperature of $T = 0$K enforced by the fixed boundary particles. This supports the hypothesis that the SPAM error is boundary driven. To finally demonstrate this we run the SPAM code for mirror boundaries as described in Sec.3.3.3. Mirror boundaries guarantee a boundary temperature of $T = 0$K. The results can be seen in Fig.5.21. Clearly the error is almost entirely eliminated by proper boundary temperatures. As previously discussed mirror boundaries offer complications for complex geometries. However their use here validates the use of Eq.5.48 to accurately model heat sources within SPAM.

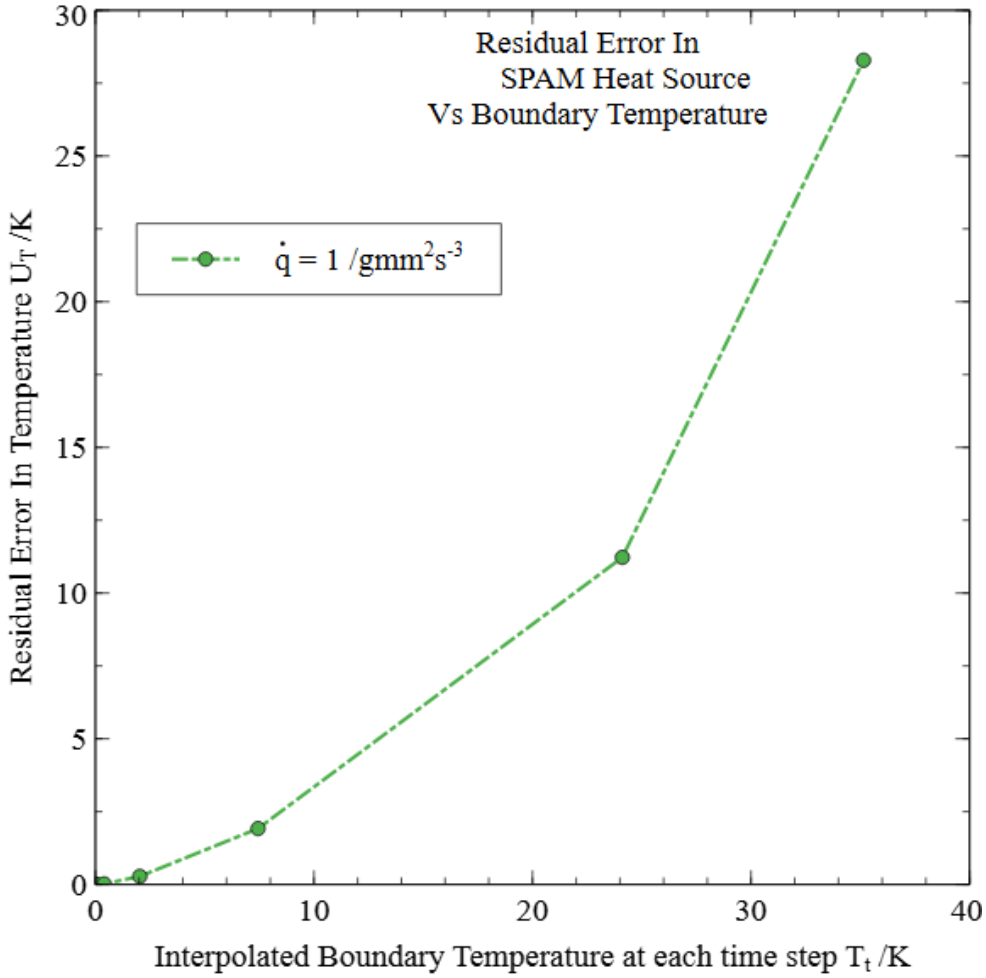

Figure 5.20: Residual error in the SPAM simulation of heat generation compared with the analytical model. Shown against the interpolated value of the boundary temperature for each time step $t = 10^n$ for $n = -1$ to 4. Shown here for a value of heat generation $\dot{q} = 1\text{gmm}^2/\text{s}^3$

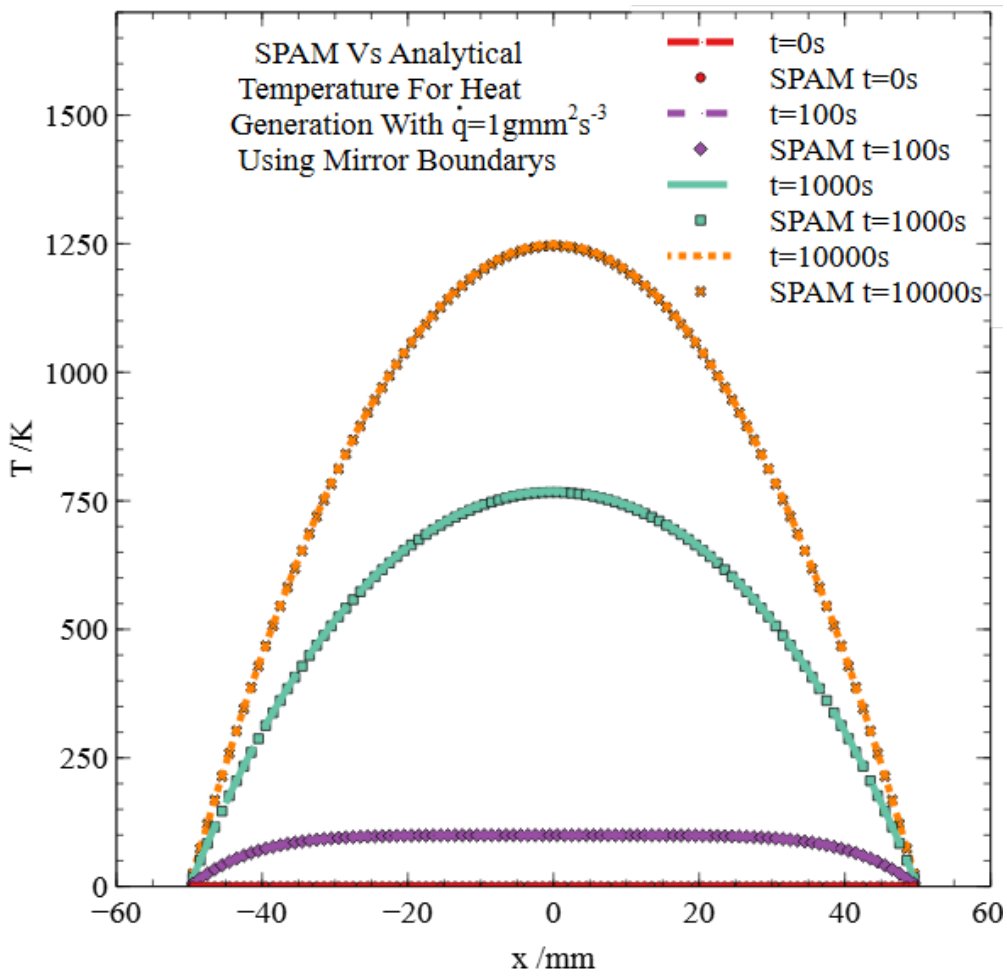

Figure 5.21: Analytical results vs SPAM results for the heat source model done with mirror boundary conditions to enforce a boundary temperature of $T = 0$K. Shown here for a value of heat generation $\dot{q} = 1\text{gmm}^2/\text{s}^3$

5.4 1D Thermal Interface Model

Within a nuclear fuel rod heat will be transferred between materials of different thermal properties. In particular the fuel element and the cladding have different thermal conductivities. It is essential therefore that the SPAM model be able to accurately model the transfer of heat at material interfaces with different conductivities. To test this the simple 1D model outlined in Fig.5.22 is presented. The materials will also have varying densities and specific heats however they have been assumed to be the same across both materials within the model presented here. We also assume negligible contact resistance.

We model two materials of individual length $L/2$ with conductivites κ_1 extending $-L/2 < x < 0$ and κ_2 extending $0 < x < L/2$. We assume constant boundary temperatures such that $T(-L/2) = T_c$ and $T(L/2) = T_h$. We then arbitrarily choose $T_c = 0K$ and $T_h = 1K$. With total system length $L = 100$mm. We set $\kappa_1 = 1\text{gmm/s}^3\text{K}$ but explore a range of four values for $\kappa_2 = 1, 2, 5, 10\text{gmm/s}^3K$. This allows for verification that the modified SPAM still reduces to the standard linear profile

expected for the $\kappa_1 = \kappa_2 = 1\text{gmm/s}^3\text{K}$ case.

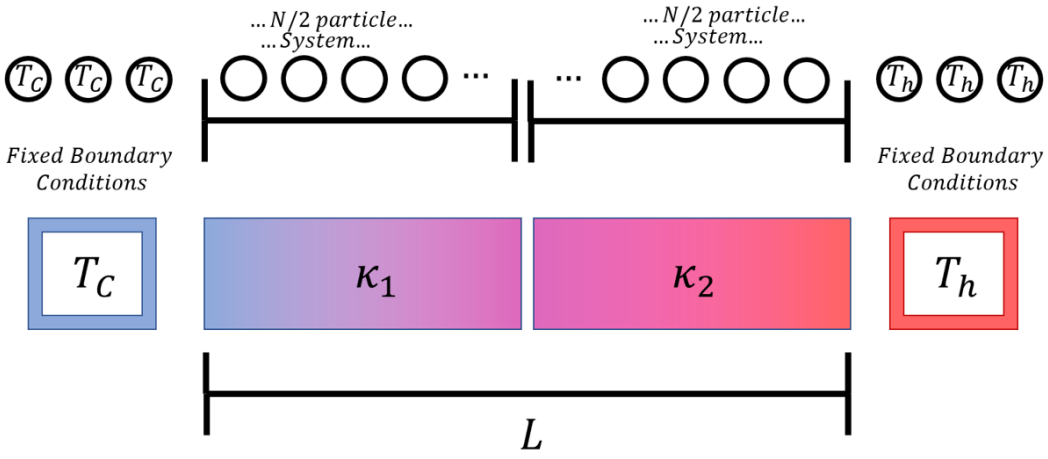

Figure 5.22: Visualisation of the 1D thermal interface model. The system is split into two material sections with two individual thermal conductivities κ_1, κ_2 which we assume to be constant. Both ends are held at fixed temperatures T_c, T_h. A visual representation of the SPAM particle formulation for the model is also shown, with fixed boundary particles at each end. We use centre $x = 0$ such that the left material extends $-L/2 < x < 0$ and the right material extends $0 < x < L/2$.

This model has already been studied by Monaghan [108] in order to demonstrate the ability of his proposed temperature evolution algorithm to handle multiple thermal conductivities. It is ideal to reuse this model in order to test a similar implementation of multiple thermal conductivities through their harmonic mean on the Hoover evolution. It is found that this kind of implementation can cause issues on the material boundary which introduces in accuracy into the method.

5.4.1 Steady State Solution

The transient solution for this case is complex and therefore avoided here. However demonstration of the steady state solution to this problem is sufficient to test the modification to the SPAM and show its validity at dealing with thermal interfaces. Let the $x < 0$ region be defined as region 1, and $x > 0$ region 2 for materiel in the region $-50 < x < 50$. We can therefore say that both regions must obey the heat equation in the steady state ($\partial T/\partial t = 0$) as:

$$\frac{\partial^2 T_1}{\partial x^2} = 0 \tag{5.49}$$

$$\frac{\partial^2 T_2}{\partial x^2} = 0, \tag{5.50}$$

with the previously given boundary conditions:

$$T_1(-L/2) = 0 \tag{5.51}$$

$$T_2(L/2) = 1 \tag{5.52}$$

It is assumed that at the interface the temperature and heat flux are continuous:

$$T_1(0) = T_2(0) \tag{5.53}$$

$$-\kappa_1 \frac{\partial T_1}{\partial x}\bigg|_{x=0} = -\kappa_2 \frac{\partial T_2}{\partial x}\bigg|_{x=0} \tag{5.54}$$

From here it is a simple matter to integrate the heat equations for both materials as:

$$T_1 = \frac{C_1 x}{\kappa_1} + C_2 \tag{5.55}$$

$$T_2 = \frac{C_3 x}{\kappa_2} + C_4 \tag{5.56}$$

Here C_n represents the constants of integration. Th first of which can be determined by the use of Eq.5.51 as:

$$C_2 = \frac{C_1 L}{2\kappa_1} \tag{5.57}$$

Similarly use of Eq.5.52 gives:

$$C_4 = 1 - \frac{C_3 L}{2\kappa_2} \tag{5.58}$$

Then use of the continuity boundary conditions Eq.5.53 and Eq.5.54 give the two relations:

$$C_3 = C_1 \tag{5.59}$$

$$C_3 = \frac{2\kappa_2}{L} - C_1 \frac{\kappa_2}{\kappa_1} \tag{5.60}$$

Combining these we arrive at:

$$C_1 = \frac{2\kappa_2 \kappa_1}{L(\kappa_1 + \kappa_2)} \tag{5.61}$$

This gives the final steady state solutions as:

$$T_1(x) = \frac{2\kappa_2 \left(x + \frac{L}{2}\right)}{L(\kappa_1 + \kappa_2)} \tag{5.62}$$

$$T_2(x) = 1 + \frac{2\kappa_1 \left(x - \frac{L}{2}\right)}{L(\kappa_1 + \kappa_2)} \tag{5.63}$$

The heat flux is given by:

$$Q_1(x) = Q_2(x) = \frac{-2\kappa_1 \kappa_2}{L(\kappa_1 + \kappa_2)} \tag{5.64}$$

5.4.2 Steady State Results

The steady state solutions are shown in Fig.5.23 for vales of $\kappa_2 = 1, 2, 5, 10 \text{gmm/s}^3\text{K}$. As expected we see the linear profile appear for the case $\kappa_1 = \kappa_2 = 1 \text{gmm/s}^3\text{K}$. Each material section in isolation creates a linear profile which is also expected as all individual material thermal conductivity are constant.

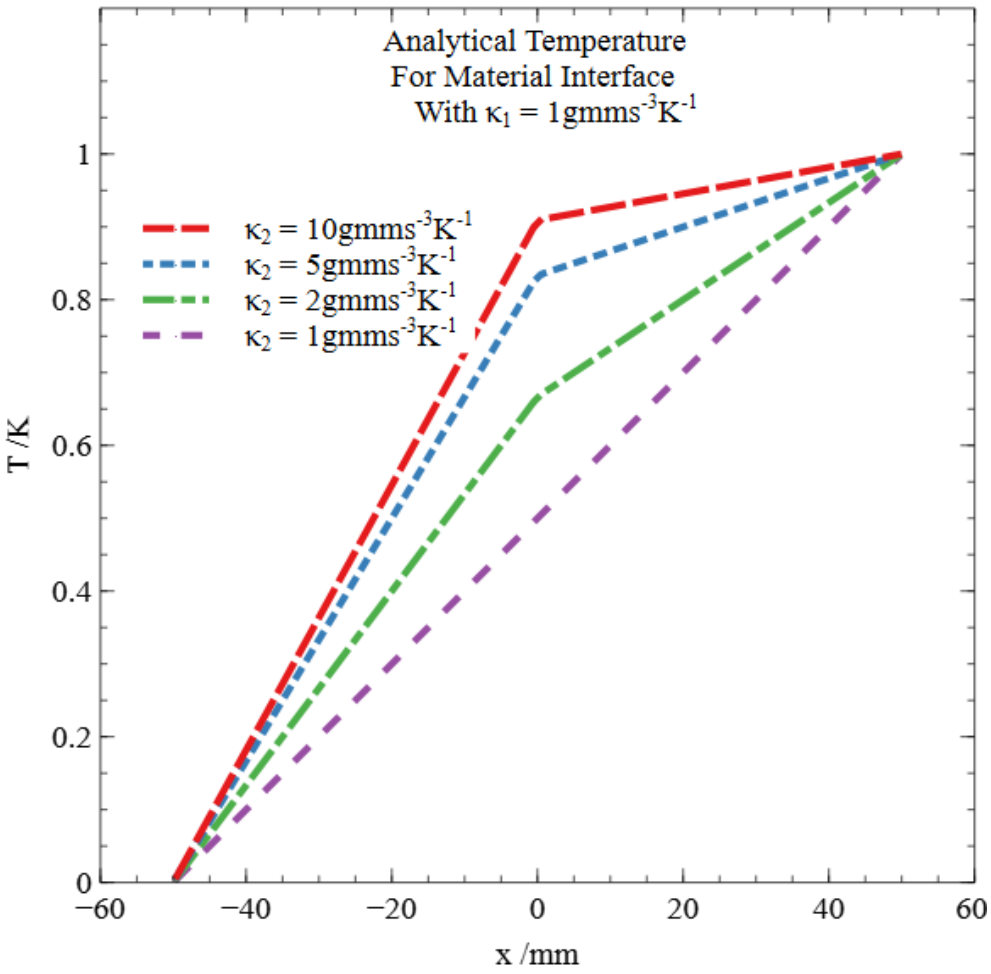

Figure 5.23: Analytical solutions for the steady state 1D thermal interface model shown in Fig.5.22. All curves have $\kappa_1 = 1\text{gmm/s}^3\text{K}$ for $-50\text{mm} < x < 0\text{mm}$. The material extending $0\text{mm} < x < 50\text{mm}$ is given four different thermal conductivity values $\kappa_2 = 1, 2, 5, 10\text{gmm/s}^3\text{K}$. The $x = -50\text{mm}$ surface is constant at $T_c = 0K$ the $x = 50\text{mm}$ most surface $T_h = 1K$.

The heat flux is shown in Fig.5.24. It can be seen that the heat flux should be constant through the whole system. The magnitude of Q is only dependant on the system length L and the two material thermal conductivities κ_1, κ_2 as demonstrated by Eq.5.64.

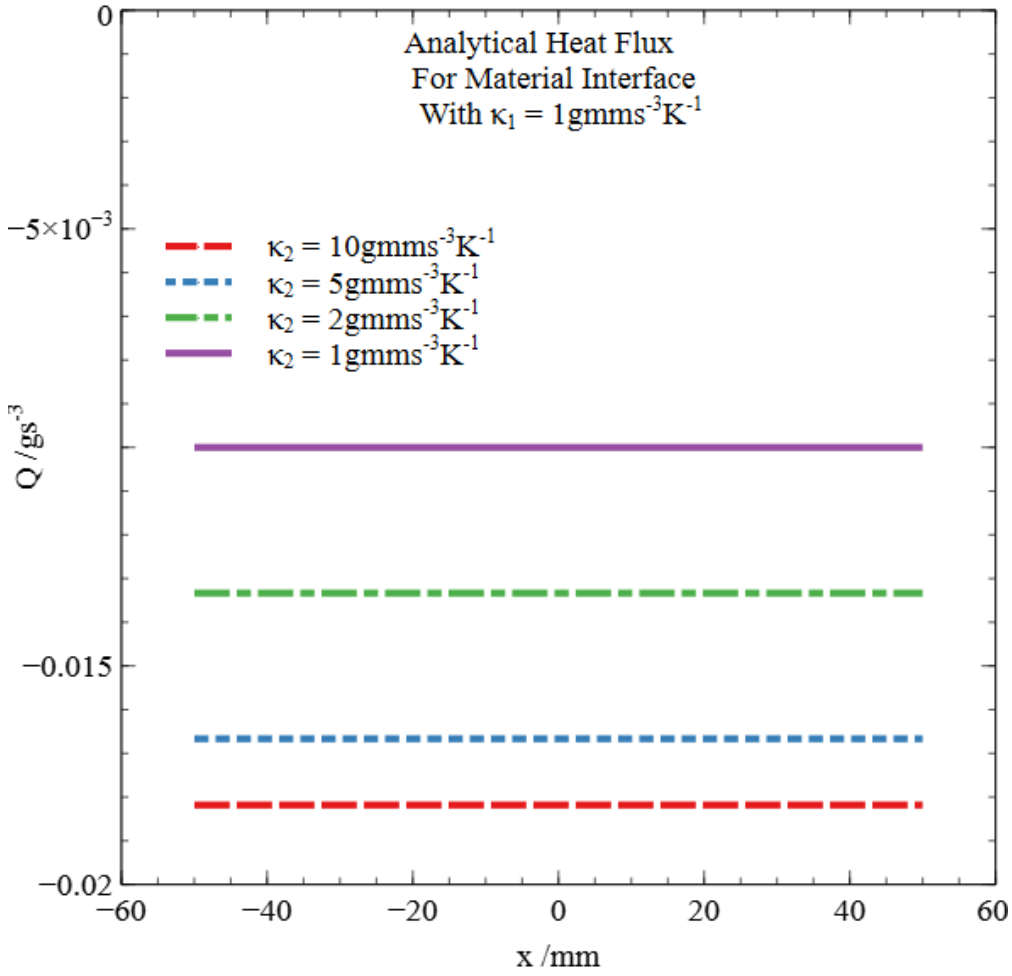

Figure 5.24: Heat flux solutions for the steady state 1D thermal interface model shown in Fig.5.22. All curves have material with constant thermal conductivity of $\kappa_1 = 1\text{gmm/s}^3\text{K}$ for $-50\text{mm} < x < 0\text{mm}$. The material extending $0\text{mm} < x < 50\text{mm}$ is given four different thermal conductivity values represented by $\kappa_2 = 1, 2, 5, 10\text{gmm/s}^3\text{K}$.

5.4.3 Thermal Interfaces within SPAM

The current formulation of Hoover's temperature evolution is given by Eq.5.20. However this formulation cannot be correct for different particle thermal conductivities κ_i, κ_j. The SPAM equations must act symmetrically on particle pairs i, j due to the conservation of energy. In its current form the addition to particle i due to particle j assuming unit density and specific heat $\rho = 1\text{g/mm}^3$,$C_p = 1\text{mm}^2/\text{s}^2\text{K}$ is:

$$\Delta_j \left(\frac{dT_i}{dt} \right) = \frac{\kappa_i}{\sum \frac{x^2 w(x)}{2}} (T_j - T_i) W(r_{ij}) \tag{5.65}$$

Here Δ_j denotes the difference due to particle j. The change however in rate of change of temperature of particle j due to i is given by:

$$\Delta_i \left(\frac{dT_j}{dt} \right) = \frac{\kappa_j}{\sum \frac{x^2 w(x)}{2}} (T_i - T_j) W(r_{ji}) \tag{5.66}$$

These expressions can be shown to be identical if and only if $\kappa_i = \kappa_j$. The thermal conductivity must therefore be replaced by some average $\bar{\kappa}$ in order to maintain symmetry. The simplest choices for this would be the arithmetic or the geometric means. Conductivity is however a rate of thermal transmission. As such, a better choice for averaging rates of change is the harmonic mean. The harmonic mean is calculated as:

$$\bar{\kappa}_{ij} = \left(\frac{\frac{1}{\kappa_i} + \frac{1}{\kappa_j}}{2} \right)^{-1} \tag{5.67}$$

This reduces to:

$$\bar{\kappa}_{ij} = \frac{2\kappa_i \kappa_j}{\kappa_i + \kappa_j} \tag{5.68}$$

This expression reduces to κ_i for $\kappa_i = \kappa_j$ as desired. The factor C in Hoover's temperature evolution for unit density and specific heat $\rho = 1\text{g/mm}^3$,$C_p = 1\text{mm}^2/\text{s}^2\text{K}$ then becomes:

$$C = \frac{2\kappa_i \kappa_j}{(\kappa_i + \kappa_j) \sum \frac{x^2 w(x)}{2}} \tag{5.69}$$

To correctly calculate the SPAM heat flux we must also modify the previously given equation with the new symmetrised thermal conductivity as:

$$Q_i = -\bar{\kappa}_{ij} \sum_j m_{ij} \left[T_j - T_i \right] \nabla_i w_{ij} / \rho_{ij} \tag{5.70}$$

5.4.4 SPAM Results

The modification to Hoover's temperature evolution given by Eq.5.69 is tested for the model with particle formulation shown by Fig.5.22. We use 6 fixed particles for each boundary with prescribed temperatures $T_c = 0K$ and $T_h = 1K$. This ensures the particle densities are properly calculated for all boundary particles within weight function range $H = 3\text{mm}$ of the boundary points. We use $dt = 0.1s$ with an initial system state of $T(t = 0) = 0$. The system is run for 100000 time steps. The results given in Fig.5.25 are therefore given for $t = 10,000s$ well after the system has reached a stable state. The SPAM results exhibit the desired behaviour with two linear regions with gradient defined by the independent thermal conductivities. One linear region is recovered for the case $\kappa_1 = \kappa_2$. Each region is length $L/2 = 50$ made up of $N/2 = 50$ particles of unit density $\rho_i = 1$ such that each material is unit density.

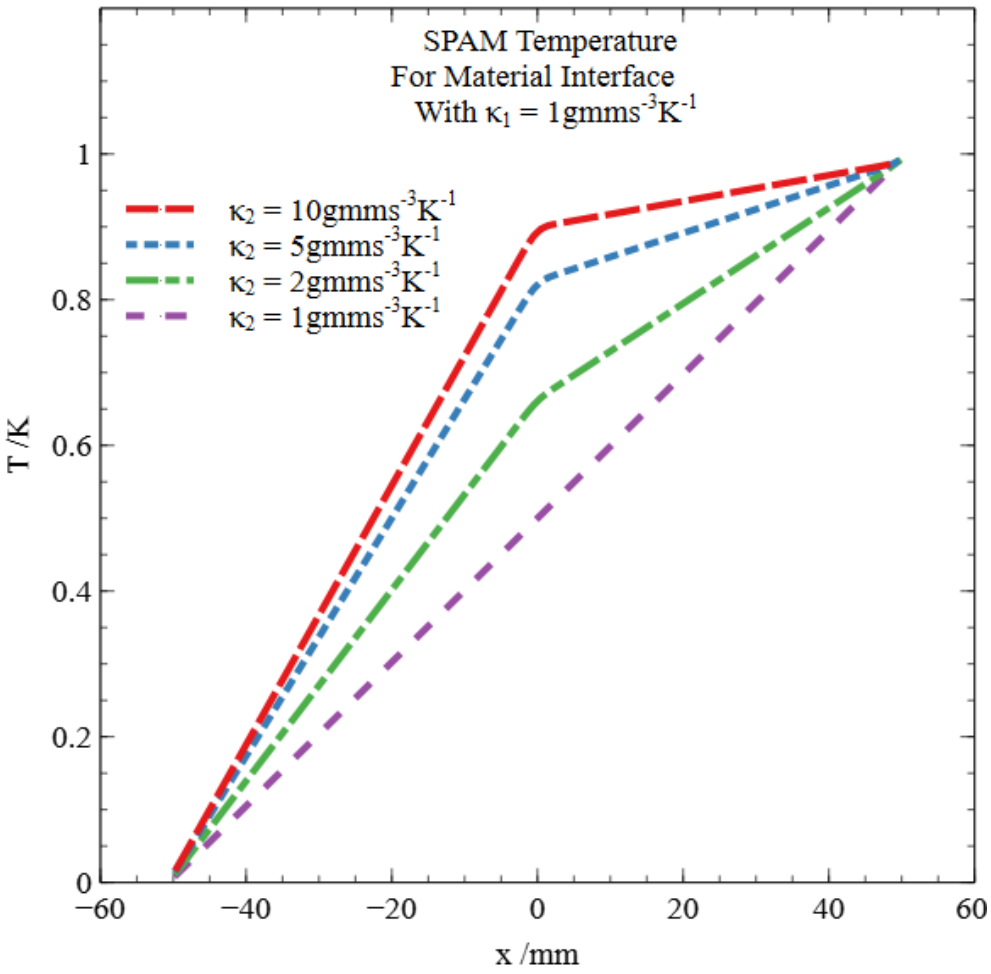

Figure 5.25: SPAM results for the steady state 1D thermal interface model shown in Fig.5.22. All curves have material with constant thermal conductivity of $\kappa_1 = 1\text{gmm/s}^3\text{K}$ for $-50\text{mm} < x < 0\text{mm}$. The material extending $0\text{mm} < x < 50\text{mm}$ is given four different thermal conductivity values $\kappa_2 = 1, 2, 5, 10\text{gmm/s}^3\text{K}$. The $x = -50\text{mm}$ surface is constant at $T_c = 0K$, the $x = 50\text{mm}$ surface $T_h = 1K$.

The heat flux within the SPAM model was calculated using Eq.5.70 for each value of κ_2 and shown in Fig.5.26. The interpolation error at the boundaries is due to the use of fixed particles with $Q = 0$. It can be seen that the interpolated heat flux is not smoothed across the material at $x = 0$. It was found that use of $\bar{\kappa}$ reduced the discontinuity in the heat flux significantly, however a constant profile is not achieved. A better estimate for $\bar{\kappa}$ which accounts for the distance between the particle pairs and weighs the thermal conductivity accordingly may reduce these errors. This may take the form:

$$\bar{\kappa}_i = \left(\frac{1-f}{\kappa_i} + \frac{f}{\kappa_j} \right) \tag{5.71}$$

where $f = \Delta_P / R_i j$. This idea is based on interface treatment in fluids [135]. Implementation of this correction was not tested within the time frame of this work.

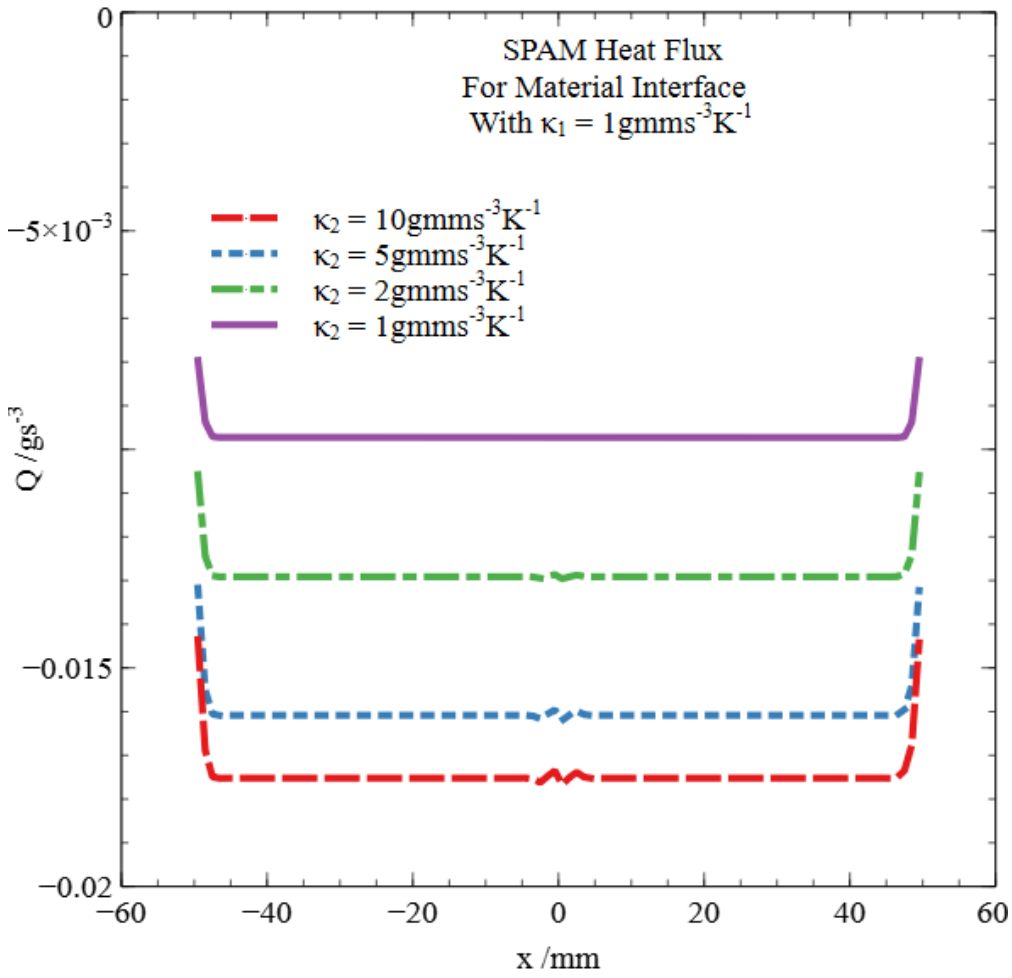

Figure 5.26: SPAM heat flux results for the steady state 1D thermal interface model shown in Fig.5.22. All results have material with constant thermal conductivity of $\kappa_1 = 1\text{gmm/s}^3\text{K}$ for $-50\text{mm} < x < 0\text{mm}$. The material extending $0\text{mm} < x < 50\text{mm}$ is given four different thermal conductivity values $\kappa_2 = 1, 2, 5, 10\text{gmm/s}^3\text{K}$. The $x = -50\text{mm}$ surface is constant at $T_c = 0K$, the $x = 50\text{mm}$ surface $T_h = 1K$.

5.4.5 Behaviour of Residual Error

Direct comparison of the steady state analytical results and the SPAM results is made in Fig.5.27. It is immediately apparent that there is a small error in the SPAM results, in the region $0\text{mm} < x < 50\text{mm}$, which appears to increase with increasing value of κ_2. Again as with the heat source case it is hypothesised that this error is likely due to incorrect calculation of the boundary temperature through the use of fixed particles. Higher values of κ_2 cause increased particle temperatures near the right boundary with fixed values $T_h = 1K$. This means that any error in the boundary particle temperature is more pronounced in the second material as the temperature gap it covers is lower, therefore an error in boundary interpolation is a far greater percentage error compared with the material temperature gap.

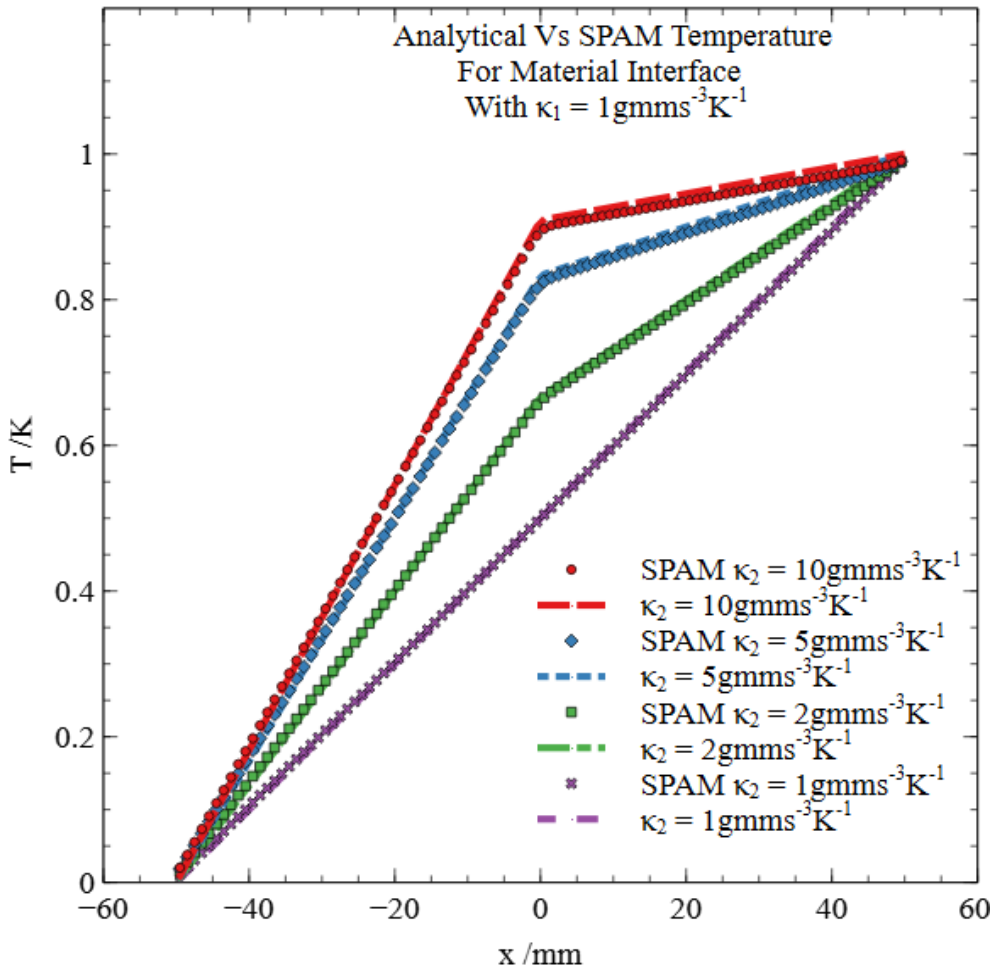

Figure 5.27: SPAM results vs analytical for the 1D heat source model shown in Fig.5.15. All curves have material with constant thermal conductivity of $\kappa_1 = 1\text{gmm/s}^3\text{K}$ for $-50\text{mm} < x < 0\text{mm}$. The material extending $0\text{mm} < x < 50\text{mm}$ is given four different thermal conductivity values $\kappa_2 = 1, 2, 5, 10\text{gmm/s}^3\text{K}$. The $x = -50\text{mm}$ surface is constant at $T_c = 0K$, the $x = 50\text{mm}$ surface $T_h = 1K$.

A similar error can be seen in the SPAM calculated heat flux shown in Fig.5.28. The discontinuous nature of the SPAM at $x = 0$ can be seen more pronounced with the plotted interpolation points. This is accompanied by an error in the predicted constant value of the heat flux which increases with the value of κ_2. It is again possible that this error is driven by error in the enforced boundary temperatures due to the fixed particle boundaries.

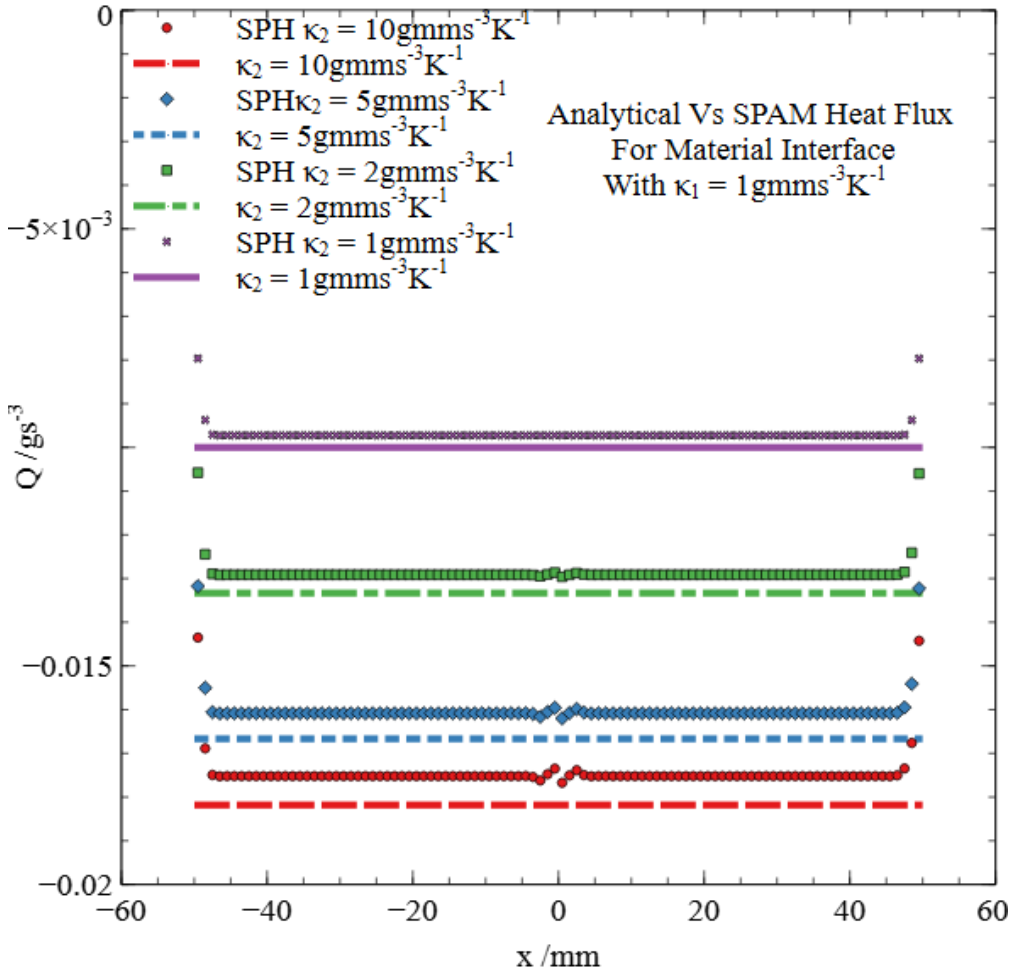

Figure 5.28: SPAM heat flux results vs analytical for the 1D heat source model shown in Fig.5.15. All curves have material with constant thermal conductivity of $\kappa_1 = 1$gmm/s^{3}K for -50mm$< x <$ 0mm. The material extending 0mm$< x <$ 50mm is given four different thermal conductivity values $\kappa_2 = 1, 2, 5, 10$gmm/s^{3}K. The $x = -50$mm surface is constant at $T_c = 0K$, the $x = 50$mm surface $T_h = 1K$.

The spatial distribution of the error for the simulation with $\kappa_2 = 10$ is shown in Fig.5.29. It is clear that the boundary conditions have an impact on the error incurred by the simulation from the non-smooth nature of the error distribution approaching the boundary. Of a greater significance however is the error distribution around $x = 0$. The error at this point appears discontinuous and is the highest deviation form the analytical results for the whole material. This supports the notion that improvements to the handling of thermal conductivity at the interface would greatly improve the results.

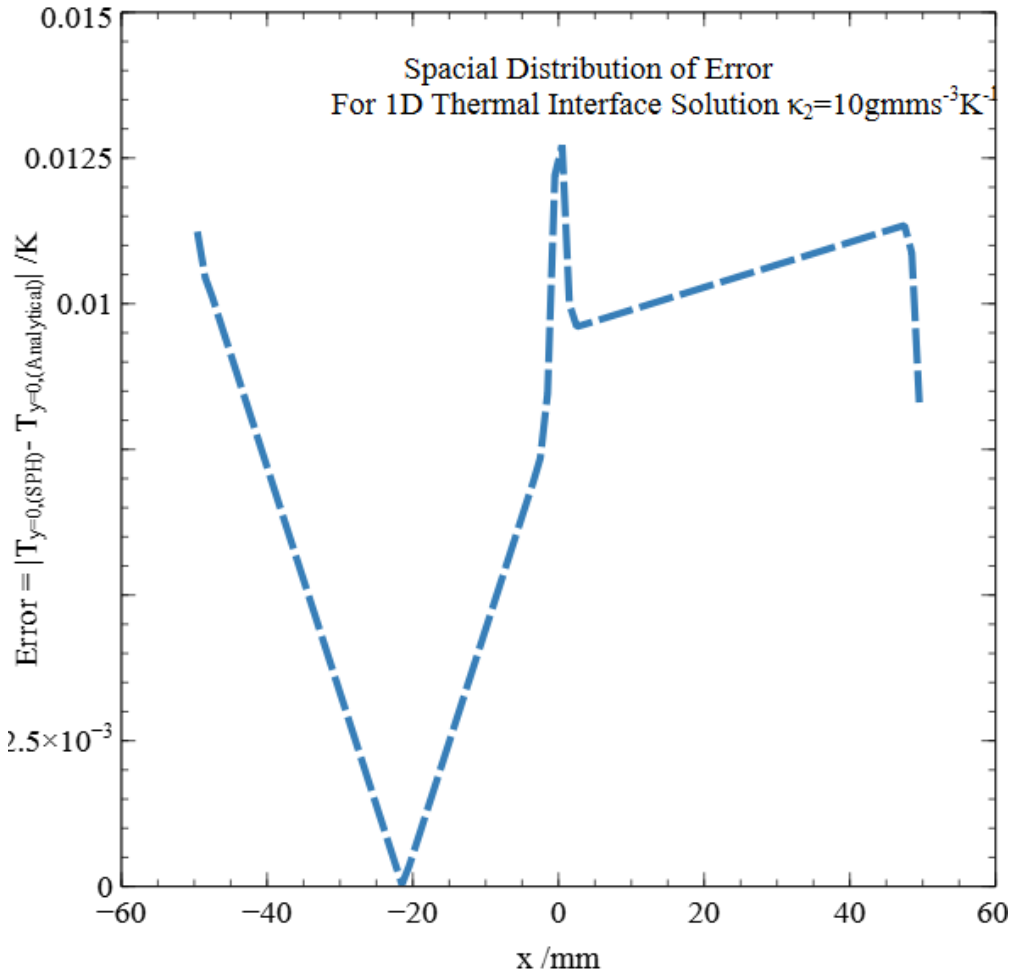

Figure 5.29: The spatial distribution of error for the SPAM results vs analytical in the 1D heat source model shown in Fig.5.15. The right most material extending 0mm$< x <$ 50mm is given thermal conductivity value $\kappa_2 = 10$.

The residual error in the SPAM is calculated using Eq.3.101. The results are shown in Fig.5.30. This shows that the error in the simulation grows logarithmically with the value of κ_2. This suggests that the magnitude of the error is directly affected by the final temperature profile of the right most material. This supports the hypothesis of interpolation errors within the boundary values being introduced into the system. To better investigate this, the SPAM results are computed for mirror boundary conditions which enforce the boundary temperature and shown in Fig.5.31. It can be seen that the error for the fixed case is almost entirely eliminated.

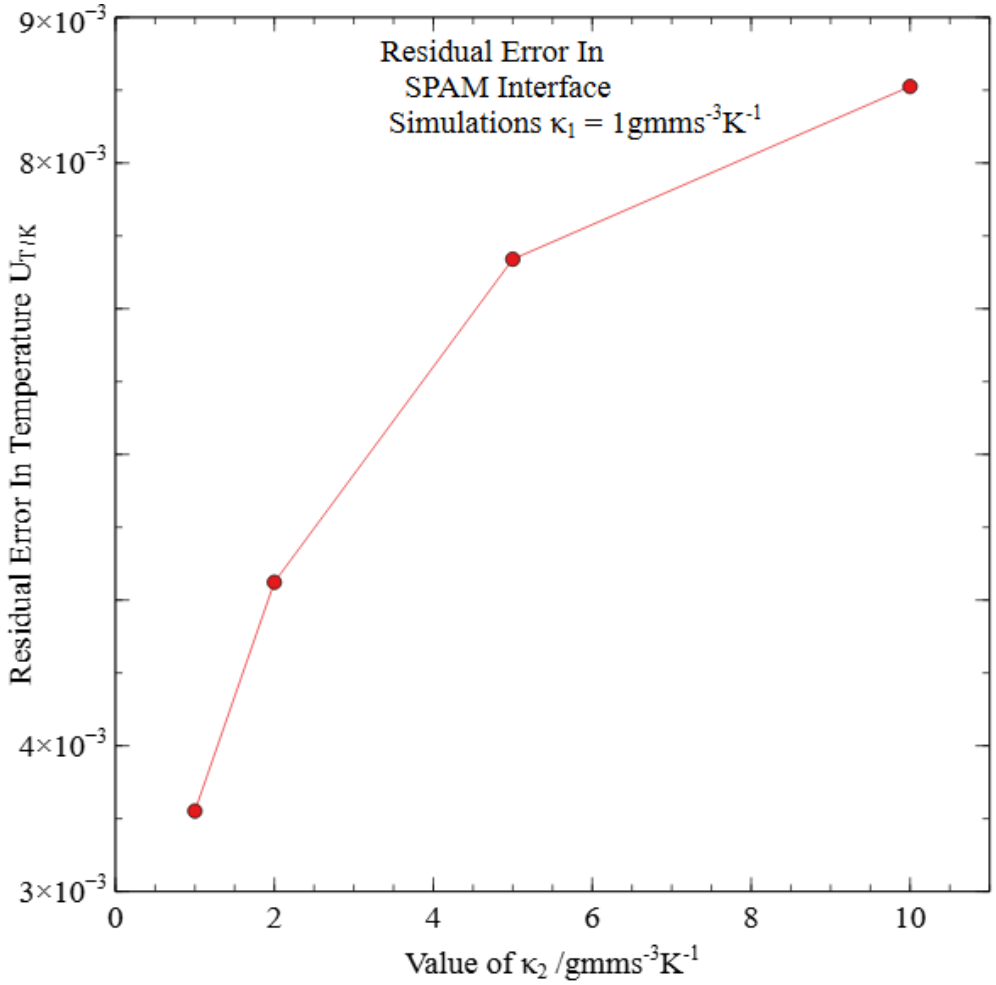

Figure 5.30: Residual error in the SPAM simulation of thermal interfaces compared with the analytical model. Shown here for four different thermal conductivity values $\kappa_2 = 1, 2, 5, 10\text{gmm/s}^3\text{K}$ for the right material.

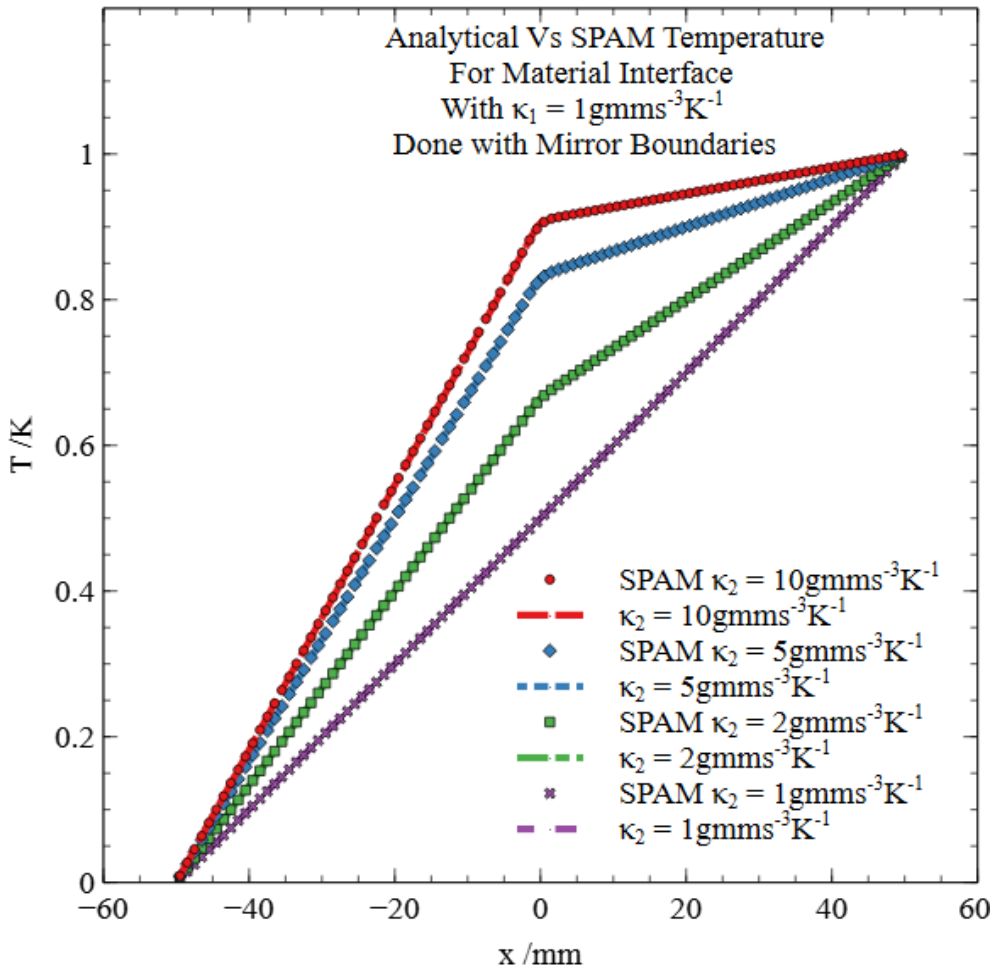

Figure 5.31: SPAM results vs analytical for the 1D heat source model done with mirror boundary conditions. All curves have material with constant thermal conductivity of $\kappa_1 = 1\text{gmm/s}^3\text{K}$ for $-50\text{mm} < x < 0\text{mm}$. The material extending $0\text{mm} < x < 50\text{mm}$ is given four different thermal conductivity values $\kappa_2 = 1, 2, 5, 10\text{gmm/s}^3\text{K}$. The $x = -50\text{mm}$ surface is constant at $T_c = 0K$ the $x = 50\text{mm}$ surface $T_h = 1K$.

Use of mirror boundary particles reduces the errors in the heat flux profiles shown in Fig.5.32, including at the interface $x = 0$ but does not entirely remove them. This suggests the error is not due to the boundary temperatures alone. Future work should focus on testing of Eq.5.71 but may also benefit from a treatment of the SPAM heat flux calculation based on the weight function W instead of the first derivative ∇W as for the temperature evolution in Eq.5.20.

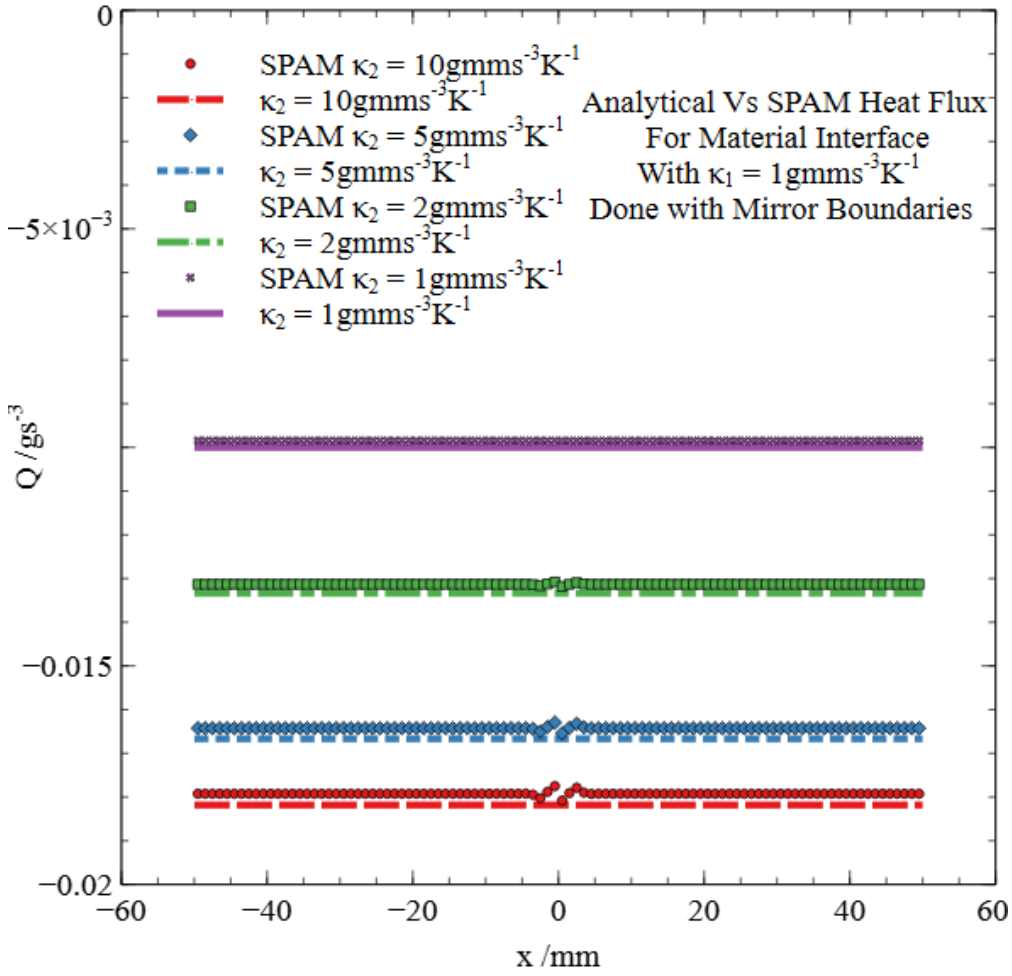

Figure 5.32: SPAM heat flux results vs analytical for the 1D heat source model done with mirror boundary conditions. All curves have material with constant thermal conductivity of $\kappa_1 = 1\text{gmm/s}^3\text{K}$ for $-50\text{mm} < x < 0\text{mm}$. The material extending $0\text{mm} < x < 50\text{mm}$ is given four different thermal conductivity values $\kappa_2 = 1, 2, 5, 10\text{gmm/s}^3\text{K}$. The $x = -50\text{mm}$ surface is constant at $T_c = 0K$ the $x = 50\text{mm}$ surface $T_h = 1\text{K}$.

5.5 1D Composite Fuel and Cladding Model

The implementation of heat sources, thermal interfaces and convective boundary conditions allows for the first simple thermal model of a fuel rod. These features have been successfully tested in isolation and will now be tested together in 1D. Consider the case of a composite material slab with no lateral heat flow. This case is then pure 1D with the heat equation obeyed only with regards to the x co-ordinate as in the previous examples.

This model assumes a layout of a 1D slice taken from the centre of radius of a fuel rod out to the coolant as outlined in Fig.5.33. The position $x = 0$ represents the centre of the fuel rod and therefore must have zero heat flux to maintain the symmetry of the problem. The right most end is assumed to undergo pure convection due to the coolant as described by Newton's law of cooling. The coolant is assumed to be at ambient temperature T_∞ and undergo convection with coefficient

h.
We assume negligible contact resistance, therefore the transfer of heat from the fuel to the cladding is defined only by the material conductivity κ_F and κ_C respectively. We assume heat generation within the fuel element at rate $\dot{q}$. To simplify the notation we assume the density and specific heat of the materials to be unity $\rho = 1\text{g/mm}^3$,$C_p = 1\text{mm}^2/\text{s}^2\text{K}$ therefore $D_T = \kappa$.
We assume that the thermal conductivity of each material is independent of temperature and thus constant throughout the simulations and solutions, not just in the steady state. We assume total fuel and cladding length of L_C with fuel length L_F. Finally to simplify the analytical solutions obtained we assume that a steady state is reached with $\frac{dT}{dt} = 0$ throughout the fuel pin. The left system boundary is assumed to be at $x = 0$.

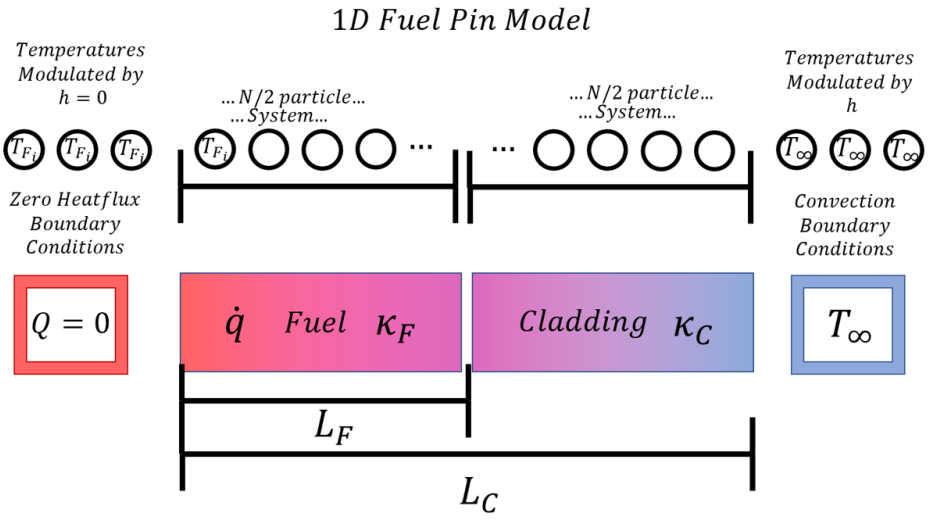

Figure 5.33: Visualisation of the 1D composite fuel and cladding model. The system is split into two material sections with two individual thermal conductivity's κ_F, κ_C which we assume to be constant. We assume heat flux $Q = 0$ at $x = 0$. We assume convection with h at $x = L_C$. A visual representation of the SPAM particle formulation for the model is also shown, with convection boundary particles at each end. Heat is produced at a rate $\dot{q}$ within the fuel component.

5.5.1 Steady State Solution

The steady state solution is derived in much the same way as for the interface model, but now with more complicated boundary conditions and an added heat source. We assume that the temperature in the fuel T_F and the temperature in the cladding T_C obey the heat equation in one dimension as:

$$\frac{\partial^2 T_F}{\partial x^2} = -\frac{\dot{q}}{\kappa_F} \tag{5.72}$$

$$\frac{\partial^2 T_C}{\partial x^2} = 0 \tag{5.73}$$

The external boundary conditions are given by:

$$-\kappa_F \frac{\partial T_F}{\partial x}\bigg|_{x=0} = 0 \tag{5.74}$$

$$-\kappa_C \frac{\partial T_C}{\partial x}\bigg|_{x=L_C} = h\left[T_C(L_C) - T_\infty\right] \tag{5.75}$$

The interface boundary condition states that temperature and heat flux are continuous:

$$T_F(L_F) = T_C(L_F) \tag{5.76}$$

$$-\kappa_F \frac{\partial T_F}{\partial x}\bigg|_{x=L_F} = -\kappa_C \frac{\partial T_C}{\partial x}\bigg|_{x=L_F} \tag{5.77}$$

From here it is simple to integrate the heat equations for both the fuel and cladding as:

$$T_F = -\frac{\dot{q}x}{\kappa_F} + \frac{C_1 x}{\kappa_F} + C_2 \tag{5.78}$$

$$T_C = \frac{C_3 x}{\kappa_C} + C_4 \tag{5.79}$$

Here C_n represents the constants of integration. Th first of which can be determined by the use of Eq.5.74 as:

$$C_1 = 0 \tag{5.80}$$

Similarly use of Eq.5.77 gives:

$$C_3 = -\frac{\dot{q}L_F}{\kappa_c} \tag{5.81}$$

Then use of the continuity boundary condition Eq.5.76 gives the relation:

$$C_2 = \dot{q}L_F^2\left[\frac{1}{2\kappa_F} - \frac{1}{\kappa_C}\right] + C_4 \tag{5.82}$$

Finally the convection condition Eq.5.75 gives:

$$C_4 = \dot{q}L_F\left[\frac{1}{h} + \frac{L_C}{\kappa_C}\right] + T_\infty \tag{5.83}$$

This gives the final steady state solutions as:

$$T_F(x) = \dot{q}\left[\frac{L_F}{h} + \frac{L_C L_F - L_F^2}{\kappa_C} + \frac{L_F^2 - x^2}{2\kappa_F}\right] + T_\infty \tag{5.84}$$

$$T_C(x) = \dot{q}L_F\left[\frac{1}{h} + \frac{L_C - x}{\kappa_C}\right] + T_\infty \tag{5.85}$$

The heat fluxes are calculated to be:

$$Q_F(x) = \dot{q}x \tag{5.86}$$

$$Q_C(x) = \dot{q}L_F \tag{5.87}$$

5.5.2 Steady State Results

The steady state solutions for the 1D nuclear fuel problem are presented in Fig.5.34. We assume a conductivity of the cladding ten times that of the fuel which are usually metal and ceramic materials respectively. Thus $\kappa_F = 1\text{gmm/s}^3\text{K}$ and $\kappa_C = 10\text{gmm/s}^3\text{K}$. We choose the arbitrarily long lengths $L_F = 50\text{mm}$ and $L_C = 100\text{mm}$ so that there are 50 unit density smoothed particles able to represent each material. The heat generation of the fuel is set to $\dot{q} = 0.1$ and the coolant temperature to $T_\infty = 300\text{K}$. Finally we examine a range of coefficients of convection $h = 0.1, 0.2, 0.5, 1\text{g/s}^3\text{K}$.

We see the expected fuel pin behaviour with the characteristic curve of temperature generated within the fuel due to the heat production and the linear temperature profile generated within the cladding. The effect of convection on the fuel element can clearly be seen with a faster convection current, represented by a higher value h, more effectively removing the fuel element heat and allowing a lower temperature operating state.

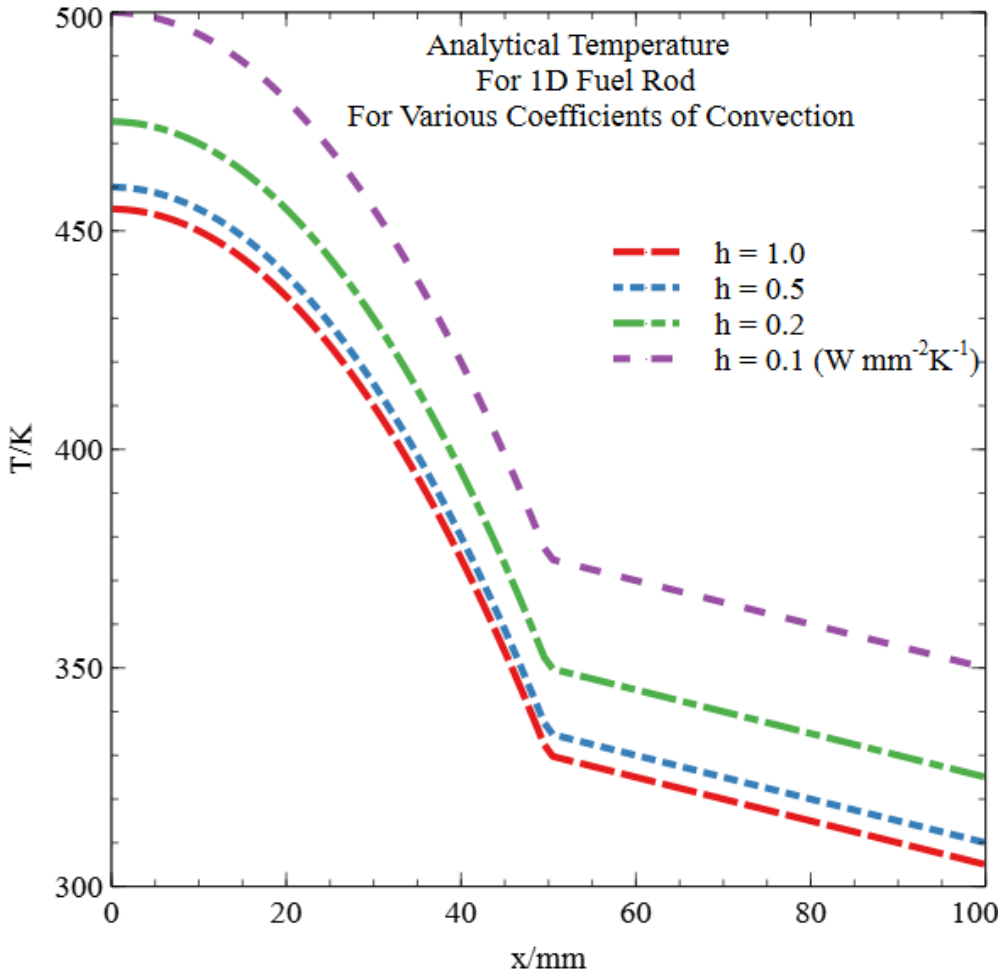

Figure 5.34: Analytical solutions for the steady state 1D composite fuel and cladding model shown in Fig.5.33. The region $0\text{mm} < x < 50\text{mm}$ shows the fuel element temperature. The region $50\text{mm} < x < 100\text{mm}$ shows the cladding temperature. The boundary $x = 100\text{mm}$ undergoes convection with a range of values $h = 0.1, 0.2, 0.5, 1\text{g/s}^3\text{K}$

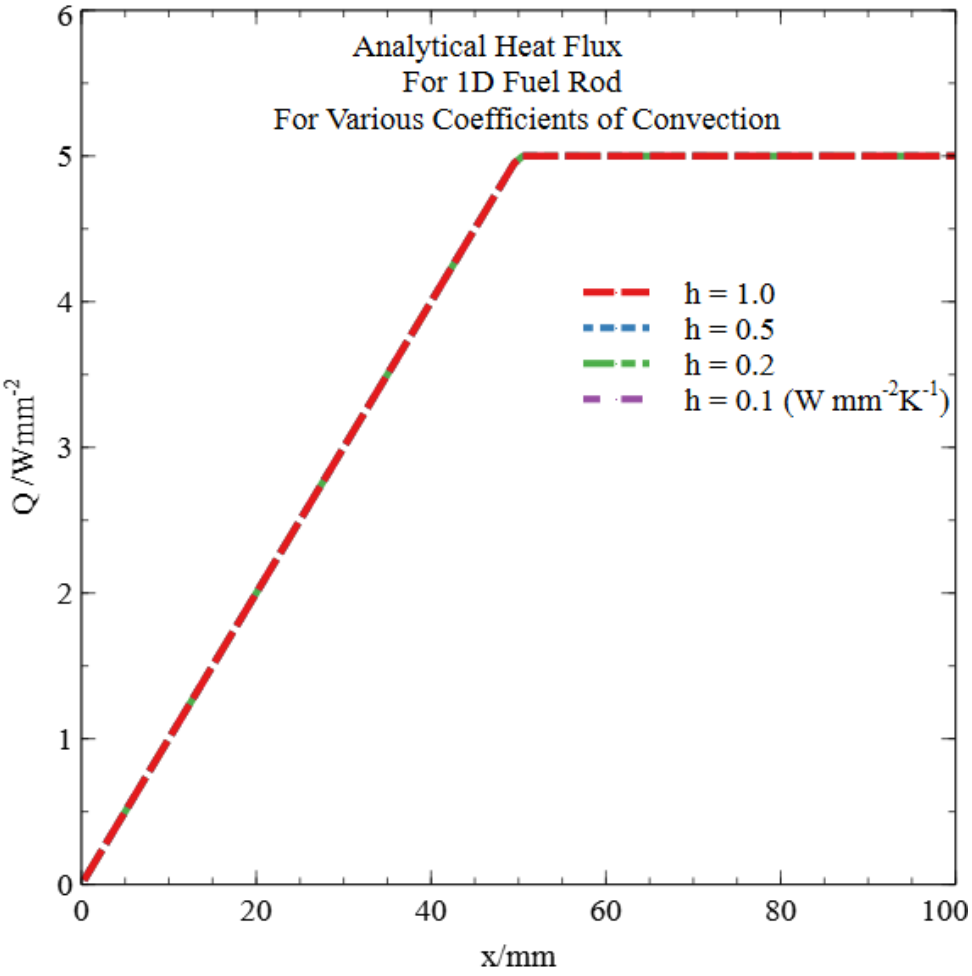

Figure 5.35: Analytical solutions the heat flux for the steady state 1D composite fuel and cladding model shown in Fig.5.33. The region 0mm$< x <$ 50mm shows the fuel element heat flux. The region 50mm$< x <$ 100mm shows the cladding heat flux. The boundary $x = 100$mm undergoes convection with a range of values $h = 0.1, 0.2, 0.5, 1\text{g/s}^3\text{K}$ which all have the same heat flux profile shown here.

5.5.3 1D Composite Fuel and Cladding Model within SPAM

The 1D composite fuel and cladding was modelled in SPAM using convective boundary conditions set out in Eq.5.25 for both system boundaries. Using convection coefficient $h = 0\text{g/s}^3\text{K}$ at $x \leq 0$ ensures that the heat flux is zero by definition. The particles on each boundary are given the same thermal conductivity as the system which they are next to. 6 particles are used for each boundary as in previous cases with a smoothing length $H = 3$mm. Each material, fuel and cladding, are represented by $N/2 = 50$ particles all with $\rho_i = 1\text{g/mm}^-3$.
The SPAM equations were integrated using RK4 with a constant time step $dt = 0.1$s. Simulations were run for 100000 time steps. Each particle was given an initial value of $T_i = 0$K. As with the analytical model $\kappa_F = 1\text{gmm/s}^3\text{K}$ and $\kappa_C = 10\text{gmm/s}^3\text{K}$ with the interface accounted for by the use of Eq.5.69. The heat generated in the fuel is given by $\dot{q} = 0.1\text{gmm}^2\text{s}^-3$ and the coolant temperature was $T_\infty = 300$K. The problem is again explored for four values of coolant convection

coefficient $h = 0.1, 0.2, 0.5, 1\text{g/s}^3\text{K}$.

5.5.4 SPAM Results

The results of the SPAM are shown in Fig.5.36. The result again show the desired behaviour as in the analytical, with smoothed continuous profiles, linear within the cladding region, quadratic within the fuel region. Heat does not appear to be crossing the internal boundary with the temperature maximal at the centre point $x = 0$mm. The results are given for $t = 10,000s$ well after the system has reached a stable state.

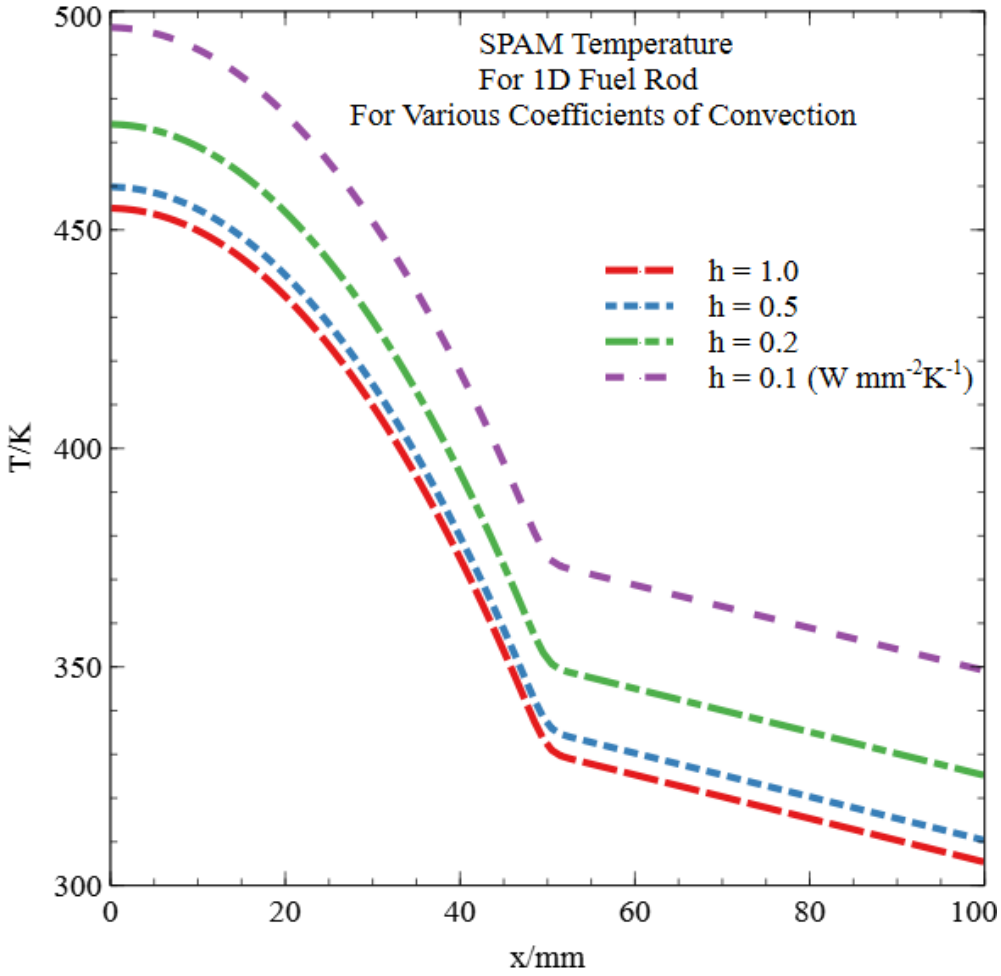

Figure 5.36: SPAM solutions for the steady state 1D composite fuel and cladding model shown in Fig.5.33. The region 0mm$< x <$ 50mm shows the predicted fuel element temperature. The region 50mm$< x <$ 100mm shows the predicted cladding temperature. The boundary $x = 100mm$ undergoes convection with a range of values $h = 0.1, 0.2, 0.5, 1\text{g/s}^3\text{K}$

5.5.5 Behaviour of Residual Error

Direct comparison of the steady state analytical results and the SPAM results is made in Fig.5.37. It is immediately apparent that there is a small error in the SPAM results which appears to increase

with decreasing values of h. This may be due to errors introduced by the convective boundary temperature estimations.

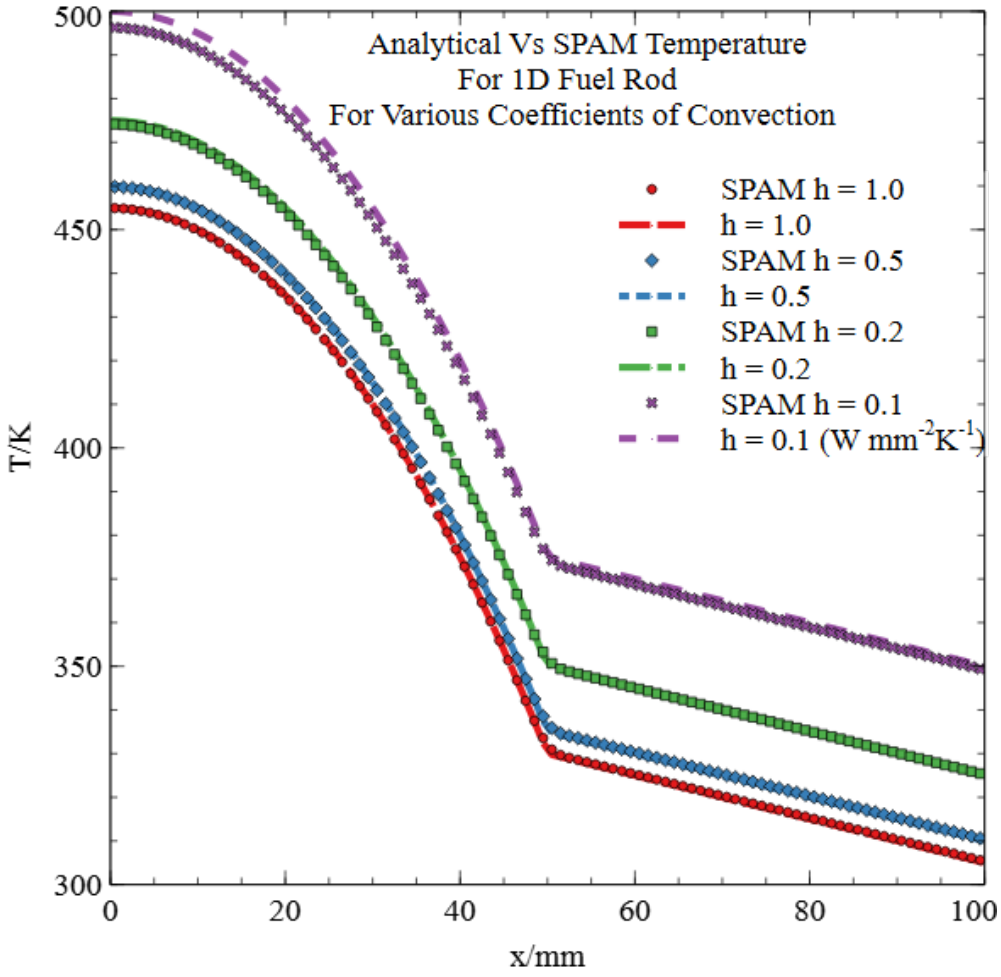

Figure 5.37: SPAM results vs analytical for the steady state 1D composite fuel and cladding model shown in Fig.5.33. The region 0mm$< x <$ 50mm shows the predicted fuel element temperature. The region 50mm$< x <$ 100mm shows the predicted cladding temperature. The boundary $x = 100$mm undergoes convection with a range of values $h = 0.1, 0.2, 0.5, 1$g/s^{3}K

The comparison of the SPAM heat flux results is shown in Fig.5.38. It can be seen that the flux through the fuel segment (left) has minimal error. The error increases toward and through the cladding section. Larger error can be seen for higher values of h. This suggests that the error is being directly introduced by the right most convective boundary representing the cladding.

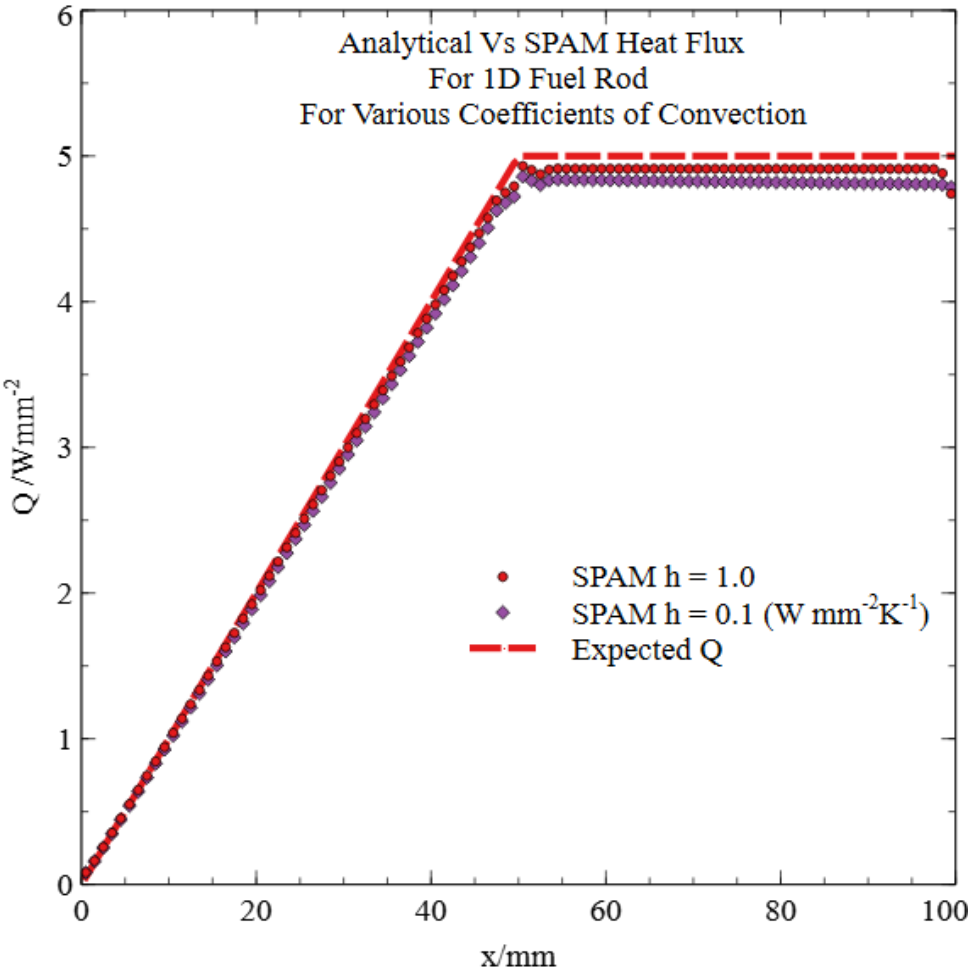

Figure 5.38: SPAM heat flux results vs analytical for the steady state 1D composite fuel and cladding model shown in Fig.5.33. The region 0mm$< x <$ 50mm shows the predicted fuel element temperature. The region 50mm$< x <$ 100mm shows the predicted cladding temperature. The boundary $x = 100mm$ undergoes convection with a range of values $h = 0.1, 0.2, 0.5, 1\text{g/s}^3\text{K}$

The spatial distribution of error for the 1D composite fuel and cladding model is shown in Fig.5.39 for coefficient of convection $h = 1\text{g/s}^3\text{K}$. The most significant result highlighted by the error distribution is the discontinuous nature of the error at the material interface. This effect was highlighted for the 1D model and clearly has a significant result on the overall accuracy of these more complex simulations and those going forward. It is again therefore highlighted that reformulation of the handling of conductivity on the material boundary is required to improve results.

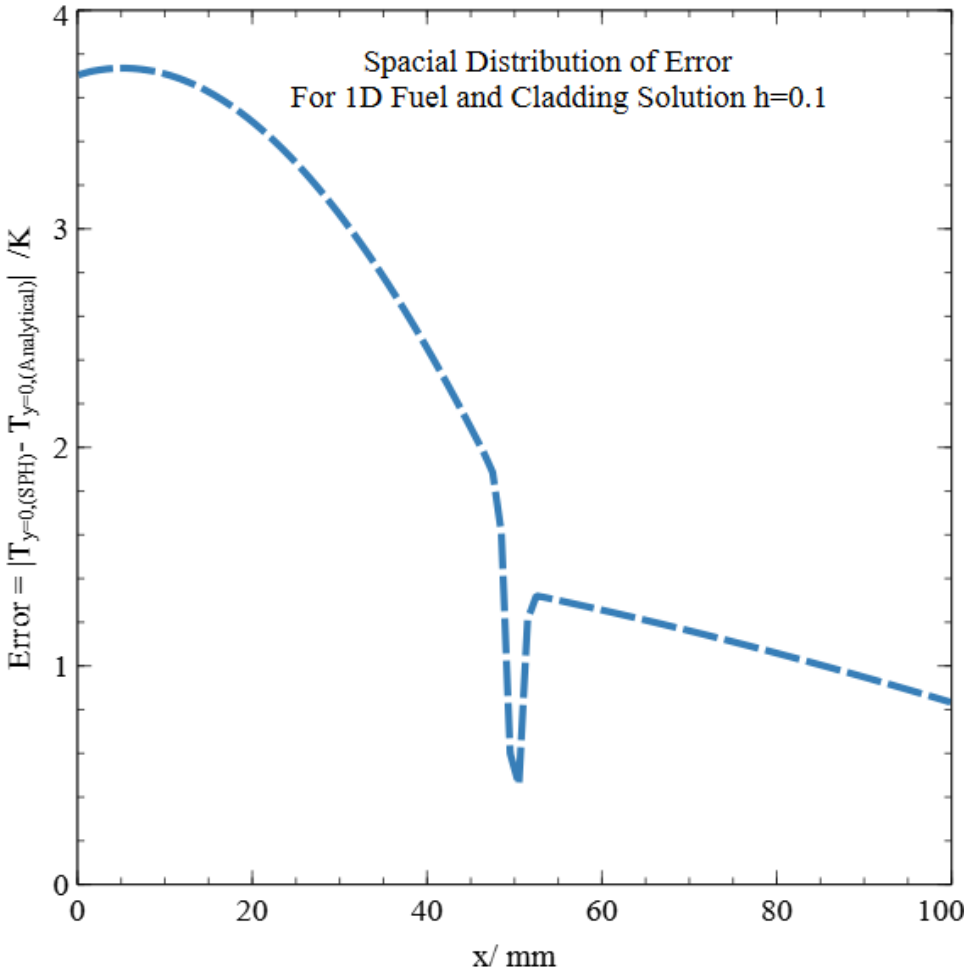

Figure 5.39: Spatial distribution of error for SPAM results vs analytical for the steady state 1D composite fuel and cladding model shown in Fig.5.33. The results are shown for boundary convection with a value $h = 1\text{g/s}^3\text{K}$

The residual error in the SPAM is calculated again using Eq.3.101. The results are shown in Fig.5.40. This shows that the error in the simulation grows with the reciprocal value of h. This suggests that the error factor is directly effected by the convection conditions at the surface furthest from the error. This is supported as the approximation given by Eq.5.25 will give errors that grow with the reciprocal of h. It can therefore be concluded that improvements to the convection approximation boundary condition given by Eq.5.25 will produce decreased error within these SPAM simulations.

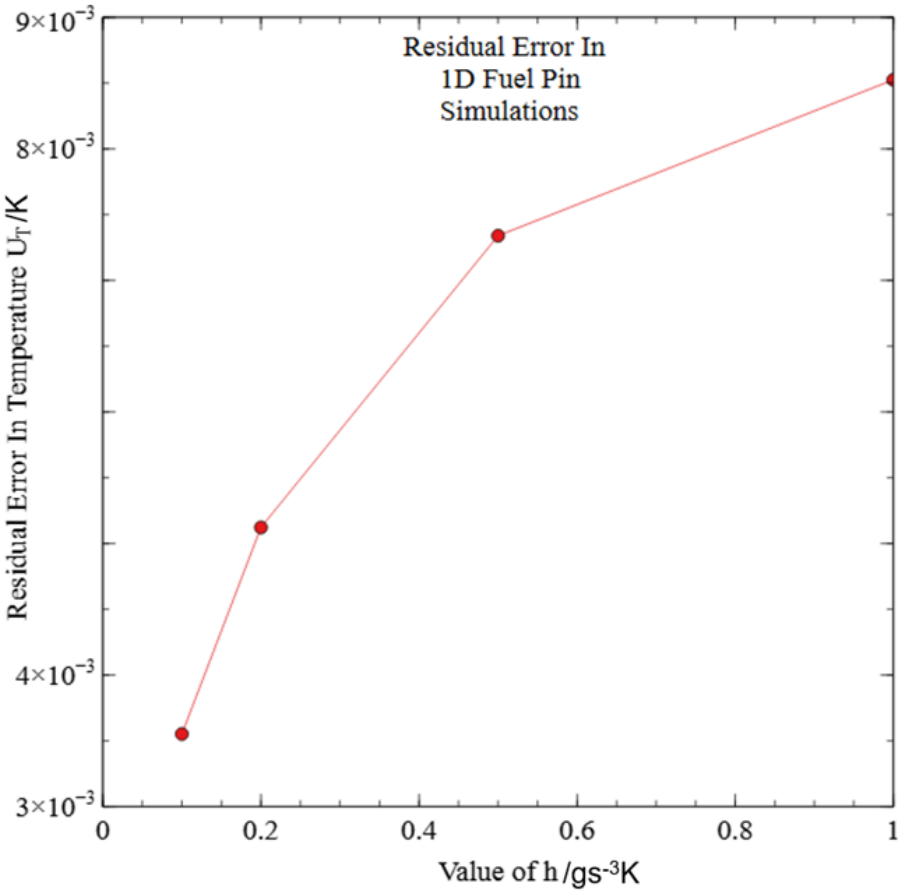

Figure 5.40: Residual error in the SPAM simulation of a 1D fuel element and cladding compared with the analytical model. Shown here for four different coefficients of convection $h = 0.1, 0.2, 0.5, 1\text{g/s}^3\text{K}$.

5.5.6 Rate of 1D Convergence

The rate of convergence is estimated for the 1D fuel and cladding model. A range of simulations are completed for increased and decreased numbers of particles. The simulations are characterised by the spacing between particles. The largest simulation contains $N = 1000$ particles with a spacing of $\Delta_P = 0.1$mm. The smallest simulation tested contains $N = 10$ particles with a spacing of $\Delta_P = 10$mm. A plot of the logarithm of the calculated residual error against the particle spacing is constructed in Fig.5.41. A line of best fit is calculated for the data points and the gradient of this line is used to estimate the nature of the dependence. Two lines for quadratic dependence and for linear dependence are shown as well. This dependence is referred to as the rate (or order) of convergence. As shown the line of best fit suggests an order of 1.3. This lies within the expected regime for SPAM with the ideal convergence theoretically approaching 2^{nd}order but the practical application often demonstrating closer to 1^{st}order [67].

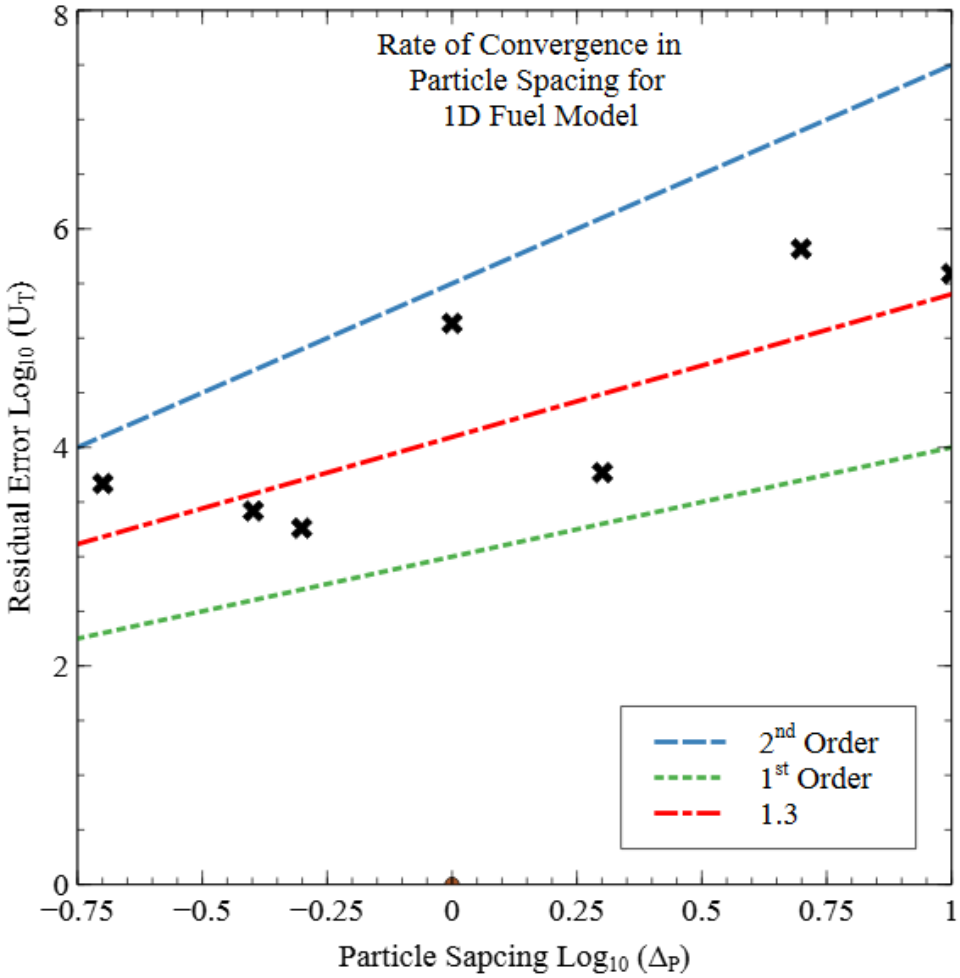

Figure 5.41: The logarithm of residual error in the SPAM simulation of a 1D fuel element and cladding is plotted against the logarithm of the particle spacing for a range of 7 simulations. Shown here for a coefficient of convection $h = 1\text{g/s}^3\text{K}$.

5.6 2D Fuel Pin Model

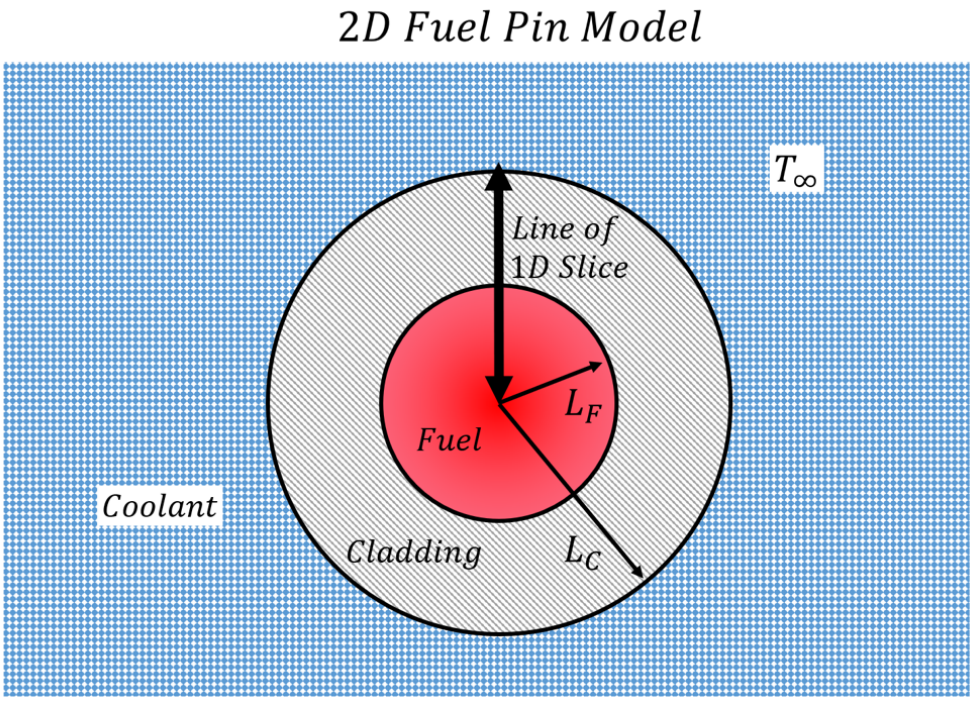

Figure 5.42: A schematic diagram showing a cross-section of a nuclear fuel pin. The fuel, cladding and coolant are represented as if from above. The slice of interest for the 1D model is highlighted.

The annular geometry of a nuclear fuel pin allows for an increased amount of heat to be transferred from the fuel element to the cladding above the 1D composite fuel and cladding representation. This means it is insufficient for any fuel simulation used with fuel performance codes to assume 1D simplified geometry. To illustrate this the analytical 2D and 1D solutions are shown along side each other for the values used within the 1D composite fuel and cladding model shown above in Fig.5.43. It can be seen that for the value $h = 0.1\text{g/s}^3\text{K}$ the peak fuel element temperature reaches ≈ 1.3 times higher for the 1D case than the 2D case.

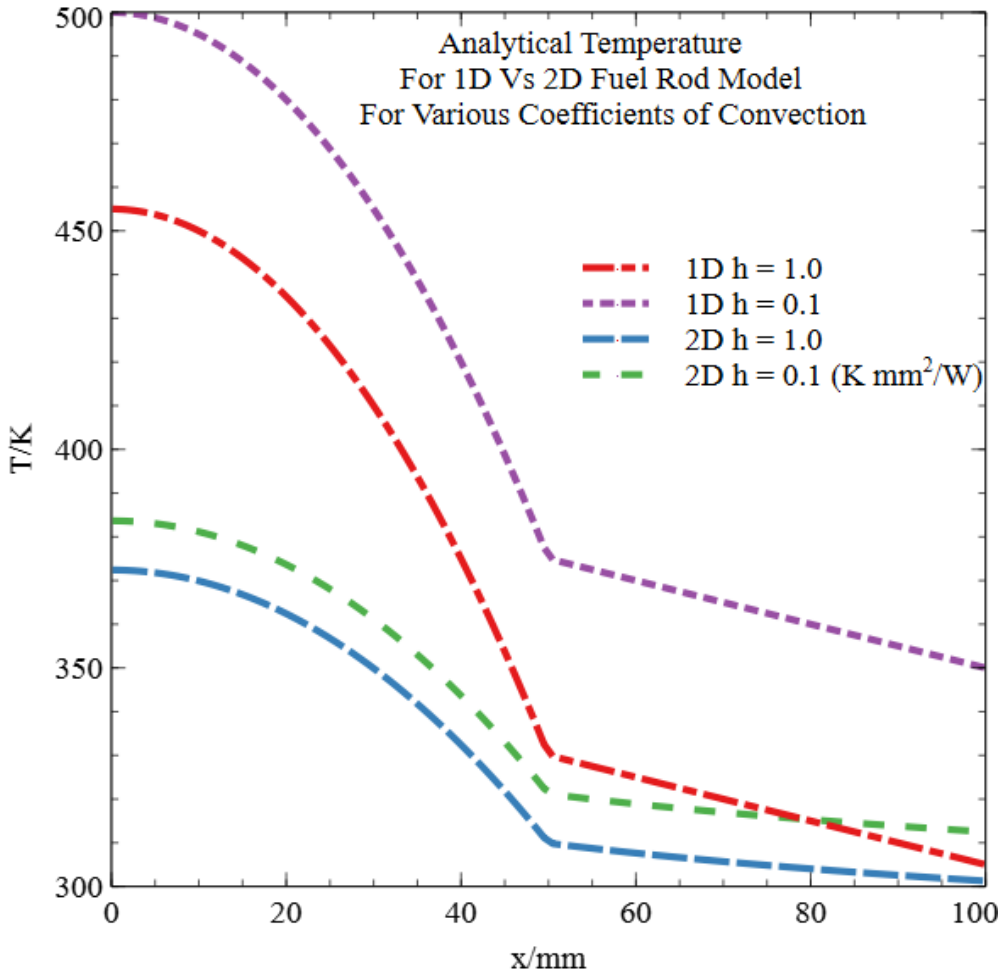

Figure 5.43: Analytical solutions for the steady state 1D composite fuel and cladding model shown in Fig.5.33 vs the 2 fuel pin model shown in Fig.5.42. The region 0mm$< x <$ 50mm shows the predicted fuel element temperature. The region 50mm$< x <$ 100mm shows the predicted cladding temperature. The boundary $x = 100$mm undergoes convection with two values $h = 0.1, 1 \text{g/s}^3\text{K}$

5.6.1 Analytical Solutions

The length of the fuel is assumed to be effectively infinite and the cross-section is assumed axisymetric. These assumptions allow for a temperature solution which depends only on the radial co-ordinate. The steady state 2D solutions are derived as in the case of the 1D composite case. For the 2D case the heat equation is described in radial co-ordinates for the fuel and cladding respectively as:

$$\frac{1}{r}\frac{\partial}{\partial r}\left(r\frac{\partial T_F}{\partial r}\right) = -\frac{\dot{q}}{\kappa_F} \tag{5.88}$$

$$\frac{1}{r}\frac{\partial}{\partial r}\left(r\frac{\partial T_C}{\partial r}\right) = 0 \tag{5.89}$$

The two PDEs in Eq.5.88 and Eq.5.89 are easily solved [136] and the solutions are given below:

$$T_F = \frac{\dot{q}R_F^2}{2}\left[\frac{ln(R_C/R_F)}{\kappa_C} + \frac{1}{hR_C}\right] + T_\infty + \frac{\dot{q}(R_F^2 - r)}{4\kappa_F} \tag{5.90}$$

$$T_C = \frac{\dot{q}R_F^2}{2}\left[\frac{ln(R_C/r)}{\kappa_C} + \frac{1}{hR_C}\right] + T_\infty \tag{5.91}$$

The heat flux is then given by:

$$Q_F = \frac{\dot{q}r}{2} \tag{5.92}$$

$$Q_C = \frac{\dot{q}R_F^2}{2r} \tag{5.93}$$

The temperature distribution is shown in Fig.5.44. We select reasonable values for representing a fuel rod within this model. The radii used are $R_F = 10$mm, $R_C = 15$mm, with conductivities $\kappa_F = 2$W/mK, $\kappa_C = 25$W/mK. The heat generation is given as $\dot{q} = 2 \cdot 10^8 \mathrm{W/m^3}$ and a range of values of coefficient of convection are shown $h = 1000, 2000, 5000, 10000 W/m^2K$. All these numbers a chosen based off the simple fuel model given in [136].

The heat flux is shown in Fig.5.45. The heat flux is identical for different values of convection h therefore only one profile is visible. Eq.5.92-5.93 show that the heat flux should only be affected by the heat generation and radius of the fuel element.

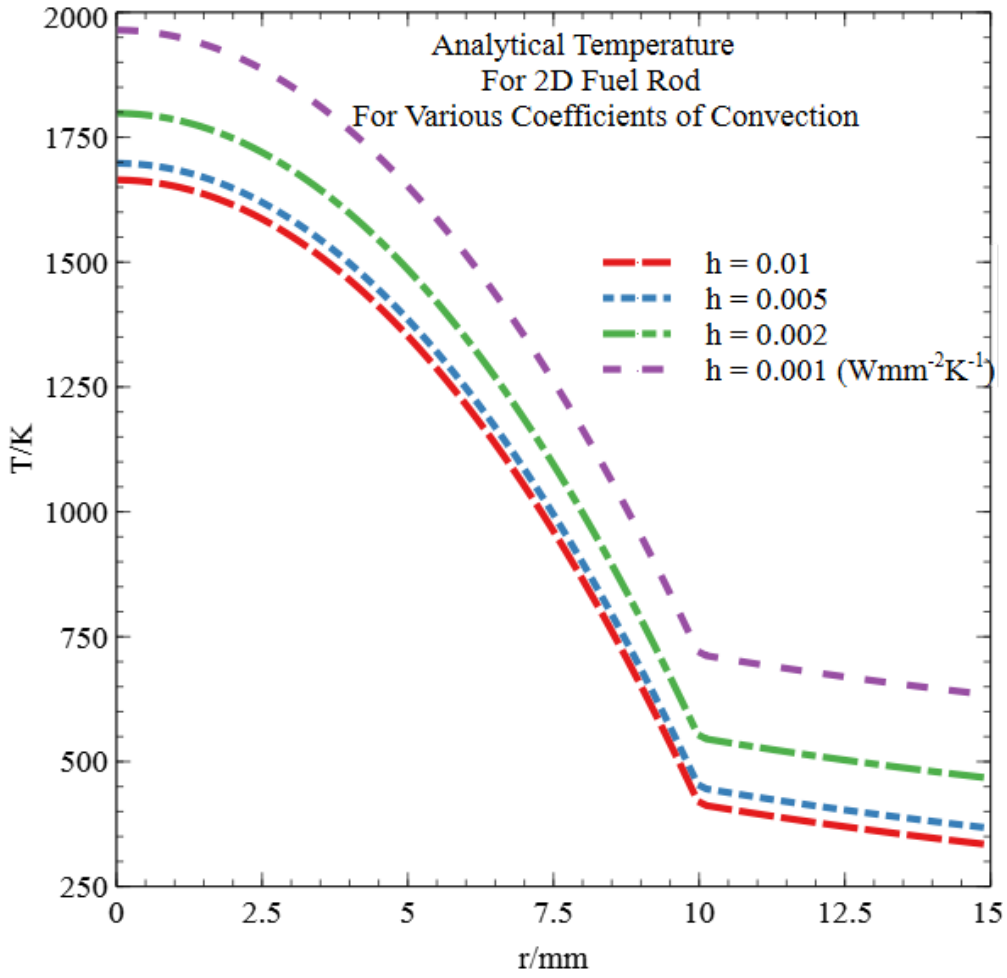

Figure 5.44: Analytical solutions for the steady state 1D composite fuel and cladding model shown in Fig.5.42. The region 0mm$< r <$ 10mm shows the predicted fuel element temperature. The region 10mm$< r <$ 15mm shows the predicted cladding temperature. The boundary $r = 15$mm undergoes convection with a range of values h

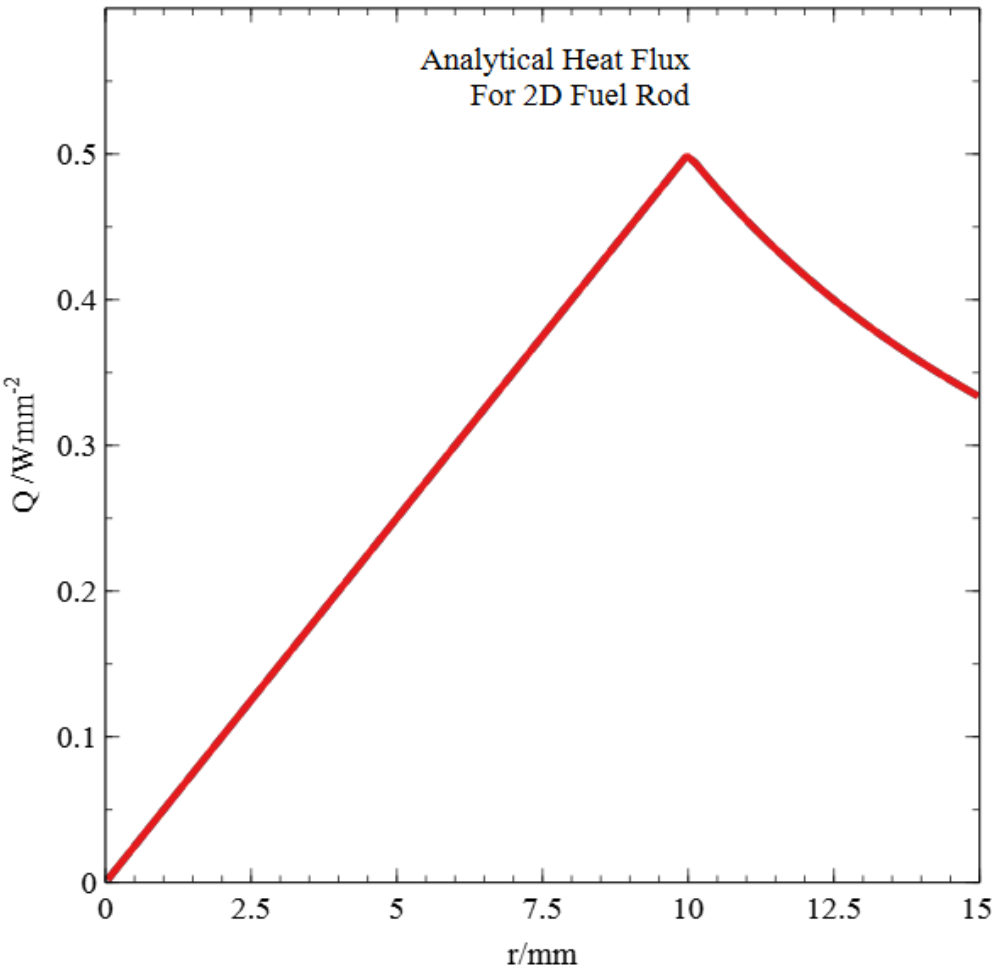

Figure 5.45: Analytical solutions of the heat flux for the steady state 1D composite fuel and cladding model shown in Fig.5.42. The region 0mm$< r <$ 10mm shows the predicted fuel element temperature. The region 10mm$< r <$ 15mm shows the predicted cladding temperature. The boundary $r = 15$mm undergoes convection with a range of values h which all have the same heat flux profile shown here.

5.6.2 SPAM Solutions

For the 2D case the convection approximation must be generalised to higher dimensions. We still require Newton's law of cooling be satisfied, however we define the boundary unit normal $\hat{r}$ for a description in higher dimensions:

$$\frac{\partial T}{\partial r}|_B = -\frac{h}{\kappa}\left[T_B - T_\infty\right] \tag{5.94}$$

We therefore follow the previous approximations but we replace:

$$\frac{\partial T}{\partial r}|_B \approx \frac{T_{B_i} - T_i}{-R} \tag{5.95}$$

where R is the distance between particles i and B_i. This gives the convection approximation as before with Eq.5.25, with the simple modification to the function of convection:

$$F_h = -\frac{h}{\kappa} R \tag{5.96}$$

The SPAM particle arrangement used for the simulations are based on a triangular lattice split into three particle zones which are the fuel, cladding and convective boundary particles which represent the coolant. The particle arrangement is shown in Fig.5.46

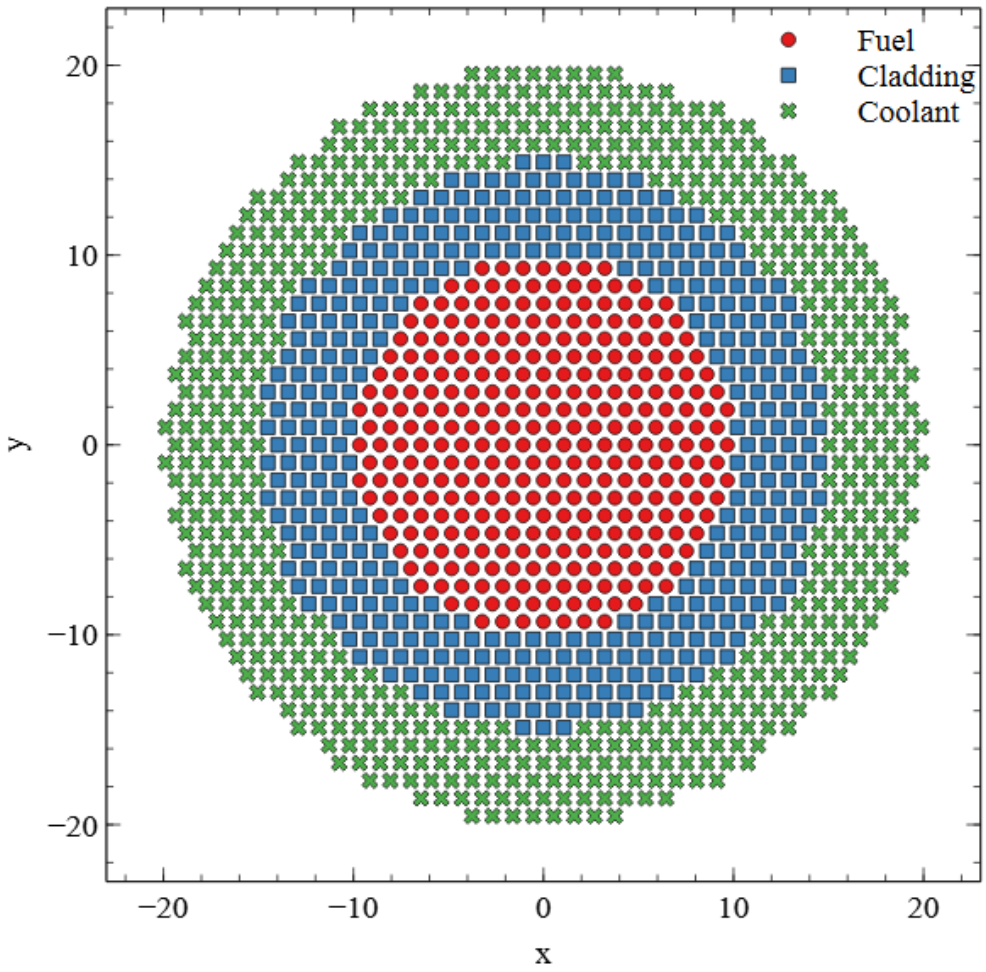

Figure 5.46: Particle arrangement used for the 2D SPAM fuel pin model. The boundary region representing the coolant is given a thickness of 5mm so that it exceeds the smoothing length. The particle arrangement contains $N = 1261$ particles in total.

The simulations were completed with a time-step $dt = 1$s for 100000 steps. A smoothing length of $H = 3$mm is used. The final interpolated temperatures are plotted in Fig.5.47 together with the analytical profiles. It can be seen that for smaller magnitudes of convection coefficient h there is a significant increase in the error in SPAM predicted temperature. This suggests that the approximation given by Eq.5.95 may be insufficient for smaller magnitudes of h.

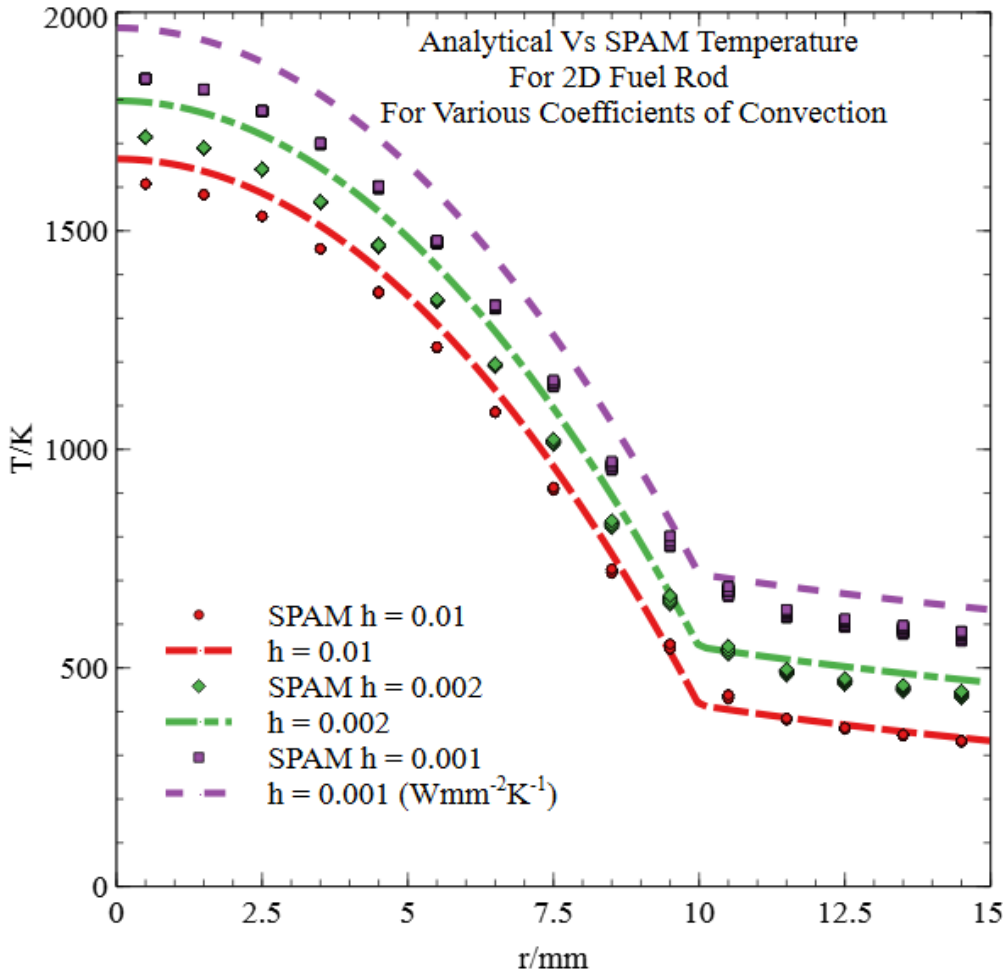

Figure 5.47: Analytical solutions for the steady state 2D fuel and cladding model shown in Fig.5.42. The region 0mm$< r <$ 10mm shows the predicted fuel element temperature. The region 10mm$< r <$ 15mm shows the predicted cladding temperature. The boundary $r = 15$mm undergoes convection with a range of values h.

This idea is supported by the heat flux results shown in Fig.5.48 as we see the SPAM predicted heat flux toward the boundary $r = 15$mm shows a significant spread of interpolated values. The peak heat flux is also not well represented by the SPAM results therefore another issue may be that the SPAM has too few particles to properly define the problem. A convergence test was therefore run on these results to determine if the error was reduced for an increase in number of particles above $N = 1261$ which is shown here.

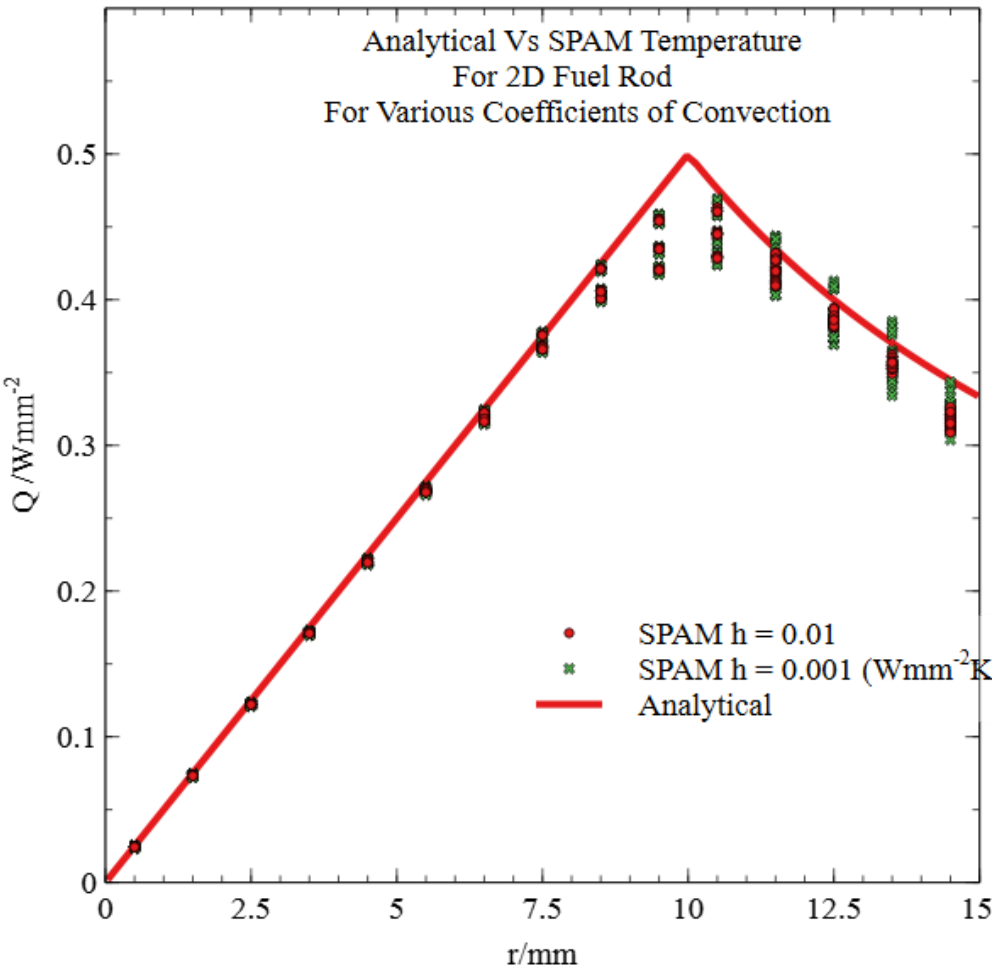

Figure 5.48: Analytical solutions of the heat flux for the steady state 2D fuel and cladding model shown in Fig.5.42. The region 0mm$< r <$ 10mm shows the predicted fuel element temperature. The region 10mm$< r <$ 15mm shows the predicted cladding temperature. The boundary $r = 15$mm undergoes convection with a range of values h which all have the same heat flux profile shown here.

5.6.3 The Rate of 2D Convergence

For this convergence test we test we use $h = 0.001\text{W/mm}^2\text{K}$ as this demonstrates the largest visible error for the results shown in Fig.5.47. There are hardware limitations to this test, we therefore restrict the largest test to approximately 10 times the number of particles.

The convergence results are as expected. The predicted temperature profiles for a selection of SPAM particle spacings are displayed in Fig.5.49. It can be seen that for $N > 10,000$ values near to $r = 0$mm are close to the expected. Slight smoothing of the transition profile at $r = 10$mm can however be seen which causes an error in values predicted along the interface of the two materials.

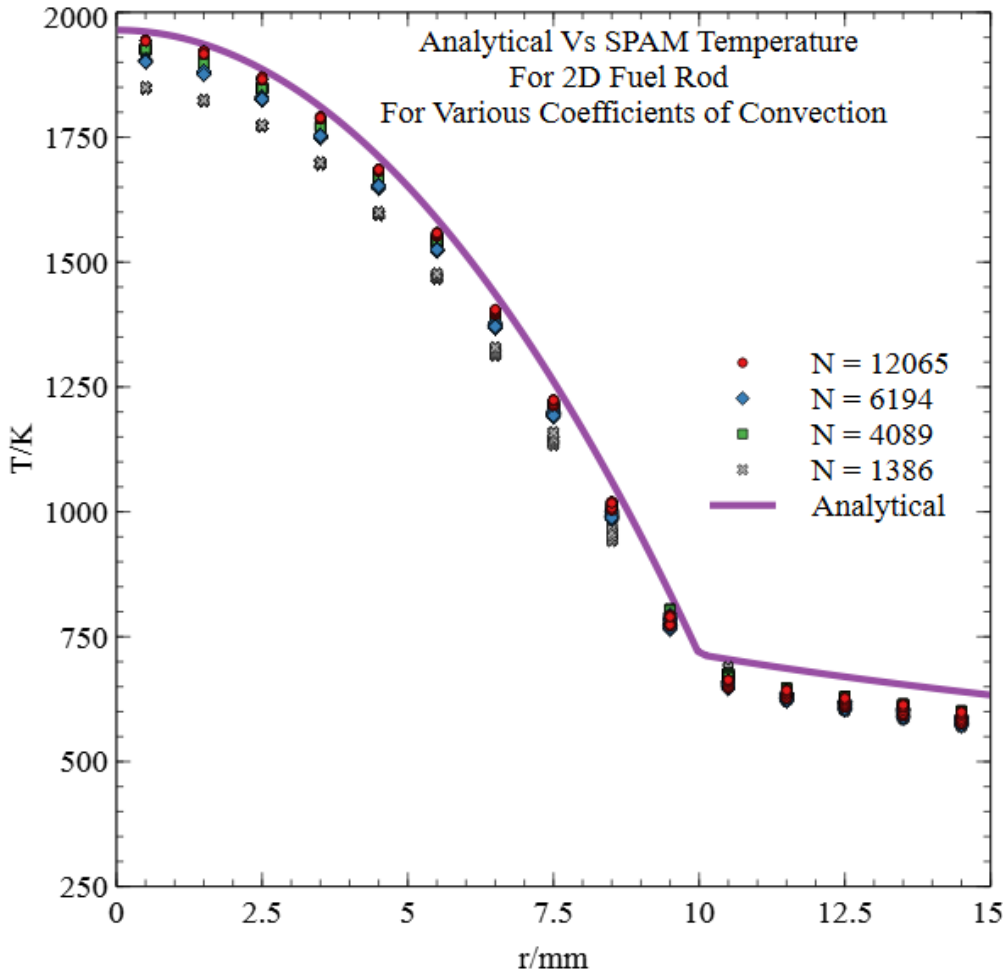

Figure 5.49: SPAM interpolated temperature profiles vs analytical solution for the steady state 2D fuel and cladding model shown in Fig.5.42. The region 0mm$< r <$ 10mm shows the predicted fuel element temperature. The region 10mm$< r <$ 15mm shows the predicted cladding temperature. The boundary $r = 15$mm undergoes convection with a range of values h. A range of particle spacing's are shown given by particle number N

The same can be seen in the heat flux profile shown in Fig.5.50. Good agreement is seen close to $r = 0$mm with a drift to higher values toward the system edge $r = 15$mm. The residual error for these simulations is calculated and the convergence shown in Fig.5.51

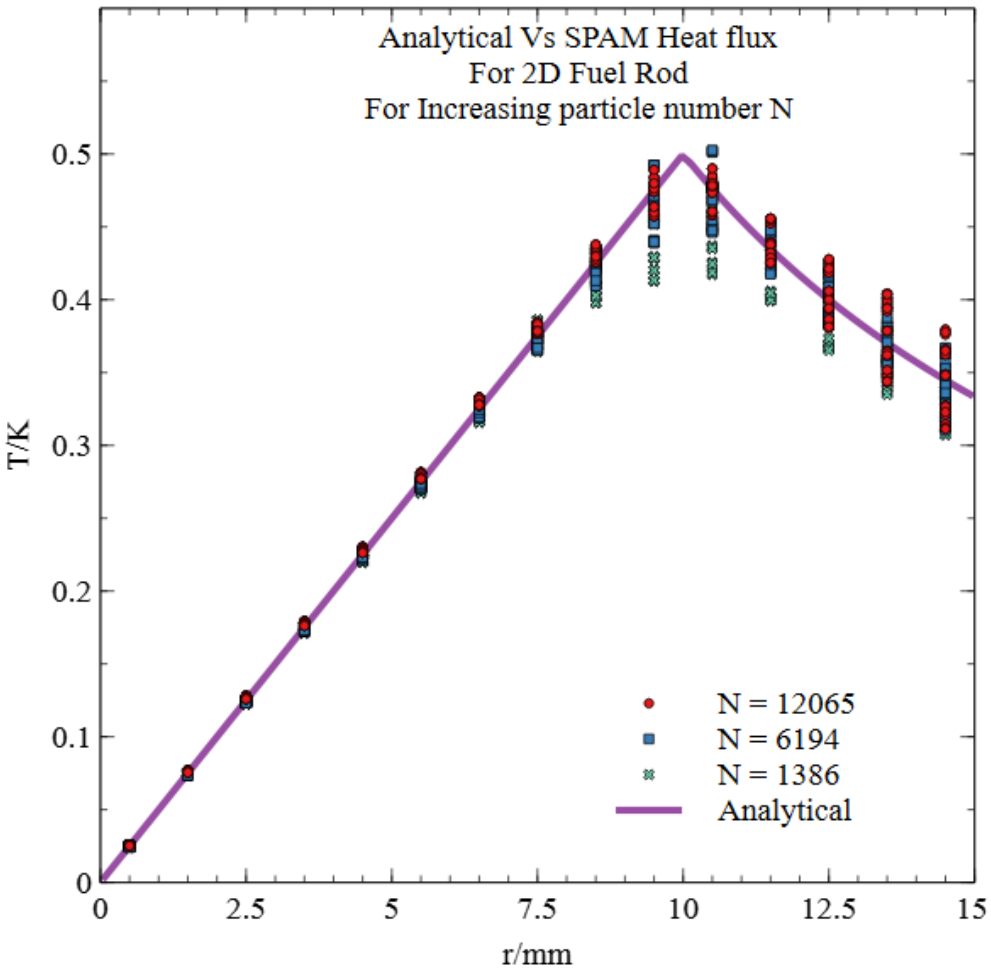

Figure 5.50: SPAM interpolated heat flux profiles vs analytical solution for the steady state 2D fuel and cladding model shown in Fig.5.42. The region 0mm$< r <$ 10mm shows the predicted fuel element temperature. The region 10mm$< r <$ 15mm shows the predicted cladding temperature. The boundary $r = 15$mm undergoes convection with a range of values h. A range of particle spacing's are shown given by particle number N

The simulations completed for the convergence test are defined by constructing particle arrangements with particle masses between $m_i = 1 \rightarrow 0.1g$ in steps of 0.1. The average particle spacing Δ_P can then be calculated for 2D as $\Delta_P = \sqrt{m_i}$. From this the appropriate smoothing length is calculated as:

$$H = 3\sqrt{m_i} \tag{5.97}$$

The smoothing lengths used for the 10 simulations are given in Table.5.2.

The error in the simulations is not the expected smoothed curve but actually increases for $N > 3000$ before having a final decreased error for $N > 10,000$. This effect is due to the error seen at the interface between the fuel and cladding. The final interface temperatures have a larger error for higher values of N than these preceding values and this causes the error behaviour displayed. Examination of the heat flux error toward the outside boundary suggests that the convection condition used may be causing convergence toward incorrect boundary heat flux which is giving

N	m_i /g	Δ_P /mm	H /mm
1261	1	1	3
1386	0.9	0.95	2.85
1586	0.8	0.89	2.67
1754	0.7	0.84	2.52
2056	0.6	0.77	2.31
2469	0.5	0.71	2.13
3016	0.4	0.63	1.89
4089	0.3	0.55	1.65
6194	0.2	0.45	1.35
12065	0.1	0.32	0.96

Table 5.2: The parameters used for the 10 simulations completed for the convergence test of the 2D fuel rod model.

rise to the errors seen. It is, however, encouraging the large reduction shown by the convergence test.

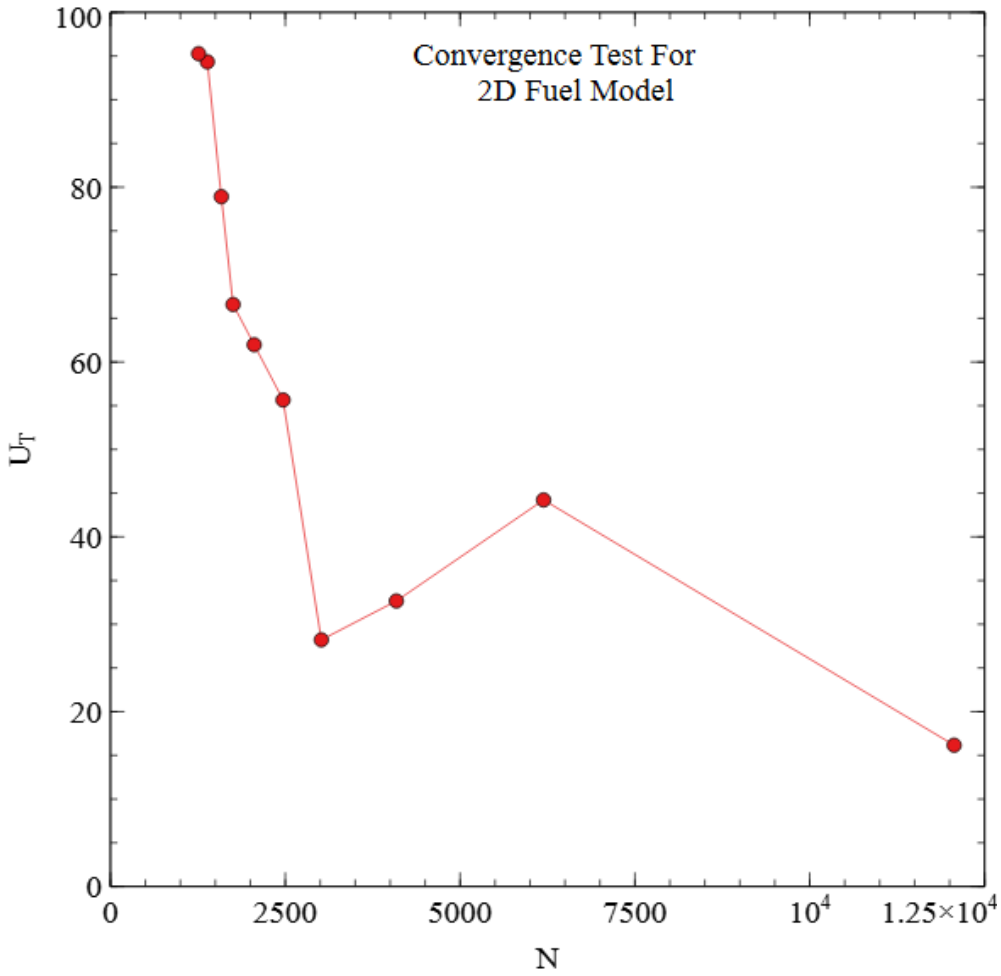

Figure 5.51: The convergence of the residual error shown for SPAM simulations of the 2D fuel model, shown in Fig.5.42, are given for $h = 0.001\text{W/mm}^2\text{K}$ across a range of number of particle points N.

The rate of convergence is estimated for the 2D fuel and cladding model. The range of simulations completed are for increased numbers of particles shown in 5.2. The simulations are characterised by the spacing between particles, all simulations are constructed from regular triangular lattices. A plot of the logarithm of the calculated residual error against the particle spacing is constructed in Fig.5.52. A line of best fit is calculated for the data points and the gradient of this line is used to estimate the rate of convergence. Two lines for quadratic dependence and for linear dependence are shown as well. As shown the line of best fit suggests an order of 0.62.

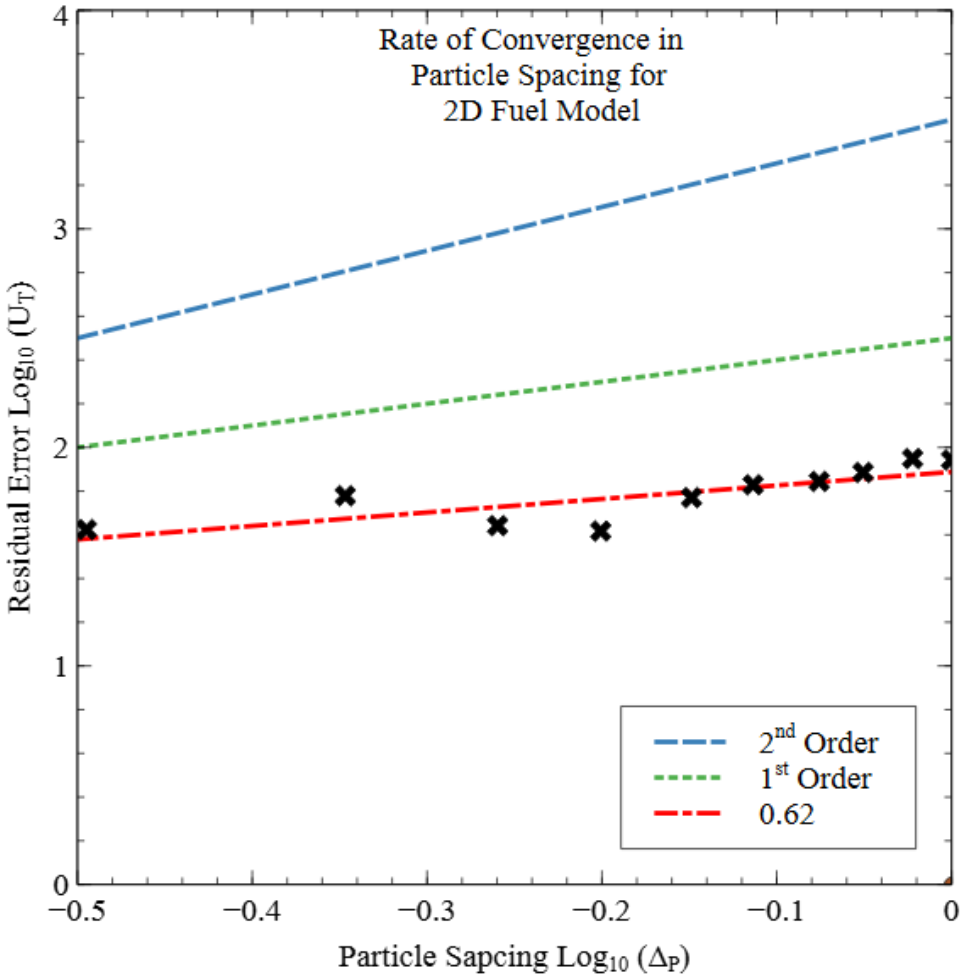

Figure 5.52: The logarithm of residual error in the SPAM simulation of a 2D fuel element and cladding is plotted against the logarithm of the particle spacing for a range of 10 simulations. Shown here for a coefficient of convection $h = 0.01$.

This rate of convergence is unexpectedly low and is more than likely affected by the interface issue with the model which is discussed above or, it is due to the increasing presence of the discretisation error identified in Chapter 2. With this in mind the convergence rate is estimated for the first 6 simulations in Fig.5.53. This reduced number of simulations supports a convergence rate of 1.2. This is as expected as the convergence of the smoothing error should at least exceed linear dependence and is expected to approach 2^{nd} order for this form of SPAM and with future improvements this simulation could approach 4^{th} order convergence [66].

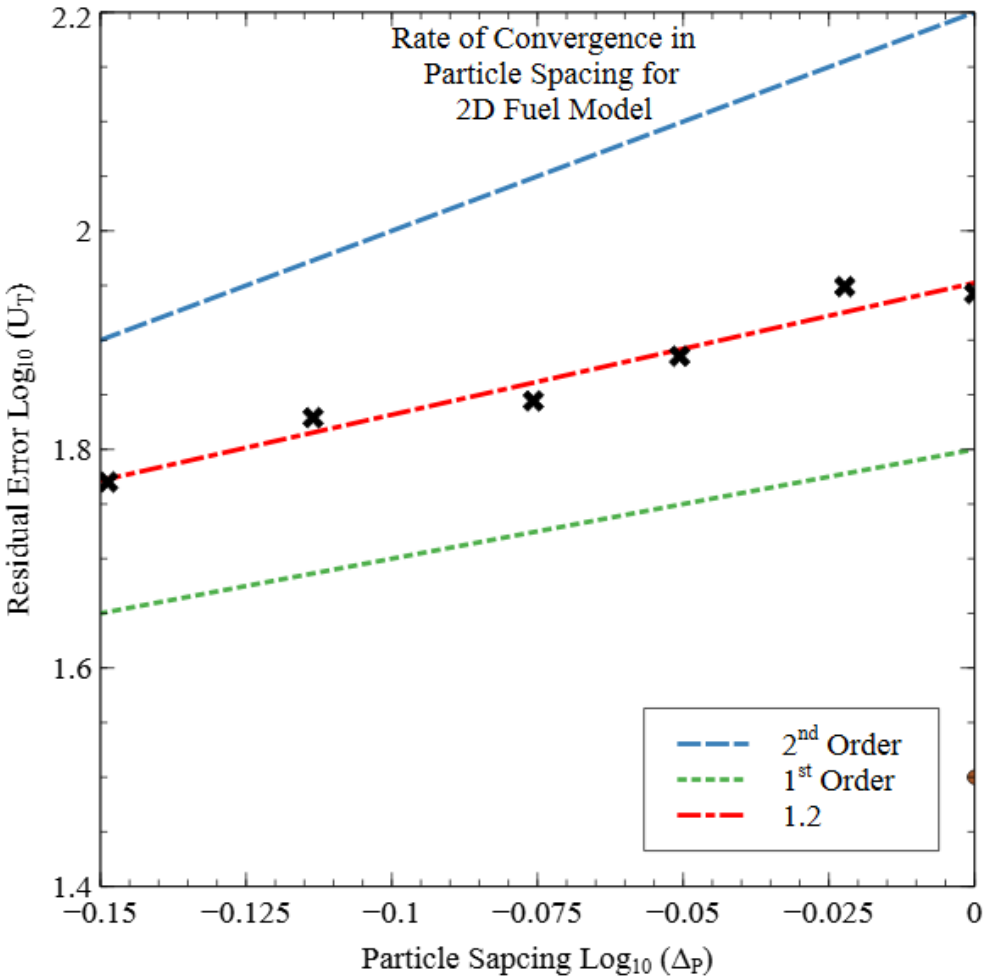

Figure 5.53: The logarithm of residual error in the SPAM simulation of a 2D fuel element and cladding is plotted against the logarithm of the particle spacing for reduced range of 6 simulations up to $N = 2469$. Shown here for a coefficient of convection $h = 0.01\text{W/mm}^2\text{K}$.

5.7 Conclusions

This chapter aimed to model heat flow through a simplified model of a fuel rod. This was completed by systematically simulating smaller 1D models to determine the best SPAM approach to handle each of these conditions. New or modified algorithms for handling boundary convection, heat generation and material thermal interfaces were proposed and shown to be successful.
The work shown in this chapter suggests that SPAM simulations are capable of modelling the thermal effects within nuclear fuel. These simulations are not, however, free from error with important consideration needing to be given to the formulation of convective boundary conditions and the number of particles used.
Of note, the simplified convective boundary condition shows a promising novel and simplified approach to modelling convection within SPAM through Eq.5.95. Future refinement of this condition with a higher order approximation of the temperature derivative or improved implementation within dynamic boundaries may give further error reductions for the method.

Overall there is promise that SPAM models used for damage modelling of nuclear fuel could be created with acceptable error within the thermal modelling to justify the use of SPAM. The models shown here cannot compete with those given by FEM models however the scope for increased complexity means full multi-physics SPAM nuclear fuel models could be a useful compliment.

Chapter 6

Thermal-Induced Strains

6.1 Introduction

Within a reactor under operation heat is generated by nuclear fission from within the pellets which causes swelling of the pellet and thus mechanical deformation of both pellet and cladding through PCMI. The conceptual fuel pin model presented within this work requires the coupling of mechanical deformations to the thermodynamics already presented in the previous chapters. SPAM has already been applied to field of thermo-elasticity. One of the most advanced of these studies examined large scale 3D deformations of solid bodies using a formulation of SPAM with governing equations based on the linear momentum of the body and the deformation gradient, co-factor, Jacobian and energy density with momentum correction and energy dissipation [137]. Although the simulations presented are impressive the models used lack experimental or analytical results with which to asses the accuracy. The problem of nuclear fuel approached in this work will begin with the basic formulations such as those presented by Monaghan [138] to better establish the error effects associated with the SPAM formulation.

To explore this we first present a basic elastic model for the stress. Thermal-induced stress is created through the use of a thermal expansion coefficient. The mechanical deformation will be explored for arbitrary material properties against analytical solutions for one and two dimensional problems.

The SPAM tensile instability exhibits itself for purely tensile system forces. Corrective methods for this instability will be explored, including velocity smoothing, artificial viscosity and artificial stress.

6.2 Thermal Stress in a 1D system

We begin our examination of thermal stress in SPAM with a computationally simple and physically intuitive model: A 1D system heated with a linear temperature profile and restricted at each end. The physical analogue of this model would be a uniform length of material wrapped with heated wire of negligible thickness, given some initial, uniform constant temperature T_C. The material can be considered restricted in movement at both ends by a static boundary wall. The heated coil delivers a linear temperature profile such that the final temperature distribution is defined by a raise in temperature to T_H on one boundary. A diagram of the model is shown in Fig. 6.1

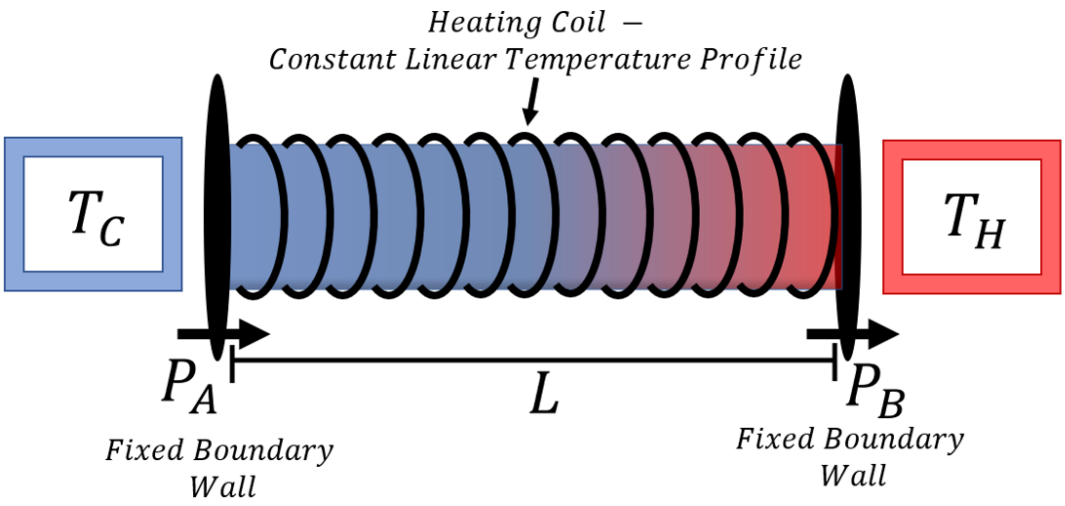

Figure 6.1: Visual representation of the 1D analytical thermal stress model presented in this section. A length L of material with uniform cross-section A and linear temperature profile provided by a heating coil. The material is suspended between fixed boundary walls which exert pressure P_A and P_B respectively.

The material is assumed to have a uniform cross-sectional area A such that the model can be considered to be one dimensional. To consider the analytical stress solution to this problem we first consider the boundary pressure acting on the material. If the material is at equilibrium the sum of forces acting on it must be equal to zero. We can therefore use Newton's third law to consider the normal reactions per cross-sectional area at both ends of the system, which we will refer to as the pressure. The pressure exerted at the boundary P_A must therefore be equal and opposite to the pressure at the boundary $P_B = -P_A$. Considering any smaller sub section of the material under the same logic suggests that that the pressure at any point x must also be constant and oppose the pressure at the boundary when at equilibrium [139]. Force is defined as the negative of pressure:

$$F(x) = -P_A \tag{6.1}$$

We assume that the thermal expansion of the material is linear and therefore can be described by a thermal expansion coefficient α as:

$$\Delta L = L_0 \cdot \alpha dt \tag{6.2}$$

where dt is the change above some reference temperature T_0. Total material strain (i.e engineering strain) is defined by the proportion of extension of length ΔL to original material length L_0:

$$\epsilon = \frac{\Delta L}{L_0} \tag{6.3}$$

Thus we define the thermal strain as:

$$\epsilon_T = \alpha \Delta t \tag{6.4}$$

Material stress is defined as the force F per unit area A:

$$\sigma = \frac{F}{A} \tag{6.5}$$

We assume the material is a linear elastic material, and thus define the elastic constant Young's modulus E as:

$$E = \frac{\sigma}{\epsilon_\sigma} \tag{6.6}$$

The material strain ϵ_σ can then be expressed in terms of the elastic constant as:

$$\epsilon_\sigma = \frac{F}{AE} \tag{6.7}$$

Taking into account all of these assumptions, the total material strain ($\epsilon = \epsilon_T + \epsilon_\sigma$) defined on the domain $-\frac{L}{2}$ to $\frac{L}{2}$ is derived as:

$$\epsilon = \int_{-\frac{L}{2}}^{\frac{L}{2}} \left(\frac{F(x)}{AE} + \alpha(T(x) - T_0) \right) dx \tag{6.8}$$

If we assume a linear final temperature distribution T_C to T_H, with $T_0 = T_C$, then the temperature profile $T(x)$ can be defined as:

$$T(x) = (T_H - T_C)\frac{x}{L} + \frac{T_C + T_H}{2} \tag{6.9}$$

As stated we expect the force to be constant at equilibrium $F(x) = F$. By integration we have the following expression for the material strain:

$$\epsilon = \left[\frac{Fx}{AE} + \alpha(T_H - T_C)\frac{x^2}{2L} + \alpha\frac{(T_H - T_C)x}{2} \right]_{-\frac{L}{2}}^{\frac{L}{2}} \tag{6.10}$$

which gives:

$$\epsilon = \frac{FL}{AE} + \alpha\frac{(T_H - T_C)L}{2} \tag{6.11}$$

Finally the constricted wall boundaries require that the total material strain be zero $\epsilon = 0$. This gives the following analytical expression for the force:

$$F = -\alpha EA\frac{(T_H - T_C)}{2} \tag{6.12}$$

The expected stress throughout the material is therefore:

$$\sigma = -\alpha E\frac{(T_H - T_C)}{2} \tag{6.13}$$

6.2.1 1D Thermal Stress SPAM Solution

A visual interpretation of the set up for the SPAM algorithm is given in Fig.6.2. The boundary particles are shown here to be fixed however the effect of dynamic boundary particles will also be explored and outlined later in this section. The key difference from the thermal models presented in the previous section is that the particles are now free to move and thus the SPAM equation of

motion must be integrated.

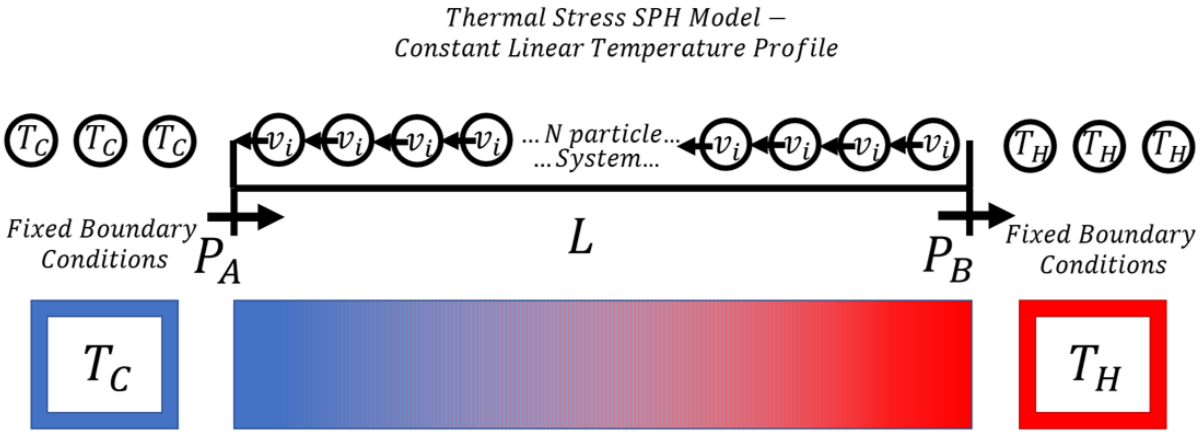

Figure 6.2: Visual outline of the 1D thermal stress SPAM model. A constant linear temperature profile is achieved through boundary temperature enforcement. The system particle positions are allowed to evolve. Boundary particle movement is restricted and pressure enforce at the boundary to restrict the total material strain to zero.

Throughout this section the SPAM solutions given all use Hoover's form for thermal evolution dependent directly on the weight function [54], not its derivatives, due to the success shown in the previous chapters. In 1D the SPAM equation of motion with respect to the stress tensor takes the form:

$$\frac{dv_i}{dt} = \sum_j m_j \left(\frac{\sigma_i}{\rho_i^2} + \frac{\sigma_j}{\rho_j^2} + \Pi_{P,ij} \right) \frac{x_{ij}}{|x_{ij}|} w'(|x_{ij}|) \tag{6.14}$$

Artificial viscosity will be required to stabilise the tensile instability, (which will be discussed in detail later in this chapter) and is added through the $\Pi_{P,ij}$ term.

Equation of state for a simple elastic material

The stress tensor is defined by the equation of state for the equilibrium pressure combined with the chosen material model, which in this case is a simple linear elastic model. The stress tensor can be separated into two parts, the equilibrium pressure P and what we will refer to as the deviatoric stress tensor, denoted as S:

$$\sigma_i = -P_i + S \tag{6.15}$$

We define the deviatoric stress as the stress due to the material strain in terms of the elastic constants. For the 1D case represented by Eq.6.6, the change in stress in terms of the material strain is simply:

$$dS = Ed\epsilon \tag{6.16}$$

To directly calculate the strain at a particle both the change in length and original length of the particle 'element' must be known. Due to the smoothed nature of SPAM this is not known and

therefore direct strain cannot be calculated. Instead the strain rates are obtained from the particle velocities:

$$\dot{\epsilon}_x = \frac{\partial}{\partial t}\frac{\partial u_x}{\partial x} = \frac{\partial v_x}{\partial x} \tag{6.17}$$

where u_x represents the particle displacement. The total change in particle strain is then obtained through time integration. Considering the smoothed particle algorithm for the gradient of the velocity, we can more directly consider the rate of change of the deviatoric stress due to strain as:

$$\dot{S}_i = E\dot{\epsilon}_i = E\frac{\partial v}{\partial x}_i = E\sum_j m_{ij}\left[v_j - v_i\right]\frac{x_{ij}}{|x_{ij}|}w'(|x_{ij}|) \tag{6.18}$$

The thermal strains are often, by convention, included within the above part of the description of the total stress due to the consideration of the strain produced. However thermal strains only contribute to the diagonal elements of the stress tensor therefore it reduces the notation to include these contributions within the equilibrium pressure. To do this the definition of the bulk modulus B for a solid is considered:

$$B = -V\frac{dP}{dV} \tag{6.19}$$

Consider again some constant cross-sectional area A for the reduction to 1D and this gives:

$$B_{1D} = -(AL)\frac{dP}{d(AL)} = -L\frac{dP}{dL} = E \tag{6.20}$$

Considering a small temperature deviation for the linear thermal expansion defined in Eq.6.2 and combining with the above equation this gives for 1D:

$$B_{1D} = E = -L\frac{dP}{(L\alpha dT)} = -\frac{1}{\alpha}\frac{dP}{dT} \tag{6.21}$$

This gives an expression for how the equilibrium pressure changes with temperature:

$$\frac{dP}{dT} = -E\alpha \tag{6.22}$$

As well as the temperature dependence of pressure, we must also consider the density dependence. The SPAM formulation used here is considered weakly compressible as the particle mass m_0 is fixed however the volume occupied by each particle is not. As stated, the exact volume element for each particle is unknown, therefore we use the smoothed density estimate to define the change in volume and thus the change in pressure:

$$\rho = \frac{m_0}{V} \tag{6.23}$$

Combining with Eq.6.19 we expect the pressure to vary with density as:

$$B = \rho\frac{dP}{d\rho} \tag{6.24}$$

This is in agreement with the commonly used equation of state [51]:

$$P = c_0^2(\rho - \rho_0) \tag{6.25}$$

where the sound speed is estimated as $c_0^2 = \frac{B}{\bar{\rho}}$. Herein, we use the geometric mean $\bar{\rho} = \sqrt{\rho_i\rho_j}$. One final consideration before presenting the full equation of state is the continuity equation, which gives the time evolution of density in terms of the divergence of the velocity field:

$$\dot{\rho} = -\rho\nabla\cdot v \tag{6.26}$$

It follows therefore that the pressure evolves as:

$$\dot{P} = -B\nabla \cdot v \tag{6.27}$$

We therefore propose two variations for the equation of state, the first based on the sum density using some initial reference point ρ_0, T_0 to directly estimate the equilibrium pressure:

$$P_i^{eq} = \frac{B}{\bar{\rho}}(\rho_i - \rho_0) + E\alpha(T_i - T_0) \tag{6.28}$$

Alternatively, for the density evolution description of SPAM, it is desirable to use the rate of change of density and by extension the rate of change of temperature to define the rate of change of equilibrium pressure and integrate along with the other variables:

$$\dot{P}_i = \frac{B}{\rho_i}\dot{\rho}_i + E\alpha\dot{T}_i \tag{6.29}$$

which takes the SPAM form:

$$\begin{aligned}\dot{P}_i = B\sum_j \frac{m_j}{\rho_j}(v_j - v_i)\frac{x_{ij}}{|x_{ij}|}w'(|x_{ij}|) \\ +E\alpha C\sum_j (T_j - T_i)W(r_{ij})\end{aligned} \tag{6.30}$$

where C is the constant for temperature evolution defined by Hoover [54] as:

$$C = \frac{D_T}{\sum \frac{x^2 w(x)}{2}} \tag{6.31}$$

Artificial Viscosity

In the absence of boundary conditions we expect a heated elastic material to expand. This expansion force can be equated to placing a sample under tensile load and thus it is expected that the simulation would exhibit instability in the form of the tensile instability. This exhibits itself in the form of particle clumping and initial tests with the SPAM simulations show that at a minimum artificial viscosity must be included to help stabilise this instability. The use of artificial viscosity also helps to smoothed contact discontinuities as in the case of the artificial conductivity discussed in the previous section. The form for artificial viscosity used within this work is based on Reimann solvers [98] and is given as:

$$\Pi_{P,ij} = \frac{\alpha^P v_{sig,ij}}{\bar{\rho_{ij}}}\frac{v_{ij}\cdot x_{ij}}{|x_{ij}|} \tag{6.32}$$

The signal velocity is calculated in the more standard method:

$$v_{sig,ij} = \frac{1}{2}[c_i + c_j - 2v_{ij}\cdot r_{ij}] \tag{6.33}$$

Here c is the particle sound speed. For solids we use the approximation $c_i = \sqrt{\frac{E}{\rho_i}}$. Instead of the dependence on temperature difference between particles the viscosity term is dependent on the magnitude of the particle velocities acting along their respective line of sight. This means it only

affects particle movement toward and away from each other. The coefficient of dissipation takes the same general from as for the conductivity:

$$\frac{d\alpha_i^P}{dt} = -\frac{\alpha_i^P - \alpha_{min}^P}{\tau_i} + S_i \tag{6.34}$$

Again with $\tau_i = 10H/v_{sig}$. For the viscosity we use a source term defined by particle divergence being negative, so as to avoid particle clumping:

$$S_i = \text{Max}\left(-\nabla \cdot v, 0\right)\left(2 - \alpha^P\right) \tag{6.35}$$

Boundary Enforcement

The thermal boundary conditions for these simulations are enforced as in the previous chapter for both fixed and dynamic conditions respectively. We require that no particle be allowed to pass through the boundary and we therefore require further conditions on particle motion. For the fixed case the obvious choice is to restrict particle velocities $v_{i'} = 0$. For this to work effectively we must assign the pressure at the fixed boundary to oppose the system particle stress, otherwise the forces acting on the system boundaries will constantly be out of equilibrium. The easy choice is to simply assign the fixed boundary pressure as the expected final pressure however this is difficult to generalise. We therefore must either allow the fixed boundary pressure to be evolved at each time step as with the system heat flux, or alternatively we can simply employ 'hybrid' boundaries by assigning the fixed boundary particle pressure at each time step equal and opposite to the local system pressure. We will explore each of these methods.

$$P_{i'} = -P_i \tag{6.36}$$

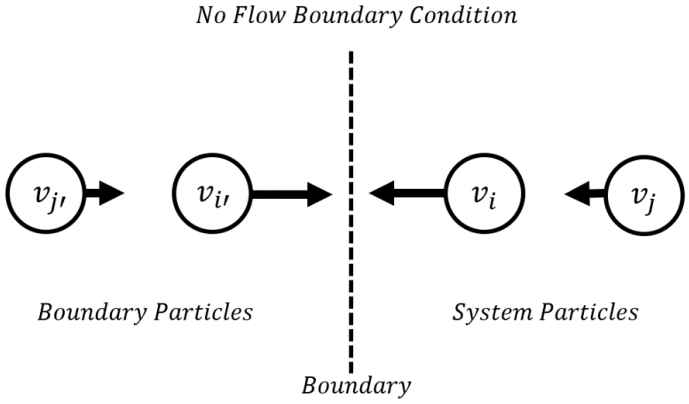

Figure 6.3: Visual representation of the no-flow wall boundary condition in 1D

For the case of dynamic (mirror) boundary conditions we use the commonly used no-flow boundary condition outlined by Hoover [54]. We require that the resultant boundary velocity be zero such that the total material strain is zero:

$$v_B = 0 \tag{6.37}$$

To achieve this we assign the mirror particle velocities equal and opposite to the system particles which they reflect:

$$v_{i'} = -v_i \tag{6.38}$$

The mirror particle position is calculated as:

$$x_{i'} = 2x_B - x_i \tag{6.39}$$

A visual interpretation of this is shown in Fig.6.3. One final consideration is the use of velocity smoothing (also referred to as XSPH). Monaghan outlines [94] the benefits of velocity smoothing in reducing particle penetration of the boundary over the no flow condition alone. Velocity smoothing takes the general form:

$$\hat{v}_i = v_i + \epsilon \sum_j m_j \frac{v_j - v_i}{\bar{\rho}_{ij}} w_{ij} \tag{6.40}$$

where $\epsilon = 0.5$ is the commonly suggested value used within this work. It is common for the smoothing at each step to be calculated taking into account the smoothing at the last step such that:

$$\hat{v}_i = v_i + \epsilon \sum_j m_j \frac{\hat{v}_j - \hat{v}_i}{\bar{\rho}_{ij}} w_{ij} \tag{6.41}$$

6.2.2 1D Thermal Stress Results

All the SPAM simulation results presented within this section were run with a Young's modulus $E = 1000\text{N/mm}^2$, a thermal expansion coefficient $\alpha = 0.01\text{mm/K}$ and a temperature increase at the hot boundary of $T_H = T_C + 0.1$. We therefore expect the final system stress state to be:

$$\sigma_{Final} = -\alpha E \frac{T_C + T_H}{2} = -0.5\text{N/mm}^2 \tag{6.42}$$

It is important to note that due to the allowance of motion within the SPAM simulation and the decisions made within the boundary enforcement, the final stress state of the SPAM system will have small expected variations at the boundary. This would also be expected for experimental validation as a completely static boundary is non-physical and small variations in strain by the constraining material would be expected.

The thermal conditions are as for the previous simulations with thermal conductivity $\kappa = 10\text{gmm/s}^3\text{K}$ and specific heat $C_p = 1\text{mm}^2/\text{s}^2\text{K}$. The time step is again chosen as $dt = 0.01s$.

An analytical solution for the time dependent case of the pressure is not easily derived. However, as shown in the previous section, the time dependence of the temperature evolution from the initial state $T_0 = 1K$ can be calculated. As before this gives us a half life decay time toward steady state as:

$$t_m = -\frac{L^2 ln(0.5^m)}{4\pi^2 D_T} \tag{6.43}$$

Here m denotes the number of half lives. From here we can use the general estimate of sound speed within a solid used in this work to estimate the time taken for the pressure to reach equilibrium:

$$c_0 = \sqrt{\frac{E}{\rho_0}} \tag{6.44}$$

It is important to check however that this is not impeded by the smoothing length which is taken to be $H = 3$mm for these simulations. For each time step this means that the effect of the pressure can only propagate a maximum of the smoothing distance. A maximum estimate for the signal propagation speed is therefore:

$$c_{Max} = \frac{H}{dt} \tag{6.45}$$

This equation can be used to create a criteria for the simulation time step. We require that $c_0 < c_{Max}$. The time step criteria is thus:

$$dt < \frac{1}{H}\sqrt{\frac{\rho_0}{E}} \tag{6.46}$$

For the chosen values this criteria hold. We can then estimate the time taken for the signal to propagate the length of the simulation domain and back as:

$$t_c = 2L\sqrt{\frac{\rho_0}{E}} \approx 6.32s \tag{6.47}$$

We can therefore estimate that the simulation error for $\sigma_{Final} < 0.1\%$ after an elapsed period of $t_{10+c} = t_{10} + t_c$. The following values are therefore calculated for error analysis:

$$\begin{aligned} t_{1+c} &\approx 23.8776s \\ t_{10+c} &\approx 181.8962s \\ t_{50+c} &\approx 884.2012s \end{aligned} \tag{6.48}$$

It becomes clear that the dominant factor in the equilibrium time calculated here is still the thermal propagation for these simulations.

All the results which follow have been run with artificial viscosity. Simulations for all boundary conditions were found to be unstable in the absence of artificial viscosity. The results for the fixed boundary case with Hoover's temperature evolution and artificial terms included is shown in Fig.6.4. It becomes immediately obvious from the density profile that some level of instability induced by constant fixed boundary pressure $P_H = P_C = -0.5\text{N/mm}^2$. Once equilibrium is reached this dies away however the time to equilibrium is accelerated by the already enforced pressure. As discussed the use of fixed boundaries is also limiting in the case where the final boundary pressure is not known. Despite this, the final residual error obtained is significantly less than the desired range with $U = 0.00031\text{N/mm}^2$ calculated from:

$$U^2 = \frac{1}{n}\sum_{i}^{n}\left(\sigma_{Analytic}(i) - \sigma_{SPAM}(i)\right)^2 \tag{6.49}$$

The results for hybrid boundary conditions given by Eq.6.36 are shown in Fig.6.5. The propagation of the stress can clearly be seen for the t_{1+c} and t_{10+c} times as predicted. Furthermore the density and stress profile remains smoothed throughout the simulation. As predicted the final stress profile is not at equilibrium for t_{10+c}, unlike for the fixed case, where the boundary enforcement drives a faster approach to equilibrium. The residual error for the t_{50+c} time step is calculated as $u = 0.00036\text{N/mm}^2$ which although worse than the fixed case is within the expected bounds of error.

Finally, we examine the use of mirror boundaries with the no flow enforcement. As discussed this is expected to help with boundary penetration and reduce the material strain at the boundary. The

results are shown in Fig.6.6. The no flow condition can be seen to cause density problems at the boundary. As previously discussed the use of velocity smoothing helps mitigate this issue. This will be demonstrated in the following section. The miscalculation of boundary values is also greatly affected by the choice of the sum density used here. Use of the density evolution formulation of SPAM helps mitigate the discontinuities at the boundary which can clearly be seen in the mirror results.

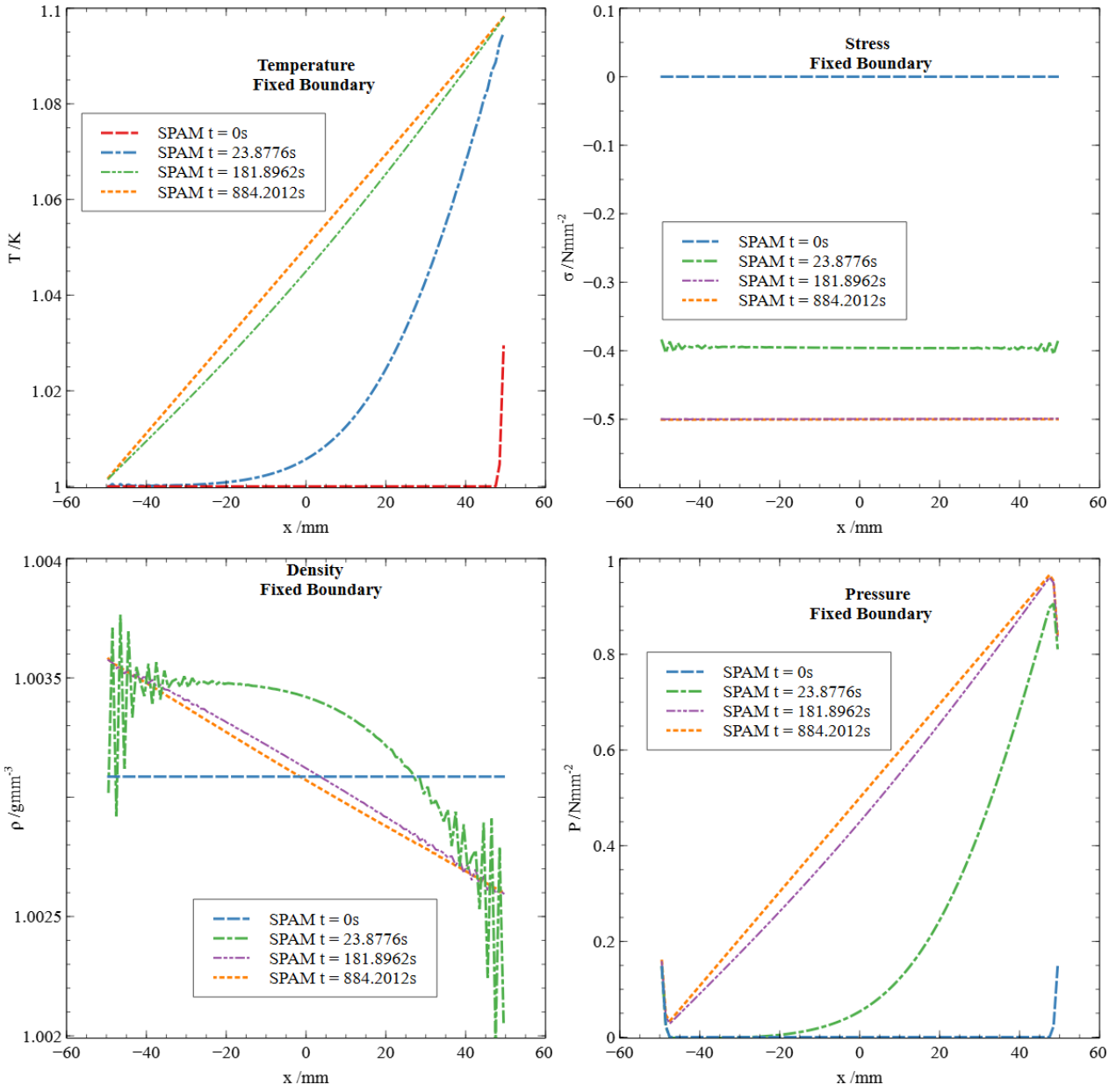

Figure 6.4: 1D thermal-induced stress SPAM results for fixed boundaries with Hoover's form of temperature evolution and artificial terms included. The given profiles are the initial profile as well as the 3 times given by Eq.6.48. Top left the temperature profile, top right the stress profile, bottom left the density profile and bottom right the pressure profile. All profiles are SPAM-interpolated results.

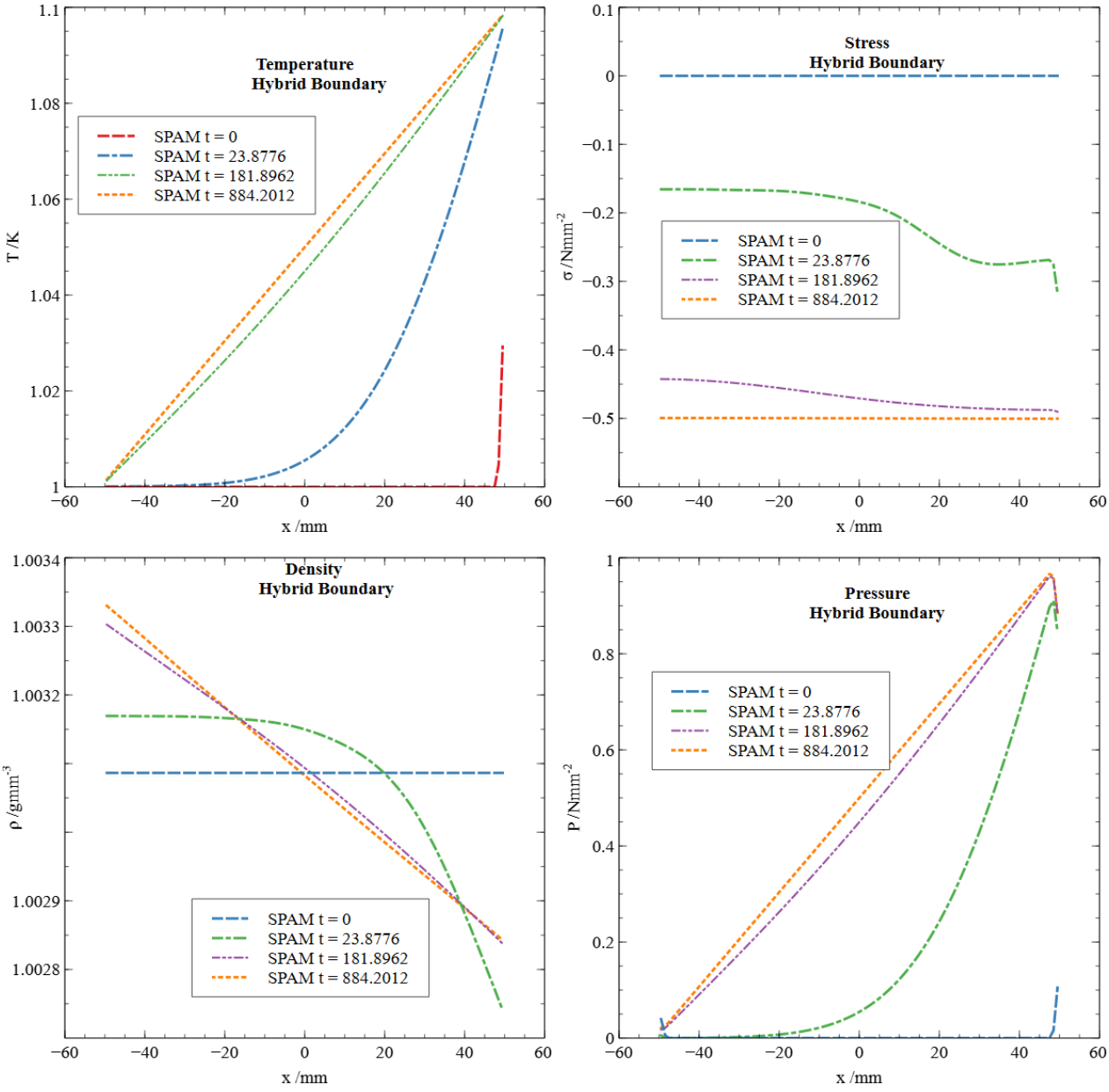

Figure 6.5: 1D thermal-induced stress SPAM results for hybrid boundaries with Hoover's form of temperature evolution and artificial terms included. The given profiles are the initial profile as well as the 3 times given by Eq.6.48. Top left the temperature profile, Top right the stress profile, bottom left the density profile and bottom right the pressure profile. All profiles are SPAM-interpolated results.

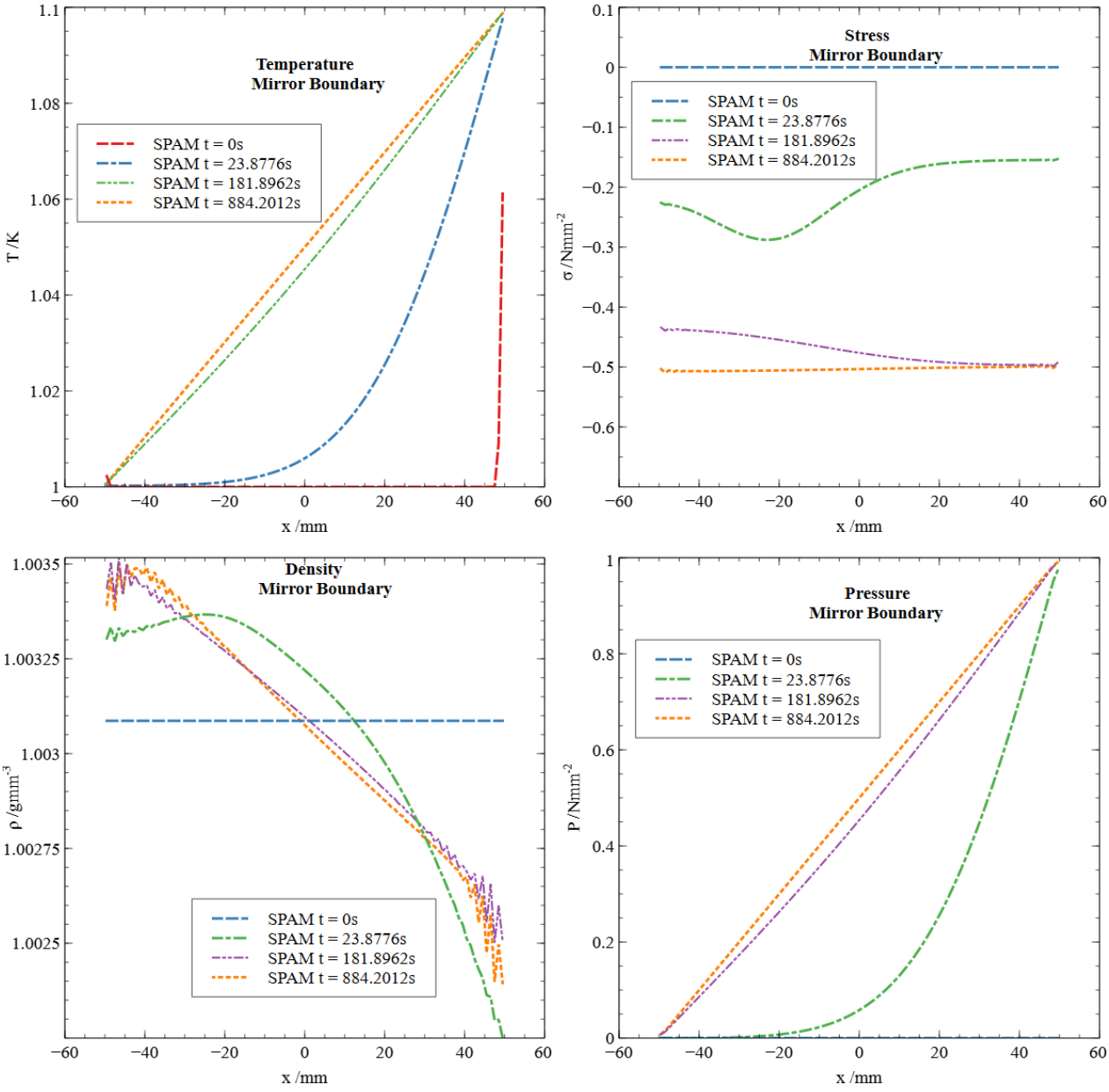

Figure 6.6: 1D thermal-induced stress SPAM results for mirror boundaries with Hoover's form of temperature evolution and artificial terms included. The given profiles are the initial profile as well as the 3 times given by Eq.6.48. Top left the temperature profile, top right the stress profile, bottom left the density profile and bottom right the pressure profile. All profiles are SPAM-interpolated results.

6.2.3 Corrective Results

As discussed for particle motion within SPAM the particle velocities and densities can introduce discontinuities into the simulation. We therefore examine the effect of velocity smoothing and the density evolution formulation of SPAM discussed earlier. The simulation profiles presented in this section are for the mirror boundary conditions, however, these methods have been tested for all

three boundary conditions and the residual errors given in Fig.6.9.

The use of velocity smoothing can be seen in Fig.6.7. Although not apparent from the profiles, there is a reduction in the residual error calculated. However, the instability present in the simulation profiles at the boundary has not been mitigated and therefore velocity smoothing alone is insufficient.

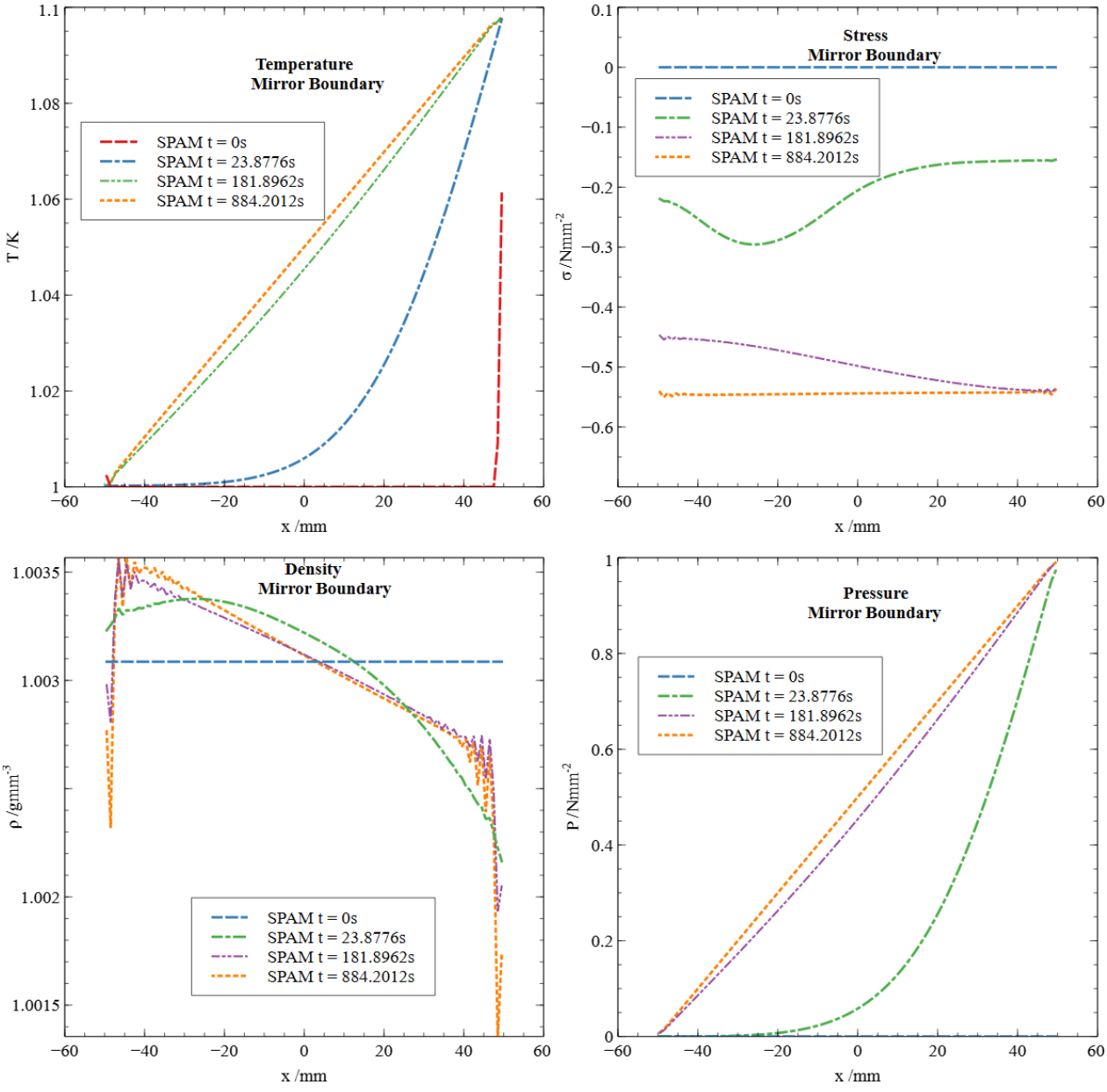

Figure 6.7: 1D thermal-induced stress SPAM results for mirror boundaries with Hoover's form of temperature evolution, artificial terms included and velocity smoothing. The given profiles are the initial profile as well as the 3 times given by Eq.6.48. Top left the temperature profile, top right the stress profile, bottom left the density profile and bottom right the pressure profile. All profiles are SPAM-interpolated results.

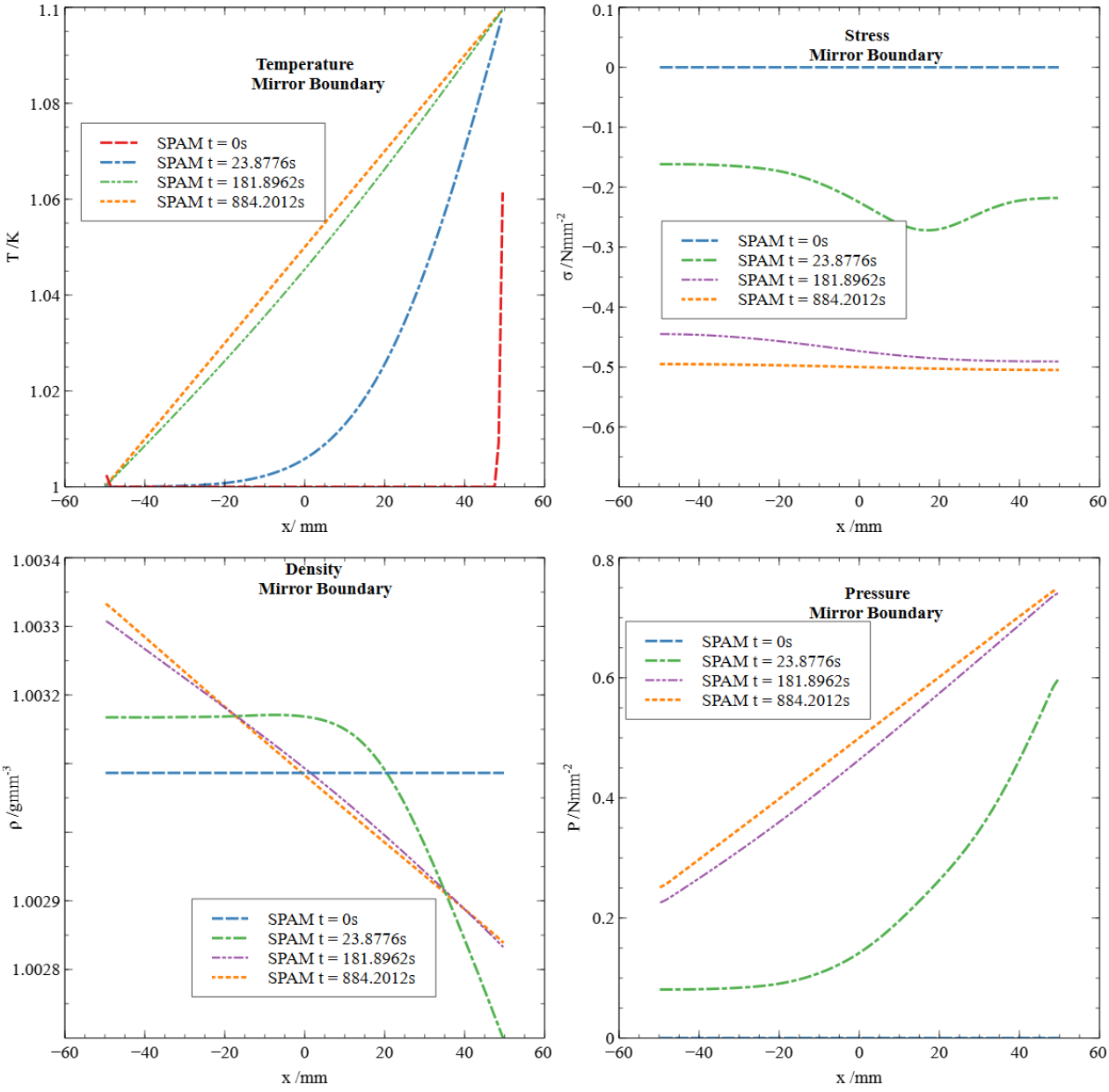

Figure 6.8: 1D thermal-induced stress SPAM results for mirror boundaries with Hoover's form of temperature evolution and artificial terms included. For this simulation the density evolution formulation of SPAM is used. The given profiles are the initial profile as well as the 3 times given by Eq.6.48. Top left the temperature profile, Top right the stress profile, bottom left the density profile and bottom right the pressure profile. All profiles are SPAM-interpolated results.

Alternatively the use of the density evolution formulation combined with the pressure and deviatoric stress evolution outlined by Eq.6.18 can be seen to completely solve the boundary issues introduced in the mirror case. These results can be seen in Fig.6.8. The smoothed profiles are as seen for the hybrid case but with the increased computational time for the dynamically calculated boundaries. It is therefore apparent that the use of hybrid boundaries provides the best possible accuracy with the most computational efficiency.

The final residual errors for all two of the three boundaries under the corrective methods discussed are shown in Fig.6.9. It is interesting to note that the use of velocity smoothing rarely causes a reduction in the residual error. Hoover [54] notes that the use of velocity smoothing with viscous force can be unstable and thus this may contribute to the increased error. The final calculated error is greatly reduced however by the use of the density evolution formulation (Eq.2.41) therefore this will be employed in future simulations. The corrective methods presented here are by no means exhaustive. Artificial terms may be added to the stress tensor [138] and more advanced implementations have used dissipation within the stress tensor in order to remove spurious stress profiles [140]. Such implementations have been used to model high deformation found in geotechnical problems and their applications here are an alternative to the artificial terms used.

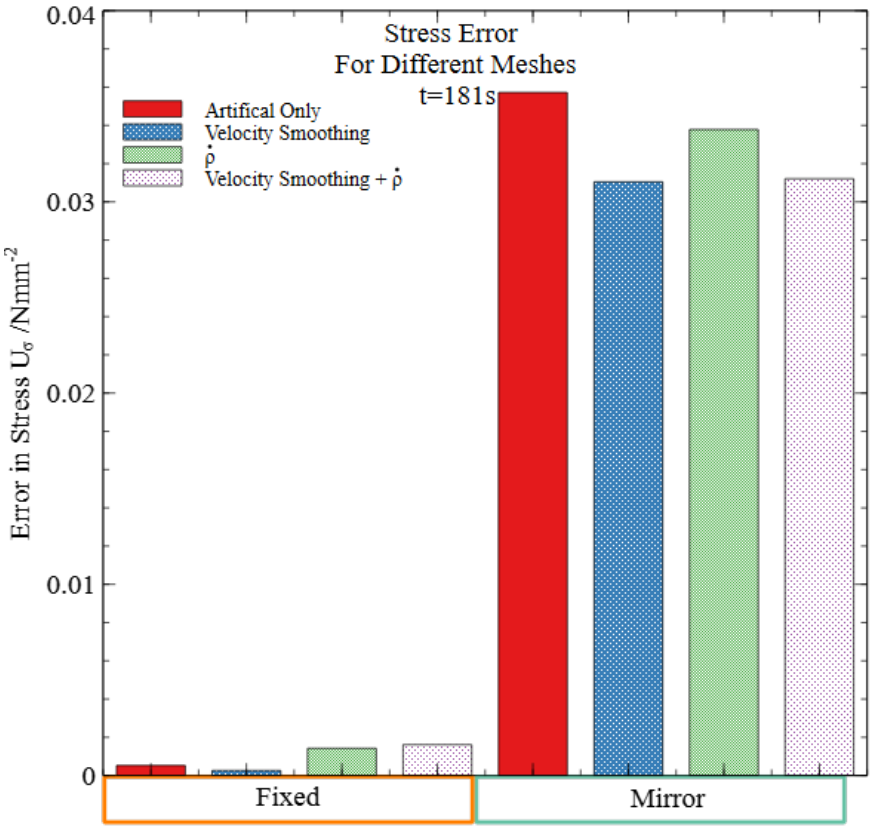

Figure 6.9: Residual error calculated for the SPAM results vs analytical results for 1D thermal stress simulations. Various corrective methods are compared for the two boundary conditions, fixed and mirror. The error is calculated using Eq.6.49 with $\sigma_{Analytic} = -0.5\text{N/mm}^2$ in both cases. The error is calculated for two time steps, above t_{10+c} and Fig.6.10 gives t_{50+c}.

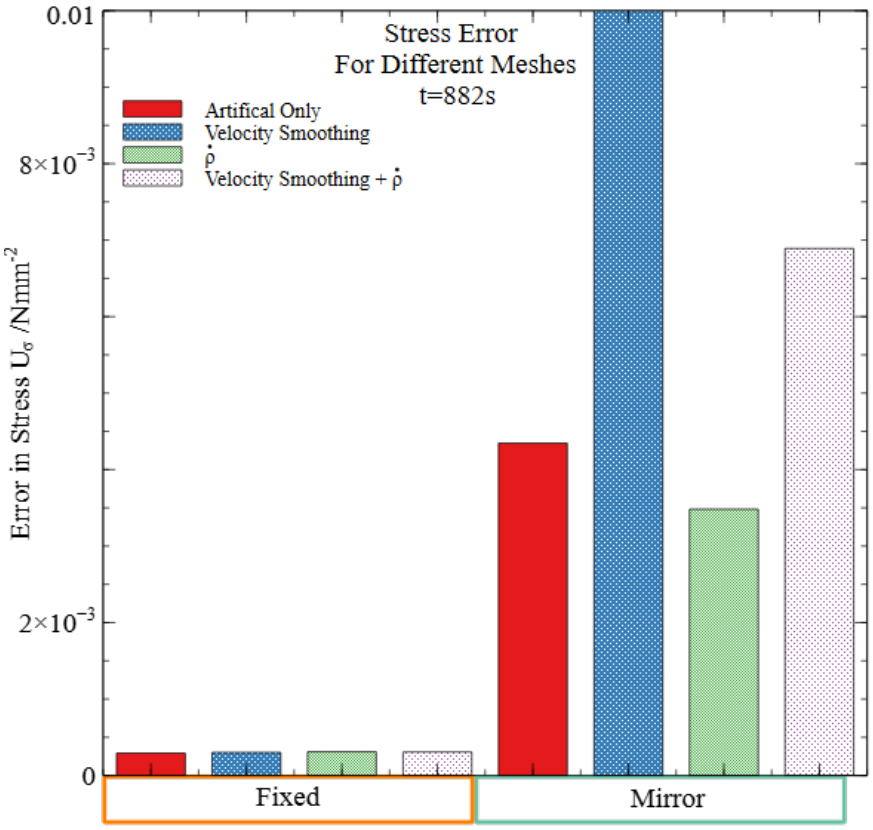

Figure 6.10: The same results as given in Fig.6.9 however the error is calculated for t_{50+c}. The case of the mirror boundary with just artificial terms is truncated from the graph to allow for clearer comparison of the other results.

6.3 Thermal Stresses in a 2D Annulus

For the 2D model, the problem of radial heat flow in an annulus is revisited. A diagram of the model is shown in Fig.6.11. An annulus of inner radius A, outer radius B is assumed to have constant inner and outer temperatures T_i and T_o respectively. The solution for the temperature profile of this model has already been calculated and is given by Eq.4.10. It is now assumed that the material experiences thermal expansion with coefficient α. Again the material is assumed to be infinite in the z direction. This now allows for the assumption that the material undergoes plane strain.

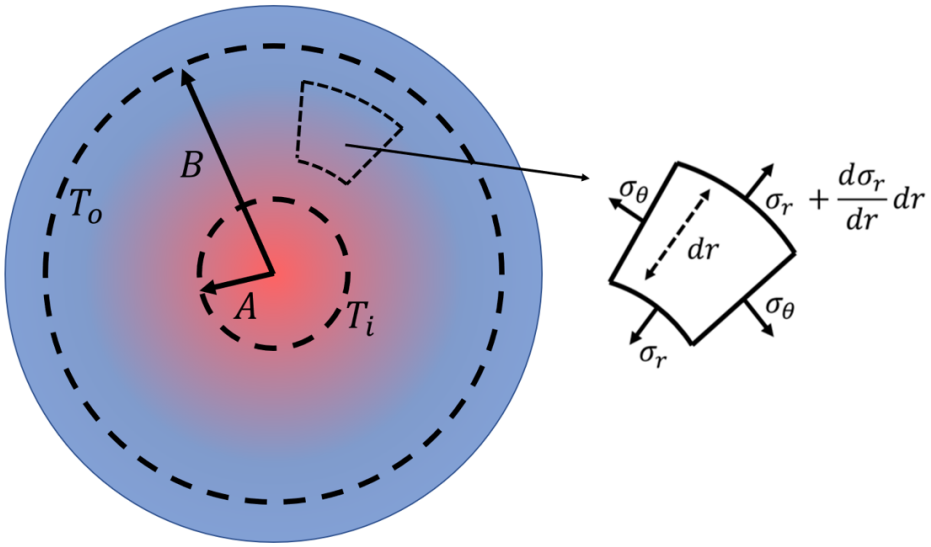

Figure 6.11: Diagram of the radial heat flow model for an annulus undergoing thermal expansion. The stresses produced on infinitesimal element due to the expansion are shown enlarged.

As with the 1D model the material is assumed to undergo purely elastic deformation with Young's modulus E. To account for the 2D nature of the model the Poisson's ratio ν must also be specified to account for the material expansion in the orthogonal axis to those under stress. We consider the temperature distribution symmetric about the axis again. However, this axial heat flow sets up non-uniform expansion of the annulus element. It is therefore expected that the model will produce both radial and tangential stresses from radial heating alone.

6.3.1 Analytical Solution

The solution is considered for the steady state temperature of the system when the material is at equilibrium. The radial and tangential strains for this model can be defined due to radial displacement:

$$\begin{aligned} \epsilon_r &= \frac{du_r}{dr} \\ \epsilon_\theta &= \frac{u_r}{r} \\ \epsilon_z &= w \end{aligned} \tag{6.50}$$

Here w is some constant due to the assumed plane strain. Again the thermal expansion is considered above some reference temperature T_0. The total deformation can be written in terms of the stresses σ and thermal expansion α as:

$$\epsilon_r = \frac{\sigma_r}{E} - \frac{\nu}{E}(\sigma_\theta + \sigma_z) + \alpha(T - T_0) \tag{6.51}$$

$$\epsilon_\theta = \frac{\sigma_\theta}{E} - \frac{\nu}{E}(\sigma_r + \sigma_z) + \alpha(T - T_0) \tag{6.52}$$

The construction of these relations as well as all the derivations given for this model can be found in more detail in [141]. Rearranging these equations gives the stresses as:

$$\sigma_r = \frac{E}{1+\nu}\left(\epsilon_r + \frac{\nu}{1-2\nu}[\epsilon_r + \epsilon_\theta + \epsilon_z]\right) - \frac{\alpha E(T-T_0)}{1-2\nu} \tag{6.53}$$

$$\sigma_\theta = \frac{E}{1+\nu}\left(\epsilon_\theta + \frac{\nu}{1-2\nu}[\epsilon_r + \epsilon_\theta + \epsilon_z]\right) - \frac{\alpha E(T-T_0)}{1-2\nu} \tag{6.54}$$

Substituting for the displacements gives:

$$\sigma_r = \frac{E}{1+\nu}\left(\frac{du_r}{dr} + \frac{\nu}{1-2\nu}[\frac{du_r}{dr} + \frac{u_r}{r} + w]\right) - \frac{\alpha E(T-T_0)}{1-2\nu} \tag{6.55}$$

$$\sigma_r = \frac{E}{1+\nu}\left(\frac{u_r}{r} + \frac{\nu}{1-2\nu}[\frac{du_r}{dr} + \frac{u_r}{r} + w]\right) - \frac{\alpha E(T-T_0)}{1-2\nu} \tag{6.56}$$

The material is assumed to be at equilibrium. Therefore, considering a single material element as shown in Fig.6.11, the forces must cancel. This gives the following relation at equilibrium:

$$\frac{d\sigma_r}{dr} + \frac{\sigma_r - \sigma_\theta}{r} = 0 \tag{6.57}$$

Substituting for the deformation expressions of stress gives:

$$\frac{d}{dr}\left[\frac{1}{r}\frac{d}{dr}(ru_r)\right] = \alpha\frac{1+\nu}{1-\nu}\frac{dT}{dr} \tag{6.58}$$

This equation can then be integrated to obtain the solution for the displacement due to the temperature. The first integration gives:

$$\frac{d}{dr}(ru_r) = \frac{1+\nu}{1-\nu}\alpha T r + 2C_1 r \tag{6.59}$$

Integrating again gives:

$$u_r = \frac{1}{r}\frac{(1+\nu)}{(1-\nu)}\int_A^r \alpha T r dr + C_1 r + C_2\frac{1}{r} \tag{6.60}$$

The integration constants C_1, C_2 are found by considering the boundary conditions on the stress. It is therefore easiest to consider the stress instead of the displacement:

$$\sigma_r = \frac{E}{1+\nu}\left(-\frac{1+\nu}{1-\nu}\frac{1}{r^2}\int_A^r \alpha T r dr + \frac{C_1}{1-2\nu} - \frac{C_2}{r^2} + \frac{\nu w}{1-2\nu}\right) \tag{6.61}$$

The radial stress is assumed to be zero at the boundaries of the annulus:

$$\sigma_r(A) = 0 \tag{6.62}$$

$$\sigma_r(B) = 0 \tag{6.63}$$

With these boundary conditions the values of C_1 and C_2 are calculated and thus the radial stress is given by:

$$\sigma_r = \frac{E}{1+\nu}\left(-\frac{1}{r^2}\int_A^r \alpha T r dr + \frac{r^2 - A^2}{r^2(B^2 - A^2)}\int_A^B \alpha T r dr\right) \tag{6.64}$$

As expected the dependence on the strain in the z axis has been completely eliminated from the solution by the constant C_1. Now by rearranging the equilibrium Eq.6.57, the tangential stress is obtained from the radial stress:

$$\sigma_\theta = \frac{E}{1+\nu}\left(\frac{1}{r^2}\int_A^r \alpha T r dr + \frac{r^2+A^2}{r^2(B^2-A^2)}\int_A^B \alpha T r dr - \alpha T\right) \tag{6.65}$$

From here the temperature solution must be substituted. This was derived in a previous chapter and given by Eq.4.10. The integral can then be derived as:

$$\begin{aligned}\int_A^r \alpha T r dr = \frac{\alpha}{2} ln\left(\frac{B}{A}\right)\Bigg[T_i\left(r^2 ln\left(\frac{B}{r}\right) - A^2 ln\left(\frac{B}{A}\right)\right) \\ + T_o r^2 ln\left(\frac{r}{A}\right) + (T_i - T_o)(A^2 - r^2)\Bigg]\end{aligned} \tag{6.66}$$

Using this the final radial and tangential stress are obtained as:

$$\begin{aligned}\sigma_r = \frac{E\alpha}{(1-\nu)ln(B/A)}\Bigg[\frac{T_o}{2}\left(-ln\left(\frac{r}{A}\right) + \frac{B^2}{B^2-A^2}\left(1-\frac{A^2}{r^2}\right) ln\left(\frac{B}{A}\right)\right) \\ - \frac{T_i}{2}\left(ln\left(\frac{B}{r}\right) + \frac{A^2}{B^2-A^2}\left(1-\frac{B^2}{r^2}\right) ln\left(\frac{B}{A}\right)\right)\Bigg]\end{aligned} \tag{6.67}$$

$$\begin{aligned}\sigma_\theta = \frac{E\alpha}{(1-\nu)ln(B/A)}\Bigg[\frac{T_o}{2}\left(-ln\left(\frac{r}{A}\right) + \frac{B^2}{B^2-A^2}\left(1+\frac{A^2}{r^2}-1\right) ln\left(\frac{B}{A}\right)\right) \\ - \frac{T_i}{2}\left(ln\left(\frac{B}{r}\right) + \frac{A^2}{B^2-A^2}\left(1+\frac{B^2}{r^2}-1\right) ln\left(\frac{B}{A}\right)\right)\Bigg]\end{aligned} \tag{6.68}$$

6.3.2 Analytical Results

The analytical solution for the radial and tangential stress are shown in Fig.6.12. The inner and outer radii are chosen as for the previous annular model explored in Sec.4. These values are $A = 8$mm, $B = 20$mm. The outer temperature is again chosen as $T_o = 1$K however the inner temperature is reduced, compared to the purely thermodynamic model, to $T_i = 1.1$K. This is done to reduce the stresses produced. As will be discussed in the following section the SPAM simulations have problems with higher values of stress.

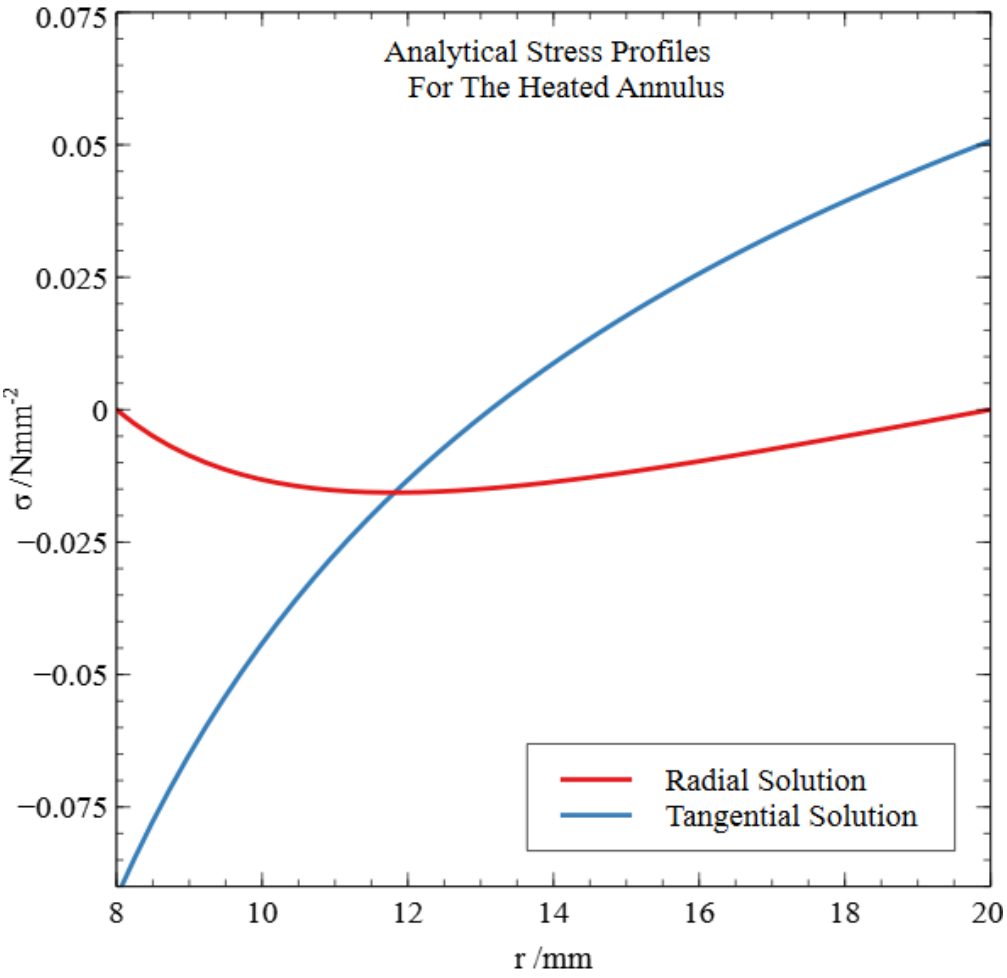

Figure 6.12: Analytical stress solution for an annulus with constant inner and outer temperatures $T_i = 1.1\text{K}$, $T_o = 1.0\text{K}$ respectively. Young's modulus $E = 1000\text{N/mm}^2$, Poisson's ratio $\nu = 0.3$ and thermal expansion $\alpha = 0.001\text{mm/K}$

6.3.3 Stress in an Annulus via SPAM

For the 2D SPAM simulations of thermal expansion, the artificial viscosity is included within the SPAM equation of motion:

$$\frac{dv_i^\alpha}{dt} = \sum_j m_j \left(\frac{\sigma_i^{\alpha\beta}}{\rho_i^2} + \frac{\sigma_j^{\alpha\beta}}{\rho_j^2} + \Pi_{P,ij} \right) \cdot \nabla_i w\left(r_{ij}\right) \tag{6.69}$$

Here α, β denote the dimensional indices of the tensor entries for the stress. the rate of change of velocity is found for each dimension α by the summation over the indices α, β and the particles are defined by the indices i, j as usual. The artificial viscosity is calculated as for the 1D case. The stress tensor requires the inclusion of Poisson's ratio as well as strains from multiple directions for

the 2D model to work. The strain rates are calculated as before from the velocity gradients:

$$\begin{aligned} \dot{\epsilon}_{xx} &= \frac{\partial v_x}{\partial x} \\ \dot{\epsilon}_{yy} &= \frac{\partial v_y}{\partial y} \\ \dot{\epsilon}_{xy} = \dot{\epsilon}_{yx} &= \frac{1}{2}\left(\frac{\partial v_x}{\partial y} + \frac{\partial v_y}{\partial x}\right) \end{aligned} \tag{6.70}$$

The velocity gradient is required to calculate the stress tensor and is calculated as:

$$\frac{dv_i^\alpha}{dx} = \sum_j \frac{m_{ij}}{\rho_{ij}} \left[\mathbf{v}_j^\alpha - \mathbf{v}_i^\alpha\right] \nabla_i^\alpha w\left(r_{ij}\right) \tag{6.71}$$

Here the symmetrised mass and density are used such that $m_{ij} = \sqrt{m_i m_j}$ and $\rho_{ij} = \sqrt{\rho_i \rho_j}$. As in the 1D case the stress is separated into the equilibrium pressure and the deviatoric stress. The rate of change of the deviatoric stress for particle i when derived for plane strain can be written in the form:

$$\dot{S}_i^{\alpha\beta} = \frac{E}{1+\nu}\left[\frac{\delta^{\alpha\beta}}{1-2\nu}\left((1-\nu)\dot{\epsilon}_i^{\alpha\beta} + \sum_{\gamma\neq\alpha}\nu\dot{\epsilon}_i^{\gamma\gamma}\right) + (1-\delta^{\alpha\beta})\dot{\epsilon}_i^{\alpha\beta}\right] \tag{6.72}$$

Here the sum γ is over the remaining spatial dimensions for each tensor dimension denoted by α, β. The delta function is noted as $\delta^{\alpha\beta}$ which takes the value 0 unless $\alpha = \beta$ then it takes the value 1. The stress tensor in 2D is given by:

$$\sigma_i^{\alpha\beta} = -P_i\delta^{\alpha\beta} + S^{\alpha\beta} \tag{6.73}$$

It was found that the use of a bulk pressure added by the equation of state given in Eq.6.25 caused the introduction of errors, therefore the pressure term is formulated with only the thermal expansion in both the standard and rate of change variations for the two methods of density calculation:

$$P_i^{eq} = \frac{E}{1-2\nu}\alpha(T_i - T_0) = 3B\alpha(T_i - T_0) \tag{6.74}$$

$$\dot{P}_i = \frac{E}{1-2\nu}\alpha\dot{T}_i = 3B\alpha\dot{T}_i \tag{6.75}$$

As before the use of density evolution is given by Eq.2.41 and the velocity smoothing terms given by Eq.6.41. Finally the SPAM simulation are run in Cartesian co-ordinates therefore the conversion of the stress tensor between Cartesian and cylindrical polar co-ordinates is required. For this, the rotation matrix $\mathbf{M_{x\to r}}$ is used:

$$\mathbf{M_{x\to r}} = \begin{pmatrix} cos\theta & sin\theta & 0 \\ -sin\theta & cos\theta & 0 \\ 0 & 0 & 1 \end{pmatrix} \tag{6.76}$$

With the conversion then given by:

$$\boldsymbol{\sigma}_{\mathbf{r},\boldsymbol{\theta},\mathbf{z}} = \mathbf{M_{x\to r}} \cdot \boldsymbol{\sigma}_{\mathbf{x},\mathbf{y},\mathbf{z}} \cdot \mathbf{M_{x\to r}^T} \tag{6.77}$$

6.3.4 Fixed Boundary Annulus

The simplest implementation of this problem within SPAM uses fixed boundary conditions. The initial particle distribution used is the triangular particle arrangement shown in Fig.6.13. The fixed particle temperatures are assigned as $T_{inner} = 1.1$K and $T_{outer} = 1$K. The boundary particles are also assigned fixed pressures and stresses equal to zero $\sigma_r = \sigma_\theta = P = 0\text{N/mm}^2$.

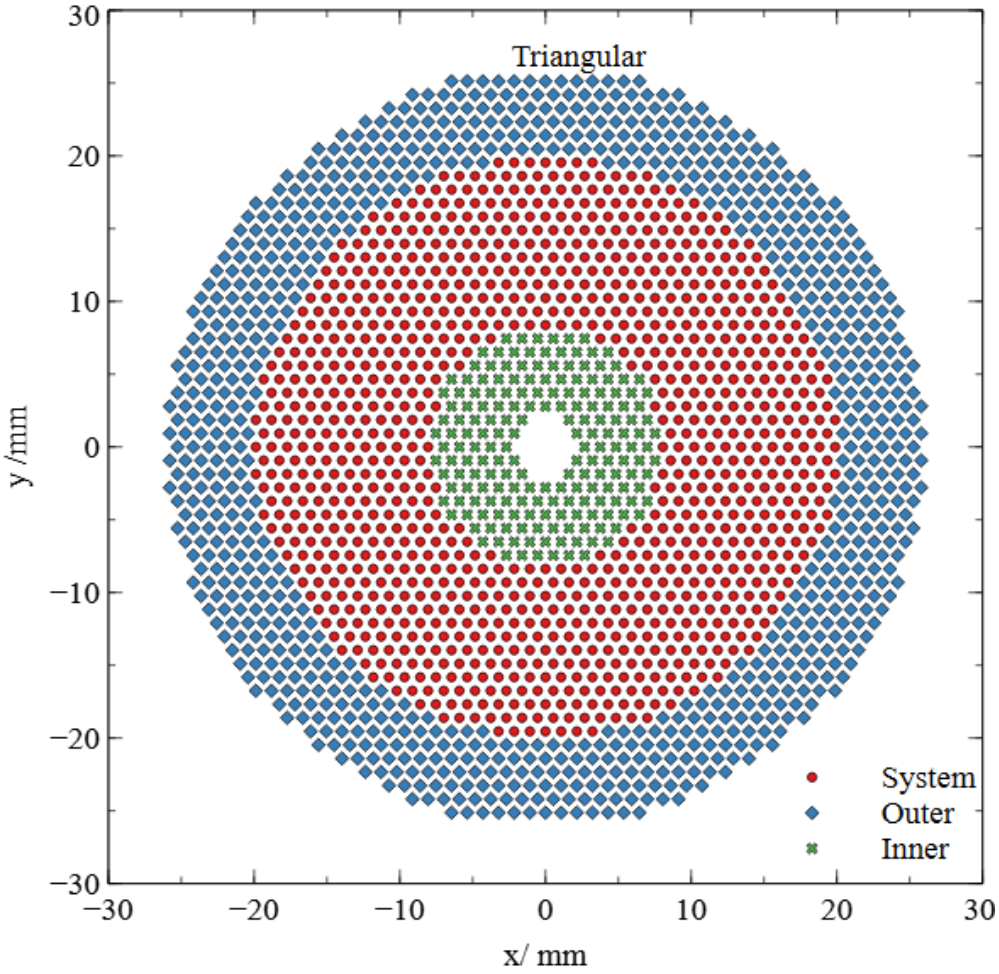

Figure 6.13: Triangular fixed particle arrangement with near unit particle spacing Δ_P and unit density ρ_0. The particle arrangement is used for simulating thermal-induced strains in an annulus.

6.3.5 Fixed Boundary Results

SPAM simulations are run with a time step of $dt = 0.05s$ for 20000 time steps. The values of thermal expansion, Young's modulus and Poisson's ratio are given as:

$$\begin{aligned} \alpha &= 0.001/K \\ E &= 1000N/mm^2 \\ \nu &= 0.3 \end{aligned} \tag{6.78}$$

The results for the unit spacing particle arrangement under both density evolution and sum density

are shown within Fig.6.14. There appears to be no visible benefit from the use of density evolution over the sum density for the case of fixed boundaries in 2D. Similarly, although not shown here, no visible difference was found for the case of velocity smoothing.

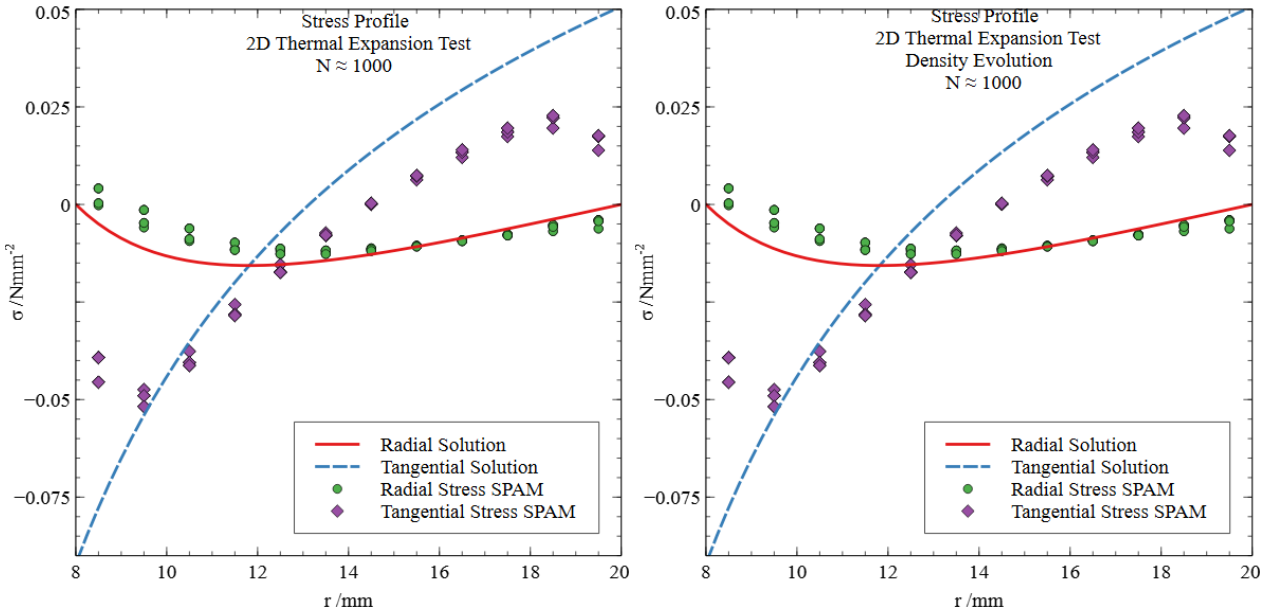

Figure 6.14: Radial and tangential stress profiles for the annulus with constant inner and outer temperature. SPAM simulation completed with fixed boundaries. Left shows the simulation with sum density, right with density evolution.

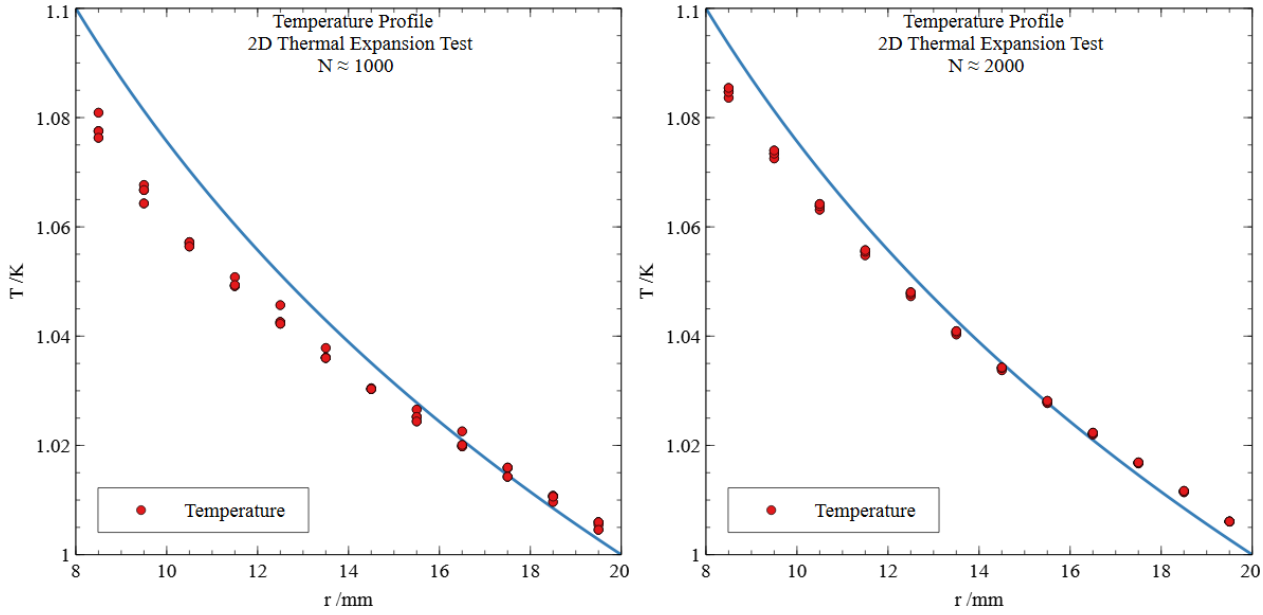

Figure 6.15: Temperature profile for the annulus with constant inner and outer temperature and thermal expansion. SPAM simulation completed with fixed boundaries. Left shows the simulation with $N \approx 1000$ particles, right with $N \approx 2000$.

Unfortunately the stress profiles are seen to deviate significantly from the analytical stress profiles. There are two main causes of this. Firstly, the discrepancy from the expected profile seen at the boundaries for the tangential stress is due to the fixed boundary enforcement of $\sigma_\theta = 0\text{N/mm}^2$ being included in the interpolated profiles. This causes the magnitude of the values interpolated at the boundary to be reduced as the tangential stress is not continuous across the boundary for the particle values.

The second cause of error, which gives rise to the shift in both stress profiles, is due to the underlying temperature profile. As shown for the radial heat flow problem in Sec.4.8, the use of fixed boundary temperatures causes the temperature *at* the boundary to incur an error away from the desired result. The underlying temperature profile is shown in Fig.6.15. Clearly the deviation from the expected profile can be seen.

To improve the stress profile it is therefore beneficial to improve the temperature profile. This was achieved for the particle arrangement test on radial heat flow by increasing the particle number and decreasing the particle mass. Fig.6.15 demonstrates this by showing the improved temperature simulation from simulation with $N \approx 2000$ with $m_i = 0.5\text{g}$. This temperature improvement is seen to also reduce the error in the stress profiles as expected. The improved results are given in Fig.6.16.

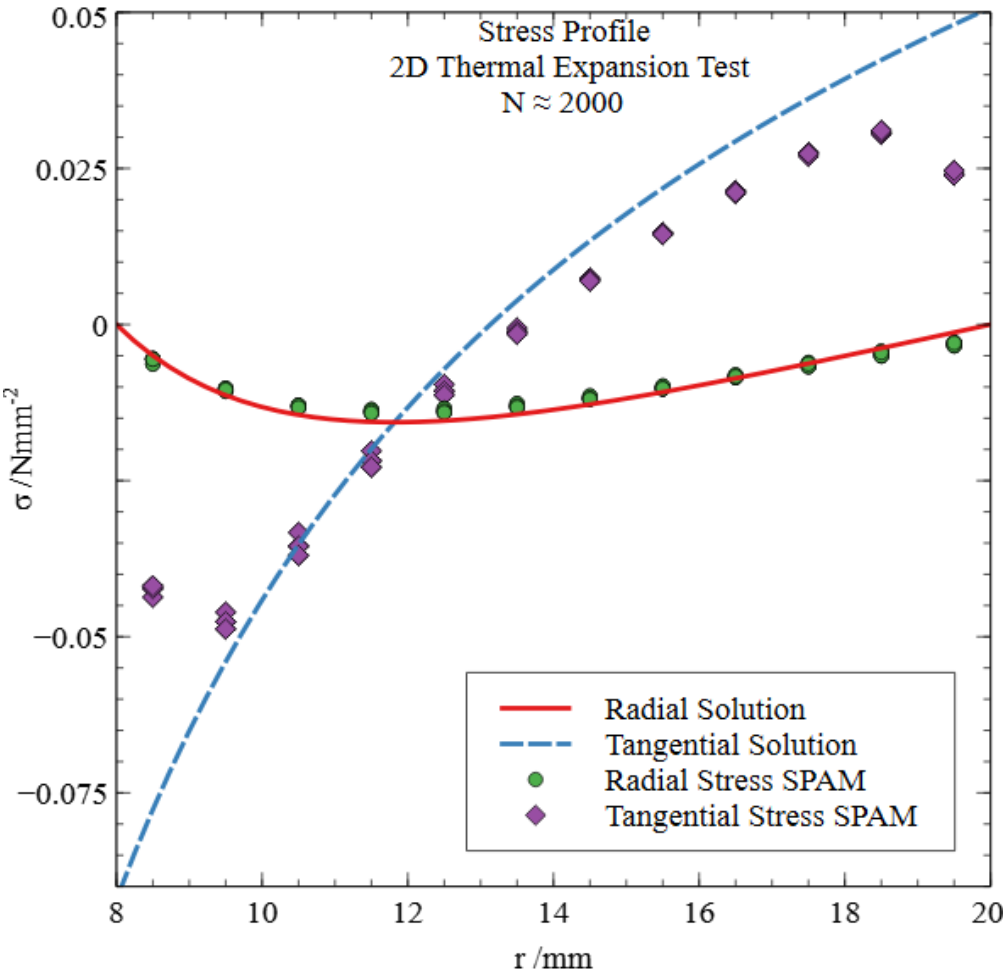

Figure 6.16: Radial and tangential stress profiles for the annulus with constant inner and outer temperature. SPAM simulation completed with fixed boundaries now with $N \approx 2000$ particles with mass $m_i = 0.5$g .

Further improvement can be made by the use of greater particle numbers, however the simulation boundary conditions are still responsible for issues with the tangential stress close to the boundary. It is therefore beneficial to revisit the hybrid boundaries proposed within this chapter.

6.3.6 2D Hybrid Boundary Implementation

To remove the error incurred at the simulation boundary for the fixed simulation results it is possible to implement the hybrid boundaries described for the 1D simulations. To achieve this, each boundary particle stores information of its closest neighbouring system particle across the boundary. A diagram to demonstrate these particle pairs is shown in Fig.6.17.

For the analytical model described for these simulations the radial stress on the boundary is assumed zero, therefore this is still enforce as with the fixed particle case $\sigma_r^B = 0$. However to better preserve the interpolation of the tangential stress profile the hybrid condition of $\sigma_\theta^B = \sigma_\theta^S$ where the system and boundary particles are noted S, B respectively.

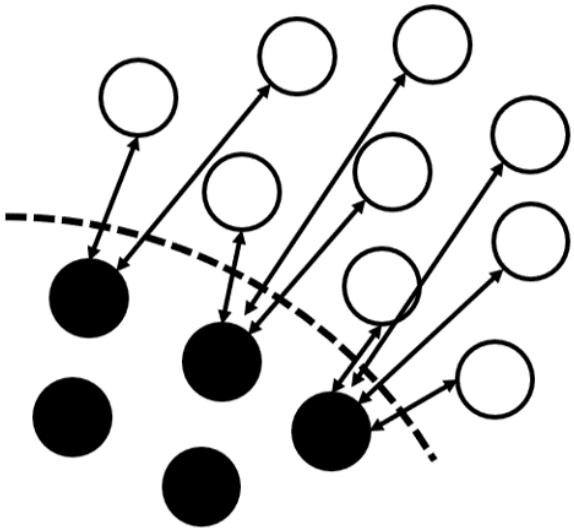

Figure 6.17: A diagram to show how closest system particles are assigned to boundary particles. Boundary particles are shown in white, system particles in black.

Hybrid boundary conditions provide the useful property of dynamic values based on the system (as in the mirror case) without the added complication of moving boundary particles. This makes hybrid boundary particles a simple yet effective alternative.

6.3.7 Hybrid Boundary Results

As with the fixed case the hybrid boundaries show no visible difference in stress profiles for the use of sum density, density evolution or velocity smoothing. To demonstrate this for the density formulations the results are presented in Fig.6.18. The boundary error in the tangential stress result has however been reduced by the used of hybrid conditions.

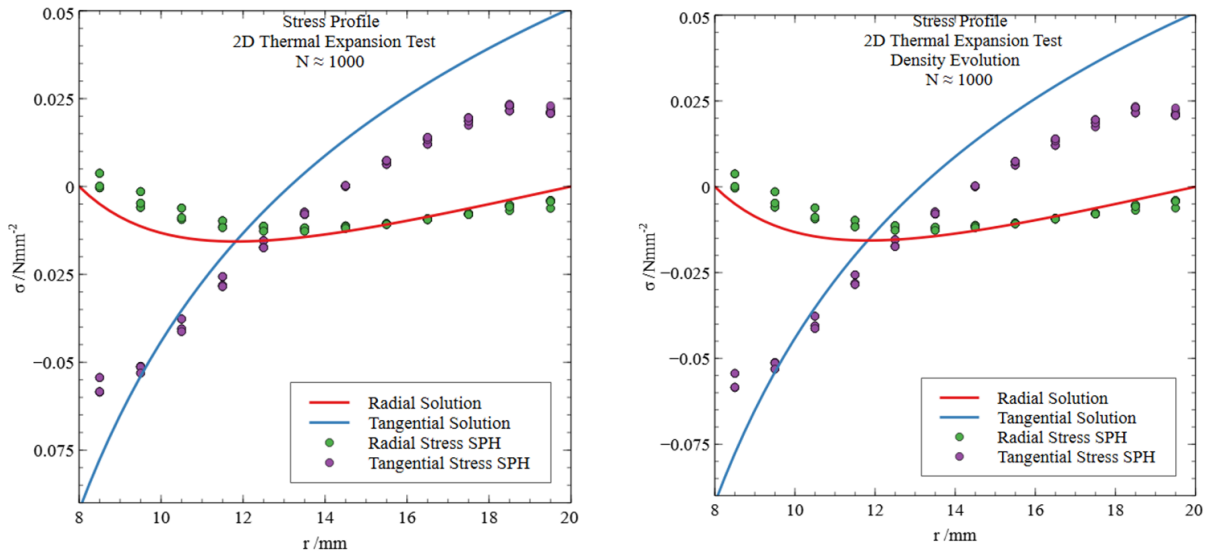

Figure 6.18: Radial and tangential stress profiles for the annulus with constant inner and outer temperature. SPAM simulation completed with hybrid boundaries. Left shows the simulation with sum density, right with density evolution.

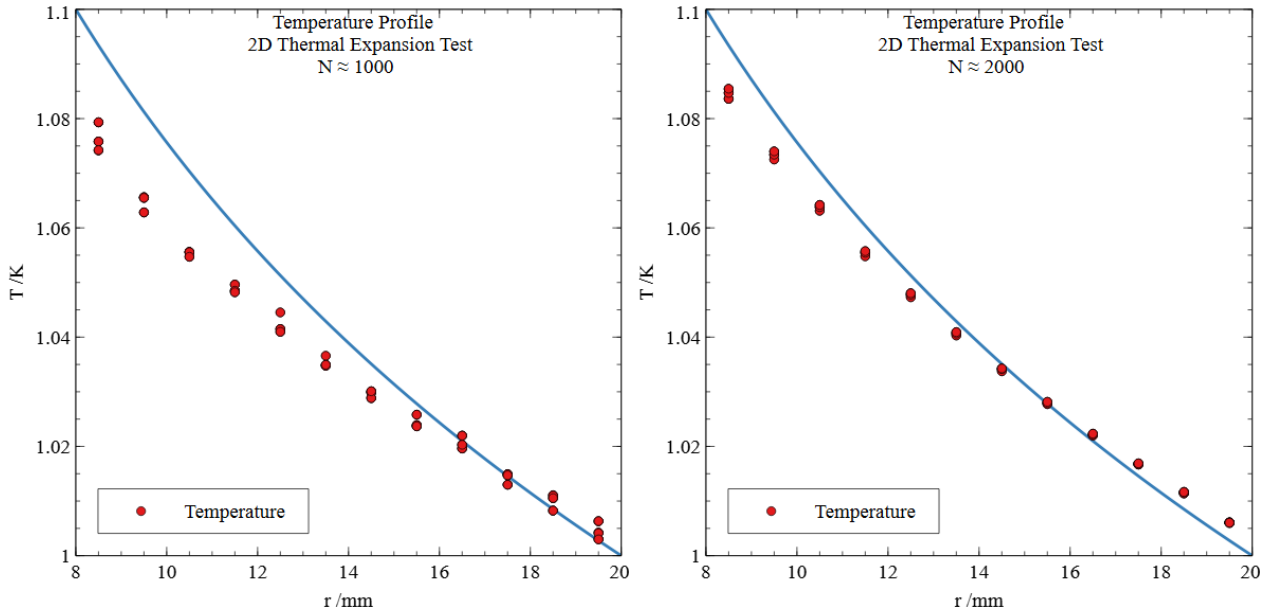

Figure 6.19: Temperature profile for the annulus with constant inner and outer temperature and thermal expansion. SPAM simulation completed with hybrid boundaries. Left shows the simulation with $N \approx 1000$ particles, right with $N \approx 2000$.

The error due to the underlying temperature is still present however and the boundary error has not completely been eliminated. This can again be achieved by increasing the particle number used. The improvement in temperature profile for the use of $N \approx 1000$ and $N \approx 2000$ particles is

shown in Fig.6.19.

The final improved stress profile is given in Fig.6.20. Both the error due to the boundaries and the deviation from the analytical profile can be seen to be reduced. The limitation of the improvement due to increased particle number will be explored for the hybrid simulations, however, it is first beneficial to discuss the mirror boundary case.

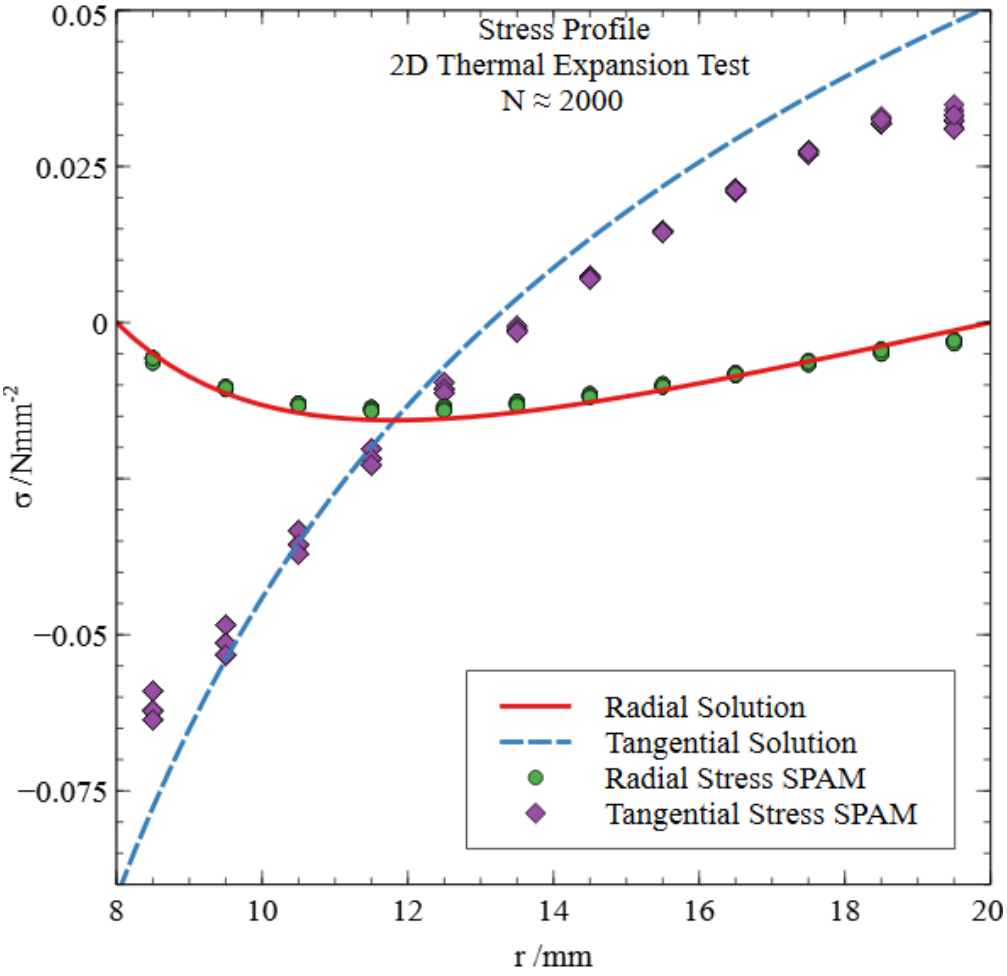

Figure 6.20: Radial and tangential stress profiles for the annulus with constant inner and outer temperature. SPAM simulation completed with hybrid boundaries now with $N \approx 2000$ particles with mass $m_i = 0.5$g.

6.3.8 Limitations of Mirror Boundaries

Unfortunately all attempts to implement these simulations with mirror boundaries were unsuccessful. It is believed the main cause of this is due to mass issues. The corrective mass described in Sec.4.4.1 breaks the symmetry relied upon for the non-slip boundary condition. It has been observed that for all simulation attempts made the internal boundary in particular (where the mass correction is the greatest) causes the simulation to become unstable with system particles escaping across the boundary.

This highlights the particular added complexity of mirror boundaries in systems with motion. Multiple attempts were made to overcome these issues with both sum density and density evolution as well as with velocity smoothing. The removal of the mass correction was also unsuccessful with a dramatic increase in the instability due to the large density gradient created.

Attempts were also made with increasing the boundary particles to approach the limit of boundary normals with system particles along the curve. Up to a boundary spacing of $\Delta_P = 0.1mm$ was attempted. As well as this, multiple variations of the boundary conditions were applied, with mirroring of only the radial component of velocity $v_{r,i'} = -v_{r,i}$, as well as the full no flow condition.

It is left to future work to create a formulation of the general shape mirror boundary condition which removes the issues of boundary penetration and successfully stabilise the simulations. Particle shifting algorithms have been used within hydrodynamic simulations [142] to deal with particle clumping and disorder at the free surface and a form of shifting algorithm could be applied to this general shape mirror algorithm in order to over come the inter particle penetration and escape at the boundary.

Another alternative would be to implement these models using the Eulerain formulation for SPAM instead of the Lagrangian formulation. This would mean that the system particles where static by design and the mass of the particles allowed to vary to allow for the flow of material. This form of SPAM had been demonstrated to be successful in simulating fluid structure interactions [113, 143] where there is a large amount of material movement and so should be more than capable of handling the deformations expected within nuclear fuel.

6.3.9 Convergence of Results

The convergence of the hybrid simulation to the analytical result was attempted for increasing particle numbers. The methodology was as previously described with particle spacing and smoothing length being reduced while mass values were reassigned to maintain the desired $\rho_0 = 1\text{g/mm}^3$. The previous results were completed with a time step of $dt = 0.05$s for $20,000$ steps. This satisfies the time step condition of Eq.6.46 for higher values of $H = 3$mm however as the value of smoothing length decreases with particle separation the time step must decrease accordingly.

The simulations run for this section were therefore run for a time step of $dt = 0.01s$ for $100,000$ time steps. This gives the same total time however the computational time is dramatically increased by a factor of 5. This is coupled with the increase in computational time due to the increasing particle numbers. The largest simulation run for this result required a computation of ≈ 12 hours in real time. It is therefore important that future work improve the code speed with modifications such as the implementation on GPUs achieved with the DualSPHysics code [8].

The particle arrangement values used for the attempted convergence test are presented in Table.6.1. Unfortunately higher particle number tests $N > 1000$ were unsuccessful at showing the convergence of results, this can be seen in Fig.6.21 with the increasing particle number giving stress profiles which deviate further from the analytical. The source of this error is unknown however as discussed in Sec.6.2.2 the sound speed within the simulation is limited by the smoothing length. It is also likely that there is an error introduced into the code of these simulations related to the particle masses, however attempts to find this have been unsuccessful.

N	m_i	Δ_P	H
1046	1	1	3
2018	0.5	0.71	2.13
5146	0.2	0.45	1.35
10472	0.1	0.32	0.96

Table 6.1: The parameters used for the initial unsuccessful tests for convergence of the 2D annulus with thermal expansion.

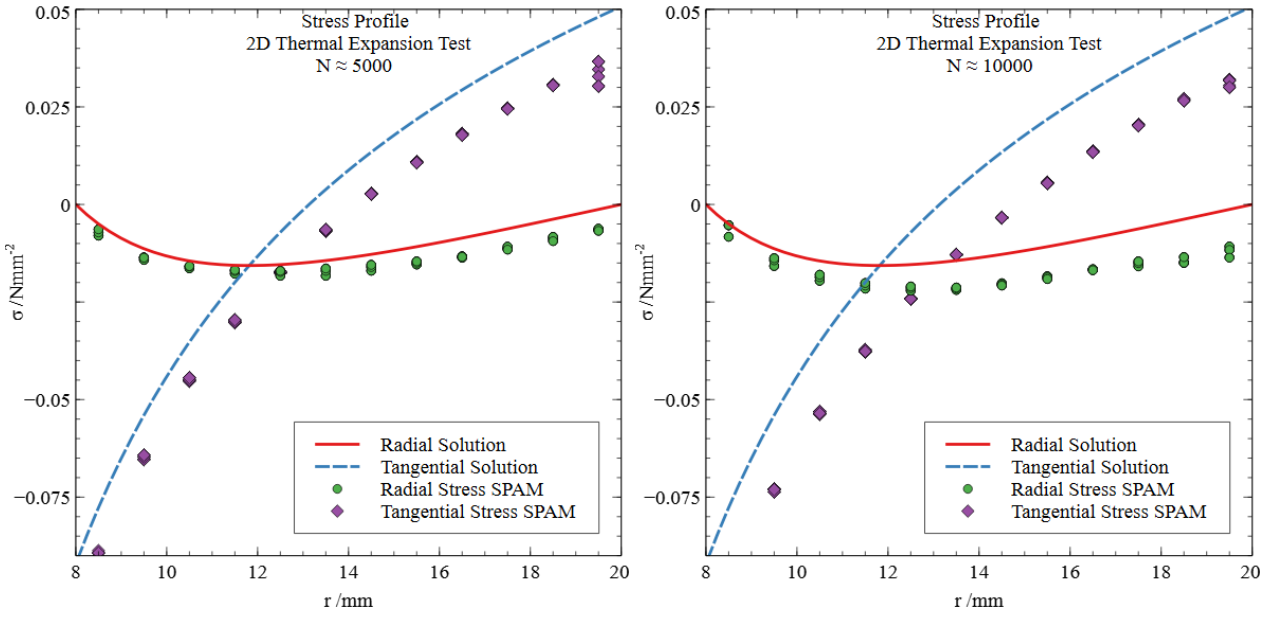

Figure 6.21: SPAM simulation of the heated annulus with thermal expansion are completed for successively larger particle numbers. The hybrid simulations are shown here for left:$N \approx 5000$ and right:$N \approx 10000$

N	m_i	Δ_P	H
820	1.3	1.14	3.42
896	1.2	1.1	3.3
972	1.1	1.05	3.15

Table 6.2: The parameters used for the 3 simulations completed for the convergence test of the 2D annulus with thermal expansion.

Despite the deviation for higher particle numbers the convergence rate for the lower particle number simulations is estimated in Fig.6.22. The new values used are given in Table.6.2. The rate of convergence is estimated for these lower particle numbers as less than linear ≈ 0.6. Again there is a clear error introduced into these simulations as the expected convergence should lie within 1^{st} and 2^{nd} order.

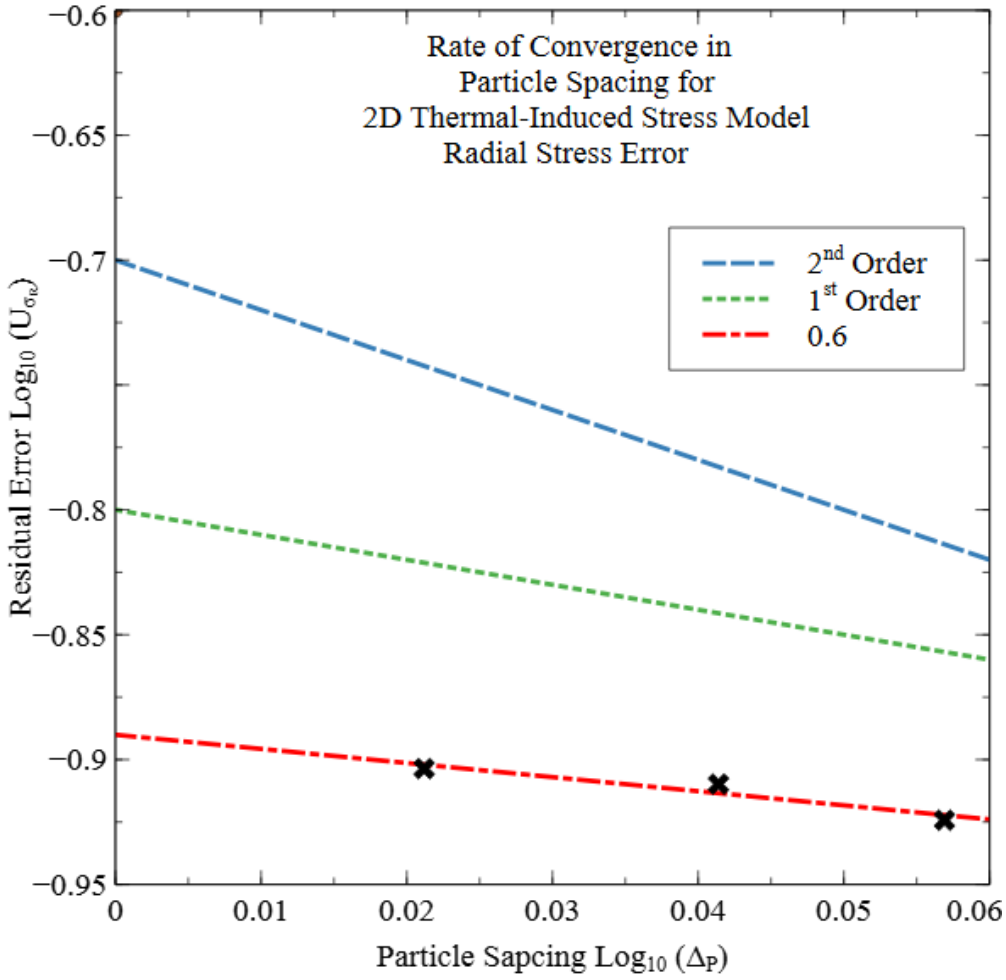

Figure 6.22: Rate of convergence estimated for 3 simulations of lower particle numbers given by Table.6.2. The residual error in the radial stress profile is used to estimate the rate of convergence at ≈ 0.6. The line for linear and second order convergence are also present.

6.4 Basic Damage Implementation

SPAM holds particular promise within nuclear fuel modelling for its ability to handle damage within simulations. This is due to the nonrestrictive nature of the particle arrangement. Complex methods of damage implementation have been proposed such as the Lagrangian description [91]. Unfortunatley a full thermo-mechanical model of nuclear fuel with damage implementation has not been achieved within the scope of this work, however the unfinished attempts are included in Appendix B as an indication of how such a model may be constructed.

6.4.1 Conclusions

Simulations of thermal strain were carried out in 1D and 2D using SPAM. In 1D it was found that the fixed boundary case required implementation of pressures to give the correct results. Hybrid boundaries were therefore proposed to allow for the dynamic assignment of fixed particle properties without the need for dynamic creation and position assignment.

All three boundary conditions were shown to be successful however the mirror boundaries required the use of density evolution instead of sum density to stabilise the result. Velocity smoothing was shown to have varied effectiveness. In general its benefit seems hard to predict with small improvements made in some cases and increases in error for others.

Of all 1D simulations presented the most promising solution appeared to be the use of hybrid boundary conditions with only the artificial terms included. This result was reinforced for simulations of thermal expansion in a 2D annulus with constant inner and outer temperature. For the 2D curved geometry the mirror case was found to be unstable for all simulation variations attempted.

The particle number and time step were found to be important factors for simulations with $N \approx 5000$ particles and above required to be stabilised. It was found that simulations of higher particle numbers suffered with problems for the evolution of the mechanical behaviour in testing. The source of this problem, although clearly mass related remains unidentified. Convergence rate estimates for lower particle numbers supports the existence of some error but does suggest convergence.

The final simulations presented show promise that SPAM simulations are capable of reproducing stress and strain behaviour accurately under the right initialisation condition and thus that the application of SPAM to damage and micro-structure simulations of nuclear fuel are worth pursing.

Further development is required to incorporate a damage model into the model presented at the end of Chapter 5. More complex equations of state must also be included. The literature includes examples of state equations for uranium and plutonium [144], as well as state equations for the effect of creep within metals for application to the cladding [145]. This work does however show the potential for future development and validation of SPAM nuclear fuel models. Emphasis must be placed on the handling of material to material boundaries in order to improve this work.

Chapter 7

Closing Remarks

7.1 Conclusions of this Research

Thermodynamic models of SPAM were created with 3 main methods of temperature evolution. Of these Hoover's method Eq.3.60 was found to have the smallest errors while dealing well with discontinuities within the simulations. Artificial terms and kernel corrections were found to be unnecessary within the thermal simulation. Fixed boundaries were demonstrated to introduce error into the simulation results. Mirror boundaries were shown to fix this issue however their use was found to be complicated for curved boundaries.

Exploration of various methods for constructing particle arrangements demonstrated that relaxation is not required to achieve good results in cylindrical geometry. The disorder of particles within the arrangement was shown to be a significant source of error. Refinement was found to have the most significant and successful reduction in error for thermal simulations.

A new approach to convective boundaries within SPAM was proposed and shown to be successful in both 1D and 2D simulations. The use of the harmonic mean for varied particle thermal conductivities was shown to be a successful modification to Hoover's temperature evolution. However, further modifications were suggested to improve the heat flux calculations. A simple implementation of heat generation for materials within SPAM was proposed and shown to be successful. All of these features were combined into a basic thermal fuel and cladding model with coolant modelled as a convective boundary. The results of the model were shown to converge toward the expected analytical solutions.

Finally, basic mechanical behaviour was implemented with thermal-induced strains. Good agreement was shown for the 1D case, however despite promising results convergence toward the analytical solution for the 2D annular model could not be demonstrated. This is assumed due to errors within the code formulation however this remains unconfirmed. Simple failure mechanics were shown as a proof of concept for future SPAM work. This mechanical behaviour was added to the 2D fuel and cladding model to demonstrate basic failure of fuel and cladding due to thermal effects. More work is required to refine these models and properly validate as was achieved for the thermal models.

The major contributions of this thesis come together within the 2D thermal model of nuclear fuel presented in Sec.5.6. A novel method for convection at the boundary within SPAM is constructed. This method represents an alternative to the current proposed method implemented in

LS-DYNA [132] which allows for multiple particle based boundary conditions to be applied simultaneously due to its nature of prescribing temperatures on boundary particles. An improved method for temperature evolution is rediscovered [54] and found to have higher accuracy than the current standard of thermal evolution equation widely used within the smoothed particle community [108]. The improved method is expanded to two dimensions and found to be effective without any requirement for corrective or artificial terms. The current standard for thermal interface modelling based on harmonic means of thermal conductivities [108] is applied to this evolution with reasonable results achieved. The interface errors however highlight a significant need for improvement of this interface handling in order to improve accuracy and convergence of the fuel and cladding model.

The most significant contribution of this work lies within the 5th grand challenge highlighted for the area of smoothed particle methods [70]. The key review work states that 'applicability to industry' is a key challenge that must be addressed for the near term development of these methods and importantly for there transferal and use towards real world problems faced in the industrial sector. This work has achieved the first step in raising the confidence of the nuclear industry by demonstrating a basic thermal model which is a direct example of the kind of basic model already implemented within the UK FPC ENIGMA. The demonstration of this model with quantification of its accuracy and limitations allows for assessment of the method by the nuclear industry, in particular NNL for whom this work has been completed, with direct comparison to the current industry standard. The potential future benefits of the method, although attractive, cannot out weigh the importance of the simple model validations carried out within this work. The early indication given by NNL that the analysis presented here has encouraged further funding and exploration of the method by the nuclear industry.

Unfortunately this work has not been without limitations. The key limiting factor throughout this research and the implementation of these models has been boundary conditions. The implementations given here may be considered simplistic compared with recent methods such as mDBC [105]. All models presented within this work were created from codes written by the author using some imported algorithms written by Dr Karl Travis. This means that new and complex boundary implementations proved beyond the scope of this work. With improved collaboration, travel and communication, which was unfortunately limited by the COVID-19 pandemic, implementation of these models may have been achieved on package software such as LS-DYNA or DualSPHysics. Although this may have generated improved results it is believed that the exploration of the simplistic boundary conditions presented within this work aids to better demonstrate the limitations of SPAM which is particularly useful for the industrial focus.

The mechanical implementation presented within this work also requires greater attention in order to properly demonstrate the model convergence as well as remove any instabilities due to boundary conditions and implement multiple materials. The success shown with the temperature evolution model in dealing with the discontinuous material boundary must be translated to the mechanical case in order to give the same confidence to industry for the thermo-mechanical model. The stress evolution chosen does not seem well suited to this and further reformulation to mirror that of the temperature evolution, based solely on the weight function without derivatives using Taylor expansions may be required.

Over all the conceptual models demonstrated within this thesis suggest that smoothed particle methods if properly implemented are capable of reproducing analytical solutions used within the validation of licensing FPCs. It is demonstrated that SPAM applications to nuclear fuel for GEN IV reactors is worthy of more exploration.

7.2 Future Work

There are many avenues of suggested future work for these models. An extensive list is included here:

- For the thermal models temperature dependent thermal conductivities can be implemented.
- Coupling to molecular dynamics codes for determination of the appropriate thermal conductivities and mechanical properties can be attempted.
- Models for fuel burn up should also be investigated with their effect on the thermal properties of the simulations over time explored.
- A more advanced determination of the interface thermal conductivity should be explored. As suggested in this work, a weighting of conductivities based on the distance from a known boundary may be effective at this.
- More test simulations in 1D should be explored for material interfaces for different elastic and plastic properties.
- Convergence of the 2D stress results must also be demonstrated
- The mirror boundary case or a more complex boundary such as mDBC must be successfully implemented for the annular stress model to allow full error comparisons.
- New boundary methods which allow the deformation of boundaries while enforcing properties such as convection must be derived to allow for proper deformation of the cladding and fuel within the model.
- Temperature and burn up dependant models for material properties must also be explored.
- More complex mechanical behaviour such as strain hardening and creep should also be tested and implemented within the simulations.
- A new equation for acceleration due to stress should be derived based on the ideas presented in the derivation of Hoover's temperature evolution.
- Models exploring multiple phases must be constructed. Attempts may be made to convert the continuum equations of phase field models to SPAM forms. This will allow smooth mapping of grain and pore structure in materials.
- Alternative multi-phase models will need to look at particles in different phases. In particular the gap conductance should be modelled using multiple phase particles for the pellet to cladding interaction.
- Damage models should be properly implemented showing material failure. This should be expanded to show crack initiation particularly due to thermal loading. A model like this may require a modified form of total Lagrangian SPAM [91].
- Micro-structural models should be created, in particular aiming to capture micro crack initiation and micro bubbles within Fuel.
- The thermo-mechanical models need to be extended to 3D to allow for demonstration of effects such as the hourglass pellet shape.

- Defect studies should be carried out. Randomised structural and material defects can be introduced into any of the above outlined models as well as the thermal fuel and cladding model presented within this work. Thousands of these randomised models can then be run to allow for statistical assessment of the uncertainty bounds that the defects introduce on the model performance and results.
- Solidification and melting need to be added to the model. This will potentially allow for basic modelling of accident conditions but will also be essential for accurate thermal modelling even within normal operating windows.
- Within the work on multi-phase there is the scope for the addition of fluid surrounding the cladding to be directly modelled, allowing for the convection currents to be studied and more directly effect the thermal modelling of the fuel.
- Chemical reactions can be implemented within the code to allow for further changes in material properties.
- Full tracking of nuclear species could be implemented to allow for a fully dynamic material dependence on burn up.
- The micro structure models should be modified for examination of plutonium and MOX fuel due to the large UK stock pile.
- Full 3D models for pellet fragment migration should be constructed
- SPAM models should also be created to examine the recent nuclear industry's interest in co-generation of hydrogen. Issues such as hydrogen embrittlement would benefit greatly from the advantages of the SPAM method, particularly at the micro structure level.
- More code couplings should be attempted such as directly with the ENIGMA code to inform micro-structure models.

These are only a few of the ideas possible for SPAM investigations of nuclear fuel. The potential for SPAM in this field is enormous due to its ability to deal with many different differential equations simultaneously allowing for multi-physics phenomena to be explored and their interactions studied.

Appendix A

Comparison by Shape Descriptors

The method of image decomposition as outlined by Sebastian et al [124] is outlined here with examples to demonstrate how the plots of Fourier-Tchebichef moments shown in this work were created.

A.0.1 Method of Image Decomposition

The famous Fourier transform is a mathematical formula for the decomposition of a signal into a sum of oscillating functions (Sine waves). This idea of decomposing signals is not limited to sums of oscillating functions or to one dimensional signals. Decomposition can be achieved with respect to any infinite sum of orthogonal functions in any number of dimensions however the order of dimensions as well as the functions chosen have a high impact on the computation time to decompose. Special care must be taken when choosing the orthogonal functions to ensure that they appropriately sample the signal space. It has been found the Zernike polynomial functions can be used effectively to describe 2D images with spherical symmetry and the full capability of these shape decriptors has been shown with respect to decomposing strain fields [146]. Alternatively for images with good 'square symmetry' Tchebichef polynomials have been proposed [147].

The first step in the calculation of the Fourier-Tchebichef moments is to complete a discrete 2D Fourier transform on the data. For an NxN full field intensity map $I(x, y)$ a transform of the following form is performed:

$$D_F(n, m) = \frac{1}{N^2} \sum_{x=0}^{N-1} \sum_{y=0}^{N-1} e^{-i2\pi\left(\frac{nx+my}{N}\right)} I(x, y) \tag{A.1}$$

The Fourier transform is performed to help with the description of any discontinuities within the intensity map, the transform is exact by the inclusion of terms $n, m = 0, 1, 2..., N$ however this means the transform does not reduce the domain of the data.

To ensure that the final calculated moments into which the data is decomposed are of an appropriate range for comparison purposes, it is suggested by Patki et al. [146] that the Tchebichef moments be calculated from the natural logarithm of the magnitude of the Fourier transform. The phase information is not need in the calculation of the Tchebichef moments. The phase information is required for reconstruction of the original full field data for error estimations in the moments.

It has been established that faster computation of the Tchebichef moments can be achieved by considering the odd, even symmetry of the Tchebichef polynomials [147]. The symmetry allows for the Tchebichef polynomials to only be calculated for one quarter of the full field data. This symmetry is described as:

$$\tilde{t}_n(N-1-x) = (-1)^n \tilde{t}_n(x) \tag{A.2}$$

where $\tilde{t}_n$ is the nth order scaled Tchebichef polynomial which can be calculated through multiple methods, including often favoured recursive methods. For this work however the scaled Tchebichef polynomials where calculated using the expansion:

$$\tilde{t}_n(x) = \frac{1}{N^n} \sum_{k=0}^{n} (-1)^{n-k} \frac{n!}{k!} \binom{N-1-k}{n-k} \binom{n+k}{n} \sum_{i=0}^{k} \binom{k}{i} x^i \tag{A.3}$$

With this in mind the Tchebichef moments are calculated as:

$$\begin{aligned} T_{pq} = \frac{1}{\tilde{\rho}(p,N)\tilde{\rho}(q,N)} \sum_{x=0}^{(N/2)-1} \sum_{y=0}^{(N/2)-1} \tilde{t}_p(x)\tilde{t}_q(y) \Big[& f(x,y) + (-1)^p f(N-1-x,y) \\ & + (-1)^q f(x,N-1-y) + (-1)^{p+q} f(N-1-x,N-1-y) \Big] \end{aligned} \tag{A.4}$$

With the factor ρ given by:

$$\tilde{\rho}(n,N) = \frac{N\left(1-\frac{1}{N^2}\right)\left(1-\frac{2^2}{N^2}\right)...\left(1-\frac{n^2}{N^2}\right)}{2n+1} \tag{A.5}$$

The values of p, q in Eq.A.4 describe the order of the Tchebichef polynomials to be included in the summation. We are free to truncate the order of polynomials included and this has the effect of reducing the domain of the data. It is suggested in reference [125] that the inclusion of moments up to the order of no more than 20 is sufficient to uniquely describe the shape of the original full field data. This suggests that any two 2D full field data sets can be compared effectively through the use of no more that 20^2 moments to describe the shape of the data. An example of the reconstructed ANSYS temperature profile from only 20 moments is shown below.

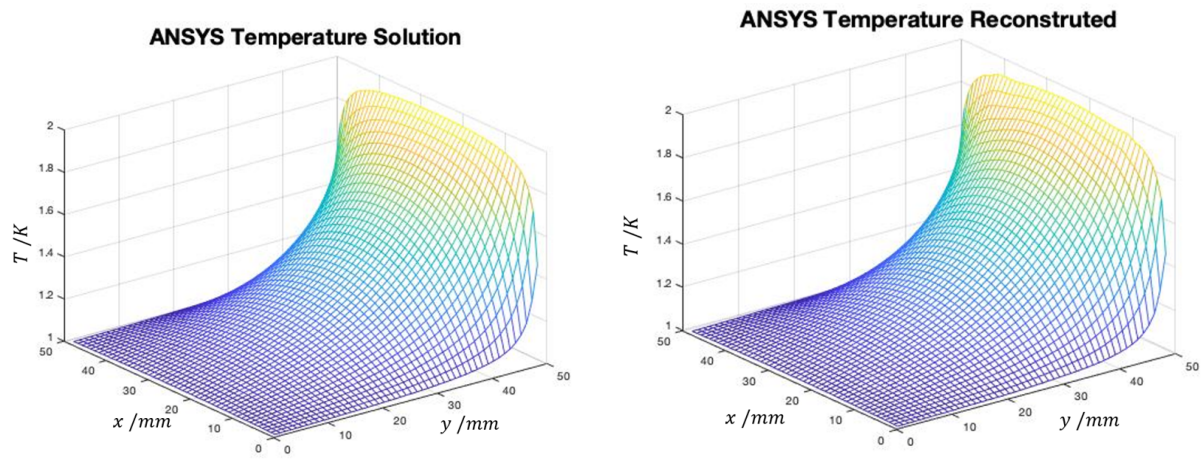

Figure A.1: Original and reconstructed temperature data taken from the FEM solution to the 2D Thermal model at steady state, produced using ANSYS. Data has been decomposed into Fourier-Tchebichef moments up to order 20, and the reconstructed data, shown right, used to estimate the residual error in the moments description of shape.

Appendix B

Damage Modelling with SPAM

Here is included the unfinished attempt to incorporate a full damage model into the thermal fuel and cladding model presented at the end of Chapter 5. This is included an a starting point and framework from which further research can construct a model for damage within nuclear fuel in operation using SPAM.

B.1 Basic Damage Implementation

SPAM holds particular promise within nuclear fuel modelling for its ability to handle damage within simulations. This is due to the nonrestrictive nature of the particle arrangement. Complex methods of damage implementation have been proposed such as the Lagrangian description [91]. For the final simulations of this project however a far simpler implementation will be explored based on the von Mises stress.

B.1.1 Tension Model

To test the basic SPAM implementation of material failure, a simple 2D tension test is proposed. A rectangular strip of material of length L_0, width A_0 is centred such that $-L_0/2 < x < L_0/2$. A force F is applied to the material in the x direction such that the material begins to stretch and then separate at the central point. The same elastic behaviour is assumed below the yield stress σ_Y with the material following plastic deformation thereafter until the ultimate tensile stress σ_T is reached, at which point material failure occurs. This formulation of tensile test should reproduce material necking followed by fracture. This behaviour is shown in Fig.B.1.

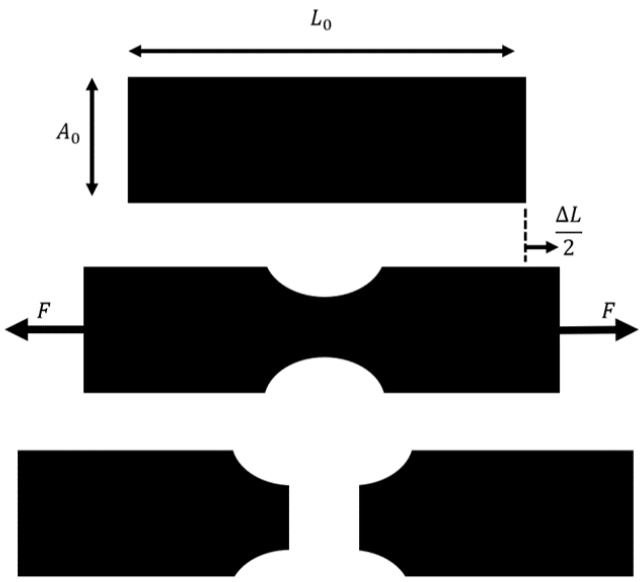

Figure B.1: Diagram of the material tension test. The material first begins to neck and then fracture as shown.

B.1.2 Plastic Modelling

As stated the plastic model implemented is the von Mises stress and yield criterion. This assumes that material yielding begins when the yield stress σ_Y is exceeded by the second invariant quantity of the deviatoric stress S. For 2D this invariant quantity used is the shear stress [54] given by:

$$\sigma_{Shear} = \sqrt{S^{xy2} + \frac{1}{4}(S^{xx} - S^{yy})^2} \tag{B.1}$$

Once the yield stress is exceeded plastic behaviour is achieved by restricting the stress values to the yield surface with the correction factor γ given by:

$$\gamma = \frac{\sigma_Y}{\sqrt{S^{xy2} + \frac{1}{4}(S^{xx} - S^{yy})^2}} \tag{B.2}$$

The stress values are then corrected as:

$$S^{xx} = \frac{1}{2}(S^{xx} + S^{yy}) + \frac{\gamma}{2}(S^{xx} - S^{yy}) \tag{B.3}$$

$$S^{xy} = \gamma S^{xy} \tag{B.4}$$

$$S^{yx} = \gamma S^{yx} \tag{B.5}$$

$$S^{yy} = \frac{1}{2}(S^{xx} + S^{yy}) - \frac{\gamma}{2}(S^{xx} - S^{yy}) \tag{B.6}$$

This gives the plastic material behaviour required for deformation. From here fracture is added when the principle stress exceeds the tensile strength σ_T:

$$\frac{1}{2}(S^{xx} + S^{yy}) > \sigma_T \tag{B.7}$$

Once this condition is met the stress tensor is simple reset to zero. This allows the material to physically break apart.

B.1.3 Plastic SPAM Implementation

The above methodology is implemented as a set of checks and correction run on the particles between time steps. To test the behaviour an SPAM tensile test is formulated. A square particle arrangement of unit mass particles is used. No boundary particles are used for this simulation therefore the particle densities are corrected using zeroth order corrections to account for the boundary deficiency:

$$\rho_i \simeq \frac{\sum_j m_j W(x_{ij})}{\sum_j m_j W(x_{ij})/\rho_j} \tag{B.8}$$

The tensile forces are achieved by adding the body force term to the equation of motion as:

$$\frac{dv_i^\alpha}{dt} = \sum_j m_j \left(\frac{\sigma_i^{\alpha\beta}}{\rho_i^2} + \frac{\sigma_j^{\alpha\beta}}{\rho_j^2} + \Pi_{P,ij} \right) \cdot \nabla_i w\left(r_{ij}\right) + F^\alpha \tag{B.9}$$

Here α, β represent the dimensional indices. Artificial viscosity $\Pi_{P,ij}$ is used throughout these simulations. The body force is added through the F term. For this simulation force is only added in the x direction, for $|x| > L_0/4$. The force increases linearly in time such that:

$$F_i^x = F_0 \frac{t}{t_{Final}} \tag{B.10}$$

Here F_0 is constant. The engineering stress and engineering strain are used to calculated the stress strain curve for the simulation to check the correct elastic-plastic behaviour is reproduced. The engineering strain ϵ_E is calculated as:

$$\epsilon_E = \frac{\Delta L}{L_0} \tag{B.11}$$

This is calculated by tracking the highest and lowest particle positions in the x direction of the simulation. The engineering stress is calculated as the force per unit area applied to the material. In 2D the cross-sectional area is simply given as the initial system width A_0. The engineering stress σ_E is calculated as:

$$\sigma_E = \frac{F}{A_0} = \sum_i \frac{|F_i^x|}{A_0} \tag{B.12}$$

For the SPAM simulations a square particle arrangement of unit grid spaced particles is used, with $\rho_0 = 1\text{g/mm}^3$.

B.1.4 Tensile Instability and Artificial Stress

The tensile instability occurs when the acceleration acting on particles forces them towards each other at close range. This causes particles to clump together and is outline in Sec.2.4.4. This can occur in SPAM simulations under tension. It is suggested by Monaghan [138] that artificial

viscosity alone is insufficient to prevent the tensile instability from occurring. This was confirmed in initial tests with an example shown in Fig.B.2

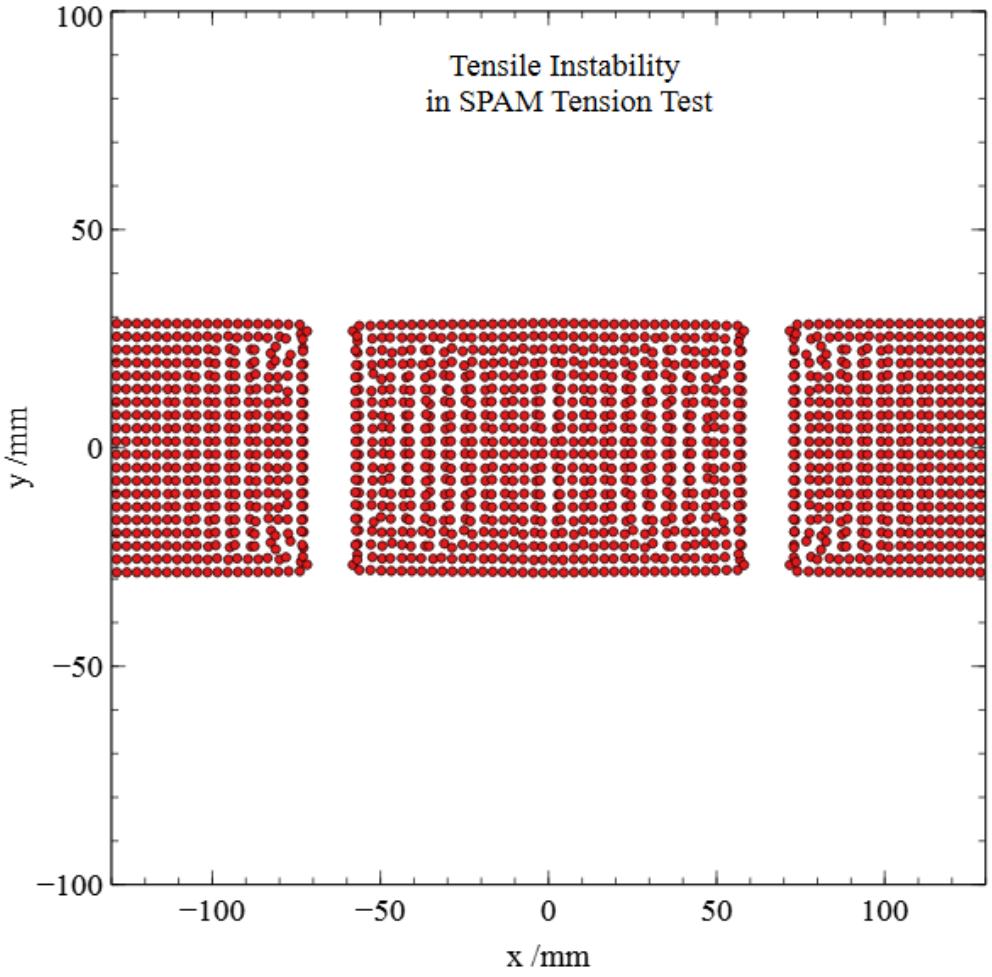

Figure B.2: SPAM tensile test with artificial viscosity showing the tensile instability with particles clumping together.

To solve this problem Monaghan suggests the use of an artificial stress term added to the equation of motion:

$$\frac{dv_i^\alpha}{dt} = \sum_j m_j \left(\frac{\sigma_i^{\alpha\beta}}{\rho_i^2} + \frac{\sigma_j^{\alpha\beta}}{\rho_j^2} + \Pi_{P,ij} + (\Pi_{\sigma,i}^{\alpha\beta} + \Pi_{\sigma,j}^{\alpha\beta}) \left(\frac{w(r_{ij})}{w(\Delta_P)} \right)^4 \right) \cdot \nabla_i w\left(r_{ij}\right) + g^\alpha \qquad \text{(B.13)}$$

where the the particle spacing Δ_P is used to reduce the impact of the artificial terms to nearest neighbour particles. The artificial terms are created from the particle stress tensor when it is in tension. To discover this the stress tensor must be in the principle axis. To achieve this the stress tensor is diagonalised. The diagonal stress tensor is denoted $\bar{\sigma}$. Now for each diagonal element of the diagonal stress tensor, if the element is greater than zero ($\bar{\sigma}_i^{\alpha\alpha} > 0$) then the particle is under

tension in that x axis. The diagonal artificial contribution is then calculated as:

$$\bar{\Pi}^{\alpha\alpha}_{\sigma,i} = -C_\sigma \frac{\bar{\sigma}^{\alpha\alpha}_i}{\rho_i^2} \tag{B.14}$$

where C_σ is the strength of the correction. For this work the suggested value of $C_\sigma = 0.4$ is used. From here the final step is to return the calculated artificial stress tensor back to the system axis. This is done by storing the matrices used for diagonalisation of the stress tensor and preforming the inverse rotation on $\bar{\Pi}$. The artificial stress was found to be successful for mitigating the tensile instability arising in the tension test.

B.1.5 Tension Test Results

The tension test results presented here are a proof of concept however further work is needed. The simulation was run for a grid of unit spaced particles with unit density $\rho_0 = 1\text{g/mm}^3$ and unit mass $m_i = 1\text{g}$. The initial system dimensions are $L_0 = 80\text{mm}$, $A_0 = 20\text{mm}^2$. Young's modulus is arbitrarily chosen as $E = 100\text{N/mm}^2$ with $\nu = 0.3$. The yield and tensile strength are set to $\sigma_Y = 12\text{g/mms}^2$, $\sigma_T = 2\text{g/mms}^2$ respectively. A small time step is required to ensure gradual loading of the sample. For this simulation the time step used is $dt = 0.001\text{s}$ for 200000 time steps.

The resulting stress strain curve is shown in Fig.B.3. The material can be seen to fail at approximately the expected tensile stress. The yield behaviour is less clear however. All behaviour ahead of the point of failure appears to follow elastic behaviour. This test suffers from a poor definition of the applied force F on the system. As the particle arrangement changes with the deformation, which particles are within the last quarter of the material, a range defined $L/4 < |x|$, changes and thus the total applied force changes. This behaviour can be seen in the oscillations of the stress strain curve.

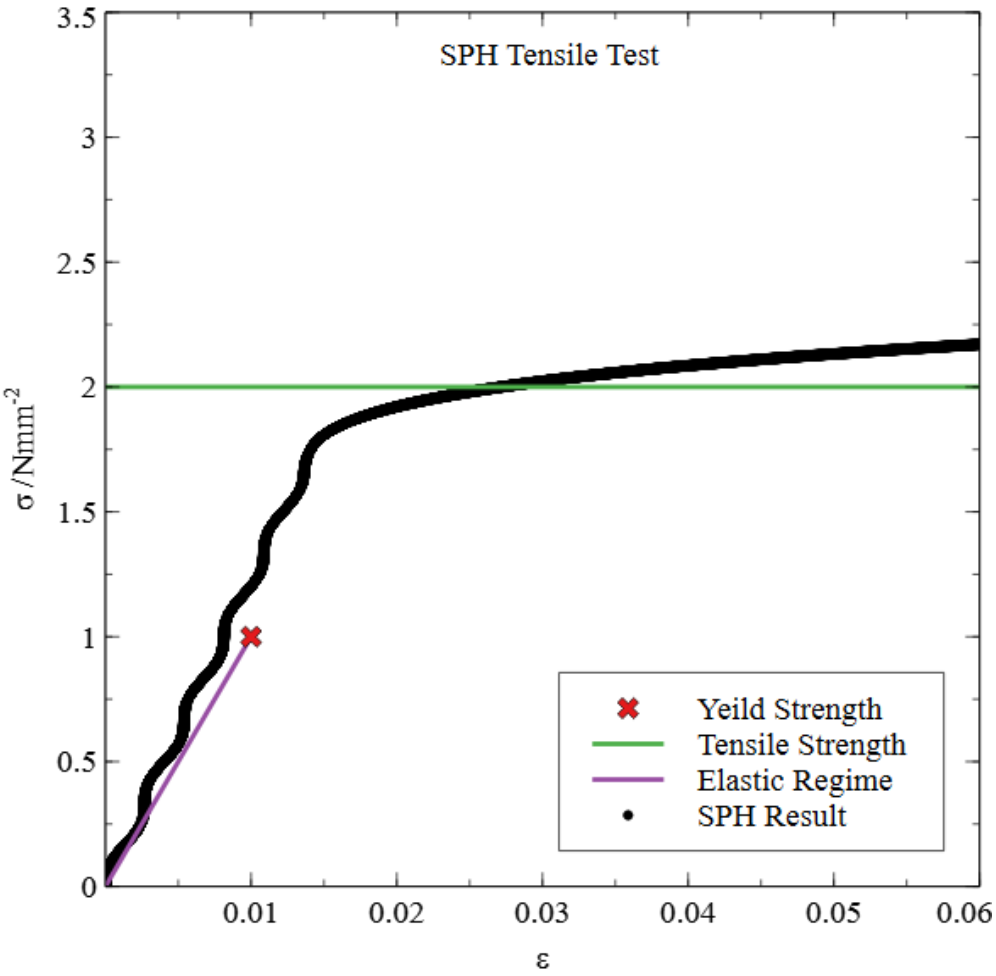

Figure B.3: Stress-strain curve produced by the SPAM tensile test of $N = 1600$ particles with artificial stress and viscosity terms included.

The qualitative behaviour of the sample is very promising however. The sample is seen to begin necking as shown in Fig.B.4. Failure of the sample occurs with total separation of the system. It is clear further testing and quantification of these results is required to validate the SPAM to the level required for nuclear fuel modelling. The results demonstrate the methodology is valid however and that damage within SPAM is possible. Although more rigorous validation was not achieved within this work a qualitative analysis of the final fuel and cladding model is given to demonstrate the future work necessary.

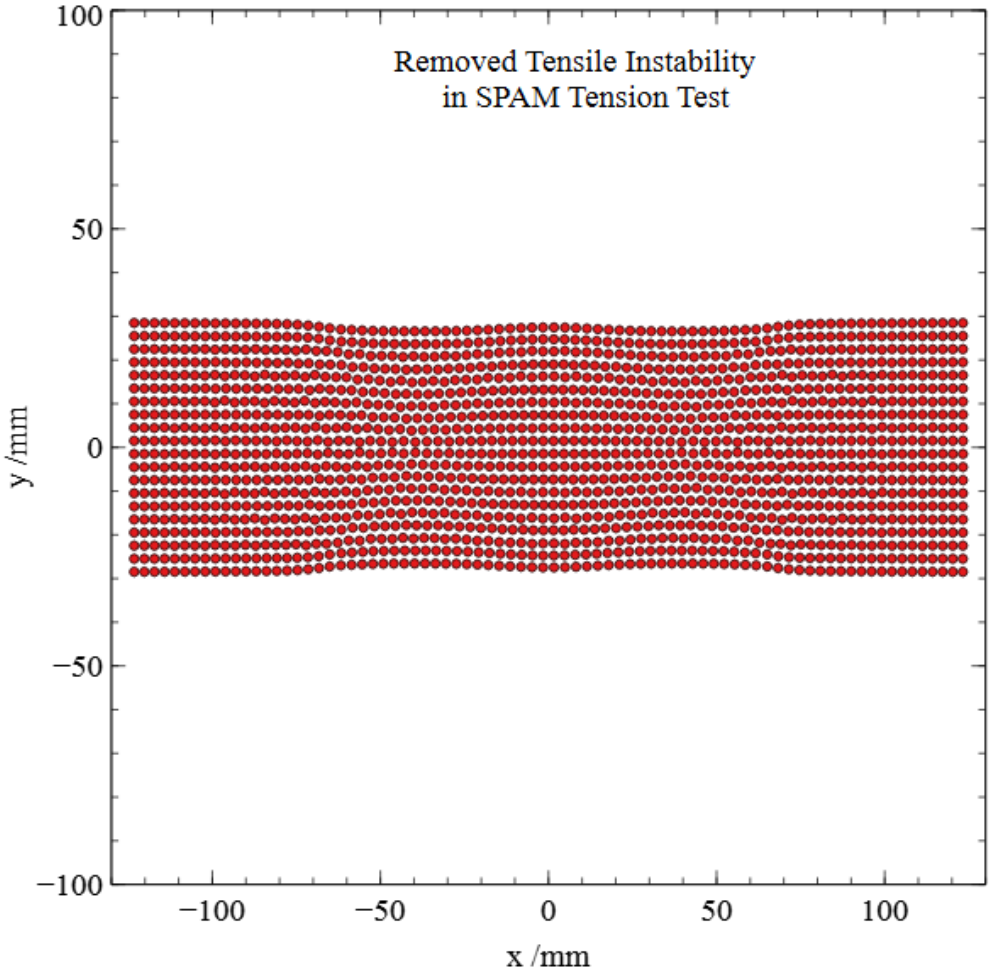

Figure B.4: SPAM tension test performed with corrective measures. The tensile instability is removed and the particles no longer clump together.

B.2 Final Fuel and Cladding Model

The preliminary results for the fuel and cladding model with mechanical behaviour are presented here. Sufficient work has been achieved to give a qualitative analysis. The model used in the fuel and cladding model from Sec.5.6. The heat flow derived by this problem simulated for a system with added elastic-plastic behaviour. The geometry of the model is shown in Fig.B.5. The outer coolant boundary is assumed to be fixed however the rest of the system including the fuel cladding boundary is allowed to move. For this model, as before the fuel and cladding thermal conductivities are assumed to be κ_F and κ_C respectively. The coolant is assumed to have coefficient of convection h and ambient temperature T_∞. Here the fuel is assumed to produce heat at rate $\dot{q}$.

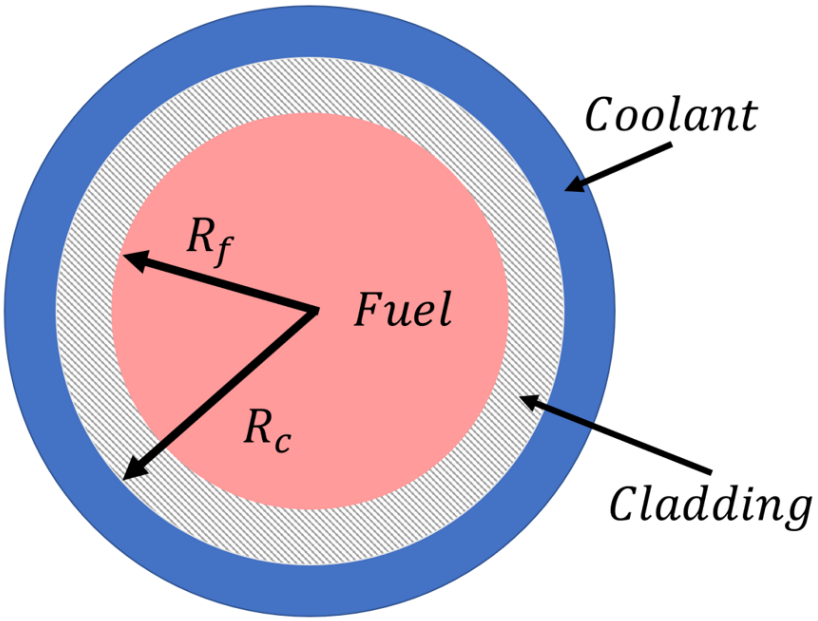

Figure B.5: Geometry of the 2D conceptual fuel and cladding model

The mechanical behaviour of the fuel and cladding are simplified in an attempt to offer analytical validation of the model. An analytical solution is attempted below. The simplification assumes that both the fuels and cladding material behave according to the same material properties E, ν and α.

B.2.1 Analytical Solution

The solution for the stress in an annulus with inner an outer radius A, B for some arbitrary temperature profile $T(r)$ was derived in Sec.6.3.1. This can be modified to the solution for a cylinder by considering $A = 0$. The outer is redefined as $B = R_C$. The value of Young's modulus for the fuel and cladding are assumed to be the same to allow for this solution. Then the radial stress becomes:

$$\sigma_r = \frac{E\alpha}{1+\nu}\left(-\frac{1}{r^2}\int_0^r Trdr + \frac{1}{R_C^2}\int_0^{R_C} Trdr\right) \tag{B.15}$$

The temperature solution was derived in the previous chapter as:

$$T_F = \frac{\dot{q}R_F^2}{2}\left[\frac{ln(R_C/R_F)}{\kappa_C} + \frac{1}{hR_C}\right] + T_\infty + \frac{\dot{q}(R_F^2 - r)}{4\kappa_F} \tag{B.16}$$

$$T_C = \frac{\dot{q}R_F^2}{2}\left[\frac{ln(R_C/r)}{\kappa_C} + \frac{1}{hR_C}\right] + T_\infty \tag{B.17}$$

Consider first the temperature integration for $r < R_F$:

$$\int_0^r T_F r dr = r^2\left(\frac{\dot{q}R_F^2}{4}\left(\frac{ln(R_C/R_F)}{\kappa_C} + \frac{1}{hR_C} + \frac{1}{2\kappa_F}\right) + \frac{T_\infty}{2}\right) - \frac{\dot{q}r^3}{12\kappa_F} \tag{B.18}$$

For $r > R_F$ the integral can be split into two parts:

$$\int_0^r Trdr = \int_0^{R_F} T_F rdr + \int_{R_F}^r T_C rdr \tag{B.19}$$

The first integral can be easily calculated from Eq.B.20 simply as:

$$\int_0^{R_F} T_F rdr = R_F^2 \left(\frac{\dot{q}R_F^2}{4} \left(\frac{ln(R_C/R_F)}{\kappa_C} + \frac{1}{hR_C} + \frac{1}{2\kappa_F} \right) + \frac{T_\infty}{2} \right) - \frac{\dot{q}R_F^3}{12\kappa_F} \tag{B.20}$$

The second integral is calculated as:

$$\int_{R_F}^r T_C rdr = \left[r^2 \left(\frac{\dot{q}R_F^2}{4} \left(\frac{ln(R_C/r)}{\kappa_C} + \frac{1}{2\kappa_C} + \frac{1}{hR_C} \right) + \frac{T_\infty}{2} \right) \right]_{R_F}^r \tag{B.21}$$

Examining the limits gives:

$$\begin{aligned} \int_{R_F}^r T_C rdr = & \left[r^2 \left(\frac{\dot{q}R_F^2}{4} \left(\frac{ln(R_C/r)}{\kappa_C} + \frac{1}{2\kappa_C} + \frac{1}{hR_C} \right) + \frac{T_\infty}{2} \right) \right] \\ & - \left[R_F^2 \left(\frac{\dot{q}R_F^2}{4} \left(\frac{ln(R_C/R_F)}{\kappa_C} + \frac{1}{2\kappa_C} + \frac{1}{hR_C} \right) + \frac{T_\infty}{2} \right) \right] \end{aligned} \tag{B.22}$$

Combining these gives the temperature integral for $r > R_F$ as:

$$\begin{aligned} \int_0^r Trdr = & \frac{\dot{q}R_F^4}{4} \left(\frac{1}{2\kappa_F} - \frac{1}{2\kappa_C} - \frac{1}{3R_F\kappa_F} \right) \\ & + r^2 \left(\frac{\dot{q}R_F^2}{4} \left(\frac{ln(R_C/r)}{\kappa_C} + \frac{1}{2\kappa_C} + \frac{1}{hR_C} \right) + \frac{T_\infty}{2} \right) \end{aligned} \tag{B.23}$$

This now allows calculation of the limit as:

$$\begin{aligned} \frac{1}{R_C^2} \int_0^{R_C} Trdr = & \frac{\dot{q}R_F^4}{4R_C^2} \left(\frac{1}{2\kappa_F} - \frac{1}{2\kappa_C} - \frac{1}{3R_F\kappa_F} \right) \\ & + \left(\frac{\dot{q}R_F^2}{4} \left(\frac{1}{2\kappa_C} + \frac{1}{hR_C} \right) + \frac{T_\infty}{2} \right) \end{aligned} \tag{B.24}$$

Now the stress can be calculated in two parts. Firstly for the region $r < R_F$:

$$\sigma_r = \frac{E\alpha}{1+\nu} \left[\frac{\dot{q}R_F^2}{4} \left(\frac{ln(R_C/R_F)}{\kappa_C} + \frac{1}{2\kappa_F} - \frac{1}{2\kappa_C} \right) + \frac{\dot{q}r}{12\kappa_F} + \frac{\dot{q}R_F^4}{4R_C^2} \left(\frac{1}{2\kappa_F} - \frac{1}{2\kappa_C} - \frac{1}{3R_F\kappa_F} \right) \right] \tag{B.25}$$

The stress for the region $r > R_F$ is given by:

$$\sigma_r = \frac{E\alpha}{1+\nu} \left[-\frac{\dot{q}R_F^4}{4} \left(\left(\frac{1}{r^2} - \frac{1}{R_C^2} \right) \left(\frac{1}{2\kappa_F} - \frac{1}{2\kappa_C} - \frac{1}{3R_F\kappa_F} \right) - \frac{ln(R_C/r)}{R_F^2\kappa_C} \right) \right] \tag{B.26}$$

These analytical solutions are not in agreement with the results as will be shown in the final section. This may be because the boundary condition of $\sigma_{r=0} = 0$ used to derive Eq.B.15 is not met by the solution, however the SPAM simulations support the boundary value derived.

B.2.2 SPAM Results

The SPAM simulation was run with $dt = 0.05s$ for 100000 time steps. The thermal values used were chosen to be a factor of 10 bigger than for the purely thermal effects shown in the previous chapter as $\kappa_C = 0.25\text{gmm/s}^3\text{K}$, $\kappa_F = 0.02\text{gmm/s}^3\text{K}$, $\dot{q} = 1gmm^2/s^3$ and $h = 0.1\text{g/s}^3\text{K}$. This modification was made so that the simulation time could be reduced as the thermal effects are then on a similar time scale to the mechanical effects. The mechanical properties chosen were $E = 1000\text{N/mm}^2$, $\nu = 0.3$, $\alpha = 0.000001$. The selection of these values is some what arbitrary in order to produce stable simulation results within a reasonable simulation time frame. True validation and property selection to better mirror a problem of nuclear fuel is required as well as separation of the fuel and cladding material properties.

The convective temperature profile achieved in the previous section is shown to be achieved again for the inclusion of thermal strains in Fig.B.6. The stress profiles for this case are shown in Fig.B.7. The analytical solution is not met, however the extreme values for the radial profile tend to the predicted ones. This implies that further testing and validation of the material interface is required.

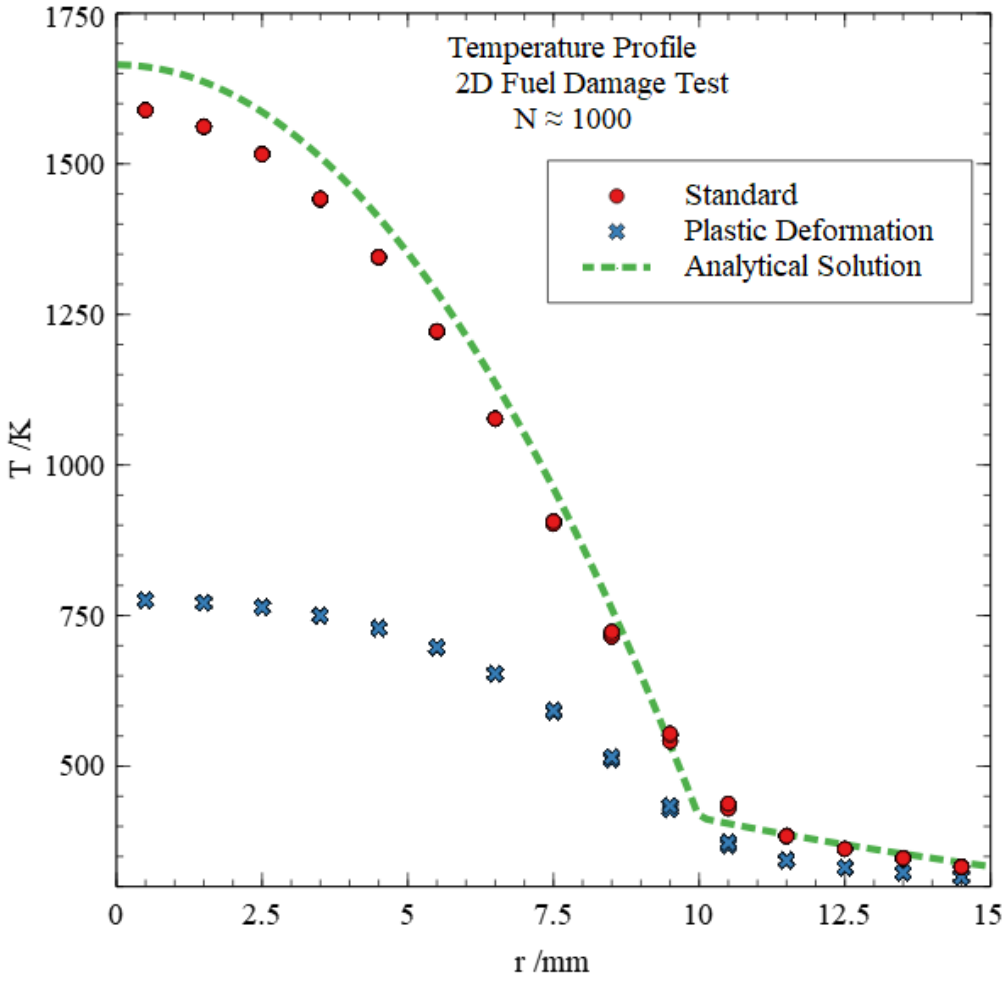

Figure B.6: Final temperature profile for the fuel and cladding model with added thermal strains. The final profile to the plastic case as damage begins to occur is shown as well marked in blue.

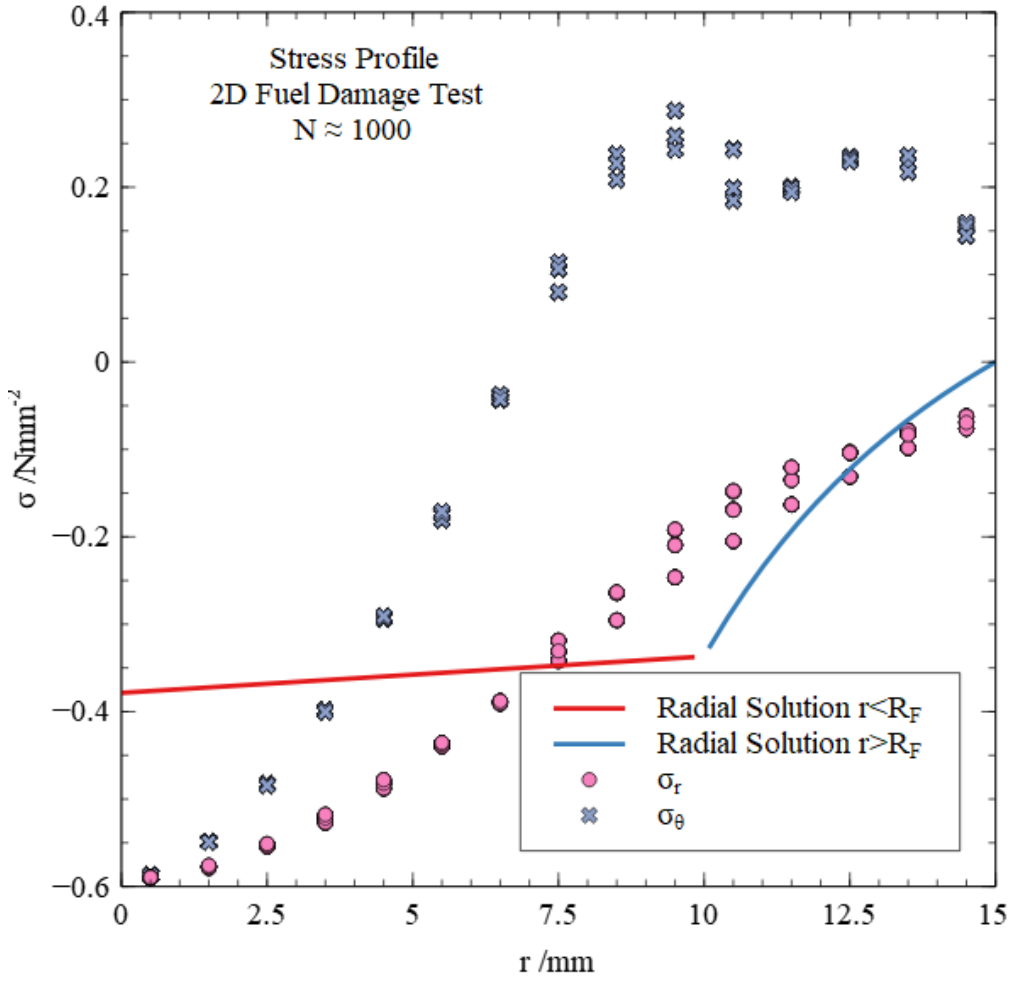

Figure B.7: Final stress profile for the fuel and cladding model with added thermal strains. The piece-wise radial analytical stress solution is included. The boundary stress is enforced by fixed particles as $\sigma_r = \sigma_\theta = 0$.

To examine the plastic and failure behaviour of this model qualitatively the simulation is re-run with the plastic behaviour now included with the tensile and yield strength deliberately chosen to give cause failure before the final steady state is achieved. The values used are $\sigma_Y = 1\text{N/mm}^2$ and $\sigma_T = 2\text{N/mm}^2$. Failure was seen to occur at time step 35000. The temperature profile at this time is shown on Fig.B.6. Visual data maps at this time step are shown in Fig.B.8. For these maps red represent high values, blue low. The damage pattern can be seen to extend out from the centre in a 6-pointed radial shape. This could show the radial nature of cracks however may also simply be an underlying artefact of the triangular particle arrangement used. The radial and tangential stresses are seen to be concentrated in opposite directions as the material fails. This behaviour supports the expected cracking due to PCMI as the stress in concentrated in points of the cladding however more analysis is clearly necessary. All of this data is purely presented as an example of the capabilities of SPAM. Further refinement and validation of this model is necessary. More complex implementations of cracking within SPAM already exist such as the total Lagrangian formulation [91]. Any future work should seek to improve upon the simplistic damage model outlined here.

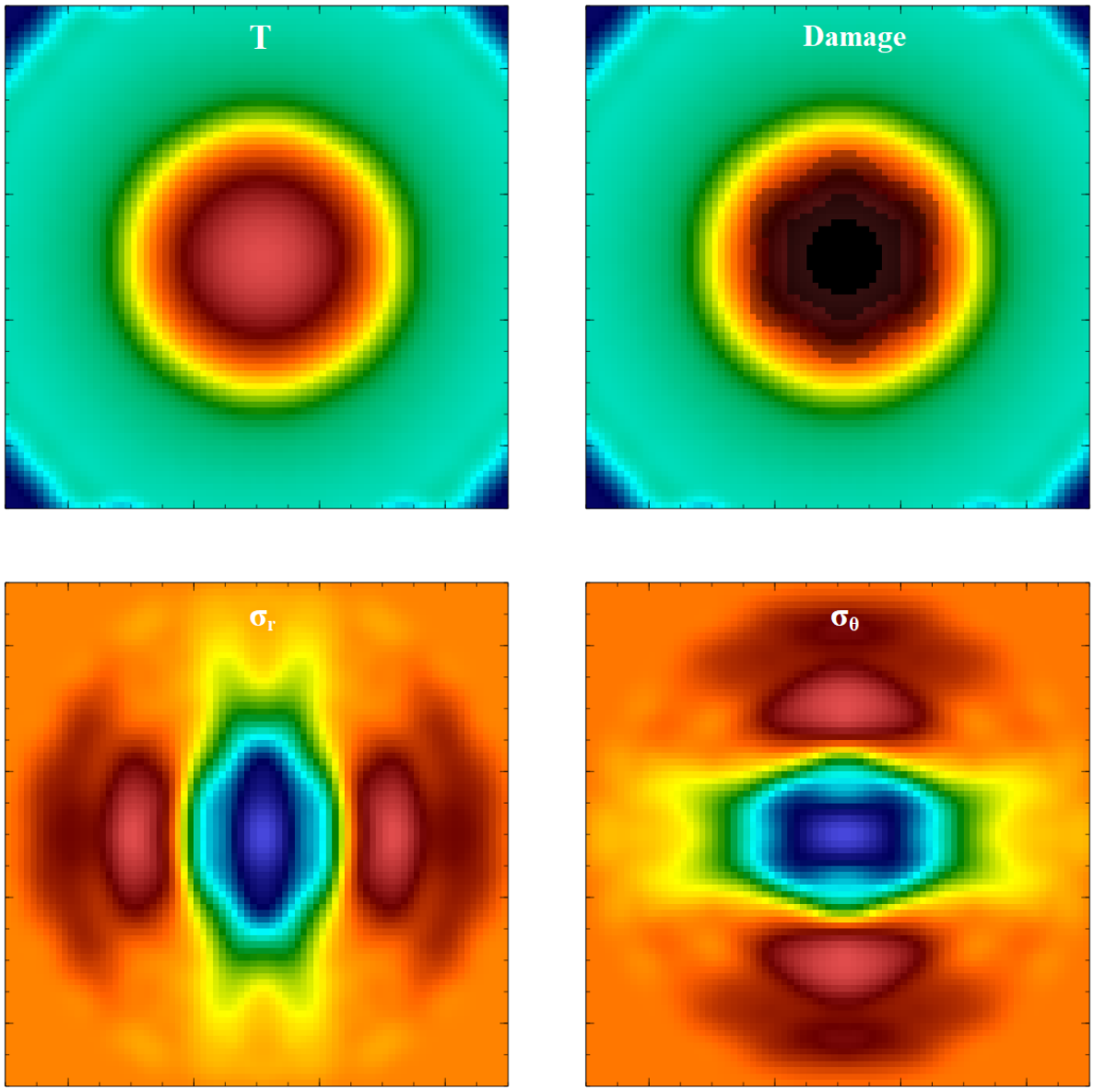

Figure B.8: Interpolated smoothed particle data maps for the fuel and cladding model as failure occurs. Top shows thermal maps with the right map including the damage pattern with the intensity of the damage marked by the darkness of the region. Bottom shows the tangential (right) and radial (left) stress maps as failure occurs.

B.2.3 Conclusions

The final simulations presented show promise that SPAM simulations are capable of reproducing stress and strain behaviour under the right initialisation condition and thus that the application of SPAM to damage and micro-structure simulations of nuclear fuel are worth pursing.

Qualitative analysis of a simplified damage model for nuclear fuel is presented. The damage be-

haviour is outlined through the use of a simple tension test and then applied the the 2D fuel and cladding model with heat generation and convection. This model shows the potential for further development and validation of SPAM nuclear fuel models. Emphasis must be placed on the handling of material to material boundaries in order to improve this work as well as on appropriate boundary conditions and more representative damage modelling.

Bibliography

[1] White Paper presented to government February 1956 *A Programme Of Nuclear Power* The National Archives, Catalogue Reference:CAB/129/73

[2] Nuclear Development in the United Kingdom *World Nuclear Association* 2016 [online] Available from: `http://www.world-nuclear.org/information-library/country-profiles/countries-t-z/appendices/nuclear-development-in-the-united-kingdom.aspx` Accessed: June 2019

[3] Department for Business, Energy & Industrial Strategy: *Advanced Modular Reactor competition: phase 1 feasibility - project descriptions* Published 5 September 2018, licensed under the Open Government Licence

[4] Rolls-Royce plc *Rolls-Royce Small Modular Reactors* 2022 [online] Available from: `https://www.rolls-royce.com/innovation/small-modular-reactors.aspx#/` Accessed: October 2022

[5] Nuclear Safety Technical Assessment Guide: *Validation of Computer Codes and Calculation Methods* NS-TAST-GD-042 Revision 5, published by the Office for Nuclear Regulation and licensed under the Open Government Licence v3.0.

[6] P. A. Jackson, J. A. Turnbull and R. J. White, *A Description of the ENIGMA Fuel Performance Code* , Proc. IAEA Technical Committee Meeting on Water Reactor Fuel Element Computer Modelling in Steady-State, Transient and Accident Conditions, Preston, UK, Sep. 19-22, 1988.

[7] L. Van Brutzel, R. Dingreville, T.J. Bartel *Nuclear fuel deformation phenomena* Nuclear Energy Agency of the OECD (NEA-NSC-R–2015-5)

[8] Domínguez, J. M.; Fourtakas, G.; Altomare, C.; Canelas, R. B.; Tafuni, A.; García-Feal, O.; Martínez-Estévez, I.; Mokos, A.; Vacondio, R.; Crespo, A. J. C.; Rogers, B. D.; Stansby, P. K.; Gómez-Gesteira, M. *DualSPHysics: from fluid dynamics to multiphysics problems* Computational Particle Mechanics, 29.03.2021

[9] P. Gonnet, M. Schaller, T. Theuns and A. B. G. Chalk *SWIFT: Fast algorithms for multi-resolution SPH on multi-core architectures.* 8th international SPHERIC workshop (2013)

[10] Framatome ANP *MOX Fuel Design Report* BAW-10238(NP) Revision 0 43-10238NP-00

[11] L. Van Brutzel, A. Chartier *A new equation of state for helium nanobubbles embedded in UO2 matrix calculated via molecular dynamics simulations* Journal of Nuclear Materials 518 (2019) 431-439

[12] Erik Nonbol *Description of the Advanced Gas Cooled Type of Reactor* Riso National Laboratory, Rosklide, Denmark. November 1986

[13] R. Mella, M. R. Wenman *Modelling explicit fracture of nuclear fuel pellets using peridynamics* Journal of Nuclear Materials 467 (2015) 58-67

[14] B. Michel, J. Sercombe, G. Thouvenin, R. Chatelet *3D Fuel Cracking Modelling in Pellet Cladding Mechanical Interaction* Engineering Fracture Mechanics 75 (2008) 3581-3598

[15] G. Rossiter, *DEVELOPMENT OF THE ENIGMA FUEL PERFORMANCE CODE FOR WHOLE CORE ANALYSIS AND DRY STORAGE ASSESSMENTS* , Nuclear Engineering and Technology, vol. 43, no. 6. Elsevier BV, pp. 489–498, 25-Dec-2011.

[16] P. Van Uffelen, J. Hales, W. Li, G. Rossiter and R. Williamson *A Review of fuel performance modelling* Journal of Nuclear Materials, 516 (2019) 373-412

[17] J. D. Hales, S. R. Novascone, G. Pastore, D. M. Perez, B. W. Spencer and R. L. Williamson *BISON Theory Manual: The Equations behind Nuclear Fuel Analysis* Fuels Modeling & Simulation Department, Idaho National Laboratory, Idaho Falls, ID (2013)

[18] *Fuel Analysis and Licensing Code: FALCON MOD01: Volume 1: Theoretical and Numerical Bases* EPRI, Palo Alto, CA: 2004. 1011307

[19] G. Rossiter *BISON Theory Manual: The Equations behind Nuclear Fuel Analysis* Nuclear Engineering and Technology, 436 (2011) 489-498

[20] B. Lautrup *Physics of Continuous Matter: Exotic and Everyday Phenomena in the Macroscopic World*. IOP Publishing Ltd. (2005)

[21] W. G. Hoover and C. G. Hoover *Microscopic and Macroscopic Simulation Techniques: Kharagpur Lectures*. IOP Publishing Ltd. (2005)

[22] R. L. Williamson, J. D. Hales, S. R. Novascone, M. R. Tonks, D. R. Gaston, C. J. Permann, D. Andrs and R. C. Martineau *Multidimensional multiphysics simulation of nuclear fuel behavior.* Journal of Nuclear Materials 423 (2012) 149-163

[23] G. J. Hyland *Thermal Conductivity of Solid UO_2: Critique and Recommendation* Journal of Nuclear Materials, 113 (1983) 125-132

[24] H. E. Schmidt *Some Considerations on the Thermal Conductivity of Stoichiometric Uranium Dioxide at High Temperatures* Journal of Nuclear Materials, 39 (1971) 234-237

[25] T. R. Pavlov, M. R. Wenman, L. Vlahovic, D. Robba, R. J. M. Konings, P. Van Uffelen and R. W. Grimes *Measurement and interpretation of the thermo-physical properties of UO_2 at high temperatures: The viral effect of oxygen defects* Acta Materialia 139 (2017) 138-154

[26] J. J. Carbajo, G. L. Yoder, S. G. Popov and V. K. Ivanov *A review of the thermophysical properties of MOX and UO_2 fuels* Journal of Nuclear Materials 299 (2001) 181-198

[27] N. Nakae, H. Akiyama, H. Miura, T. Baba, K. Kamimura, S. Kurematsu, Y. Kosaka, A. Yoshino and T. Kitagawa *Thermal property change of MOX and irradiated up to high burnup of 74 GWd/t* Journal of Nuclear Materials 440 (2013) 515-523

[28] C. R. A. Catlow *Thermodynamics of Mixed Oxide Reactor Fuels* Journal of Nuclear Materials 67 (1977) 236-238

[29] K. Kurosaki, K. Yamada, M.Uno, S. Yamanaka, K. Yamamoto and T. Namekawa *Molecular dynamics study of mixed oxide fuel* Journal of Nuclear Materials 294 (2001) 160-167

[30] J. Oh, Y. Koo, and B. Lee *Simulation of High Burnup Structure in Using Potts Model* Nuclear Engineering and Technology, Vol.41 (2009) No.8

[31] V. Tikare and E. A. Holm *Simulation of Grain Growth and Pore Migration in a Thermal Gradient* Journal of the American Ceramic Society, 81 [3] 480-484 (1998)

[32] S. Rokkam, A. El-Azab, P. Millett and D. Wolf *Phase Field Modeling of Void Nucleation and Growth in Irradiated Metals* Modelling Simul. Mater. Sci. ENg. 17 (2009) 064002

[33] L. Chen *Phase Field Models for Microstructure Evolution* Annu. Rev. Mater. Res. (2002) 32:113-40

[34] V. Tikare, E. A. Holm and L. Chen *Comparison of Phase-Field and Potts Models for Coarsening Processes* Acta mater. Vol. 47, No. 1, pp. 363-371 (1999)

[35] M. R. Tonks, G. Hansen, D. Gaston, C. Permann, P. Millett and D. Wolf *Fully-coupled engineering and mesoscale simulations of thermal conductivity in fuel using an implicit multiscale approach* Journal of Physics: Conference Series 180 (2009) 012078

[36] M. Tonks, D. Gaston, C. Permann, P. Millett, G. Hansen and D. Wolf *A coupling methodology for mesoscale-informed nuclear fuel performance codes* Nuclear Engineering and Design 240 (2010) 2877-2883

[37] M. R. Tonks, D. Gaston, P. C. Millett, D. Andrs and P. Talbot *An object-oriented finite element framework for multiphysics phase field simulations* Computational Materials Science 51 (2012) 20-29

[38] R. L. Williamson, N. A. Capps, W. Liu, Y. R. Rashid and B. D. Wirth *Multi-Dimensional Simulation of LWR Fuel Behavior in the BISON Fuel Performance Code* JOM, Vol. 68, No. 11, 2016

[39] Y. R. Rashid *Ultimate Strength Analysis of Prestressed Concrete Pressure Vessels* Nuclear Engineering and Design 7 (1968) 334-344

[40] S. A. Silling *Reformulation of elastic theory for discontinuities and long-range forces* Journal of the Mechanics and Physics of Solids 48 (2000) 175-209

[41] LAMMPS Molecular Dynamics Simulator *LAMMPS Developer Guide* [online] `https://lammps.sandia.gov/doc/Developer.pdf` (2011)

[42] Y. Wang, X. Zhou, M. Kou *Peridynamics investigation on thermal fracturing behavior of ceramic nuclear fuel pellets under power cycles* Ceramics International 44 (2018) 11512-11542

[43] P. Lindan and M. Gillian *A molecular dynamics study of the thermal conductivity of CaF_2 and UO_2* J. Phys.: Condens. Matter 3 (1991) 3929-3939

[44] S. Higuchi *A Molecular Dynamics Study of Thermal Conductivity of UO_2 with Impurities* Journal of Nuclear Science and Technology, 35:11 (1998) 833-835

[45] P. J. Daivis and B. D. Todd *A simple, direct derivation and proof of the validity of the SLLOD equations of motion for generalized homogeneous flows* J. Chem. Phys. 124, 194103 (2006)

[46] H. A. Posch, W. G. Hoover and O. Kum *Steady-state shear flows via nonequilibrium molecular dynamics and smoothed-particle applied mechanics* Physical Review E, 52:2 (1995) 1711-1720

[47] M.R. Tonks, D. Andersson, S.R. Phillpot, Y. Zhang, R. Williamson, C.R. Stanek, B.P. Uberuaga, S.L. Hayes *Mechanistic materials modeling for nuclear fuel performance* Annals of Nuclear Energy, Volume 105 (2017) Pages 11-24, ISSN 0306-4549,

[48] Valot C, Bertolus M, Konings R, Somers J, De Groot S. *Basic research in support of innovative fuels design for the GEN IV systems: The F-BRIDGE project* NUCLEAR ENGINEERING AND DESIGN 241 (9); 2011. p. 3521 - 3529. JRC68287

[49] L. B. Lucy *A Numerical approach to the testing of the fission hypothesis* Astron. J. 82 (1977) 1013-24

[50] R. A. Gingold and J. J. Monaghan *Smoothed Particle Hydrodynamics: theory and application to non-spherical stars* Mon. Not. R. Astron. Soc. 181 (1977) 375-89

[51] J. J. Monaghan *Smoothed Particle Hydrodynamics* Reports on Progress in Physics (2005) 68 1703

[52] W. Benz and E. Asphaug *Impact Simulations with Fracture. I. Method and Tests* Icarus 107 (1994) 98-116

[53] W. Benz and E. Asphaug *Simulations of brittle solids using smoothed particle hydrodynamics* Computer Physics Communications 87 (1995) 253-265

[54] W. G. Hoover. *Advanced Series In Nonlinear Dynamics Volume 25: Smoothed Particle Applied Mechanics - The State Of The Art.* World Scientific Publishing Co. Pte. Ltd. (2006)

[55] W. G. Hoover and H. A. Posch *Numerical heat conductivity in smoothed particle applied mechanics.* Phys. Rev. E, 54 (1996) 5142-5145

[56] K. P. Travis and T. Hiddleston *Multiscale Modelling of material failure using particles* Molecular Simulation, Vol. 40, Nos. 1-3 (2014) 141-153

[57] J. H. Jeong, M. S. Jhon, J. S. Harlow and J. van Osdol *Smoothed Particle Hydrodynamics: Applications to heat Conduction* Computer Physics Communications 153 (2003) 71-84

[58] J. J. Monaghan, H. E. Huppert, M. G. Worster *Solidification using smoothed particle hydrodynamics.* Journal of Computational Physics 206 (2005) 684-705

[59] A. Farrokhpanah, M. Bussmann and J. Mostaghimi *New smoothed particle hydrodynamics (SPH) formulation for modeling heat conduction with solidification and melting.* Numerical Heat Transfer, Part B, 71 (2017) 299-312

[60] J. W. Swegle, D. L. Hicks and S. W. Attaway *Smoothed Particle Hydrodynamics Stability Analysis.* Journal of Computational Physics 116 (1995) 123-134

[61] D. A. FULK And D. W. QUINN *An Analysis of 1-D Smoothed Particle Hydrodynamics Kernels* Journal Of Computational Physics 126, 165–180 (1996)

[62] N.J. Quinlan, M. Lastiwka *Truncation error in mesh-free particle methods* Int. J. Numer. Meth. Engng. (2006) 66: 2064-2085

[63] J. Bonet, M.X. Rodrıguez-Paz *Hamiltonian formulation of the variable-h SPH equations* Journal of Computational Physics 209 (2005) 541–558

[64] S.J. Lind, P.K. Stansby, *High-order Eulerian incompressible smoothed particle hydrodynamics with transition to Lagrangian free-surface motion*, Journal of Computational Physics, Volume 326, 2016, Pages 290-311,

[65] F. Macià, P.E. Merino-Alonso, A. Souto-Iglesias, *On the convergence of the solutions to the integral SPH heat and advection–diffusion equations: Theoretical analysis and numerical verification*, Computer Methods in Applied Mechanics and Engineering, Volume 397, 2022, 115045,

[66] A.M.A. Nasar, G. Fourtakas, S.J. Lind, B.D. Rogers, P.K. Stansby, J.R.C. King *High-order velocity and pressure wall boundary conditions in Eulerian incompressible SPH* Journal of Computational Physics 434 (2021) 109793

[67] S.J. Lind, B.D. Rogers and P.K. Stansby *Review of smoothed particle hydrodynamics: towards converged Lagrangian flow modelling* Proc. R. Soc. A 476: 20190801.

[68] D. Violeau *Fluid Mechanics and the SPH Method* Oxford University Press (2012)

[69] K. Dolag , M. Bartelmann , H. Lesch *SPH simulations of magnetic fields in galaxy clusters* Astron. Astrophys. 348 (1999) 351-363

[70] R. Vacondio, C. Altomare, M.D. Leffe, X. Hu, D.L. Touzé, S. Lind, J.C. Marongiu, S. Marrone, B.D. Rogers, A.S. Iglesias *Grand challenges for Smoothed Particle Hydrodynamics numerical schemes* Computational Particle Mechanics (2021) 8:575–588

[71] J. Bonet , T.-S.L. Lok *Variational and momentum preservation aspects of Smoothed Particle Hydrodynamic formulations* Comput. Methods Appl. Mech. Engrg. 180 (1999) 97-115

[72] D.J. Barker, P. Brito-Parada and S.J. Neethling *Application of B-splines and curved geometries to boundariesin SPH* Int. J. Numer. Meth. Fluids2014;76:51–68

[73] P. M. Campbell *Some new algorithms for boundary value problems in smoothed particle hydrodynamics* Technical Report, 6 Jun. 1988 - 6 Jun. 1989 Mission Research Corp., Albuquerque, NM.

[74] S.Adami, X.Y.HuN, A.Adams *A generalized wall boundary condition for smoothed particle hydrodynamics* Journal of Computational Physics Vol 231, 21 (2012) 7057-7075

[75] F. Maciá, M. Antuono, L. M. González, A. Colagrossi *Theoretical Analysis of the No-Slip Boundary Condition Enforcement in SPH Methods* Progress of Theoretical Physics, Vol 125, 6 (2011) 1091–1121

[76] V. Jones, Q. Yang, L. McCue-Weil *SPH Boundary Deficiency Correction for improved Boundary Conditions at Deformable Surfaces* Ciencia Y tecnología De Buques, 4(7), 21-30

[77] J. Wang, H. Hua C. Gu *On the correction of the boundary deficiency in SPH for the frictional contact simulation* Science China Technological Sciences vol 57 (2014) 86–100

[78] L. Sigalotti, J. Klapp, O. Rendón, C. Vargas, F. Peña-Polo *On the kernel and particle consistency in smoothed particle hydrodynamics* Applied Numerical Mathematics Vol 108 (2016) 242-255

[79] Q. Zhu1, L. Hernquist, and Y. Li *Numerical Convergence in smoothed particle hydrodynamics* The Astrophysical Journal, Vol 800, 1 (2015)

[80] J. K. Chen, J. E. Beraun C. J. Jih *An improvement for tensile instability in smoothed particle hydrodynamics* Computational Mechanics vol 23 (1999) 279–287

[81] A.A. Lukyanov, K. Vuik *A stable SPH discretization of the elliptic operator with heterogeneous coefficients* Journal of Computational and Applied Mathematics, Vol 374, 15 (2020) 112745

[82] S. Marrone, M. Antuono, A. Colagrossi, G. Colicchio, D. Le Touze, G. Graziani *δ-SPH model for simulating violent impact flows* Computer Methods in Applied Mechanics and Engineering Vol 200, 13–16 (2011) 1526-1542

[83] A.N. Parshikov, S.A. Medin, I.I. Loukashenko, V.A. Milekhin *Improvements in SPH method by means of interparticle contact algorithm and analysis of perforation tests at moderate projectile velocities* International Journal of Impact Engineering 24 (2000) 779796

[84] A.N. Parshikov, S.A. Medin *Smoothed Particle Hydrodynamics Using Interparticle Contact Algorithms* Journal of Computational Physics 180, 358–382 (2002)

[85] J.J. Monaghan *A Study on Application of Smoothed Particle Hydrodynamics to Multi-Phase Flows* International Journal of Nonlinear Sciences and Numerical Simulation, Vol 13, 6 (2012)

[86] A. Rafiee, D. Dutykh, F. Dias *Numerical simulation of wave impact on a rigid wall using a two-phase compressible SPH method* Procedia IUTAM Vol 18 (2015) 123-137

[87] J.J. Monaghan, A. Kocharya *SPH simulation of multi-phase flow* Computer Physics Communications 87 (1995) 225-235

[88] G.Fourtakas, B.D.Rogers *Modelling multi-phase liquid-sediment scour and resuspension induced by rapid flows using Smoothed Particle Hydrodynamics (SPH) accelerated with a Graphics Processing Unit (GPU)* Advances in Water Resources, Vol 92 (2016) 186-199

[89] G.X. Zhu, L. Zou, Z. Chen, A.M. Wang, M.B. Liu *An improved SPH model for multiphase flows with large density ratios* International Journal for Numerical Methods in Fluids, Vol 86,2 (2017) 167–184

[90] J. Lemaitre, J.P. Sermage R. Desmorat *A two scale damage concept applied to fatigue* International Journal of Fracture, vol 97, 67 (1999)

[91] T. De Vuyst, R. Vignjevic *Total Lagrangian SPH modelling of necking and fracture in electromagnetically driven rings* International Journal of Fracture volume 180 (2013) 53–70

[92] D.J. Price *Modelling discontinuities and Kelvin-Helmholtz instabilities with SPH* Journal of Computational Physics, Vol 227, 24 (2008) 10040-10057

[93] F. Xu, Y. Zhao, R. Yan, T. Furukawa *Multidimensional discontinuouse SPH method and its application to metal penetration analysis* International Journal for Numerical Methods in Engineering 93,11 (2013) 1125-1146

[94] J.J.Monaghan *On the problem of penetration in particle methods* Journal of Computational Physics, Vol 82, 1 (1989) 1-15

[95] W.G. Hoover, C.G. Hoover, E.C. *Smoothed-particle applied mechanics: Conservation of angular momentum with tensile stability and velocity averaging* Phys. Rev. E, 69 (2004) 016702-1–10

[96] LB. Lucy *A numerical approach to the testing of the fission hypothesis* Astronomical Journal, vol. 82, Dec. 1977, p. 1013-1024.

[97] X. Li, T. Zhang, Y. Zhang, and G. Liu *Artificial viscosity in smoothed particle hydrodynamics simulation of sound interference* Proc. Mtgs. Acoust. 22, 040005 (2014)

[98] J.J. Monaghan *SPH and Riemann Solvers* Journal of Computational Physics, Vol 136, 2 (1997) 298-307

[99] M. Ferrand, D.R. Laurence, B.D. Rogers, D. Violeau and C. Kassiotis *Unified semi-analytical wall boundary conditions for inviscid, laminar or turbulent flows in the meshless SPH method* Int. J. Numer. Meth. Fluids 2013; 71:446–472

[100] J.J. Monaghan *Simulating free surface flows with SPH* J Comput Phys 1994;110:399–406

[101] M. Ferrand1, D.R. Laurence, B.D. Rogers, D. Violeau and C. Kassiotis *Unified semi-analytical wall boundary conditions for inviscid, laminar or turbulent flows in the meshless SPH method* Int. J. Numer. Meth. Fluids 2013; 71:446–472

[102] V. Jones, Q. Yang, L. McCue-Weil *SPH Boundary Deficiency Correction for Improved Boundary Conditions at Deformable Surfaces* Ship Science Technology - Vol. 4 - n.° 7 - (21-30) July 2010

[103] A Ferrari, M Dumbser, E.F. Toro, A. Armanini *A new 3D parallel SPH scheme for free surface flows* Computers & Fluids 38 (2009) 1203–1217

[104] R. Vacondio, B.D. Rogers and P.K. Stansby *Smoothed Particle Hydrodynamics: Approximate zero-consistent 2-D boundary conditions and still shallow-water tests* Int. J. Numer. Meth. Fluids 2012; 69: –226 253

[105] A. English · J. M. Domínguez · R. Vacondio · A. J. C. Crespo · P. K. Stansby · S. J. Lind · L. Chiapponi · M. Gómez-Gesteira *Modified dynamic boundary conditions (mDBC) for general-purpose smoothed particle hydrodynamics (SPH): application to tank sloshing, dam break and fish pass problems* Computational Particle Mechanics (2022) 9:911–925

[106] W. G. Hoover *Computational Statistical Mechanics* Elsevier Science (2012)

[107] J. Kolafa *Gear formalism of the always stable predictor-corrector method for molecular dynamics of polarizable molecules* The Journal Of Chemical Physics 122, 164105 (2005)

[108] P.W. Cleary and J.J. Monaghan *Conduction Modelling Using Smoothed Particle Hydrodynamics* Journal of Computational Physics 148, 227–264 (1999)

[109] R. Rook , M. Yildiz S. Dost *Modeling Transient Heat Transfer Using SPH and Implicit Time Integration* Numerical Heat Transfer, Part B: Fundamentals, 51:1, 1-23

[110] J.H. Jeong, M.S. Jhon, J.S. Halow, J. van Osdol *Smoothed particle hydrodynamics: Applications to heat conduction* Computer Physics Communications 153 (2003) 71–84

[111] J.B.J Fourier *Théorie Analytique de la Chaleur* Paris: Firmin Didot (1822)

[112] H. D. Weymann *Finite Speed of Propagation in Heat Conduction, Diffusion, and Viscous Shear Motion* American Journal of Physics35, 488 (1967)

[113] A.M.A. Nasar, B.D. Rogers, A. Revell, P.K. Stansby *Flexible slender body fluid interaction: Vector-based discrete element method with Eulerian smoothed particle hydrodynamics* Computers and Fluids 179 (2019) 563–578

[114] H. S. Carslaw and J. C. Jaeger *Conduction of heat in solids* Oxford University Press, 1946

[115] J.J. Monaghan *Simulating free surface flows with SPH* Journal of Computational Physics, (1994) 110, 399–406.

[116] Daniel. J. Price *Modelling discontinuities and Kelvin-Helmholtz instabilities in SPH.* Journal of Computational Physics Vol 227, 24,Pages 10040-10057 (2008)

[117] S. Sibilla *An algorithm to improve consistency in Smoothed Particle Hydrodynamics* Computers Fluids 118 (2015) 148–158

[118] C. Huang, J. M. Lei, M. B. Liu and X. Y. Peng *A kernel gradient free (KGF) SPH method* Int. J. Numer. Meth. Fluids 2015; 78:691–707

[119] J.P.Holman *Heat Transfer* McGraw-Hill, Inc (1986)

[120] H.Y.Miaoa, S.Larosea, C.Perrona, M. Lévesque *Numerical simulation of the stress peen forming process and experimental validation* Advances in Engineering Software 42 (2011) 963-975

[121] M.Strycker1, P.Lava1,W.V.Paepegem, L.Schueremans and D.Debruyne *VALIDATION OF WELDING SIMULATIONS USING THERMAL STRAINS MEASURED WITH DIC* Applied Mechanics and Materials 70 (2011) 129-134

[122] P.Bolourchi1, H.Demirel1, S.Uysal1 *Target recognition in SAR images using radial Chebyshev moments* Signal, Image and Video Processing, 11 (2017) 1033-1040

[123] I . A. Ismail, M . A. Ramadan, T. El danf, A. H. Samak *Multiresolution Fourier- Wavelet Descriptor for Fingerprint Recognition* International Conference on Computer Science and Information Technology 2008

[124] C. Sebastian, E. Patterson, D. Ostberg *Comparison of numerical and experimental strain measurements of a composite panel using image decomposition* Applied Mechanics and Materials, 70 (2011) 63-68

[125] C. Sebastian, E. Hack, E. Patterson *An approach to the validation of computational solid mechanics models for strain analysis* J Strain Analysis 48 (2012) 36-47

[126] J. Li, G. Wang, J. Zhan, S. Liu, Y. Guan, H. Naceur, D. Coutellier, J. Lin *Meshless SPH analysis for transient heat conduction in the functionally graded structures* Composites Communications 24 (2021) 100664

[127] A. Colagrossi, B. Bouscasse, M. Antuono, S. Marrone *Particle packing algorithm for SPH schemes* Computer Physics Communications 183 (2012) 1641–1653

[128] P. Rastelli, R. Vacondio, J.C. Marongiu, G. Fourtakas, B.D. Rogers *Implicit iterative particle shifting for meshless numerical schemes using kernel basis functions* Comput. Methods Appl. Mech. Engrg. 393 (2022) 114716

[129] Y.R.L. Opez, D. Roose *DYNAMIC REFINEMENT FOR FLUID FLOW SIMULATIONS WITH SPH* International Conference on Particle-based Methods - Fundamentals and Applications (2011)

[130] S.C. Whitehouse, M.R. Bate, and J.J. Monaghan *A faster algorithm for smoothed particle hydrodynamics with radiative transfer in the flux-limited diffusion approximation* Mon. Not. R. Astron. Soc. 364, 1367–1377 (2005)

[131] B. Moballa, M. Chern and E. Odhiambo *Incompressible smoothed particle hydrodynamics modeling of thermal convection* Interaction and Multiscale Mechanics, Vol. 6, No. 2 (2013) 211-235

[132] K. Fraser, L.I. Kiss, L. St-George *Adaptive Thermal Boundary Conditions for Smoothed Particle Hydrodynamics* 14th International LS-DYNA Users Conference (2016)

[133] S. J. Farlow *Partial Differential Equations for Scientists and Engineers* DOVER PUBLICATIONS, INC. New York (1983)

[134] K. Szewc, J. Pozorski, A. Tanière *Modeling of natural convection with Smoothed Particle Hydrodynamics: Non-Boussinesq formulation* International Journal of Heat and Mass Transfer Vol. 54, Issues 23–24 (2011) Pages 4807-4816

[135] S.V. Patankar *Numerical Heat Transfer and Fluid Flow* CRC (1980)

[136] A.S. Lavine, D.P. DeWitt, and F.P. Incropera *Fundamentals of heat and mass transfer* John Wiley Sons (2000)

[137] A. Ghavamian, C. H. Lee, A. J. Gil, J. Bonet, T. Heuzé, L. Stainier *An entropy-stable Smooth Particle Hydrodynamics algorithm for large strain thermo-elasticity* Comput. Methods Appl. Mech. Engrg. 379 (2021) 113736

[138] J.P.Gray, J.J. Monaghan, R.P. Swift *SPH Elastic Dynamics* Computer Methods in Applied Mechanics and Engineering Vol 190, 49–50 (2001) 6641-6662

[139] Roy R. Craig, JR. *Mechanics Of Materials 3rd ed.* John Wiley Sons (2011)

[140] R. Feng, G. Fourtakas, B. D. Rogers, D. Lombardi *Large deformation analysis of granular materials with stabilized and noise-free stress treatment in smoothed particle hydrodynamics (SPH)* Computers and Geotechnics 138 (2021) 104356

[141] S. Timoshenko *Strength of Materials - Part II Advanced Theory and Problems* D. Van Nostrand company, inc. (1930)

[142] S.J. Lind, R. Xu, P.K. Stansby, B.D. Rogers *Incompressible smoothed particle hydrodynamics for free-surface flows: A generalised diffusion-based algorithm for stability and validations for impulsive flows and propagating waves* Journal of Computational Physics 231 (2012) 1499–1523

[143] A.M.A. Nasar, B.D. Rogers, A. Revell, P.K. Stansby, S.J. Lind *Eulerian weakly compressible smoothed particle hydrodynamics (SPH) with the immersed boundary method for thin slender bodies* Journal of Fluids and Structures 84 (2019) 263–282

[144] Dalton Ellery Girão Barroso *Equation of State of Uranium and Plutonium* Military Institute of Engineering, Department of Nuclear Energy, (2012) Internal report

[145] D. Jones, M. Ashby *Mechanisms of Creep, and Creep-Resistant Materials* Engineering Materials 1 (Fifth Edition) An Introduction to Properties, Applications and Design (2019) 381-394

[146] A.S. Patki, E.A. Patterson *Decomposing Strain Maps Using Fourier-Zernike Shape Descriptors* Experimental Mechanics 52 (2012) 1137-1149

[147] R. Mukundan, S.H. Ong, P.A. Lee *Image Analysis by Tchebichef Moments* IEEE Transactions on Image Processing 10 (2001) 1357-1364